Oklahoma Department of Transportation
200 NE 21st Street, Oklahoma City, OK 73105-3204

FINAL REPORT ~ FHWA-OK-16-06

DEVELOPMENT OF INEXPENSIVE VEHICLE SENSOR NODE SYSTEM FOR VOLUME, TURN MOVEMENT AND COLLISION AVOIDANCE

Hazem Refai, Ph.D.

Walid Balid, Graduate Student

Hasan Tafish, Graduate Student

School of Electrical and Computer Engineering (ECE)

Gallogly College of Engineering

The University of Oklahoma

Norman, Oklahoma

November 2016

Oklahoma Department of Transportation

The Oklahoma Department of Transportation (ODOT) ensures that no person or groups of persons shall, on the grounds of race, color, sex, religion, national origin, age, disability, retaliation or genetic information, be excluded from participation in, be denied the benefits of, or be otherwise subjected to discrimination under any and all programs, services, or activities administered by ODOT, its recipients, sub-recipients, and contractors. To request an accommodation please contact the ADA Coordinator at 405-521-4140 or the Oklahoma Relay Service at 1-800-722-0353. If you have any ADA or Title VI questions email ODOT-ada-titlevi@odot.org.

DEVELOPMENT OF INEXPENSIVE VEHICLE SENSOR NODE SYSTEM FOR VOLUME, TURN MOVEMENT AND COLLISION AVOIDANCE

FINAL REPORT ~ FHWA-OK-16-06

ODOT SP&R ITEM NUMBER 2252

Submitted to:

Dawn R. Sullivan, P.E.
Director of Capital Programs
Oklahoma Department of Transportation

Submitted by:

Hazem Refai, Ph.D.
Walid Balid, Graduate Student
Hasan Tafish, Graduate Student
School of Electrical and Computer Engineering (ECE)
The University of Oklahoma

November 2016

TECHNICAL REPORT DOCUMENTATION PAGE

1. REPORT NO.	2. GOVERNMENT ACCESSION NO.	3. RECIPIENT'S CATALOG NO.
FHWA-OK- 16-06		

4. TITLE AND SUBTITLE	5. REPORT DATE
Development of Inexpensive Vehicle Sensor Node System for Volume, Turn Movement and Collision Avoidance	Oct 2016
	6. PERFORMING ORGANIZATION CODE

7. AUTHOR(S)	8. PERFORMING ORGANIZATION REPORT
Hazem Refai, Ph.D. Walid Balid Hasan Tafish	The University of Oklahoma 202 W. Boyd St., Room 104 Norman, OK. 73019-0631

9. PERFORMING ORGANIZATION NAME AND ADDRESS	10. WORK UNIT NO.
School of Electrical and Computer Engineering, The University of Oklahoma	
	11. CONTRACT OR GRANT NO. ODOT SP&R Item Number 2252

12. SPONSORING AGENCY NAME AND ADDRESS	13. TYPE OF REPORT AND PERIOD COVERED
Oklahoma Department of Transportation Office of Research and Implementation 200 N.E. 21st Street, Room 3A7 Oklahoma City, OK 73105	Final Report Oct 2013 - Oct 2016
	14. SPONSORING AGENCY CODE

15. SUPPLEMENTARY NOTES

16. ABSTRACT

Real-time traffic surveillance is essential in today's intelligent transportation systems and will surely play a vital role in tomorrow's smart cities. The work detailed in this paper reports on the development and implementation of a novel smart wireless sensor for traffic monitoring. Reliable and computationally efficient algorithms for vehicle detection, speed and length estimation, classification, and time-synchronization were fully developed, integrated, and evaluated. Comprehensive system evaluation and extensive data analysis were performed to tune and validate the system for a reliable and robust operation. Several field studies conducted on highway and urban roads for different scenarios and under various traffic conditions resulted in 99.98% detection accuracy, 97.11% speed estimation accuracy, and 97% length-based vehicle classification accuracy. The developed system is portable, reliable, and cost-effective. The system can also be used for short-term or long-term installment on surface of highway, roadway, and roadside. Implementation cost of a single node including enclosure is US $40.

17. KEY WORDS	18. DISTRIBUTION STATEMENT
Intelligent Transportation System (ITS), Magnetometer Sensors, Traffic Surveillance, Vehicles Detection, WSN	No restrictions. This publication is available from the Office of Research and Implementation, Oklahoma DOT.

19. SECURITY CLASSIF. (OF THIS REPORT)	20. SECURITY CLASSIF. (OF THIS PAGE)	21. NO. OF PAGES	22. PRICE
Unclassified	Unclassified	240	N/A

SI* (MODERN METRIC) CONVERSION FACTORS

APPROXIMATE CONVERSIONS TO SI UNITS

SYMBOL	WHEN YOU KNOW	MULTIPLY BY	TO FIND	SYMBOL
		LENGTH		
in	inches	25.4	millimeters	mm
ft	feet	0.305	meters	m
yd	yards	0.914	meters	m
mi	miles	1.61	kilometers	km
		AREA		
in^2	square inches	645.2	square millimeters	mm^2
ft^2	square feet	0.093	square meters	m^2
yd^2	square yard	0.836	square meters	m^2
ac	acres	0.405	hectares	ha
mi^2	square miles	2.59	square kilometers	km^2
		VOLUME		
fl	fluid ounces	29.57	milliliters	mL
oz	gallons	3.785	liters	L
gal	cubic feet	0.028	cubic meters	m^3
ft^3	cubic yards	0.765	cubic	m^3
		MASS		
oz	ounces	28.35	grams	g
lb	pounds	0.454	kilograms	kg
T	short tons (2000 lb)	0.907	megagrams (or "metric ton")	Mg (or "t")
		TEMPERATURE (exact degrees)		
°F	Fahrenheit	5 (F-32)/9	Celsius	°C
		or (F-32)/1.8		
		ILLUMINATION		
fc	foot-candles	10.76	lux	lx
fl	foot-Lamberts	3.426	candela/m^2	cd/m^2
		FORCE and PRESSURE or STRESS		
lbf	poundforce	4.45	newtons	N
lbf/in^2	poundforce per square inch	6.89	kilopascals	kPa

APPROXIMATE CONVERSIONS FROM SI UNITS

SYMBOL	WHEN YOU KNOW	MULTIPLY BY	TO FIND	SYMBOL
		LENGTH		
mm	millimeters	0.039	inches	in
m	meters	3.28	feet	ft
m	meters	1.09	yards	yd
km	kilometers	0.621	miles	mi
		AREA		
mm^2	square millimeters	0.0016	square inches	in^2
m^2	square meters	10.764	square feet	ft^2
m^2	square meters	1.195	square yards	yd^2
ha	hectares	2.47	acres	ac
km^2	square kilometers	0.386	square miles	mi^2
		VOLUME		
mL	milliliters	0.034	fluid ounces	fl oz
L	liters	0.264	gallons	gal
m^3	cubic meters	35.314	cubic feet	ft^3
m^3	cubic meters	1.307	cubic yards	yd^3
		MASS		
g	grams	0.035	ounces	oz
kg	kilograms	2.202	pounds	lb
Mg (or "t")	megagrams (or "metric ton")	1.103	short tons (2000 lb)	T
		TEMPERATURE (exact degrees)		
°C	Celsius	1.8C+32	Fahrenheit	°F
		ILLUMINATION		
lx	lux	0.0929	foot-candles	fc
cd/m^2	candela/m^2	0.2919	foot-Lamberts	fl
		FORCE and PRESSURE or STRESS		
N	newtons	0.225	poundforce	lbf
kPa	kilopascals	0.145	poundforce per square h	lbf/in^2

*SI is the symbol for the International System of Units. Appropriate rounding should be made to comply with Section 4 of ASTM E380.(Revised March 2003)

Acknowledgements

PI Dr. Refai and his research team recognize Oklahoma Department of Transportation (ODOT) for providing fund to support the research activities of this project. Additionally, ODOT personnel are highly acknowledged for support in coordinating highway deployments, testing developed system, and engaging in insightful discussions throughout this project.

Table of Contents

List of Tables

List of Figures

Executive Summary

Traffic surveillance is an integral part of the intelligent transportation systems (ITS) network. Providing reliable, real-time traffic surveillance is crucial for 21st century ITS. These solutions facilitate instantaneous decision-making, improve roadway efficiency; and maximize existing transportation infrastructure capacity, making transportation systems safe, efficient, and more reliable in anticipation of the rapidly approaching era of smart cities. The work detailed in this report introduces the design, development, and implementation of a novel, fully-autonomous, intelligent wireless sensor for real-time traffic surveillance. Multi-disciplinary, innovative integration of state-of-the-art ultra-low-power embedded systems, smart physical sensors, and wireless sensor networks, coupled with intelligent algorithms—will address the components composition of the developed platform, namely *Intelligent Vehicle Counting and Classification Sensor* (*i*VCCS). Reliable and computationally efficient intelligent algorithms for vehicle detection, speed and length estimation, vehicle classification, time-synchronization, and drift compensation were fully developed, integrated, and evaluated. Several length-based vehicle classification schemes for the state of Oklahoma were developed, implemented, and evaluated using machine learning algorithms and probabilistic modeling of vehicle magnetic length. A feature extraction employing different technique was developed to find the optimal features for magnetic signature-based vehicle classification. Comprehensive system evaluation and extensive data analysis were performed to fine-tune and validate the sensor, ensuring reliable and robust operation. Several field studies were conducted on a number of highways and urban roads under different scenarios and various traffic conditions, resulting in 99.98% detection accuracy, 97.4782% speed estimation accuracy, and 97.6951% classification rate when binning vehicles into four groups based on their magnetic length, and 81% magnetic signature-based vehicle classification accuracy. The developed platform is portable and cost-effective—a single sensor node costs only $40. It can be used for short-term installment (e.g., work zone safety, traffic flow studies, roadways and bridges design, and traffic management in atypical situations), as well as long-term deployment (e.g., collision avoidance at intersections, traffic monitoring, and others) on highway, roadway, or roadside surfaces. This platform is expected to significantly supplement other data collection methods used

for traffic monitoring throughout the United States. This technology will surely play a vital role in tomorrow's smart cities.

Chapter 1: INTRODUCTION

1.1 Introduction

The rapidly increasing rate of surface transportation—driven by an ever-growing population—and its impact on traffic safety has been a major concern for the nation's transportation agencies over the last decades. The U.S. Federal Highway Administration (FHWA) predicts a 23% increase in vehicle miles traveled by 2032 [1].

Statistical studies by the World Health Organization (WHO) reported 1.25 million people die and up to 50 million injuries occur every year on the world's roads [2]. The U.S. National Highway Traffic Safety Administration (NHTSA) reported 32,719 fatalities and 2.313 million injuries in 2013, 28% of which were speed-related [3]. Annual traffic fatalities caused by trucks reportedly cause 4,000 deaths and 100,000 injuries to travelers. Vehicular fatalities on U.S. roadways have an annual direct economic cost of $242 billion, resulting from 24 million crashes. This figure represents 1.6% of the $14.96 trillion U.S. Gross Domestic Product (GDP) reported in 2010 [4]. This total increases to $836 billion when considering societal harm from vehicle crashes. Furthermore, 44% of the U.S. roadways are congested. According to the 2015 Urban Mobility Scorecard report [5], traffic congestion costs the U.S. $160 billion each year as a result of 7 billion lost hours and 3 billion fuel gallons wasted. Additionally, 31% of carbon dioxide emissions come from vehicle tailpipes [6].

Additionally, when compared with passenger vehicles, trucks or commercial vehicles have a significant impact on pavement service life. For example, a vehicle hailing a 40-ton load causes over 4,000 times more road damage than a five-ton loaded vehicle. Moreover, according to [7], approximately 4,000 fatalities and more than 95,000 injuries reported in 2013 involved large trucks. Such an impact requires appropriate and distinctive traffic planning strategies to mitigate the effect of anticipated increases in truck traffic. Adequate information about freight volume and vehicle classification is needed to support geometric and structural design of roadways and bridges.

Without assertive, proactive solutions, traffic crashes are predicted to rise, and roadways congestion is estimated to worsen. The annual delay in the U.S. will grow to 8.3 billion hours, resulting in an increased cost of $192 billion [5].

Although vehicle travel on U.S. highways increased by 39% from 1990 to 2013, new road mileage increased by only 4%. Hence, to mitigate the impact of continued growing demand on transportation and to prevent worsening levels of roadway congestion, it has been suggested that the U.S. FHWA will be required to expand current transportation infrastructure capacity by 23%. One option to achieve this goal is adding 4,200 miles of new roadway each year [8]. Another clever option is developing intelligent transportation system (ITS) technologies that maximize existing transportation infrastructure capacity and improve efficiency, making transportation systems safe, efficient, and more reliable for the rapidly approaching era of smart cities.

1.2 Intelligent Transportation Systems and Smart Cities

ITS are an integral part of nationwide traffic management systems (TMS). ITS performance depends substantially on accuracy of reported data and spatial distribution of traffic sensors [9], which in-turn has a major influence on the efficiency and safety of highways and roadways. Designing and planning ITS are a complex task that requires extensive analysis of public demand for transportation. In order to determine transportation needs, it is important to understand the underlying characteristics of traffic patterns, such as vehicle classifications, vehicle volume and occupancy, and travel time, among many others. This understanding is an essential aspect of assisting traffic projection studies and transportation planning [10].

Real-time traffic monitoring systems play a key role in the transition toward smart cities and more efficient ITS. Autonomous traffic sensing is at the heart of smart city infrastructures, wherein smart wireless sensors are used to measure traffic flow, predict congestion, and adaptively control traffic routes. Doing so effectively provides an awareness that enables a more efficient use of resources and infrastructure.

Internet of Things (IoT) are reshaping the future. Experts project that by 2020 nearly four billion people, more than 25 million Apps, and 26 billion embedded devices will be connected to the internet, producing 50 trillion gigabytes of data and revenue opportunities of up to four trillion US dollar [11]. For ITS to be effective in the era of IoT, traffic surveillance systems should have sufficient spatial distribution that allows all network elements to be interconnected, providing reliable information about traffic conditions; enabling real-time data exchange among various infrastructure components; and facilitating instantaneous decision-making. In the context of ITS for smart cities, IoT technology will allow new services aimed at greatly improving quality of life.

1.3 Current Traffic Surveillance Technologies

Vehicle detection and traffic surveillance technologies are a core component of ITS. Both functions are subject to continuous improvement toward enhancing vehicle presence detection, speed estimation, and vehicle classification. Traffic detection and volume prediction methods are dependent upon a number of factors, including current and historic traffic measurements. Widely used traffic surveillance technologies can be classified into three groups: intrusive, non-intrusive, and off-roadway sensors.

1) Intrusive sensors include inductive loops (IDL), magnetic detectors, pneumatic road tubes, piezoelectric, and weight-in-motion (WIM) sensors. These technologies are embedded in the road surface after saw-cutting the surface or adding roadway holes.
2) Non-intrusive sensors include vision systems, microwave radar, and infrared and ultrasonic detectors. These technologies can be installed atop roadway or roadside surfaces or mounted overhead.
3) Off-roadway sensors, (e.g., remote sensing via aircraft or satellite and probe vehicles equipped with Global Positioning System (GPS) receiver) do not require installation on roadways.

A description of these technologies can be found in [8], [12]. Both intrusive and non-intrusive sensors are power-hungry, expensive, and have been known to cause installation difficulties. They sensors typically require wired infrastructures and power lines for energy supply. Other drawbacks of intrusive sensors include its large-size, short life—as short as 48h for tubes [13], and high maintenance cost, which require lane closure and traffic disruption. Furthermore, piezoelectric and WIM sensors rely on pavement geometry, meaning that a deterioration in pavement will result in unreliable data. Moreover, resurfacing or repairing roadways requires reinstalling sensors. Worker safety for those deploying intrusive systems has been a concern [13]. Although vision and radar systems are widely considered accurate and typically do not disrupt traffic, their performance is subject to weather conditions (e.g. fog, rain, snow, or wind). Off-roadway sensors provide limited traffic statistics at fixed location and are limited due to their dependence on the number of probe vehicles [8], [12]. Consequently, the high cost associated with the aforementioned technologies (e.g., initial cost, regular maintenance and calibration costs, and others) limits the spatial distribution and large-scale integration of these technologies. Scalability and availability of traffic monitoring systems are essential for efficient and reliable, real-time ITS [9].

1.4 Wireless sensor networks

Wireless sensor networks (WSN) are emerging as promising technology and a key enabler for an enormous number of physical-world sensing applications that have not previously been possible (e.g., IoT) [14]. WSN have demonstrated exceptional features such as flexibility, scalability, reliability, and power efficiency [15]. Network scalability is exceptionally important for ITS, particularly as systems are able to accommodate an increased number of nodes connected in an ad-hoc, self-configurable manner [16]. A comprehensive survey of WSN for ITS applications can be reviewed in [15].

Systems employing WSN consist of medium to large networks of inexpensive wireless nodes capable of sensing, processing, and collaboratively distributing data acquired from the physical-world [14].

1.5 Magnetometer Sensors

Rapid technology advancements in solid electronics, embedded computing, and wireless communication protocols have transformed magnetometer sensors (MAG) into cost-effective and energy-efficient alternatives to IDLs. Unlike other methods, MAG are immune to poor weather condition and environmental factors. They do not require line-of-sight and they have a longer lifetime [17]. Integrating WSN with state-of-the-art embedded MAG has enabled autonomous methods for real-time traffic surveillance application (e.g., vehicle detection on roadways, and in parking lots, speed estimation, and vehicle classification). Many credit the PATH program at University of California [12] for initiating the use of MAG sensors in traffic surveillance applications.

1.5.1 Magnetometer Sensor Theory of Operation

The earth's magnetic field or geomagnetic field ($\boldsymbol{B}_{\gamma}$) is nearly uniform at any specific place on the earth's surface, ranging between approximately 25 and 65 microtesla (μT)—0.25 to 0.65 gauss (G). However, the field's direction and intensity change from place-to-place and over time. For example, in Oklahoma, USA, current field intensity is $F_M \approx 51\mu T$, which is the magnitude of three geomagnetic field components: north $B_X \approx 21.95\mu T$, east $B_Y \approx 1.135\mu T$, and vertical $B_Z \approx 46\mu T$ components [18].

$\boldsymbol{B}_{\gamma}$, is a three dimensional vector that can be approximately modeled at Earth's surface as a magnet dipole (i.e., geocentric axial dipole), as it is tilted by 11.5° along the Earth's spin axis. Its south pole points towards geomagnetic north pole (see Figure 1-1).

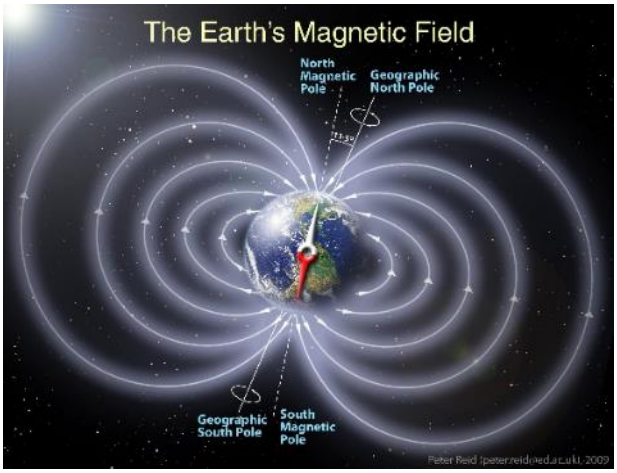

Figure 1-1 Earth's magnetic field lines distribution [19]

Geographic heading can be estimated by transferring $\boldsymbol{B}_\gamma$ to coordinate plane and knowing the declination angle. The field coordinate plane is shown in Figure 1-2. $\boldsymbol{B}_\gamma$ vector is described using seven components: 1) northerly intensity $\boldsymbol{B_x}$; 2) easterly intensity $\boldsymbol{B_y}$; 3) vertical intensity $\boldsymbol{B_z}$; 4) horizontal intensity $\boldsymbol{H}$; 5) total intensity $\boldsymbol{F_M}$; 6) inclination angle $\boldsymbol{I}$—angle between the magnetic field B and horizontal plane; and 7) declination (magnetic variation) angle $\boldsymbol{D}$—angle between the Geographic North and H. The quantities H, F_M, I, and D, can be determined using Eq. 1-1, Eq. 1-2, Eq. 1-3, and Eq. 1-4, respectively, from the orthogonal magnetic field components B_x, B_y, and B_z. Figure 1-2 depicts $\boldsymbol{B}_\gamma$ vector elements in coordinate plane. Table 1-1 shows the range of magnetic elements at the Earth's surface.

$$H = \sqrt{B_x^2 + B_y^2} \qquad \textbf{Eq. 1-1}$$

$$F_M = \sqrt{H^2 + B_z^2} = \sqrt{B_x^2 + B_y^2 + B_z^2} \qquad \textbf{Eq. 1-2}$$

$$I = \tan^{-1}\frac{B_z}{H} = \tan^{-1}\frac{B_z}{\sqrt{B_x^2 + B_y^2}} \qquad \textbf{Eq. 1-3}$$

$$D = \tan^{-1}\frac{B_x}{B_y} \qquad \textbf{Eq. 1-4}$$

$$\Psi = \tan^{-1}\frac{B_y}{B_x} \mp D = \tan^{-1}\frac{B_y}{B_x} \mp \tan^{-1}\frac{B_x}{B_y} \qquad \textbf{Eq. 1-5}$$

Vehicles have a large mass of highly permeable ferrous materials (e.g., iron, steel, nickel, aluminum, or cobalt) that cause a small local disturbance in the Earth's magnetic field flux lines. Steel, in particular, has the capacity to concentrate flux lines, as its magnetic permeability is high relative to surrounding air. A vehicle with a significant amount of steel in its structure can be detected from a significant distance (e.g., 10m). As a vehicle passes through the Earth's magnetic field, the magnetic flux lines are absorbed in a non-uniform manner, creating a non-uniformity in flux lines, as shown in Figure 1-3. The magnitude and direction of the disturbance depends on several factors, including speed, size, density, and permeability of vehicle structure. Different vehicles have different structures, hence, different disturbance factors relative to the geomagnetic field. This measured disturbance represents a vehicle's magnetic signature (VMS), which is unique and can be measured using MAG. VMS can be analyzed to distinguish between different types of vehicles.

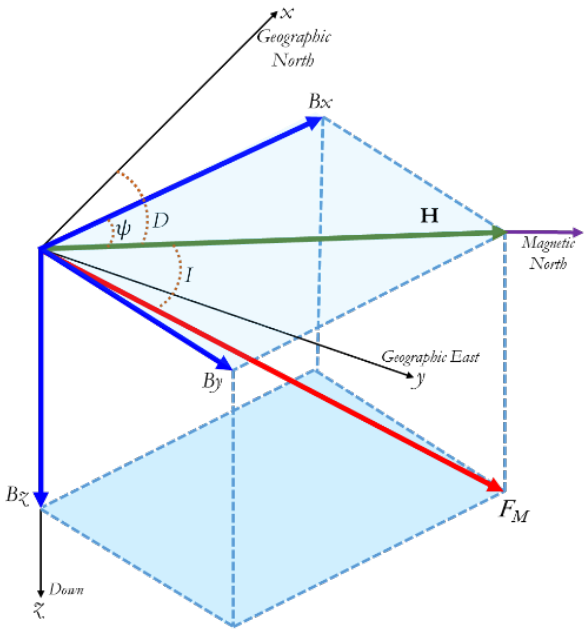

Figure 1-2 The seven elements of the B_Y vector in coordinate plane

Table 1-1 Ranges of magnetic elements at the Earth's surface [20]

Element	Name	Range		Positive sense
		Min	Max	
B_x	Northerly intensity	-17μT	42μT	North
B_y	Easterly intensity	-18μT	17μT	East
B_z	Vertical intensity	-67μT	61μT	Down
H	Horizontal intensity	0μT	42μT	NA
F_M	Total intensity	22μT	67μT	NA
I	Inclination	-90°	+90°	Down
D	Declination	-180°	+180°	East/CW

From a magnetic perspective, the disturbance in magnetic field $\boldsymbol{B_\gamma}$ caused by a vehicle can be modeled as a large number of magnetic dipoles [21], each with its own moment μ and direction r in a three-dimensional space (see Figure 1-4) as given by Eq. 1-6 [22], where B_0 is the localized Earth's magnetic field vector; μ_0 is the magnetic permeability of free space given by $\mu_0 = 4\pi \times 10^7 \times N/A^2$; μ_i is the magnetic dipole moment of the i^{th} dipole; and r_i is the vector the i^{th} dipole moment μ_i to sensor location.

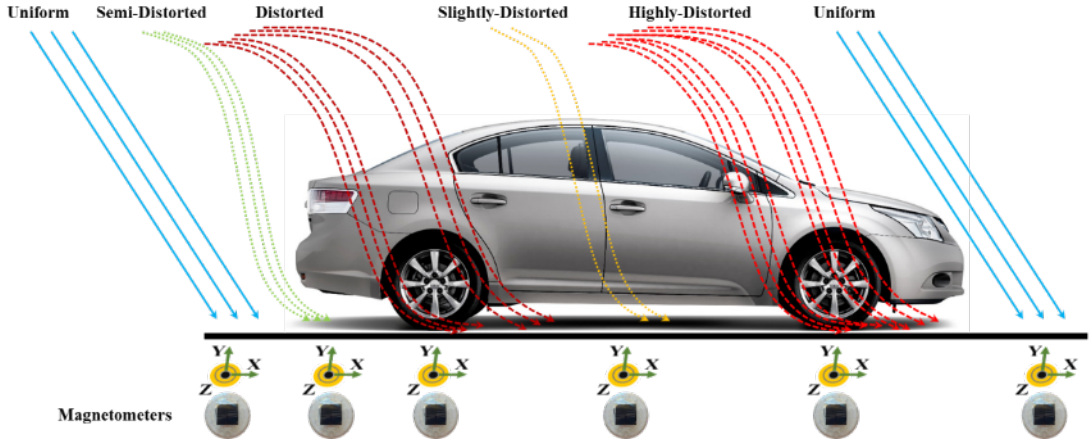

Figure 1-3 Earth's magnetic field lines distorted by passing vehicle

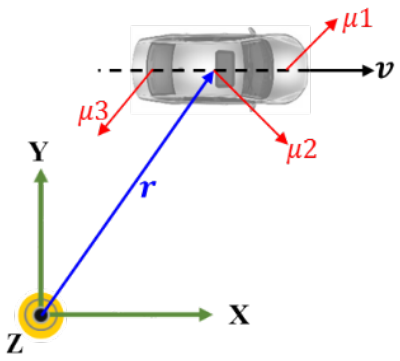

Figure 1-4 Earth's magnetic field lines distorted by passing vehicle

$$B_i(\overrightarrow{\mu_1}, \overrightarrow{r_1} \ldots \overrightarrow{\mu_n}, \overrightarrow{r_n}) = B_0 + \frac{\mu_0}{4\pi} \sum_{i=1}^{n} \frac{3(\overrightarrow{\mu_i}.\vec{r_i})\vec{r_i} - \overrightarrow{\mu_i}|\vec{r_i}|^2}{|\vec{r_i}|^5}; \quad \textbf{Eq. 1-6}$$

$$\overrightarrow{\mu_i}, \vec{r_i} \in \mathbb{R}^3 \quad and \quad i \in \{x, y, z\}$$

A VMS can be described mathematically using a single point dipole model with a moment μ equal to the geometric sum of all dipoles and centered in the vehicle [23], as MAG measure the geometric sum of all dipoles on x, y, and z-axes. Hence, Eq. 1-6 can be written as in Eq. 1-7, where i=1. If a vehicle is moving, $\vec{B}(\vec{\mu}, \vec{r})$ becomes time-variant field, and distance r becomes a function of time t, as shown in Eq. 1-8. Eq. 1-8 can ultimately be used to estimate the maximum magnetic field strength at distances r from a vehicle; also, it can be used to estimate vehicle trajectory, as well as its speed [24], [25].

$$\vec{B}(\vec{\mu}, \vec{r}) = B_0 + \frac{\mu_0}{4\pi} \frac{3(\vec{\mu}, \vec{r})r - \vec{\mu}|\vec{r}|^2}{|\vec{r}|^5} \quad \textbf{Eq. 1-7}$$

$$\vec{B}(t) = B_0 + \frac{\mu_0}{4\pi} \frac{3(\vec{\mu}, \vec{r}_{(t)})r_{(t)} - \vec{\mu}|\vec{r}_{(t)}|^2}{|\vec{r}_{(t)}|^5} \quad \textbf{Eq. 1-8}$$

Assuming that background noise induced by on-board electronic components is modeled as an additive white Gaussian noise (AWGN), then data obtained from the sensors can be modeled as the sum of $\vec{B}(t)$ in Eq. 1-8 and AWGN $\emptyset$.

$$\hat{B}(t) = \vec{B}(t) + \emptyset_{\mu,\sigma} \quad \textbf{Eq. 1-9}$$

1.6 Research Motivation

The *primary objective* for this research is to design, develop, and implement: a) a non-intrusive, inexpensive, and portable vehicular traffic monitoring sensor that accurately detects, counts, estimates speed and length, and classifies vehicles in real-time; b) a sensor that can be used for short-term deployment (e.g., work zone safety, temporary roadway design studies, traffic management in an atypical situation such as evacuations, and other similar situations), as well as long-term deployment (e.g., traffic management, turn movement, and collision avoidance); and c) a sensor easy-to-install by simply affixing the sensor shell into the surface of highways, roadways, or even roadsides without any intrusive work. Such a solution will maximize existing transportation infrastructure capacity and improve efficiency, making transportation systems safe, efficient, and more reliable for the rapidly approaching era of smart cities.

The *secondary objective* is in response to the critical need of the Oklahoma Department of Transportation (ODOT) for an autonomous surveillance technology to monitor various traffic conditions. Results can be used to supplement current ITS installed throughout the state.

Because traffic volume has significant implications for highway and roadway safety, planning, and design, ODOT—like other US transportation departments—is responsible for collecting permanent and temporary traffic characteristic data (e.g., vehicle count and class) from various statewide locations each year. Initially, data is used for transportation planning strategies and management processes. Unfortunately, many sites are not equipped with a vehicle counter. In this case ODOT personnel either conduct a manual count for short time or hire a contracting company. Manual count requires intensive labor to visit hundreds of sites. Also, this method is simply not feasible on congested highways with several lanes. Moreover, manual count is usually conducted for only a few hours, which doesn't represent accurate traffic volume. Alternative methods used to collect vehicle count and class information in Oklahoma employ: 1) weight-in-motion (WIM) or automatic vehicle classifiers (AVC) deployed on permanent sites located throughout the state or 2) pneumatic road tubes (PRT) installed temporarily for study proposes [26].

PRT are placed on the road surface, crossing the lanes, and then fastened to the roadway. The axle of a passing vehicle causes a differential pressure in the tubes, which triggers axle detection. Speed is estimated by measuring axle travel time from one tube

to another. AVC, on the other hand, employ piezoelectric sensors with inductive loops that are embedded in the roadway. These technologies are known to be highly accurate; however, the systems have several drawbacks and have been known to cause installation difficulties. PRT, for instance, have a short life—as short as 48h [13], can monitor only two lanes, and are prone to error (e.g., over count) fake pulses caused by tubes bouncing after being hit by heavy vehicles traveling at high speeds [26]. Moreover, PRT installation might require road closure and traffic disruption, making their use and the high cost of maintenance prohibited. AVC are permanent systems, deployed only at logistic locations where heavy truck volume has previously been observed. AVC have limited spatial distribution across the state because they are expensive and recorded data is typically accurate only if maintenance and calibration is conducted every three or four months. Moreover, the safety of on-site workers deploying these system remains a major concern [13].

ODOT is in critical need of a technology that is inexpensive, nonintrusive, portable, and easy-to-install to supplement current ITS throughout the state and collect accurate traffic information on a large-scale for extended period of time. Ideally, the system should come at a lower cost than the thousands of dollars paid every year for temporal counting studies at each AVC site.

1.7 Proposed Research

The proposed research aims at developing and implementing a novel, fully-autonomous, intelligent wireless sensor for various traffic surveillance applications. The sensor integrates state-of-the-art components, including an ultralow power, high-performance embedded microcontroller; an energy-efficient wireless transceiver; smart embedded sensors (i.e., 3D MAG and ACCEL); a highly-accurate low-power embedded Global Positioning System (GPS) receiver; dual data storage units; a battery fuel gauge; and atmospheric sensors. All components are managed by distinctive algorithms for implementing various traffic monitoring applications.

A 3-axis MAG sensor is used for measuring magnetic disturbance to the Earth's magnetic field caused by an overpassing vehicle, and a 3-axis ACCEL sensor is used for measuring road surface vertical acceleration resulting from the motion of dynamic loads. Other components include a GPS module for auto-localization and global-synchronization; and an RF module for wireless data transmission. Sensor node firmware can be upgraded over-the-air, which allows a customizable configuration to support

various studies and applications. The sensor is functional in either standalone or peer-network mode wherein an intelligent access-point (*i*AP) manages WSN data transfer. Estimated cost for populating a four-lane highway in both directions is approximately $1000, which includes a 16-sensor node, a handheld wireless sensors configuration device, and an *i*AP.

1.8 Research Contributions

This report introduces the design, development, and implementation of a novel, fully-autonomous, intelligent wireless sensor for various traffic surveillance applications. The sensor integrates state-of-the-art embedded components, all of which are managed by distinctive algorithms for implementation of various traffic monitoring applications.

The developed sensor is portable, inexpensive (i.e., $40 per node), and easy-to-install into the surface of highways, roadways, or even roadsides without intrusive labor. The sensor can be used for short-term deployment (e.g., work zone safety, temporary roadway design studies, traffic management in an atypical situation such as evacuations), as well as long-term deployment (e.g., traffic management, turn movement, collision avoidance, etc.).

A novel multi-threshold-based detection algorithm is also introduced, wherein a drift in geomagnetic reference field baseline threshold (due to variations in temperature, background noise, relative Earth's magnetic field over time, or aging) is adaptively auto-compensated in real-time. This method will aid in solving common problems reported in literature by keeping magnetic signal variation at a minimum; hence, providing reliable vehicle speed estimation under congested traffic, low- and high-speed conditions.

A highly accurate and energy-efficient time-synchronization algorithm that utilizes GPS reference signal PPS (Pulse-Per-Second) was developed and implemented as part of research for this report, as was an algorithm for adaptive compensation of RTC Frequency Drift due to variations in temperature.

The repeatability of VMS and the consistency of MAG sensor output were investigated to determine degree of similarity between several magnetic signatures produced by multiple MAG sensors for the same vehicle under same testing condition.

Several computationally efficient, real-time, length-based vehicle classification schemes developed for the state of Oklahoma were implemented and evaluated via machine learning algorithms and probabilistic modeling. Also, a classification model was

designed and applied to classify vehicles into six groups based on vehicle magnetic signature.

1.9 Report Structure

This report consists of seven chapters, which are organized as follows:

Chapter 1: Includes a general introduction of the scope of this report, including a discussion about current technologies used in ITS; ITS for Smart Cities; wireless sensor networks in ITS; MAG theoretical concept and its application in traffic surveillance; the motivation for this research; and research contributions.

Chapter 2: Includes a literature review of related work and focuses on relevant research contributions in vehicle surveillance using MAG, including vehicle detection, speed and length estimation, vehicle classification, and time-synchronization in WSN.

Chapter 3: Introduces a detailed description of the sensor system level design, including design aspects, components selection, and system architecture and networking.

Chapter 4: Includes information about software development and introduces various distinctive real-time algorithms developed for vehicle detection, speed and length estimation, time synchronization, drift correction, and others.

Chapter 5: Reports on field testing and data collection studies conducted on various highways and roadways throughout the state of Oklahoma.

Chapter 6: Introduces an optimization study and analytical analysis of detection error in vehicle detection algorithms used by MAG.

Chapter 7: Provides an extensive data analysis and performance evaluation of the various functionalities of the developed platform.

Chapter 8: Presents research outcome, and makes recommendations for further research work.

Chapter 2: BACKGROUND & EXISTING KNOWLEDGE

2.1 Introduction

Vehicle-counting and classification data, in particular, play a vital role in designing roadways and bridges; predicting freight; scheduling maintenance operations for resurfacing, reconditioning, and reconstruction of pavement; planning traffic; developing weight enforcement strategies; and analyzing road safety and environmental impact, among a number of other purposes [13]. Over the last decades a vast number of methods have been proposed in literature. Each leverages various types of sensors and focuses on investigating and developing new innovative solutions for traffic surveillance. The methods aim to replace antiquated traffic surveillance technologies by implementing smart WSN. One approach for traffic surveillance that is gaining research attention is utilizing wireless MAG [27]–[53].

2.2 Traffic Monitoring using MAG

The use of magnetic sensors in vehicle detection can be traced to early 1978 [27] when a fluxgate magnetic sensor was used to actuate a lighting system as a vehicle passed the sensor. A recent study [28] proposed a 2-axis MAG for detecting vehicle driving direction. A high detection rate of 99% was observed when traveling vehicles passed closely to the sensor. Performance degraded to 89% as the signal-to-noise ratio (SNR) decreased. A two-threshold, four-state machine algorithm was proposed in [29] for vehicle detection using 3-axis AMR sensor. An active magnetic detection method was introduced in [30]. Although this method solved the baseline drift problem, it was not efficient in power, cost, or size. Authors in [31] proposed a short-time transform detection and recognition algorithm using a MAG sampled at 2KHz. Work proposed in [32] integrated IEEE 802.15.4 transceiver with 32-bit MCU and 1-axis AMR for a vehicle counting and collision warning application. A 3-axis MAG was used in [33] for vehicle detection in parking lots. In [34], a street parking system using a MAG was introduced, and in [35], researchers proposed a vehicle parking detection method using a normalized cross-correlation of a 3-axis MAG signal. Authors in [36] proposed a scheme for identifying the heading direction of a moving vehicle using a two-axis MAG. A wireless link budget study for intersection monitoring using MAG was proposed in [37].

Vehicle speed estimation is a key parameter for traffic surveillance applications [13]. Essential applications demanding speed estimation included length-based vehicle classification [54]; travel time estimation [55]; ramp-metering queue length estimation [56]; work zone safety [57]; curve warning [58]; vehicle emissions estimation [59]; and traffic light control, among many others. Lately, solutions based on cost- and power-efficient sensors (e.g., acoustic, MAG, and ACCEL sensors) have become more and more popular. Each of these has advantages and disadvantages. For example, acoustic and ultrasound sensors are very sensitive to dirt and background noise (e.g., vehicles or wind). In this study, vehicle speed was estimated by means of MAG sensors.

A speed estimation algorithm using MAG was proposed in [38]–[40]. In these studies, a cross-correlation factor R was calculated via FFT by a master node from raw data received from two roadside sensor nodes. Time delay was obtained by R when the resulting signal was maximized. Although this method achieved relatively accurate estimates, it proved computationally expensive, hence, energy inefficient. A region-based approach for speed estimation was proposed in [41]. In this work, the first order derivative was calculated on each sensor node, and a region of each signal was selected based on a threshold sent to the server for processing. Study [42] claimed 90% average speed estimation accuracy by analyzing magnetic length using a single roadside node composed of an accelerometer (ACCEL) and MAG. Two magnetic sensor nodes were used in [43] to estimate speed, and a third node was used for data fusion. Actual speed was under-estimated at an error rate of 20%. Authors in [44] proposed using four magnetic sensor nodes per lane—two on each side of the lane. A 10% error in speed estimation under low speed test (e.g., 6–13m/s) was reported. Studies in [45], [46] proposed algorithms for speed estimation using a single MAG. Notably, this method was designed to estimate only average speed for the number of passing vehicles over time.

Four roadside MAG nodes were used in [38] for detection, speed estimation, and vehicle classification into four groups based on length and height ratio. Two sensor nodes were longitudinally separated by 90cm to estimate vehicle speed. A third sensor node was placed orthogonal to the first sensor node with a separation of 10cm to identify any false detection from an adjacent lane. A fourth sensor node was placed upright the first sensor on a 30cm elevation to differentiate trucks from other vehicles, as height is proportional to the ratio of z-axis of both sensors. Vehicles were classified into four groups based on length and height ratio. Group 1 included sedans; Group 2

included SUVs, pickups, and vans; Group 3 included buses, as well as two and three axle trucks; and Group 1 included four- to six-axle trucks. Acceptable accuracy was reported. However, the proposed method worked for only single lane urban roads. Furthermore, the major dataset was composed of small vehicles records; only a few trucks were included. Thus, results would prove inconclusive. Vehicle classification and detection using a single-axis magnetic sensor and an improved one-against-all support vector machine (ISVM) classifier was proposed in [47]. The proposed algorithm uses concavity and convexity of magnetic signatures to distinguish among heavy tracked, tracked, and light-wheeled vehicles. A limited dataset of 93 vehicles resulted in 90% classification accuracy. In [48], a 3-axis MAG was used for detection and classification in low-speed congested traffic. A fixed-threshold state machine algorithm was employed for vehicle detection, and a tree-based algorithm was implemented for classification. Vehicles were divided into four-groups, namely motorcycles, saloon, buses, and SUVs. Five features were extracted to distinguish between the groups: duration, energy, average energy of vehicle signature, and ratio of positive to negative energy on both X and Y axis. The dataset included only 253 vehicles. Although high detection and classification rates were reported, the dataset was limited to a small number of samples, and trucks and pickups were not considered. Authors in [60] proposed a vehicle classification system using two nodes installed on roadside, each combining an ACCEL and MAG. Three features, namely the integral of each of MAG magnitude, ACCEL magnitude, and magnitude distribution, were extracted and normalized to vehicle speed. Several machine-learning (ML) methods (e.g., logistic regression, neural networks, Naïve based, and space vector machine) were tested. A 93.4% classification accuracy was reported for distinguishing between three groups: motorcycles, passenger cars and pickups, and heavy trucks. However, more than 90% of the dataset was composed of passenger cars. Moreover, class variation in the dataset was limited, and class 5 vehicles with trailers were missing. This class can significantly hinder classification accuracy, as it can be seen on both urban and highway roads and can cause classification confusion due to significant variations in the class. Furthermore, accurate clock synchronization is required for speed estimation, as all extracted features are normalized to speed. In [50], an array of MAG and ACCELs sensors was proposed for vehicle detection, speed estimation, and classification. In this study, three MAG nodes positioned longitudinally reported vehicle arrival and departure times, and six ACCELs spaced six inches apart were positioned over half the lane to detect vehicle axles via a peak detection algorithm. This method was used to guarantee that at least one wheel on each axle would step on one of the ACCELs. Although this

method showed promising results for detecting 2-axle, 3-axle, and 5-axle vehicles, it was deemed expensive and required an enormous amount of intrusive work and high processing capability. Authors in [51] developed a features selection model for vehicle classification using a single MAG in which 17 features were initially identified and extracted, but only 10 optimal features were eventually selected. A limited dataset of 460 vehicles—mostly small cars—resulted in 92.8% average classification accuracy among four-groups, including buses, small-medium cars, and large trucks. Authors in [52] proposed a detection and classification approach using a state machine detection algorithm, a shared adaptive threshold to compensate background noise, and a neuron classifier. A two-axis AMR sensor was employed. A 90% recognition rate was reported for simulation and on-road testing. Authors in [53] integrated MAG, ACCEL, acoustic, and infrared sensors within a single sensor node for vehicle classification. Several features were extracted, including infrared signal peaks count and the minimum and maximum values of MAG and ACCEL signals. A back-propagation neural network was trained to classify vehicles into three groups—light, medium, and heavy vehicles. Dataset was limited to only 50 vehicles. Medium vehicles were classified with acceptable accuracy. However, 25% of light vehicles and 16.7% of heavy vehicles were misclassified. Authors in [61] proposed vehicle detection algorithms based on a state-machine normalized cross-correlation between two sensors placed along the roadside. The study implemented 1) a Gaussian filter to eliminate any interference induced by moving vehicles from adjacent lanes; 2) a k-means clustering for setting a reference for cross-correlation detection state; and 3) a normalized cross-correlation computation between two magnetic signals for speed estimation. A 99.65%, 99.44%, and 92% accuracy was reported for arrival detection, departure detection, and speed estimation of vehicle, respectively. Although this method showed a good accuracy, it required transmitting the magnetic signature from all sensors to a central access point for processing. Finally, in addition to aforementioned platforms, a number of commercial platforms based on MAG are also currently available [62]–[64].

In the aforementioned solutions, vehicles were detected using a single magnetic sensor; vehicle speed was mostly estimated using two sensors at predefined distance; length was calculated from speed and occupancy time; and vehicle classification was achieved by employing either multiple MAG or ACCELs, or a combination of both. A standardized wireless protocol (e.g., IEEE 802.15.4) was considered for node-to-node and node-to-AP communications and synchronization. Nevertheless, in most of these

solutions, sensors had to be embedded in roadway lanes. Although the time required for installing a few systems [62]–[64] into the pavement was comparatively small, these systems are relatively expensive, intrusive, and cannot be used for temporary studies or portable traffic surveillance applications (e.g., work zone safety, roadway design studies, and managing traffic in emergency situations, like evacuations, among others). Although a variety of detection, speed estimation, and classification methods have been proposed, limited evaluation has been performed to measure detection or classification accuracy per vehicle class over a full range of speeds. Furthermore, presented results do not reflect actual performance, as testing datasets were small and limited. Notably, classes 5 to 13 were highly underrepresented. Additionally, some proposed methods [38], [40] are energy-inefficient (i.e., computationally very expensive) and require transmission of big chunks of data to the access point for processing. This is a fundamental limitation in WSN, as the sensors are battery-powered and their network operates in an unlicensed spectrum wherein bandwidth is shared among a vast number of different technologies and devices. Hence, high data loss is highly probable as a consequence of unstable wireless link due to either interfering or heavy trucks traveling over the detection zone. Other methods [42] relied on the assumption that vehicles of the same class moving at the same speed have almost identical signatures. This assumption is misleading for the following reasons: 1) Magnetic length does not represent an actual length of vehicle; 2) lateral distance might change for the same vehicle; and 3) magnetic length estimation accuracy depends on the sensor's sampling rate tolerance, which normally has a ±5% error and can be affected by temperature variations. Additionally, little activity has been performed to evaluate detection and speed accuracy per vehicle class over a full range of speed. A single method fails to encompass variances between different magnetic characteristics.

More importantly and to the best of our knowledge, no study reported detection error types, how to optimize MAG for ideal performance, or consistency of MAG sensors output. Furthermore, limited information was provided in the literature about system design, algorithm development, and comprehensive analysis in various realistic scenarios.

2.3 Vehicle Classification Schemes

2.3.1 Axle-based Vehicle Classification Scheme

In general, vehicle class data is collected from WIM and AVC sites, which use inductive loops (IDL) and piezoelectric sensors for reporting vehicle class according to FHWA Scheme F with 13 classes, as depicted in Figure 2-1.

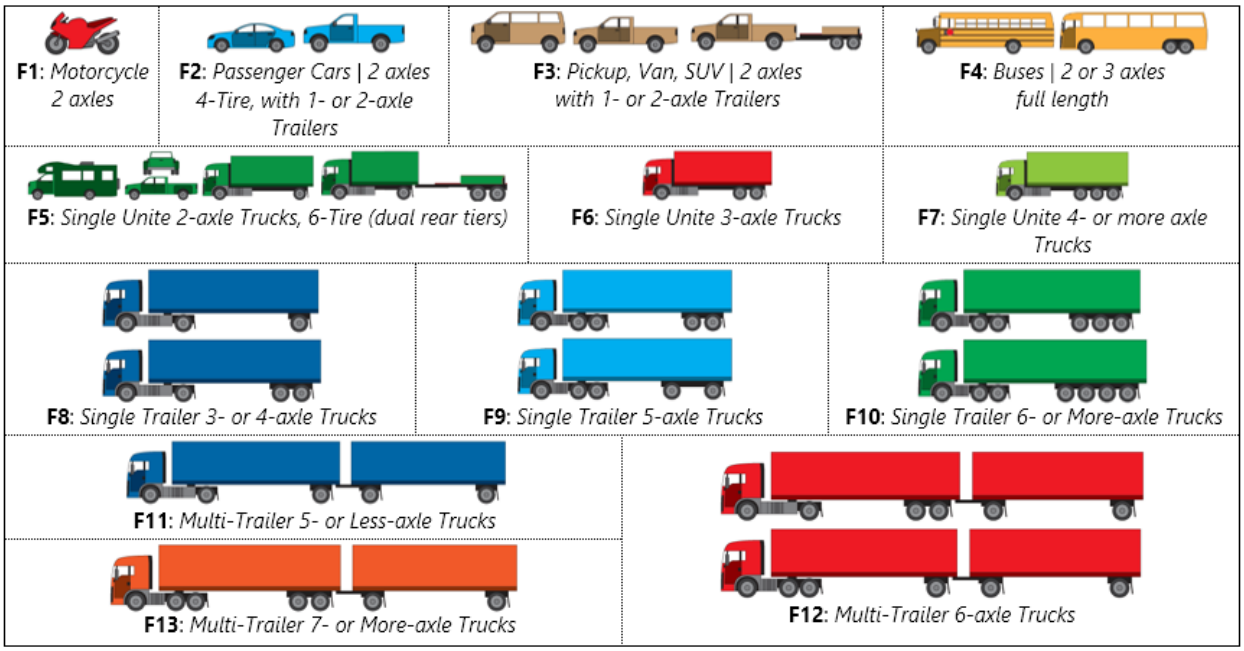

Figure 2-1 U.S. FHWA Classification Scheme F with 13 class

Scheme F was developed during the 1980s and is based on manual classification of visually identifiable vehicle characteristics. The scheme was later amended to provide computational classification based on number of axles and wheelbase axle spacing. Such axle-based vehicle classification (ABVC) systems require intrusive sensors that are plagued with a number of drawbacks, chiefly their reliance on pavement geometry. This means that pavement deterioration will cause unreliable ABVC data. A study [65] conducted by WECAD center at the University of Oklahoma reported high classification inaccuracy rates resulting from sensor misconfiguration at the state's AVC sites. ABVC schemes have proven problematic due to overlapping among vehicle classes, especially with regard to vehicles pulling one-, two-, or three-axle trailers [65]. For example, in one study, 43% of class 3 were falsely classified as class 2 and 45% of class 5 were falsely classified as class 3. In fact, three- or four-axle class 3 trucks often overlap with class 8 trucks, which—upon sensor overpass—causes class 3 to be classified as class 8. Class 6 trucks also overlap with class 4 three-axle buses. Significant overlap has been observed for three- or four-axle class 5 with trailers and classes 8 and 5, as well as buses [65].

As stated earlier, high costs associated with ABVC scheme technologies, as well as high regular maintenance and calibration costs, limit spatial distribution of such systems that are often installed only at strategic points. Thus, the availability of ABVC data is limited. Additionally, the feasibility of collecting ABVC data in urban areas is significantly hindered by bumper-to-bumper congestion during peak hours. Vehicle acceleration/deceleration and stop-and-go scenarios at signals are factors contributing to erroneous data. ABVC using MAG is yet challenging and still ongoing research.

2.3.2 Length-Based Vehicle Classification Schemes

Most traffic planning and engineering requires information only about car vs. truck volume, not about detailed data like number of axels. Traffic flow characteristics are directly affected by long vehicles (i.e., trucks), and trucks have a major impact on road service life [66]. Hence, it is crucial for U.S. DOT agencies to estimate percentage of roadway damage. Accordingly, the *FHWA Traffic Monitoring Guide* [13] provides a generic length-based vehicle classification (LBVC) scheme based on nationwide IDL data. Yet, it is practically impossible to define LBVC boundaries for FHWA F Scheme with 13 classes. Clearly, vehicle magnetic length (VML) overlapping occurs between a number of classes (e.g., class 2 through 5 and class 8 through 10). The proposed LBVC scheme [13] categorizes vehicles into four groups, namely passenger vehicles (PV), single-unit trucks (SU), combination-unit trucks (CU), and multi-unit trucks (MU). The scheme is inexpensive and works best with dual-IDL stations. Notably, the FHWA guide permits states to develop their own LBVC scheme and define length threshold boundaries that best fit vehicle characteristics that vary among states.

Since there is no generic definition for LBVC boundaries, several states have begun to adopt a LBVC scheme to replace outdated ABVC based on local vehicular data collected from AVC and WIM sites located throughout a state's roadways [67], [68]. Many states have defined different length boundaries for their developed schemes. Some have adopted a four-group LBVC scheme; others use a three-group scheme by combining group 3 and 4. For example, the Ohio DOT has adapted a statewide three-group LBVC scheme that bins FHWA Scheme F vehicles into PV, SU, and MU [69], [70]. Florida, Illinois, Washington, and Idaho have also adopted three-group LBVC schemes that classify the same Scheme F vehicles into PV, short trucks (ST), and long trucks (LT) [71]. Minnesota's DOT (MDOT) proposed a four-group LBVC scheme (e.g., motorcycles (MC), short (S), medium (M), and long (L) vehicles) and recognizes a fifth-group, namely

very long (VL), in areas with significant numbers of seven-or-more axle, multi-trailer trucks [67]. Table 2-1, Table 2-2, and Table 2-3 summarize LBVC schemes from a number of states and provides a list of their boundaries. These were identified from data collected using IDLs. Notably, very few efforts attempt to assess the feasibility of defining magnetic length boundaries based on data collected using wireless MAG.

Table 2-1 Three-group LBVC schemes boundaries for different states

Description	FHWA	Illinois	Washington	Idaho	Florida	Ohio	New York
Passenger Car(PV)	F1—F3	0→6.7m	0→6.1m	0→7m	0→6.52m	0→8.53m	0→6.7m
Short trucks (ST)	F4—F7	6.7→11.9m	6.1→12.8m	7→12.2m	6.52→12.9 m	8.53→14m	6.7→11.9m
Long trucks (LT)	F8—F13	≥11.9m	≥12.8m	≥12.2m	≥12.9m	≥14m	≥11.9m

Table 2-2 Four-group FHWA-LBVC scheme boundaries

Description of Vehicles	FHWA-ABVC	FHWA-LBVC
Passenger vehicles (PV)	F1—F3	0→3.96m
Single unit trucks (SU)	F4—F7	3.96→10.67m
Combination trucks (CU)	F8—F10	10.67→18.59m
Multi-trailer trucks (MU)	F11—F13	18.59→36.58m

Table 2-3 MDOT-LBVC scheme boundaries

Description of Vehicles	FHWA-ABVC	Minnesota
Motorcycle (MC)	F1	0→1.98m
Short vehicle (S)	F2—F3	1.98→6.55m
Medium vehicle (M)	F4—F7	6.55→14.93m
Long vehicle (L)	F8—F13	14.93→36.58m

Unlike VMS produced by IDL, vehicle signatures sampled using MAG have less consistent peak magnitude. This is due to several factors, such as differences in sensitivity, vehicle trajectory, and non-symmetry of detection zone. Moreover, IDLs are active magnetic sensors, meaning they generate magnetic field in the IDL zone and resonate at a constant frequency that increases when the generated field is induced by a passing vehicle. When this occurs, a detection state is triggered. Unlike IDLs, MAG are passive sensors that rely on the disturbance of the Earth's magnetic field relative to the presence of a metallic object (i.e., vehicle). Hence, the amount of preamble ferrous

materials in a vehicle structure plays a major role in the sensor's detection range [72]–[74]. A vehicle with a large amount of steel can be detected from quite a lengthy distance, creating significant variations in VML per class. These factors make using MAG for LBVC extremely challenging. The development and implementation of computationally efficient, real-time LBVC schemes for wireless MAG will be introduced in Chapter 6.

2.3.3 Time Synchronization in WSN

Time synchronization (T-sync) is crucial in communication systems to ensure accurate functioning and data fusion, coordinated actuation, and power-efficient duty cycling. T-sync for wired communication networks has been studied thoroughly, and numerous algorithms have been developed in the last decades. The Network Time Protocol (NTP) is perhaps one of the most advanced and time-tested systems [75]. Networks that use NTP externally synchronize nodes to a global reference time that is injected into the network at many places via a set of master nodes, which, in their turn, are synchronized using GPS. Power consumption and computational energy constraints make NTP unfeasible for WSN. Hence, maintaining a T-sync within WSN is challenging, yet critical.

Tremendous effort has been made to implement T-sync protocols for WSN. Authors in [76] introduced *Reference Broadcast Synchronization* (RBS) protocol for WSN. In RBS, nodes broadcast reference beacons to neighbor nodes. Nodes use the beacon signal as a point of reference for their internal clock phase alignment. Authors in [77] proposed *T-sync Protocol for Wireless Sensor Networks* (TPSN). The principle of TPSN is that a multi-level hierarchical network topology is created in which all nodes are assigned levels based on number of hops from root node (level 0). After the topology is created, a root node initiates a synchronization phase wherein every node belonging to level i synchronizes to a node in level $i-1$, and so on, until network-wide synchronization is achieved. TPSN achieves an average synchronization error equal to $16.9\mu S$, which is a considerable improvement above the $29.13\mu S$ error in RBS. Authors in [78] introduced *Energy-Efficient Time Synchronization Protocol* (ETSP), implementing a switching mechanism between RBS and TPSN to reduce node power consumption. The switching threshold relies on the number of transmissions required to maintain synchronization, which, in turn, depend on the number of network nodes. Authors in [79] proposed *Distributed Multi-hop Low cost Time Synchronization* (DMLTS) protocol

based on RBS and TPSN. DMLTS is an improved ETSP, synchronizing a group of nodes by hearing the timing messages of a pair of nodes. This reduces the number of exchanged messages and, notably, the overall energy consumption. In addition to aforementioned protocols, *Flooding T-sync Protocol* (FTSP) [80], *Gradient T-sync Protocol* (GTSP) [81], and *Lightweight Time Synchronization* (LTS) [82] are widely used in WSN. Such protocols have reasonable T-sync precision; however, several challenges remain, for example: 1) failure in wireless communication during synchronization; 2) drift error in T-sync over multi-hop (3.68μs, 20μs, and 3μs on 4 hops in RBS, TSPN, and FTSP, respectively) [83]; 3) required master node, 4) required linear regression (e.g., FTSP), which is computationally demanding and power consuming; 5) TSPN-required hierarchical structure of nodes; and 6) RBS need for separate timestamp synchronization messages for which average error grows with $O(\sqrt{n})$ over multi-hops. These challenges make protocol implementation impractical for a large-scale WSN and infeasible for strict deterministic T-sync requirements. Moreover, T-synch through a periodic or frequent exchange of timing packets among network nodes imposes high power budget demand. According to [84], energy cost of 1Kbit data transmission for a 100m distance is approximately the same as executing 3-million instructions on a 100 MIPS/Watt processor. Thus, local processing is crucial in multi-hop WSN to minimize power consumption.

Due to rapid technology advancement and increased demand, embedded GPS modules have quickly improved in signal sensitivity, accuracy, performance, cost, size, and, more importantly, power consumption. Embedded GPS modules can now be considered the simplest, cost effective solution for high precision timing and clock synchronization. Previously, this approach was not recommended due to a number of factors, most notably energy consumption and cost. Recent studies have investigated the feasibility of using GPS for T-sync in WSN. For example, the feasibility of using low-cost GPS receiver for T-sync of wireless smart sensors for structural health monitoring was investigated in [85]. Authors in [86] developed a GPS-based time synchronization algorithm for WSN with nanosecond accuracy. Authors in [87] claimed ±23μs T-sync accuracy of a single-hop coordinated WSN. The proposed algorithm aimed at correcting sensor node internal clock drift by transmitting a beacon from a corresponding coordinator every 245.76ms. Upon beacon packet arrival, the RF chip generates an interrupt and triggers an internal MCU's timer to measure the internal clock, calculate the difference, and compensate the drift. The coordinators, on the other hand, use the

(Pulse-Per-Second) PPS signal from a GPS module to calculate their internal clock drift and compensate the drift error. This method, however, doesn't account for measurement uncertainties, a variety of propagation paths, or interference from other devices in the ISM band where calculated drift can be affected by jitter. Moreover, several accumulated errors are not considered (e.g., RF chip interrupt tolerance), which renders results unrealistic. Authors in [88] used a GPS DSP platform to control the processor's RTC drift and compensate phase shift when using a 1-PPS signal. Authors reported T–sync accuracy. Details on T-sync protocols for WSN can be found in [83], [89].

Chapter 3: SENSOR DESIGN & SYSTEM INTEGRATION

The roadmap to design and to implement a real-time, standalone, smart wireless sensor that exploits MAG in traffic surveillance applications requires an in-depth understanding of embedded systems hardware-software development process, including component selection, hardware design, software development, system integration, and debugging. The design process and system integration of the intelligent vehicle counting and classification sensor (*i*VCCS) are introduced in the next sections. Various algorithms developed for *i*VCCS are introduced in the next chapter.

3.1 System Overview

The multi-disciplinary, innovative integration of systems modeling coupled with state-of-the-art smart physical sensors, wireless sensor networks, embedded systems, and intelligent algorithms will address the components composition of the developed platform. The developed system is purposefully designed to support various traffic surveillance applications and studies. Figure 3-1 illustrates a conceptual diagram of the various components that compose the developed system, where *i*VCCS nodes are installed into enclosures. Two enclosures are deployed in each lane on a roadway at predefined distance *d*. The system's wireless networking between *i*VCCS nodes and an intelligent access point (*i*AP) is facilitated through IEEE 802.15.4 protocol with ZigBee application layer on top. Wireless networking between *i*AP and server is managed over a cellular network that is assisted by a Quad-Band GSM/GPRS/LTE chipset with GPS module on-board.

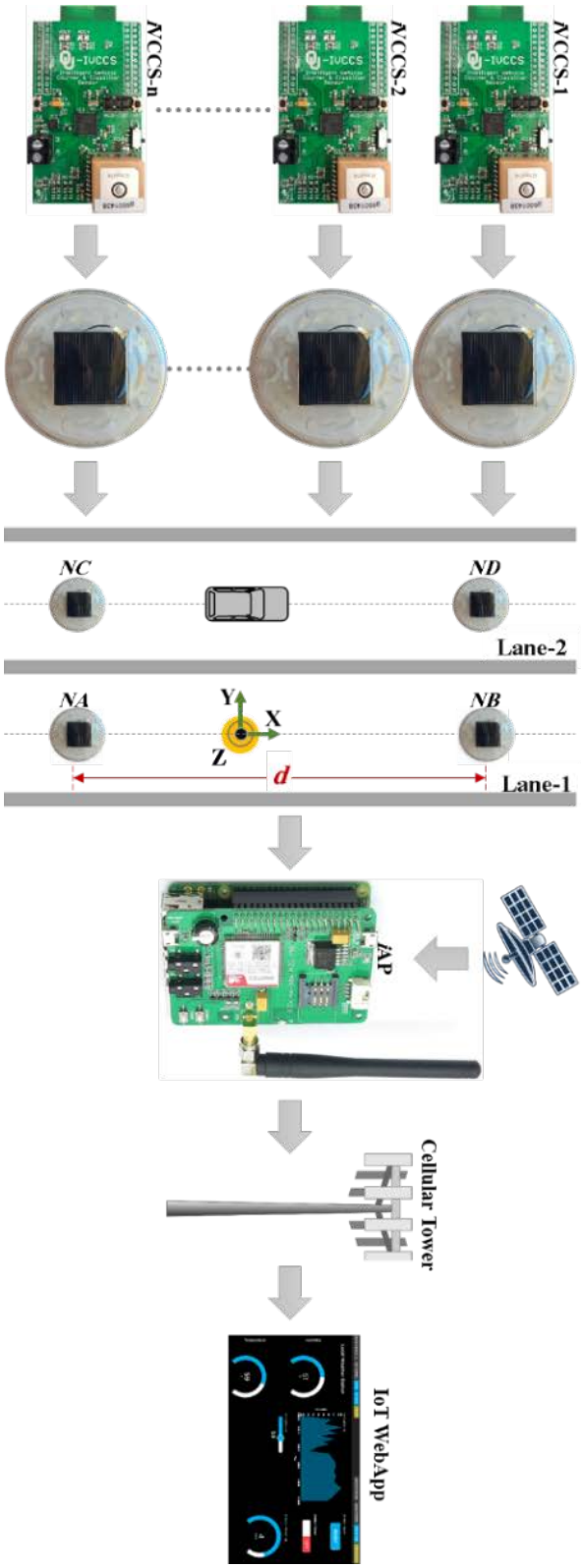

Figure 3-1 Conceptual diagram of developed system

3.2 Design Objectives and Requirements

Two prototypes—representing two generations (G1 and G2) of *i*VCCS—were designed during this research work period. The focus during the first prototype was developing and validating various algorithms and firmware to achieve a highly accurate, real-time traffic monitoring using MAG. As algorithms were developed and validated, the focus in the second prototype was on finalizing the sensor's hardware and implementing self-powering and wireless charging features. Both prototypes share the same design objectives, which are listed in Table 3-1.

Table 3-1 *i*VCCS design objective

Requirement	Discerption
1) Cost	→ Inexpensive technology that can be deployed in mass-quantities
2) Setup	→ Nonintrusive technology that is easy-to-install and doesn't disturb traffic
3) Energy budget	→ Power-efficient technology that can run on battery for long time
4) Performance	→ High accuracy and real-time execution should not be compromised
5) Reliability	→ Should be highly reliable and able to recover from any system faults
6) Lifetime	→ Sensor components should be supported for the next 10 years
7) Portability	→ Can be used for permanents or temporary traffic monitoring studies
8) Flexibility	→ Programmable to supports various traffic monitoring studies applications
9) Scalability	→ System network can be easily expanded by adding more sensors
10) Adaptability	→ Sensor components should function in wide temperature range
11) Size/Weight	→ Should be as small as possible in size and lightweight

3.3 Components Selection Methodology

The primary objective of the selection process is identifying groups of components that should be evaluated for potential integration in the design. A selection criteria was developed to rank and evaluate each component individually based on three factors: 1) characteristics, 2) cost, and 3) size. Component characteristics can be obtained from the component's datasheet; this defines the features and performance of the component at various conditions, including power consumption and operating temperature. The criteria and important aspects of the selection process for each component are explained in the following sections.

3.4 *i*VCCS$_{G1}$ Platform Overview

The *i*VCCS.G1 is a battery-powered, smart wireless sensor node. All components that compose the sensor, shown in Figure 3-2, were selected to achieve minimal power consumption while maintaining low cost and high-performance of the sensor. Figure 3-3 shows *i*VCCS$_{G1}$ printed circuit board (PCB) and component distribution on both layers—top and bottom. Board dimensions are 65(L)×36(W)×16mm(H).

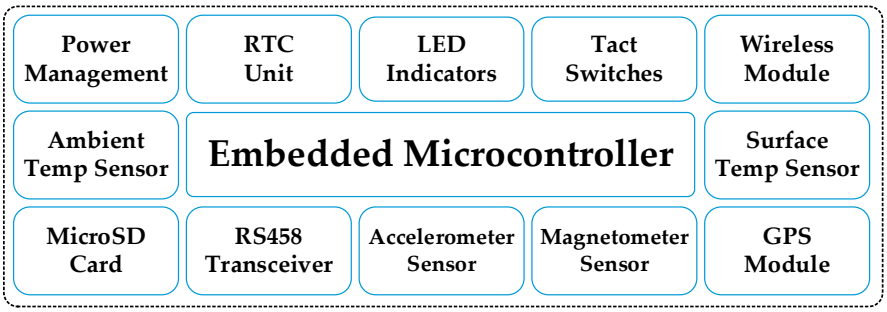

Figure 3-2 *i*VCCS$_{G1}$ functional components block diagram

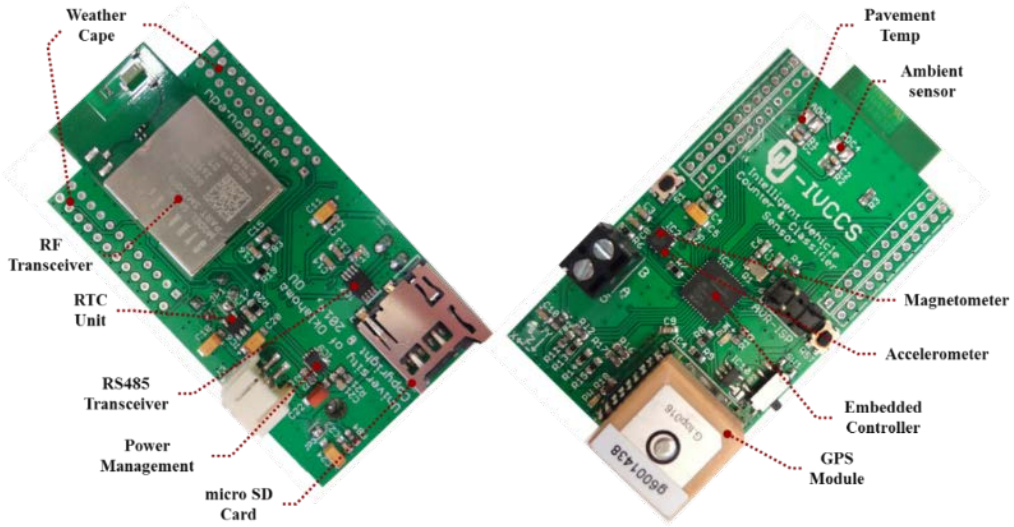

Figure 3-3 *i*VCCS$_{G1}$ printed circuit board with all components marked

3.4.1 Embedded Microcontroller

The core component of *i*VCCS$_{G1}$ is ATxmega128A4—a high-performance, pico-power, 8-bit microcontroller from Atmel [90]. Figure 3-4 illustrates the ATxmega128A4 block diagram and pin layout. ATxmega128A4 has an eight-channel event system with four-channel DMA controller that simultaneously manages eight inter-peripheral signals at 32MHz without CPU intervention. The chip also combines 128KB in-System-

Programmable flash memory for developing advanced codes and algorithms for future applications. The event handler enables the system to avoid software-managed context switching and interrupt handling. Tasks are achieved with event-response time in nanoseconds. ATxmega128A4U also has a programmable multi-level interrupt controller, 34 GPIOs, and rich peripherals and serial interfaces, including USART, TWI, SPI, 12-bit A/D and D/A converter, and RTC, among other on-board peripherals.

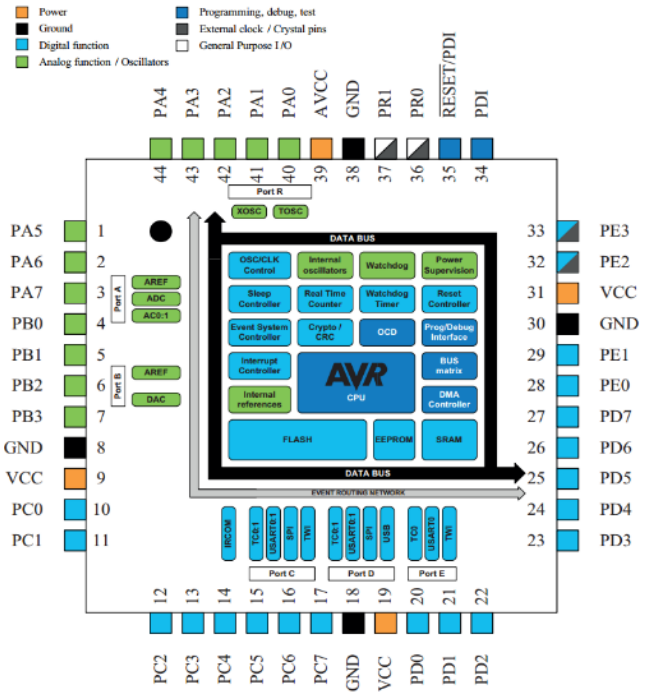

Figure 3-4 ATxmega128A4 internal block diagram and pin-layout

ATxmega128A4 has 10mA, 3.8mA, 1.4μA, and 1μA power consumption in active, idle, power-down, and power-save modes, respectively. It requires 5μs to wake-up from power-down mode and transition to active mode. All these features, in addition to the fact that Atmel was confirmed in 2013 as the fastest growing among top 10 suppliers for 8-bit MCUs, made ATxmega128A4 the best 8-bit MCU candidate.

3.4.2 Magnetometer & Accelerometer Sensors

An extensive search was conducted to find the MAG/ACCEL that best fit the selection criteria. Essential characteristics considered in the selection and evaluation process were output data rate (ODR), sensitivity, resolution, measurement range, disturbing field, power consumption, and cost. Table 3-2 lists specifications of the top three industry-leading MAG sensors in the 2014 marketplace.

FXOS8700CQ was the best fit for design requirements. FXOS8700CQ is an intelligent digital chipset, combining a 3-axis magnetic tunnel, junction-based MAG and a 3-axis ACCEL sensor in one package [91]. The MAG has a dynamic range ±1200μT and 16-bit ADC resolution with sensitivity of 0.1μT/LSB. Power consumption is as low as 8μA and only 2μA in standby mode. FXOS8700CQ has the highest ODR among all other sensors and incorporates the industry's most advanced embedded features. These enable significant system optimization for low power with substantially more savings when the application is driven by interrupt signals. In addition, the chip has a wide measurement range, high resolution (0.1μT/LSB), very low noise density (0.1μT/$\sqrt{Hz}$ at 100Hz bandwidth), high sensitivity, low output noise range (0.3–1.5μT_{RMS} for sampling rates 1.563–800Hz), ability to manage a high disturbing field, low cost, and low power consumption. Unlike other AMR sensors, FXOS8700C uses micro-electro-mechanical system (MEMS) technology with advantages in terms of cost, size, weight, and energy [92]. Figure 3-5 shows FXOS8700CQ block diagram.

Table 3-2 Top MAG candidates for *i*VCCS$_{G1}$

	Freescale FXOS8700CQ 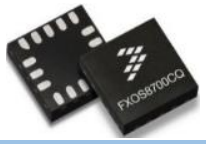	**STMicroelectronics LSM303DLHC** 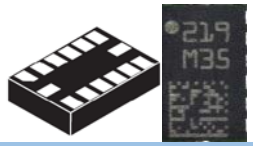	**Honeywell HMC5883L** 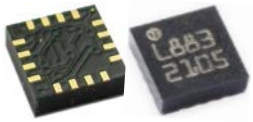
Interface	I^{2}C/SPI + 2-INT	I^{2}C + 2-INT	I^{2}C + 1-INT
Integration	6-axis ACCEL-MAG	6-axis ACCEL-MAG	3-axis MAG
Measurement Range	±12 Gauss	±1.3 ~ ±8.1 Gauss	±1 ~ ±8 Gauss
Update Rate (ODR)	1.563Hz ~ 800Hz	0.75Hz ~ 220Hz	0.75Hz ~ 75Hz
Measurement Period	0.64s ~ 1.25ms	1.33s ~ 4.55ms	1.33s ~ 13.33ms
Resolution	16-bit ADC	14-bit ADC	12-bit ADC
Sensitivity	1 mGauss	2 mGauss	4 mGauss
Disturbing Field	100 Gauss	20 Gauss	-
Maximum Field	1000 Gauss	10,000 Gauss	-
Power Consumption	240μA / 2μA (Idle)	110μA / 1μA (Idle)	100μA / 2μA (Idle)
Cost	US$1.25	US$3.00	US$1.75
Package	QFN-16 (3×3×1.2 mm)	LGA-14 (3×5×1 mm)	QFN-16 (3×3×1.2 mm)

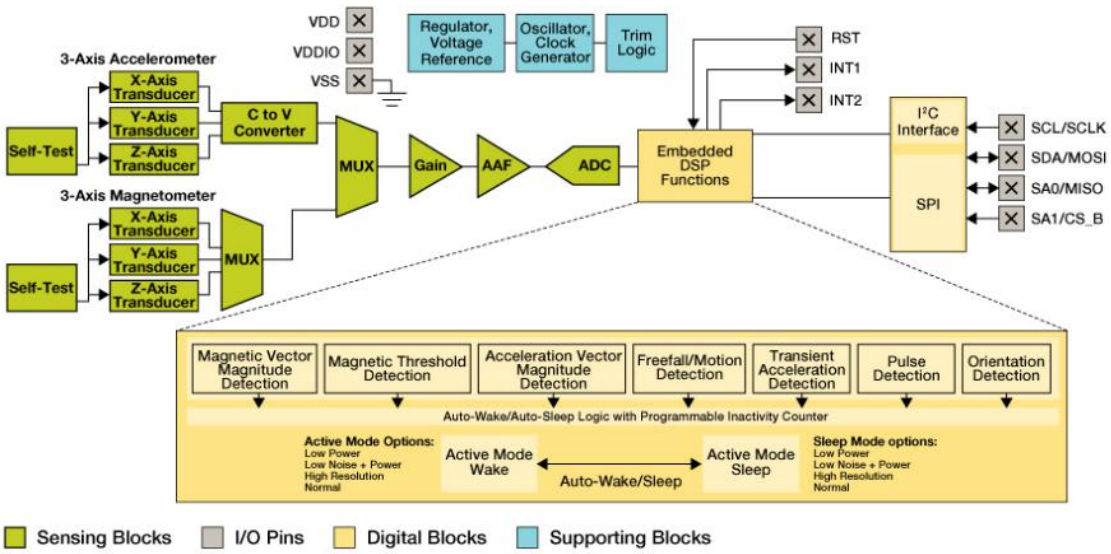

Figure 3-5 Freescale FXOS8700CQ System Block Diagram

The integration of MAG and ACCEL can be used not only for vehicle detection, but also to classify vehicles [50], such that the MAG detects presence of a vehicle by measuring disturbance to the Earth's magnetic field and ACCEL detects number of axels by measuring the vertical acceleration of a road surface due to motion of dynamic loads.

3.4.3 Embedded RF Engine

Networking between *i*AP and *i*VCCS.G1 nodes is facilitated through a low-power wireless protocol. ZigBee is one of the key enabling wireless technologies for IoT devices. This technology operates in sub-GHz and 2.4 GHz ISM (industrial, scientific and medical) radio bands based on IEEE 802.15.4 physical and MAC layers.

Among many available commercial ZigBee modules, Synapse's SM200P81 RF Engine [93] has proven to be superior in all selection criteria aspects. For example, transmit power is 3dBm with range of 1500ft and data transfer rate up to 2Mbps. More importantly, power consumption can be as low as 1.37μA with 22.5mA data transmission and 20.5mA during data receiving. Receiver sensitivity is -100dBm. Unit size is 30×19mm and costs about $17.9/1KU. Outdoor line-of-sight (LOS) range can go up to 450 meter. SM200P81 incorporates Synapse's SNAP mesh network operating system [94], which facilitates multi-hop, instant-on, self-healing, and internet-enabled mesh networking between all network devices. Figure 3-6 illustrates SM200P81 physical module and its internal block diagram.

3.4.4 Real-Time Clock

Time-stamping are enabled by Maxim Integrated DS3231M [95], an extremely accurate, low-cost, real-time clock (RTC) unit. It incorporates the industry's first temperature-compensated MEMS resonator with ±5ppm accuracy (±0.432 second/day). MEMS reduces crystal mechanical failure susceptibility. The chip has two programmable alarms and a 1Hz output (PPS), as well as a battery backup (3V) for continuous timekeeping for 10 years. In 2014, DS3231M was considered the most accurate RTC chip in the market.

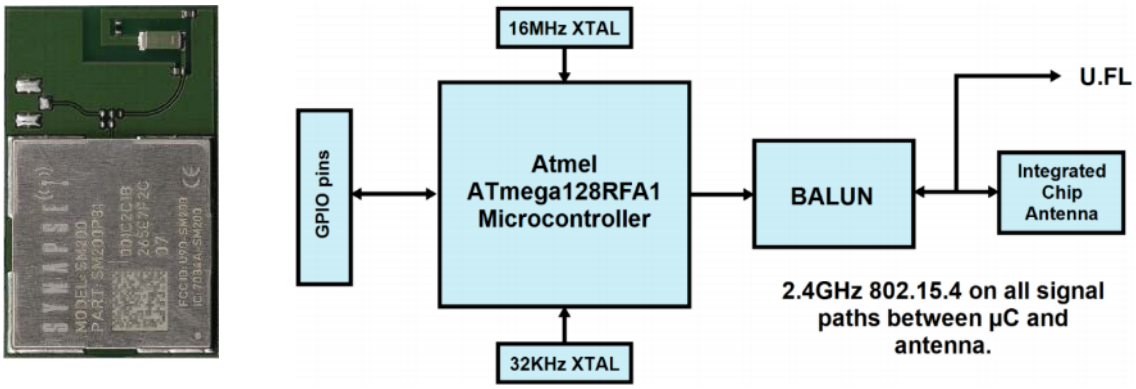

Figure 3-6 SM200P81 Module block diagram

3.4.5 Embedded GPS Module

To enable self-configuration, auto-localization, and accurate synchronization of a scalable network, a Titan 2 Gms-g6 GPS module was incorporated on *i*VCCS [96]. Titan 2 is a compact, dual-system GPS receiver module with built-in patch antenna, featuring up to 210 PRN channels, including 99 search channels and 33 simultaneous tracking channels. Titan 2 provides 2.5m positioning accuracy, ±10ns timing accuracy, and up to 10Hz update rate, as well as low-power consumption at a cost of only $16 per module. Titan 2 has a backup power mode that runs the internal RTC unit even when main power is off. This feature helps retain satellite information, locking satellites in about 1-sec on power-up instead of performing a lengthy 30-sec cold start. Power consumption is 9µA in backup mode, 350 µA in standby mode, 23mA in tracking mode, and 25mA in accusation mode. Module size is 16×16×6.8 mm. Figure 3-7 shows the Titan 2 module.

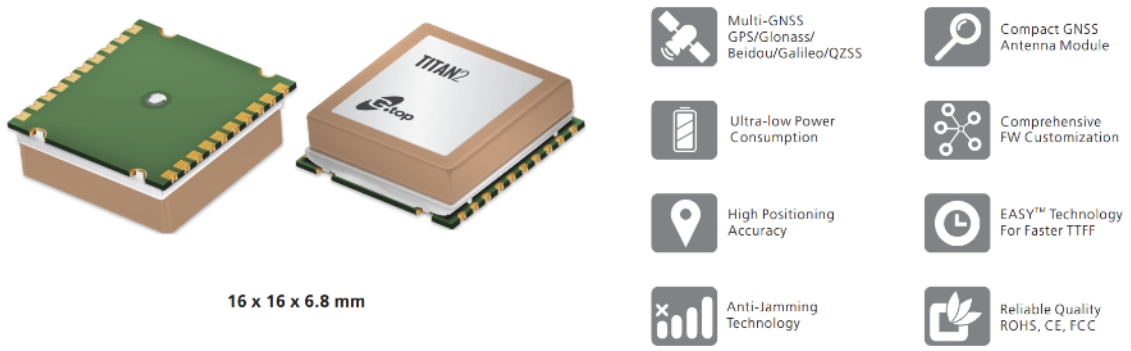

Figure 3-7 Titan 2 Gms-g6 GPS module

3.4.6 Power Management Unit

Quiescent current (Iq) is a very important parameter when comparing the low-power performance of different integrated chips, hence selecting the best components for low-power design. Iq can be defined as the current drawn by a device in a load-free state (i.e., Iq represents the minimal current that enables the device's basic functionalities). Iq can be used to estimate battery run time.

The power management unit included TPS78333, an ultra-low quiescent current (i.e., Iq=500nA) with low dropout voltage (i.e., 150mV) 3.3V linear voltage regulator. TPS78333 has a thermal shutdown and overcurrent protection. Shutdown current is 18nA.

A 3.7V/2000mAh Polymer Li-Ion battery is used to supply the system. Li-Po batteries are a best fit for powering handheld and portable devices. Although they are small, lightweight, and durable, the batteries should never be discharged too low. If battery voltage drops below approximately 3.0V per cell, it will no longer accept a full charge and may not hold voltage under load. As such, the load must be discounted the moment voltage drops below 3V.

MAX17043 was used to protect battery from deep-discharging [97]. MAX17043 is ultra-compact, low-cost, host-side, fuel-gauge system for Li-Po batteries. The chip uses sophisticated algorithms to detect battery state and voltage. Shutdown current is 0.5μA. In addition to estimated capacity data sets, battery measurements can be accessed be the MCU over I^2C bus and later reported by the *i*VCCS to *i*AP.

TPS78333 provided with a shutdown pin that is controlled by MAX17043. In the event that battery voltage drops below a predetermined threshold, the MAX17043's ALT pin will shut down the regulator output.

3.4.7 Data Storage Unit

Since the sensor should support various studies and applications—which might include sampling the geomagnetic field at high sampling rate and store raw data for a long time—a microSD card was incorporated on board. Several microSD cards were tested. ScanDisk microSD cards were selected, as they have the lowest power consumption and they support automatic switching between active and sleep mode. In general, the card will remain in sleep mode except when accessed by the host for data read or write. After completion of an operation in 5ms, the card will automatically return to and remain in sleep mode until a new command is issued by the host. Power consumption during a page-write operation at 10MHz rate is around 20mA. Buffering the data is recommended before transferring it into the card to ensure ample time to remain in sleep mode.

3.4.8 Road Surface Condition Sensors

In addition to aforementioned peripherals, *i*VCCS.G1 is equipped with road surface condition monitoring, including temperature and wet-dry sensors. The temperature sensor is a negative temperature coefficient (NTC) resistor (e.g., NXFT15WF104FA2B025), and the wet-dry sensor is an impedance grid resistor (IGR). Both sensors are connected through low-pass-filters (LPF) to the MUC's analog-digital-converter inputs.

3.4.9 Atmospheric Sensors Extension Module

Additional extended atmospheric measurements can be obtained from *i*VCCS by attaching a weather-sensing module (WSM), including ambient pressure, humidity, temperature, light, acoustic sound, and lightning sensors. Figure 3-8 illustrates the block diagram of WSM. Figure 3-9 shows the WSM printed circuit board (PCB).

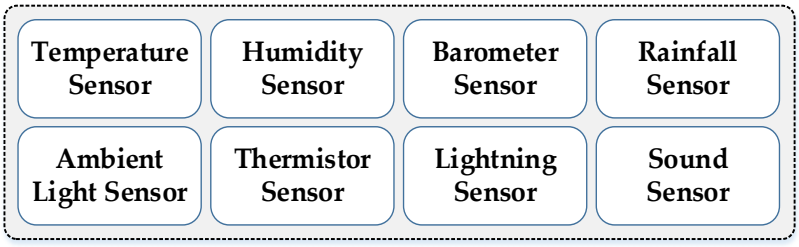

Figure 3-8 WSM sensing components block diagram

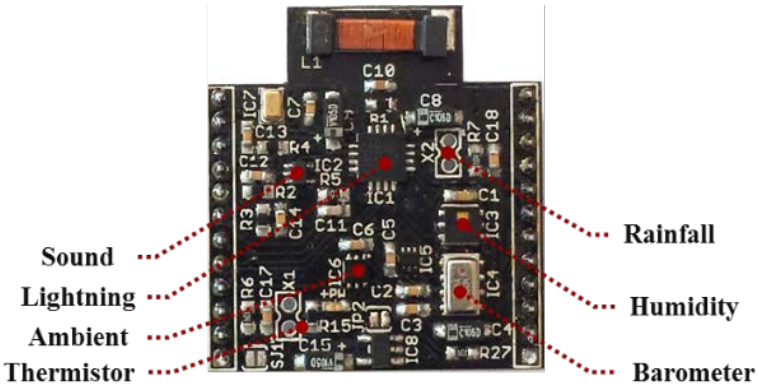

Figure 3-9 WSM PCB with all sensing components marked, 25×28mm

A comprehensive search was carried out to select the most embedded sensors for weather sensing in a WSN application. Selection criterion was based on the following factors: sensitivity and accuracy; power consumption; size; cost; and communication interface (i.e., analog or digital). Selected sensors—complete with part numbers—are shown in Figure 3-10. HTU21D is a digital Humidity Sensor; MPL3115A2 is a digital absolute extrinsic smart pressure sensor; ADMP401 is analog omnidirectional MEMS microphone module; MAX44009 is digital ambient light sensor; TMP102 is low power digital temperature sensor; AS3935 is Franklin lightning detector with embedded algorithm that warns of lightning storm activity within a radius of 40kM; and the surface temperature sensor is NXFT15WF104FA2B025. More information on these sensors is located on their datasheets and application notes.

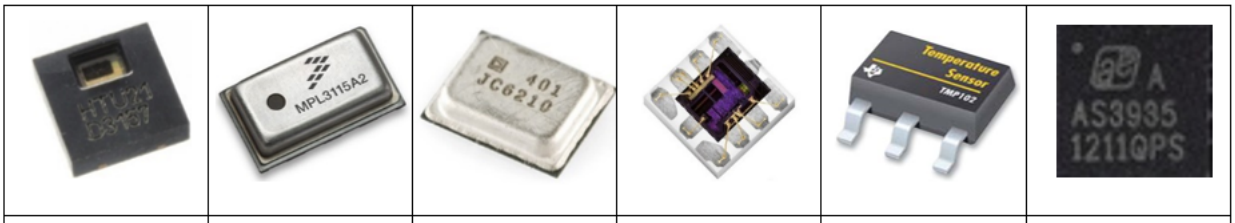

HTU21D	MPL3115A2	ADMP401	MAX44009	TMP102	AS3935

Figure 3-10 Selected Atmospheric Sensors for WSM

3.4.10 Road Surface Condition Sensors

Road surface temperature can rise to 200ºC on a hot summer day. A cost-effective method for measuring road surface temperature is by using NTC glass-based

Thermistors. These sensors feature an extremely fast response time, high reliability, and an operating temperature range between -50°C and +300°C. Note that the sensor glass should be coated to ensure moisture-proof robustness. For *i*VCCS$_{G2}$, an NTC with at least 100kΩ rated resistance at 25°C (e.g., Semitec's 104NT-4-R025H43G [98], costs US$0.7/1KU) is recommended to guarantee minimal power dissipation.

3.4.11 Passive Components Selection Does Matter

ULP design should consider the leakage current, not only from active components, but also from passive components (e.g., capacitors). It is also imperative to understand and evaluate the effect of DC bias, temperature variation, and tolerance of the bypass capacitor, as well as technology of the selected capacitor.

TMJ S1gma™ SMD tantalum capacitors from AVX were used in *i*VCCS$_{G2}$. This capacitor has extremely low DC leakage current (i.e., 0.001CV), as well as high stability over an operation temperature range between -55 and +125°C [99].

3.5 System Architecture and Networking

All *i*VCCS nodes can operate in either online or offline modes. In offline mode, all traffic measurements, events, and magnetic signatures are logged into an on-board data logging unit. Data can be retrieved by replacing the microSD card or accessed anytime via an available wireless link. In online mode, data are reported upon request to either *i*AP or collaborative nodes. To conserve power, the data logging unit remains in sleep mode except when accessed by the host (i.e., MCU).

The network is organized in three tiers, as illustrated in Figure 3-11. At the lowest tier lies the *i*VCCS nodes, each equipped with a ZigBee RF module and a unique ID. The unique ID is reported with node coordination—obtained from an on-board GPS module—to a corresponding *i*AP for mapping purposes. *i*APs are located in the second tier, each equipped with a long-range ZigBee transceiver and an embedded industrial GPRS module [100]. *i*AP has a 10MB data cache and a powerful operation system that facilitates optimal connection timing to maximize traffic savings and minimize communication cost. Data can be accessed via dynamic DNS or public IP.

System wireless networking between *i*VCCS nodes and *i*AP is facilitated through IEEE 802.15.4 protocol with ZigBee on top. Wireless networking between *i*AP and the

server is managed over a cellular network assisted by a Quad-Band GSM/GPRS chipset with an on-board GPS module.

Each *i*AP was set to manage up to 12 subordinate *i*VCCS nodes. Upon *i*VCCS node startup, multicast remote procedure calls (RPCs) are sent to inquire about the address of an *i*AP for managing the same channel and network. One *i*AP responds to the call by sending its address to the originating *i*VCCS node. In the event that *i*AP fails to send a response after a number of inquiries within a defined period, *i*VCCS node switches to offline mode. If a connection is established, *i*VCCS node switches to online mode wherein data is exchanged with the designated *i*AP upon request. Data received by any *i*AP will be processed, analyzed, and logged on a local memory. Processed data will be moved to an IoT cloud server over a cellular network, given an established connection. Otherwise, data can be retrieved by the server at any time. The IoT cloud server lies in the third tier wherein traffic data can be monitored anywhere in real-time. The cloud server can also manage and control the network configuration, as well as facilitate a system's over-the-air firmware upgrade. This hierarchical topology allows a fully scalable, self-configurable, and robust system network [101].

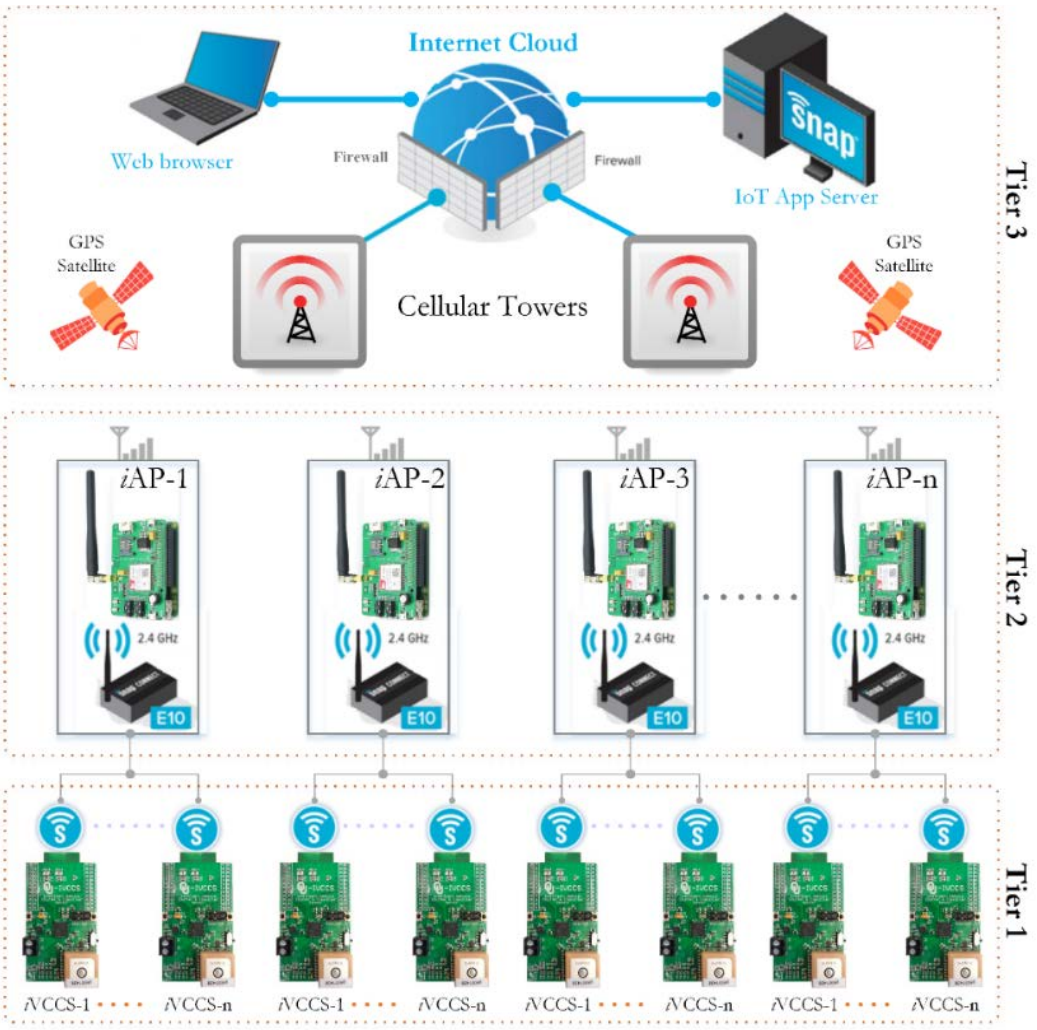

Figure 3-11 Architecture of the traffic surveillance system network

Once the connection is established (and upon request), *i*VCCS nodes exchange data with designated *i*AP. The request is managed by serial inquiry frames and commands.

*i*AP uses *Inquiry Frame* '*IQF*' to send an inquiry to either a specific node (unicast) or all nodes (multicast) requesting information (e.g., battery health; memory status; number of counted vehicles; time and date; and sensor status, raw data, and temperature). The corresponding node responds with *Inquiry Response Frame* '*IQRF*.'

*i*AP also uses *Command Frame* '*CMDF*' to send a command to either a single node (unicast) or all nodes (multicast) asking for a specific task to be executed by the node (e.g., 'configure magnetometer', 'do recalibration'). The corresponding node responds with *Command Confirmation Frame* '*CCF*' to confirm the task by writing the binary value

‘10101010’ in the CMD byte or deny it by writing the binary value ‘01010101.’ Note that Sender/Receiver ID is software-coded and is not related to the MAC address.

Inquiry Frame (IQF)

1-byte	*1-byte*	*1-byte*	*1-byte*
S_{ID}	R_{ID}	**IQ**	**CRC**

Inquiry Response Frame (IQRF)

1-byte	*1-byte*	*1-byte*	*1-byte*	*1-250 byte*	*1-byte*
S_{ID}	R_{ID}	**IQ**	**CNT**	**DATA**	**CRC**

Command Frame (CMDF) / Command Confirmation Frame (CCF)

1-byte	*1-byte*	*1-byte*	*1-byte*
S_{ID}	R_{ID}	**CMD**	**CRC**

Field	**Discerption**
S_{ID}	*Sender ID (software)*
R_{ID}	*Receiver ID (software)*
IQ	*Inquiry*
CMD	*Command*
CNT	*Data bytes count*
DATA	*Data stream*
CRC	*8-bit Cyclic Redundancy Check*

Chapter 4: ALGORITHMS DESIGN & FIRMWARE DEVELOPMENT

4.1 Introduction

Providing reliable traffic-monitoring data requires precise vehicle detection and highly accurate speed estimation. Precise detection necessitates a consistent baseline (i.e., a maintain static localized geomagnetic field) and coherent sampling rate. Speed estimation relies on precise time-stamping of vehicle arrival and departure, which is dependent on the accuracy of the time-synchronization (T-Sync) algorithm. In this chapter, the development and implementation of various distinctive algorithms for real-time traffic monitoring will be discussed in detail. This includes vehicle detection, speed estimation, geomagnetic field baseline drift compensation, T-Sync, RTC drift correction, and others. Figure 4-1 illustrates a block diagram of relationships among various developed algorithms and associated interconnection with the system's hardware interfaces and physical components. The hieratical implementation shows three levels. Peripheral algorithms and drivers are implemented in the third level, namely "*Embedded Firmware,*" which interacts with various "*Physical World*" components and sensors in the first level through "*Embedded Hardware*" peripherals in the second level.

All algorithms discussed in this chapter are hardware independent, meaning they will perform the same intended objectives. However, execution performance is hardware dependent—*i*VCCS$_{G2}$ has an advance performance MCU and more energy efficient components than *i*VCCS$_{G1}$. Firmware development experience also plays a major role in algorithm efficiency during implementation. Pseudo-codes and flowcharts will be provided to maintain efficient implementation of algorithms on various platforms.

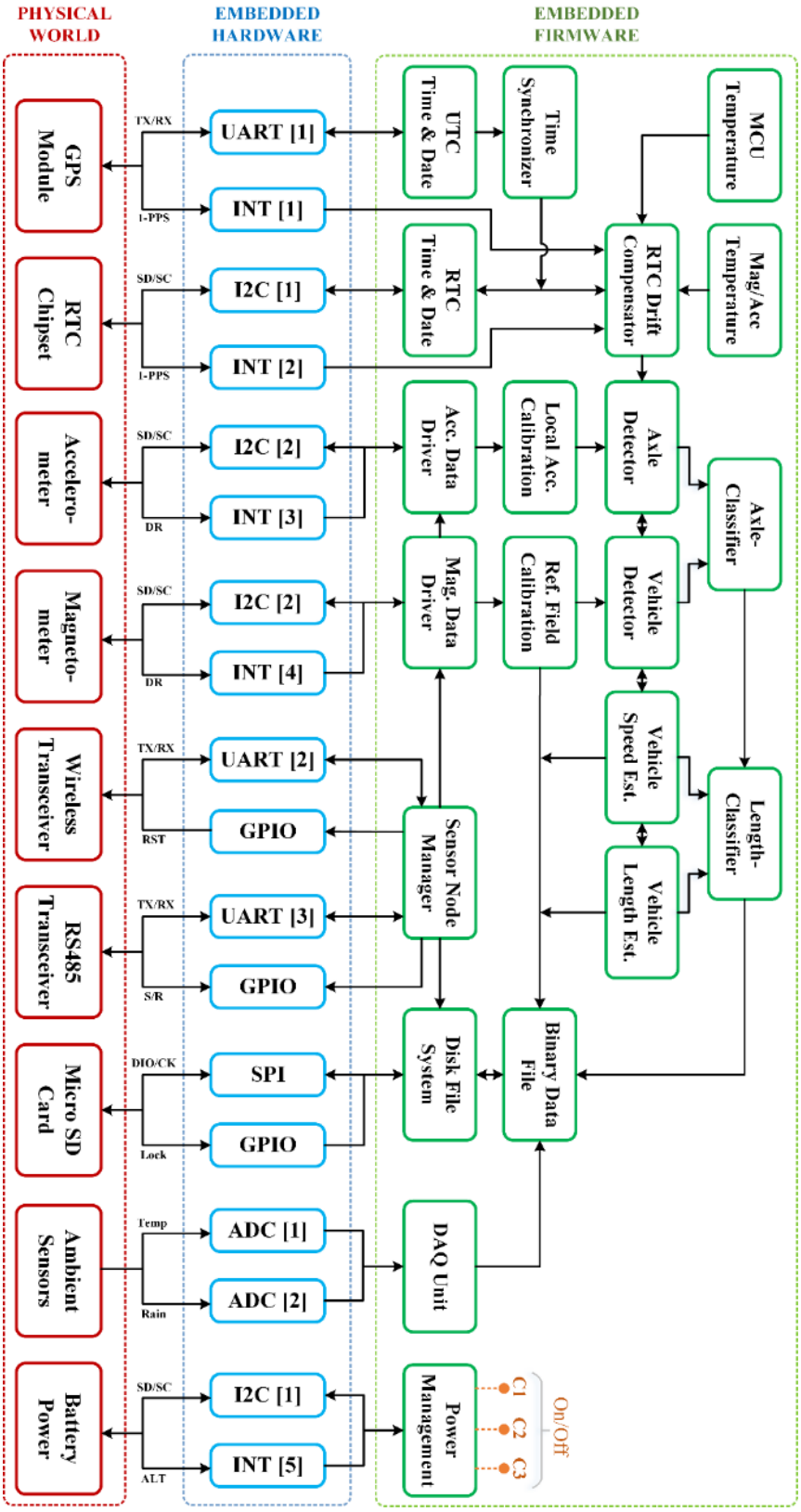

Figure 4-1 Hierarchal integration of hardware and software in *i*VCCS

4.2 Real-Time Vehicle Detection & Counting Algorithm

4.2.1 An Overview on Implementation of Vehicle Detection Algorithms

In literature, fixed [38] or adaptive [52] thresholds have been proposed for vehicle-detection algorithms. Adaptive algorithms are aimed at maintaining a detection threshold above a reference level that could drift due to variations in temperature, background noise, vibrations, aging, or relative earth magnetic field over time.

In this work a multi-threshold-based detection algorithm was developed. A drift in geomagnetic field baseline is adaptively auto-calibrated in real-time. This method aids in solving problems reported in [48] by keeping magnetic signal variation at a minimum, hence, providing reliable vehicle-speed estimation in low-speed, as well as high speed, congested traffic.

4.2.2 Embedded Magnetometer Sensors

This work features a single MAG for measuring variations in geomagnetic field components (B_X, B_Y, and B_Z) caused by an overpassing vehicle. Figure 4-2 and Figure 4-3 illustrate variations in three geomagnetic field components and the corresponding flux magnitude (F_M): square-root of B_X, B_Y, and B_Z for the Honda Accord 2004 EX-V6, sampled at 200Hz; y-axis is the direction of the traffic.

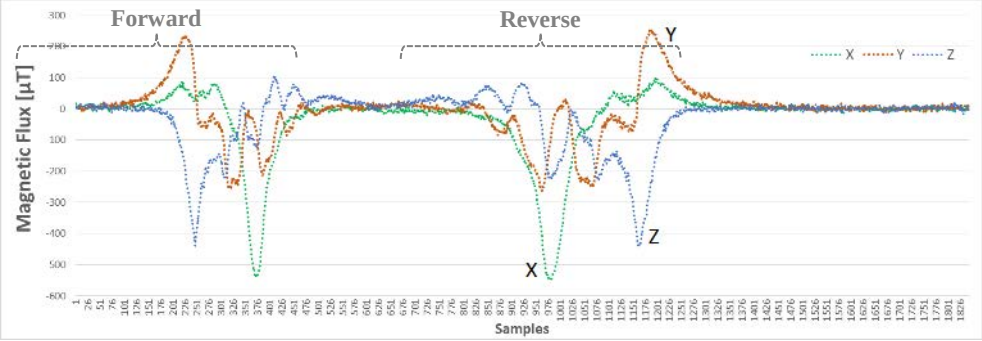

Figure 4-2 Variations in B_x in forward and reverse driving directions

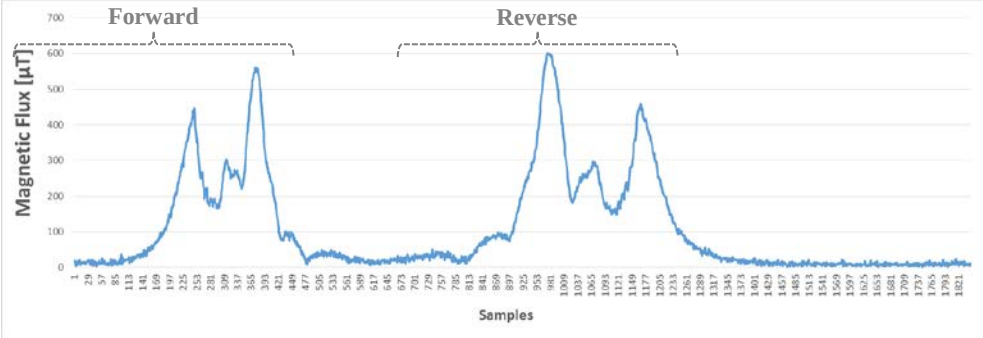

Figure 4-3 Variations in F_M in forward and reverse driving directions

4.2.3 Detection and Counting using an iVCCS in Roadway Setup

A five-state machine process algorithm was developed for real-time vehicle detection and counting, utilizing a single *i*VCCS node. The algorithm acts as an observer for disturbance in the Earth's magnetic field instigated by a passing vehicle. Localized flux lines pull away from the sensor as a vehicle passes the sensor zone and push back toward the sensor as the vehicle drives away (see Figure 1-3), creating fluctuations in F_M. The five-state machine process analyzes fluctuations for valid vehicle detection by leveraging three adaptive thresholds (TH) and three adaptive debounce timers (DT), as shown in Figure 4-4.

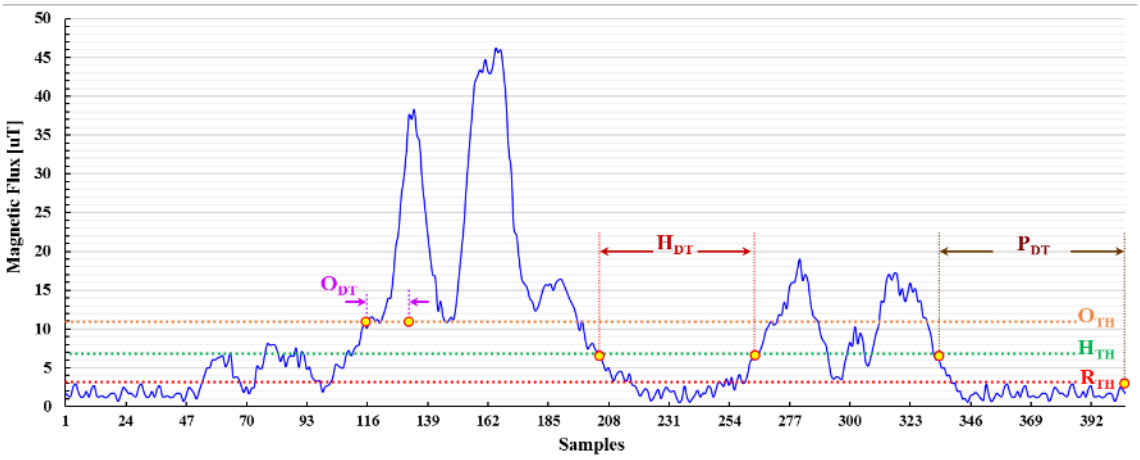

Figure 4-4 Detection Algorithm Parameters applied on a Vehicle Flux Magnitude

Detection Thresholds are defined as follows:

1. *Onset threshold* (O_{TH}): vehicle arrival
2. *Holdover threshold* (H_{TH}): vehicle departure
3. *Baseline threshold* (R_{TH}): re-calibration call

Debounce timers are defined as follows:

1. *Onset debounce timer* (O_{DT}): eliminates misdetection and false events due to a glitch or transient state
2. *Holdover debounce timer* (H_{DT}): eliminates misdetection due to fluctuations in F_M when part of the vehicle has relatively small magnetic density (e.g., long trucks)
3. *Detection period debounce timer* (P_{DT}): indicates stationary detection

The algorithm was developed based on MCU interrupts (INT) and an event system to ensure real-time performance and CPU offloading to prolong battery life. Figure 4-5 details a functional block diagram for the detection and counting algorithm. Figure 4-6 illustrates a finite state machine (FSM) diagram for the five-state machine process detection algorithm.

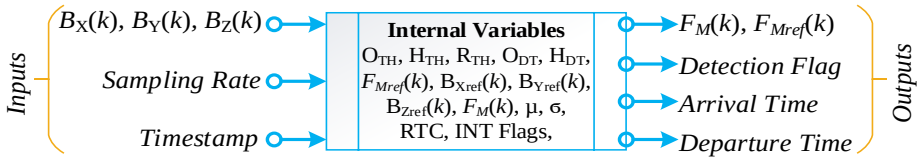

Figure 4-5 Vehicles detection and counting algorithm functional block

Upon system power up, an initialization process triggers a *calibration state* where MAG samples localized reference magnetic field components (B_{Xref}, B_{Yref}, and B_{Zref}) for a period T_S in the absence of vehicles. During this time the reference magnetic field flux magnitude F_{Mref} is calculated using Eq. 4-1.

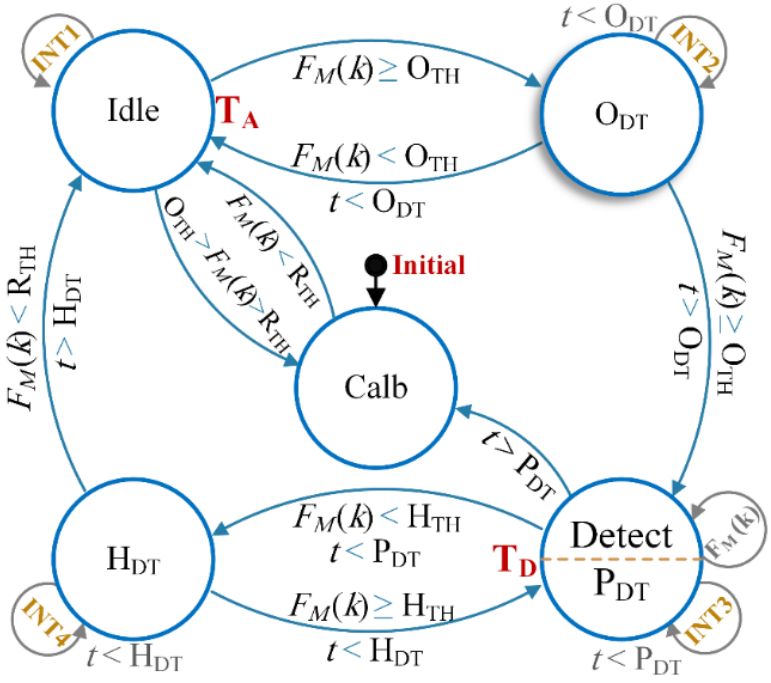

Figure 4-6 State machine process for vehicle detection and counting

$$F_{Mref}(k) = \sqrt{B_{Xref}(k)^2 + B_{Yref}(k)^2 + B_{Zref}(k)^2} \qquad \textbf{Eq. 4-1}$$

F_{Mref} is normally distributed with a mean μ and STD σ such that $F_{Mref} \propto \mathcal{N}(\mu, \sigma)$. By statistically analyzing F_{Mref}, *baseline threshold* R_{TH} is estimated using Eq. 4-2. Consequently, *onset threshold* O_{TH} and *holdover threshold* H_{TH} are calculated according to Eq. 4-3 and Eq. 4-4, respectively. α and β are experimentally defined coefficients according to the detection zone and signal-to-noise ratio (SNR), and $\alpha > \beta$ provides a hysteresis property in detection. F_{Mref} should be unilaterally and adaptively tracked and compensated, as described below in section 4.2.5.

$$R_{TH} = \mu + 2\sigma \qquad \textbf{Eq. 4-2}$$

$$O_{TH} = \mu + \alpha \times \sigma \qquad \textbf{Eq. 4-3}$$

$$H_{TH} = \mu + \beta \times \sigma \qquad \textbf{Eq. 4-4}$$

After calibration is complete, the node remains in *idle state* until MAG data-ready interrupt (*INT1*) triggers *onset debounce timer* O_{DT}, given that the state condition $F_M(k) \geq O_{TH}$ (i.e., vehicle in detection zone) is true; $F_M(k)$ is found using Eq. 4-5.

$$F_M(k) = \sqrt{\left(B_X(k) - B_{Xref}\right)^2 + \left(B_Y(k) - B_{Yref}\right)^2 + \left(B_Z(k) - B_{Zref}\right)^2} \quad \textbf{Eq. 4-5}$$

This function simply compares the magnitude defined by O_{TH} vector with the difference of two vectors, namely sampled magnetic field $F_M(k)$ and localized magnetic field reference $F_{Mref}(k)$. If the former is greater than the latter for a minimum duration of time specified by O_{DT}, then a true detection event is raised.

This can be expressed using vectors, as in Eq. 4-6. The MAG sample is denoted by $\vec{M}$, and $\overrightarrow{M_{ref}}$ is programmable offset. Eq. 4-6 can be rewritten as Eq. 4-7, where F_M and F_{Mref} are magnitudes of $\vec{M}$ and $\overrightarrow{M_{ref}}$, and α is the angle between vectors.

$$\left|\vec{M} - \overrightarrow{M_{ref}}\right| = \sqrt{\left(\vec{M} - \overrightarrow{M_{ref}}\right).\left(\vec{M} - \overrightarrow{M_{ref}}\right)} > O_{TH} \quad \textbf{Eq. 4-6}$$

$$\sqrt{\vec{M}.\vec{M} - 2.\vec{M}.\overrightarrow{M_{ref}} + \overrightarrow{M_{ref}}.\overrightarrow{M_{ref}}} = \sqrt{{F_M}^2 + {F_{Mref}}^2 - 2F_M F_{Mref}\cos\alpha} > O_{TH} \quad \textbf{Eq. 4-7}$$

A transition into *detect* state occurs after O_{DT} is elapsed and the state condition $F_M(k) \geq O_{TH}$ is still true. In *detect* state, the sensor samples the magnetic field, calculates $F_M(k)$, and logs $B_X(k)$, $B_Y(k)$, and $B_Z(k)$ into a storage memory.

To eliminate double-detection errors resulting from fluctuations in F_M that could possibly occur between O_{TH} and H_{TH}—given that part of the vehicle has relatively small magnetic flux density (e.g., long combination trucks), a *holdover debounce-timer* H_{DT} is utilized. H_{DT} plays a significant role in reducing detection errors.

A transition from *detect* state to H_{DT} state occurs when $F_M(k) < H_{TH}$ (i.e., vehicle departed the detection zone). A transition into *idle* state occurs when *INT4* triggers after H_{DT} is elapsed and $F_M(k) < H_{TH}$.

Vehicle counter will then be incremented by one, and vehicle arrival time (T_A) and departure time (T_D) will be logged. T_A and T_D are accurately captured in exactly 12 CPU cycles when *INT1* and *INT3* triggers, respectively.

The system stays in *idle* state until *INT1* is triggered again or $F_M(k) \geq R_{TH}$ (i.e., a drift in the localized magnetic field baseline.

Detection period debounce-timer P_{DT} can be configured according to the intended application. For example, P_{DT} can be used as a watch-dog-time on highways to clear

errors resulting from an accidental change in field baseline during a detection event (e.g., high speed loaded truck hitting a sensor) and to trigger recalibration. P_{DT} can also be configured as a stationary detection timer for parking lot applications.

4.2.4 Detection and Counting using a iVCCS in Roadside Setup

*i*VCCS can be deployed on roadsides adjacent to the lane, in favor of a roadway setup in the center of a lane. The system uses the algorithm indicated in Figure 4-6 for vehicle detection. However, if a motorcycle or small vehicle driving on the far side of the lane opposite the sensor side, the SNR could be significantly low, causing misdetection. Figure 4-7 shows variations in geomagnetic field components and magnitude caused by the Honda Accord 2004 EX-V6 when passing *adjacent* to the sensor at a distance of 1 meter. Y-axis is the traffic direction. When compared with *roadway* setup in Figure 4-8, it is clear that the magnitude in *roadside* setup is three times weaker. Moreover, signal variations in *roadside* setup are relatively uniform when compared with roadway setup.

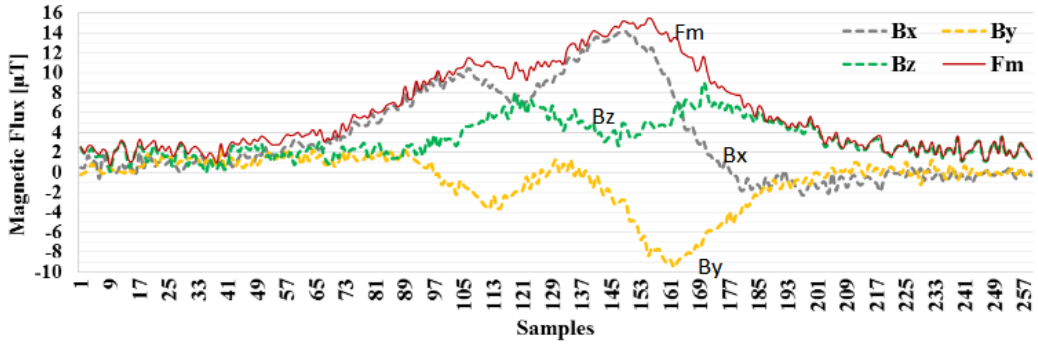

Figure 4-7 Class 2 vehicle magnetic signature sampled by *i*VCCS on roadside

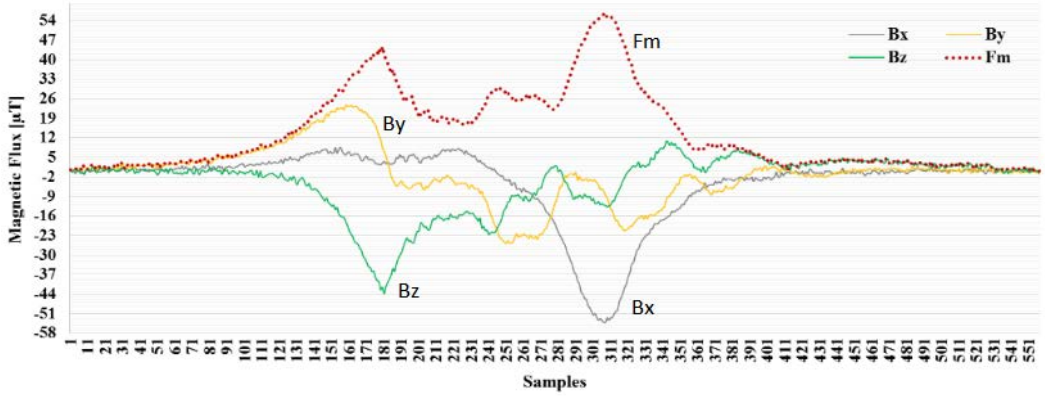

Figure 4-8 Class 2 vehicle magnetic signature sampled by *i*VCCS on roadway

To mitigate this issue, a moving average filter (MAF) with gain coefficient *w* must be employed to reduce signal fluctuations and increase signal SNR. $F_{M_{gain}}(k)$, calculated using Eq. 4-8 and Eq. 4-9, is the input of detection algorithm in Figure 4-6. One drawback of roadside setup is that it only works for roads with no more than two lanes.

$$F_{M_{gain}}(k) = \frac{w}{N}\sum_{i=0}^{N-1} F_M(k-i)\,; \quad w = 4,\ N = 5 \qquad \textbf{Eq. 4-8}$$

$$F_{M_{gain}}(k) = \begin{cases} w \times \dfrac{F_M(k) + F_M(k-1) + \cdots + F_M(k)}{k}; & k < N \\ w \times \dfrac{F_M(k) + F_M(k-1) + \cdots + F_M(k-N+1)}{N}; & k \geq N \end{cases} \qquad \textbf{Eq. 4-9}$$

4.2.5 Adaptive Geomagnetic Baseline Drift Compensation

Variations in temperature, vibrations, and aging will cause a considerable drift in the mean value of $F_{Mref}(k)$, which causes detection errors and unreliable speed and length estimation. Thus, $F_{Mref}(k)$ should be tracked so that B_{Xre}, B_{Yref}, and B_{Zref} are compensated for any drift. Tracking $F_{Mref}(k)$ is achieved using a MAF when $F_M(k) < O_{TH}$. The algorithm computes new B_{Xref}, B_{Yref}, and B_{Zref} values, as in Eq. 4-10, if Eq. 4-11 is satisfied.

$$B_{ref}^{(\gamma)} = \frac{1}{M}\sum_{i=0}^{M-1} B^{(\gamma)}(k-i)\,; \quad \gamma = \{X, Y, Z\} \in \mathbb{R}^3 \qquad \textbf{Eq. 4-10}$$

$$\frac{1}{M}\sum_{i=0}^{M-1} \left[F_{M_{ref}}(k-i) - F_{M_{ref}}(k)\right] \geq R_{TH} \qquad \textbf{Eq. 4-11}$$

A high-level description of the baseline drift compensation algorithm is shown in

. A flowchart is detailed in Figure 4-9.

The drift compensation algorithm simply tracks geomagnetic field over time to maintain reference magnetic signal variations at a minimum. The function stores $B_X(k), B_Y(k)\ and\ B_Z(k)$, and calculates $F_M(k)$ when MAG data ready interrupt (INT1) triggers. $F_M(k)$ MAF output is compared to *baseline threshold* R_{TH}. New geomagnetic field reference level components $B_{ref}^{(\gamma)}$ are calculated and set using MAF when $F_{MAvg}(k) > R_{TH}$.

Inputs: $B_X(k)$, $B_Y(k)$, $B_Z(k)$

Outputs: B_{Xref}, B_{Yref}, B_{Zref}

WHILE $F_M(k) < O_{TH}$
  WAITFOR Magnetometer *Data-Ready INT*
  BUFFER ← COMPUTE $F_M(k)$ ← READ $B_X(k)$, $B_Y(k)$, $B_Z(k)$
  $Idx \leftarrow Idx + 1$
  IF $Idx = M$ **THEN**
    $F_{M.Avg} \leftarrow \frac{1}{M}\sum_{j=0}^{M-1} F_M[k-j]$
    IF $O_{TH} > F_{M\text{-}Avg} \geq R_{TH}$ **THEN**
      $B_{Xref}, B_{Yref}, B_{Zref} \leftarrow \frac{1}{M}\sum_{i=0}^{M-1} B^{(\gamma)}[k-i]$
    ENDIF
    $Idx \leftarrow 0$: BUFFER ← 0
  ENDIF
LOOP
$Idx \leftarrow 0$: BUFFER ← 0

Adaptive Geomagnetic Baseline Drift Compensation Pseudocode

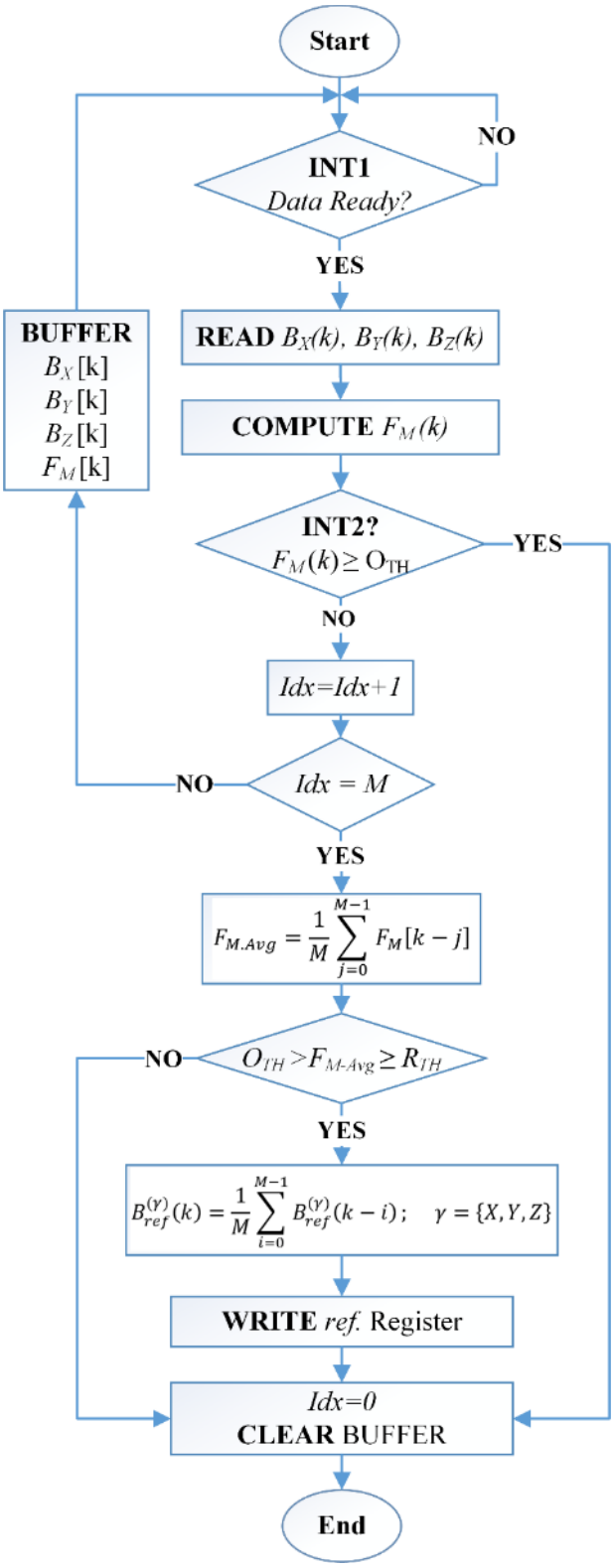

Figure 4-9 Flowchart for adaptive compensation of geomagnetic baseline drift

4.3 Vehicle Speed Estimation and Time Synchronization

In this section, the development and implementation of various algorithms for real-time vehicle speed estimation and time synchronization are discussed.

4.3.1 Real-Time Vehicle Speed Estimation using Two Sensor Nodes

The most accurate method to measure vehicle speed is by calculating travel time between two longitudinally positioned sensor nodes ($N_A \rightarrow N_B$) separated by distance *d*, as shown in Figure 4-10.

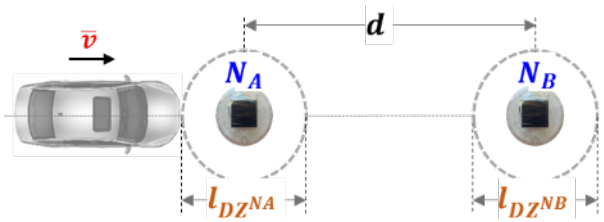

Figure 4-10 Speed estimation deployment setup

Two measures of speed can be identified: 1) per-vehicle or instantaneous speed ($\bar{v}_i$), which is the attained speed of a vehicle at time instant *t*, and 2) aggregated or time-mean speed ($\bar{v}_t$), which is the average speed of *n* vehicles *v* over time period *t* at a specific location. $\bar{v}_i$ and $\bar{v}_t$ are calculated using Eq. 4-12 and Eq. 4-13, respectively. $T_A^{(N_i)}$is the vehicle arrival time, $T_D^{(N_i)}$ is the departure time, and *q* is number of vehicles traveling at the same speed.

$$\bar{v}_i \approx \frac{d^{(N_A \rightarrow N_B)}}{T_A^{(N_B)} - T_A^{(N_A)}} \approx \frac{d^{(N_A \rightarrow N_B)}}{T_D^{(N_B)} - T_D^{(N_A)}} \approx 2\frac{d^{(N_A \rightarrow N_B)}}{T_A^{(N_B)} - T_A^{(N_A)} + T_D^{(N_B)} - T_D^{(N_A)}} \quad \textbf{Eq. 4-12}$$

$$\bar{v}_t = \frac{1}{n}\sum_{i=1}^{n} \bar{v}_i = \frac{\sum_{i=1}^{n} q_i . \bar{v}_i}{\sum_{i=1}^{n} q_i} = \frac{\sum_{i=1}^{n} q_i . d}{\sum_{i=1}^{n} q_i . t_i} = \frac{\sum_{i=1}^{n} q_i . d^{(N_A \rightarrow N_B)}}{\sum_{i=1}^{n} q_i \, (T_i^{(N_B)} - T_i^{(N_A)})} \quad \textbf{Eq. 4-13}$$

Timestamps $T_A^{(N_i)}$and $T_D^{(N_i)}$are sent by sensor nodes and received by an *i*AP, which in turn process speed and length estimation and classification.

For reliable, accurate estimation of vehicle speed and length, a high precision time synchronization must be considered. Failing to synchronize all sensor nodes within a network will cause inaccurate measurements and confuse decision-making in the intelligent controller. Such circumstances might lead to an unsafe condition as a consequence of a false alarm. For instance, consider a vehicle travelling 90 mph on a

highway where two sensor nodes are deployed on a single lane 6 meters apart. If a required speed estimation error is anticipated to be less than ε=±1%, maximum timing error $T_{sync-err}$ should be less than 1.5ms, as indicated by Eq. 4-14 (1mph=0.44704m/s). Optimal distance between sensors depends on speed range. Increasing *d* would reduce error. [102] recommends *d*=3.1—3.7 meter for arterial setup and *d*=6.1—7.3 meter for freeway setup.

$$T_{sync-err} = \frac{d}{v} \times \varepsilon = \frac{6}{90 \times 0.44704} \times 0.01 \approx 1.5\, ms \qquad \textbf{Eq. 4-14}$$

4.3.2 Real-Time Vehicle Speed Estimation using Single Sensor Node

Three interrelated parameters, namely vehicle magnetic length (VML), speed (v), and occupancy time ($T_{Occ}^{(N_i)}$), can be directly estimated or measured for each passing vehicle when two sensor nodes are used per lane, as in Eq. 4-15. However, when using a single sensor node, only $T_{Occ}^{(N_i)}$ can be directly calculated, as in Eq. 4-16.

$$\overline{VML} = \bar{v} \times T_{Occ}^{(N_i)} \qquad \textbf{Eq. 4-15}$$

$$T_{Occ}^{(N_i)} = T_D^{(N_i)} - T_A^{(N_i)} \qquad \textbf{Eq. 4-16}$$

Several studies have reported different techniques for estimating vehicle speed using a single IDL detector. One technique depends on assuming an average length and aggregating a large number of estimated speed samples within a time window to reduce estimation error resulting from uncorrelated length and speed measurements. However, this method is prone to error when mean length deviates (i.e., too many long vehicles).

In this work, an improved speed estimation method developed in [103] for a single IDL detector was adopted using single MAG. The first method employs a moving median, as in Eq. 4-17.

$$v_{median} = \frac{VML_{average}}{median\left(T_D^{(N_x)} - T_A^{(N_x)}\right)} \qquad \textbf{Eq. 4-17}$$

The moving median method uses fixed window of *n* samples (i.e., vehicle speed values) centered on the current sample. The window moves one vehicle for each sample and calculates median speed for the current vehicle, and so on. Sample buffer should be

selected with size enough to ensure minimal speed estimation error. Based on statistical data collected using MAG, a fixed window of 37 samples and average length of 7.2m was selected. A high-level description for moving median algorithm is shown in the following pseudo-code snippet.

Given that the ratio of short to long vehicle fluctuates, the sequence method can be applied to further improve speed estimation. Because the sensor's occupancy time ratio between two successive vehicles should be proportional to their length, we can statistically determine a ratio threshold between the mean of long vehicles (LV) and short (SV) vehicles based only on occupancy time, as in Eq. 4-18. Authors in [103] suggested a ratio 3.5:1 for IDL. The statistical analysis conducted in Chapter 6 revealed a ratio 3.7:1, LV for MAG. Given multiple sequences within the sample window, the algorithm estimates speed for each sequence and then assigns median speed from all individual estimates to the sample. Otherwise, given no such sequences within the sample window, the algorithm falls back to the moving median method. A high-level description for the moving median algorithm is shown in Figure 4-11.

Inputs: window_size = 37, $VML_{average} = 7.2m$

Outputs: v_{median}

1: **WHILE (1)**

2: *Computer occupancy of each vehicle in the window of current vehicle*

3: *Search for median value within all values in the window*

4: $v_{median} \leftarrow VML_{average}$*/ median occupancy*

5: *Shift the window index to the right by 1*

6: **LOOP**

Moving median speed estimation algorithm

$$\hat{v}_{SV} = \frac{L_{SV}^{A}}{\left(T_D^{(N_x)} - T_A^{(N_x)}\right)_{SV}}; \qquad \hat{v}_{LV} = \frac{L_{LV}^{A}}{\left(T_D^{(N_x)} - T_A^{(N_x)}\right)_{LV}} \qquad \textbf{Eq. 4-18}$$

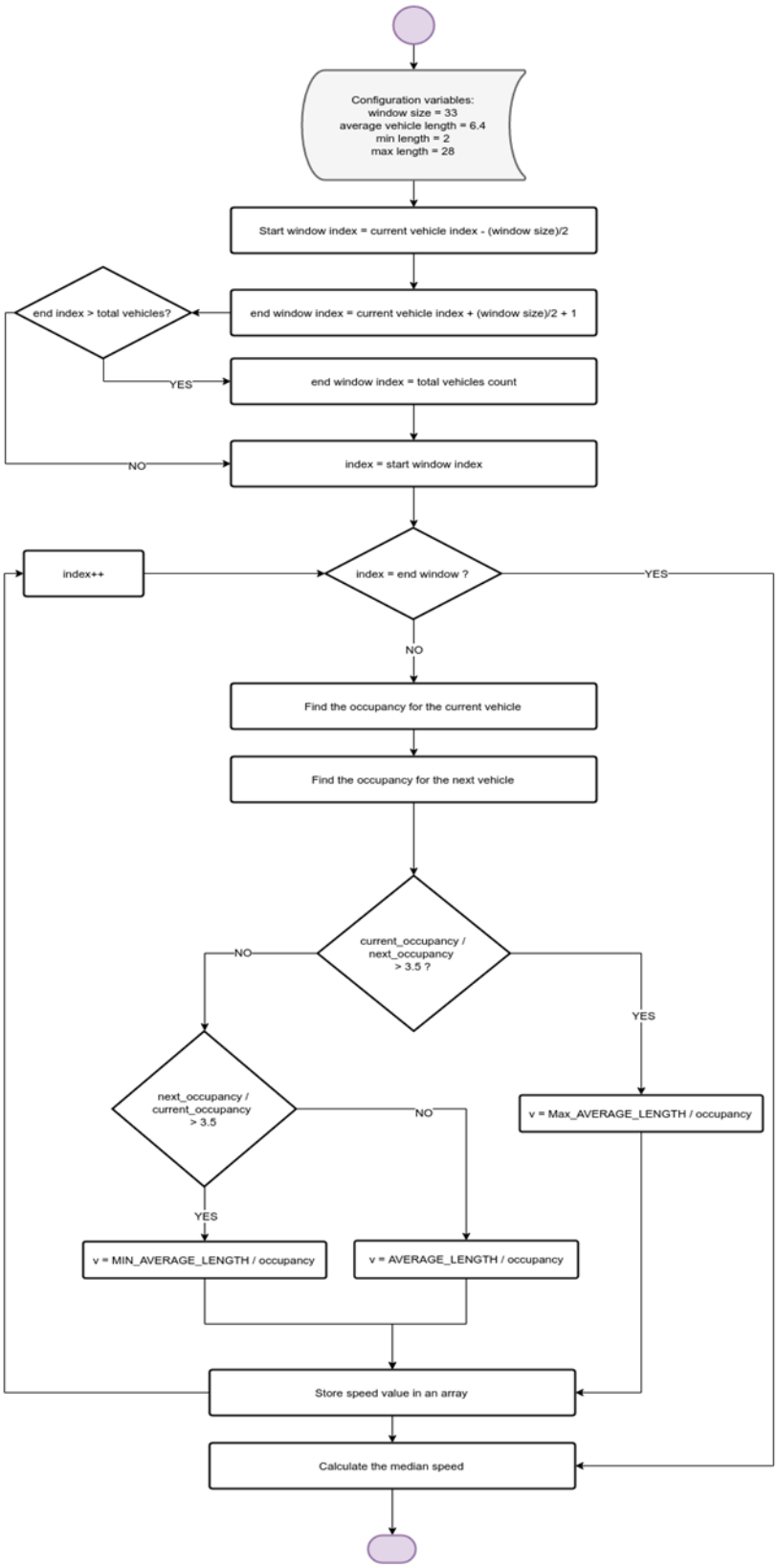

Figure 4-11 Speed estimation algorithm using sequence method

4.4 Time Synchronization using Embedded GPS Module

Each sensor node relies on an onboard GPS module and RTC unit to maintain an independent local clock that is globally synchronized to the GPS pulse-pre-second (PPS) signal. Therefore, wireless connectivity is not necessary for accurate functioning of *i*VCCS nodes. Time stamping, timekeeping, and failure recovery functions are enabled by the MCU's internal RTC unit, which is calibrated and aligned using the PPS signal.

Upon *i*VCCS node power-up, the embedded MCU enables the GPS module via an ultra-low, quiescent-current load switch. Once the GPS receiver is successfully locked to available satellites, the Coordinated Universal Time (UTC) information packet is used to set RTC time and date. The rising edge of PPS signal, which is globally synchronized with ±10ns timing accuracy, is used to align RTC clock phase. This will independently synchronize all WSN-node RTC clocks to the same reference signal (i.e., PPS) on a global scale without exchanging messages over the wireless network.

Once RTC is synchronized, MCU sets the GPS module in backup mode. Location coordination of the sensor node and its ID will be reported to the corresponding *i*AP for mapping purposes. Procedure inputs and outputs are depicted in Figure 4-12. Time zone is denoted by TZ, and daylight saving time is DST. A high-level description of RTC settings and phase alignment using a GPS module is illustrated in the following pseudo-code snippet.

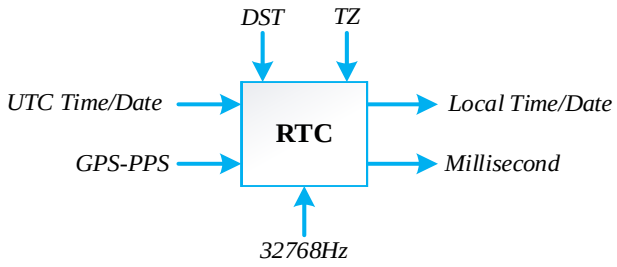

Figure 4-12 GPS-based RTC clock setting and phase alignment block

The method detailed above provides extremely accurate T-Sync, although RTC phase alignment error calculated using Eq. 4-21 is subject to frequency tolerance $f_{osc\text{-}tol}$ of the MCU oscillator. For *i*VCCS, $f_{osc\text{-}tol} = \pm 5ppm$ and $f_{osc} = 32\text{MHz}$. Another factor affecting T-Sync accuracy is RTC frequency drift [72], [73], which is discussed in the next section.

$$RTC_{phaseErr} = \frac{f_{osc-tol}^{(MCU)}}{10^6} = \frac{\pm 5_{ppm}}{10^6} \approx \pm 5\mu s \qquad \textbf{Eq. 4-19}$$

Inputs: Time Zone, DST,

Outputs: Local Time/Date, Geographic coordinates,

1: DISABLE *RTC clock*, INITIALIZE *GPS Module*

2: **WHILE** *GPS-3D-Fix* **IS** *BUSY* **LOOP**

3: **WHILE** *GPS-PPS* **IS** *INACTIVE* **LOOP**

4: **WHILE** *NMEA <> $GPRMC | $GNRMC* **LOOP**

5: **{***UTC Time, Date, Coordinates***}** ← **READ** $GPRMC|$GNRMC

6: COMPUTE *Local Time/Date*, *Sec ← Sec+1, DST, Leap Year*

7: **WAIT FOR** *GPS-PPS Rising Edge Interrupt*

8: SET *RTC(Time/Date) ← GPS(Time/Date)*

9: ENABLE *RTC clock*, SET *GPS Module into Power Saving mode*

Pseudo-code for RTC setting and phase alignment using GPS-PPS

4.4.1 Adaptive Compensation of the RTC Frequency Drift

RTC accuracy is dependent on a 32.768 kHz crystal oscillator ($32Khz_{osc}$) with maximum resolution of 30.517µs (i.e., 1/32769 = 30.517µs). $32Khz_{osc}$ accuracy is subject to several factors, including manufacturing tolerances in the $32Khz_{osc}$, passive PCB components, temperature excursions, and aging. The primary T-Sync error when using RTC is caused by the $32Khz_{osc}$ uncompensated frequency drift.

i$VCCS_{G1}$ uses ABS07-32.768KHZ-T, a 32.768kHz SMD low profile crystal, which has an extended temperature operation -55°C to +125°C for industrial applications. Output of $32KHz_{osc}$ has parabolic frequency dependence over temperature, as depicted in Figure 4-13. Frequency drift at temperature *T* is expressed in Eq. 4-20, where β is a temperature coefficient, given in ppm/T^2, that is always negative (i.e., RTC oscillator slows down at cold or hot temperatures around T_0). T_0 is a turnover temperature—

25°C±5°C. If β=-0.036ppm/T^2±15% and T_0 = 25°C±5°C, the corresponding frequency drift at T=50°C, for example, is found using Eq. 4-20.

$$\frac{\Delta f}{f_0} = \boldsymbol{\beta}(\boldsymbol{T} - \boldsymbol{T_0})^{\boldsymbol{2}} = -0.036 \times (50 - 25)^2 = -22.5\, ppm \qquad \textbf{Eq. 4-20}$$

A -22.5ppm with respect to time is equal to:

$$-\frac{22.5}{10^6} \times 60 \times 60 \times 24 = -1.944\frac{sec}{day} = -81\frac{msec}{hour} = -1.35\frac{msec}{min} = -22.5\frac{\mu sec}{sec}$$

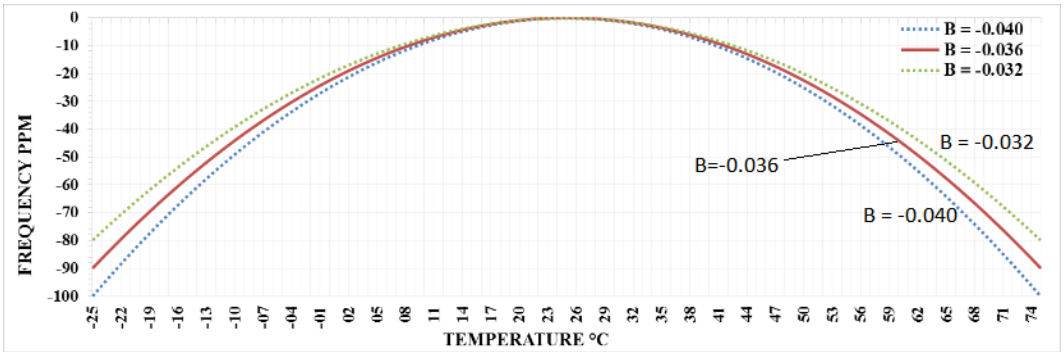

Figure 4-13 Frequency stability vs. Temperature characteristics for ABS07

The 32Khz$_{osc}$ drift ε_{RTC} at constant T has a slope m=1, meaning that change in ε_{RTC} is constant over time at constant temperature. Measuring ε_{RTC} at 26°C for one hour showed a constant drift of 15μs (i.e., 54ms/hour), which can be modeled as a linear equation in Eq. 4-21, where current RTC time is denoted by t_{RTC}; corrected RTC time is $\hat{t}_{RTC}$; GPS time at calibration moment is t_{GPS}; and $\xi_{RTC}^{(T_{osc})}$ is the accumulated error at T_{osc}. T_{RTC} is the compensated RTC time.

$$\hat{t}_{RTC} = m \times t_{RTC} \pm \xi_{RTC}^{(T_{osc})} \;\; ; \qquad \xi_{RTC}^{(T_{osc})} = \varepsilon_{RTC}^{(T_{osc})}(\hat{t}_{RTC} - t_{GPS}) \, , m = 1 \qquad \textbf{Eq. 4-21}$$

Any temperature variations will cause drift in the 32Khz$_{osc}$ output. To maintain T-Sync error in Eq. 4-14 within an intended range, RTC drift should be tracked for compensation, meaning it is possible to correct t_{RTC} drift by knowing T_{OSC}. Corresponding frequency drift can then be calculated, with respect to time, using Eq. 4-20, and $\hat{t}_{RTC}$ value can be then found using Eq. 4-21.

The objective of this method is rejecting the disturbance (i.e., variations in T_{OSC}). Measuring T_{OSC} is not possible, because oscillator does not have a built-in temperature sensor. Nevertheless, and to a greater extent, under steady-state conditions T_{OSC} can be

assumed equal to the temperature of surrounding components. In addition to an on-board thermistor, MAG has an on-die temperature sensor that can be used to extrapolate T_{OSC}. This approach is appropriate, given that 32Khz$_{osc}$ output has a frequency tolerance ≤±5μs and aging factor of ≤±1°C@25°C/*year*. It is important to realign RTC phase when temperature changes approximately 3°C. A re-synchronization using GPS is also required every few hours to correct any residual errors. Figure 4-14 illustrates the RTC drift correction process.

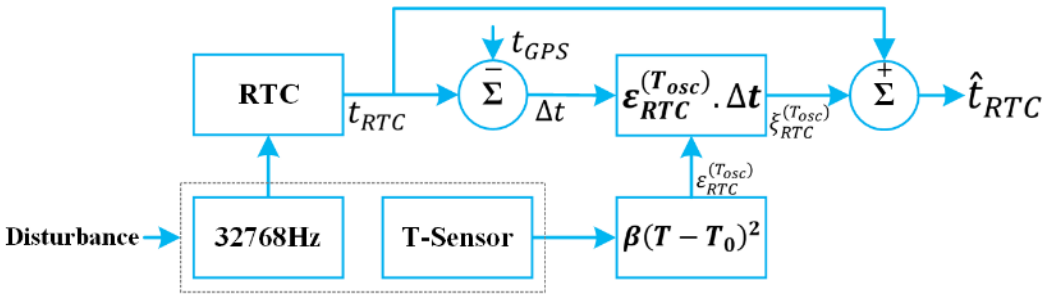

Figure 4-14 RTC drift correction system block diagram

A second approach to correct 32Khz$_{osc}$ output drift was developed. RTC-1Hz signal frequency $f_{RTC}^{(MCU)}$ was compared to an accurate reference frequency $f_{PPS}^{(GPS)}$, PPS signal frequency. In this scheme, both clocks are sampled using high frequency clock $f_{TCLK}^{(MCU)}$, driven from the MCU's 32MHz oscillator. $f_{TCLK}^{(MCU)}$has a tolerance ±5*ppm*; however, since both signals are measured using the same clock at the same time, tolerance error is canceled out. If T_{osc} changes approximately 3°C, the algorithm awakens the GPS module, aligns the RTC phase, and computes a new time correction coefficient $\xi_{RTC}^{(T_{osc})}$. Figure 4-15 illustrates the RTC phase correction system.

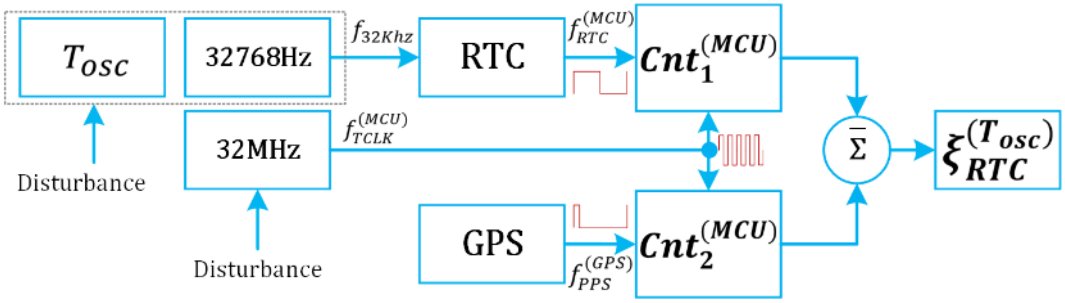

Figure 4-15 PPS-based RTC time drift correction system block diagram

Once RTC phase is aligned, the algorithm configures two 16-bit MCU counters (*Cnt*$_1$ and *Cnt*$_2$) in an overflow interrupt (OVI) mode. *Cnt*$_1$ is triggered by an external interrupt, generated on the rising edge of GPS-PPS signal. *Cnt*$_2$ is triggered by 1-sec RTC

timer interrupt, which is generated each time MCU's RTC timer reaches the top value 32,768 and then transitions to zero. Elapsed time at Cnt_1 or Cnt_2 overflow interrupt is calculated (See Eq. 4-22), where D_v is a clock divider and N is timer precision.

$$Cnt_{Tmax}^{(i)} = \frac{2^N \times D_v}{f_{TCLK}^{(MCU)}} = \frac{65536 \times 1}{32 \times 10^6} = 2.048\, msec \qquad \textbf{Eq. 4-22}$$

Because 2.048ms is maximum count time for Cnt_1 or Cnt_2, 488.28125 OVIs is required to count 1-sec, as evident in Eq. 4-23. OVI fraction value is equal to 0.28125/65536=18432 count. Total number of counts, calculated in Eq. 4-24, is number of OVI multiplied by counter precision plus the residual value in the counter register. New time correction coefficient $\xi_{RTC}^{(T_{osc})}$ is calculated, as in Eq. 4-25, where $Cnt_{avg}^{(i)}$ is the average count of n measurements (i.e., n-sec).

$$OVI_{1s}^{(Cnt^{(i)})} = \frac{t_{target}}{Cnt_{Tmax}^{(i)}} = \frac{1sec}{2.048ms} = 488.28125 \qquad \textbf{Eq. 4-23}$$

$$Cnt_{Total}^{(i)} = \left[2^N \times OVI^{(Cnt^{(i)})}\right] + Cnt^{(i)} \qquad \textbf{Eq. 4-24}$$

$$\boldsymbol{\xi_{RTC}^{(T_{osc})}} = \frac{Cnt_{avg}^{(2)} - Cnt_{avg}^{(1)}}{f_{TCLK}^{(MCU)}}; \qquad Cnt_{avg}^{(i)} = \frac{1}{n}\sum_{k=1}^{n} Cnt_{Total}^{(i)}(k) \qquad \textbf{Eq. 4-25}$$

$\xi_{RTC}^{(T_{osc})}$ value represents timing error (i.e., drift) or, in other words, time difference between measured periods of GPS-PPS-1Hz reference signal and RTC-1Hz signal.

Once the correction process is complete, GPS module is set to power-down mode. Corrected timestamp is the instantaneous RTC value plus the accumulated correction coefficient value over time.

Measurement resolution is one-cycle of $f_{TCLK}^{(MCU)}$, which is equal to 31.25ns. Correction algorithm should be executed at regular intervals (e.g., every hour) to adjust and realign the RTC phase and keep nodes synchronized. A high-level description of RTC frequency drift compensation using GPS-PPS signal is presented in the following algorithm. A flowchart representation is depicted in Figure 4-16.

Inputs: Sec, 60minCnt

Outputs: $\xi_{RTC}^{(T_{osc})}$, RTC-CNT

1: **IF** Sec = 0 **THEN**

2: $T(k) \leftarrow \frac{1}{M}\sum_{i=0}^{M-1} T(k-i) \leftarrow$ READ Temperature

3: **IF** $T(k) \geq T(k-i)+3$ or $T(k) \leq T(k-i)-3$ or 60minCnt **THEN**

4: INITIALIZE GPS in Tracking Mode

5: **WHILE** GPS-3D-Fix **IS** BUSY **LOOP**

6: **WAITFOR** *GPS-PPS Rising Edge Interrupt*

7: RTC-CNT←1{*Realign RTC Phase*, *Reinitialize RTC Reg.*}

8: $OVI^{(Cnt^{(i)})} \leftarrow 0$, $Cnt^{(i)} \leftarrow 0$, START $Cnt^{(i)}$; $i = \{1,2\}$

9: **WHILE** n < 2

10: **WAITFOR** *GPS-PPS Rising Edge Interrupt, RTC-1sec Interrupt*

11: $Cnt_{Total}^{(i)}(n) = \left[2^N \times OVI^{(Cnt^{(i)})}\right] + Cnt^{(i)}$; $i = \{1,2\}$

12: **LOOP**

13: GPS Module ← Power Saving mode, 60minCnt ← 0

14: $Cnt_{avg}^{(i)} = \frac{1}{n}\sum_{k=1}^{n} Cnt_{Total}^{(i)}(k)$; $i = \{1,2\}$

15: $\xi_{RTC}^{(T_{osc})} = \frac{Cnt_{avg}^{(2)} - Cnt_{avg}^{(1)}}{f_{TCLK}^{(MCU)}}$

16: **ENDIF**

17: **ENDIF**

PPS-based RTC frequency drift compensation algorithm

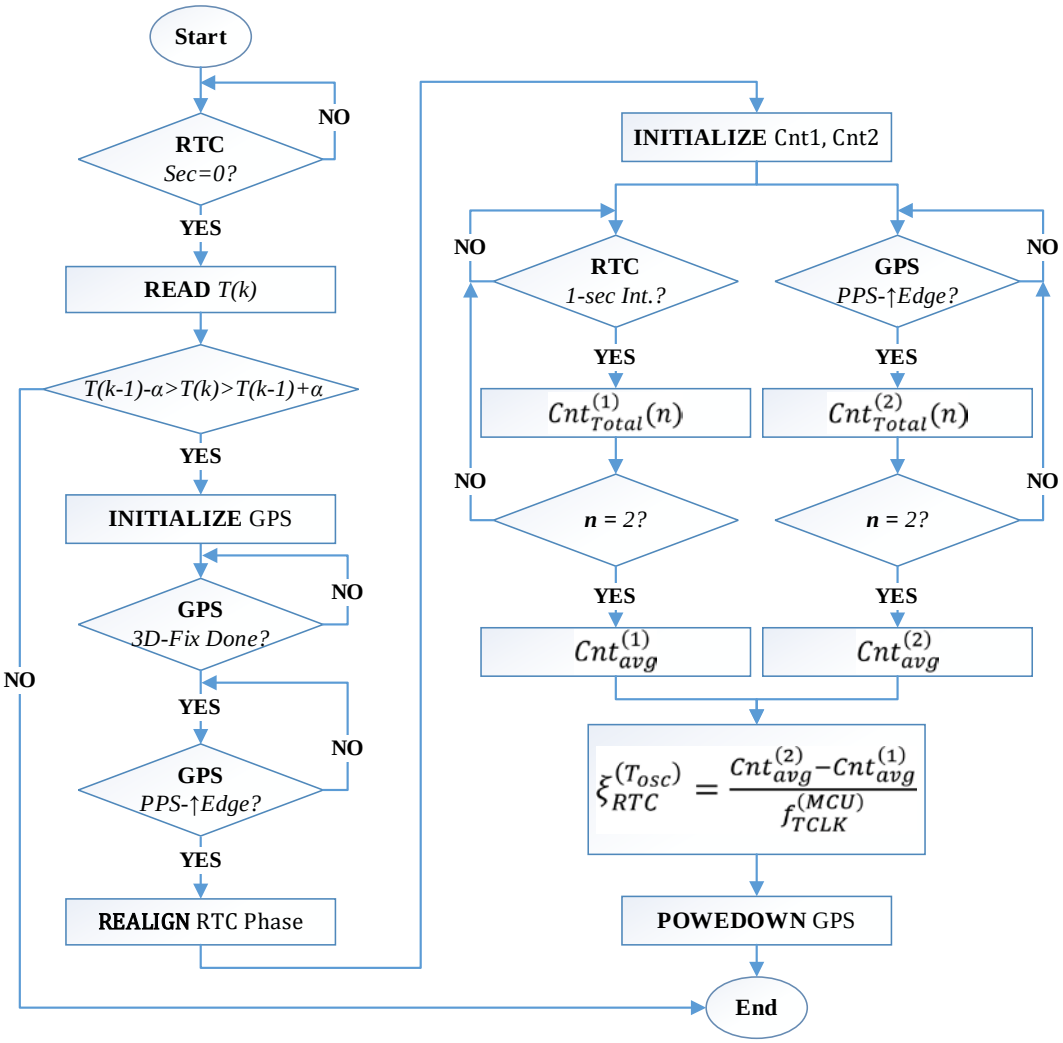

Figure 4-16 PPS-based RTC frequency drift compensation flowchart

A third approach to overcome 32Khz$_{osc}$ output drift was implemented in *i*VCCS$_{G2}$. *i*VCCS$_{G2}$ uses SiT1552 [104], an ULP 32.768KHz MEMS TCXO, to provide highly accurate clock source to the MCU's RTC unit. SiT1552 consists of MEMS resonator and a programmable analog circuit as depicted in Figure 4-17. Unlike quartz crystals that have a classic tuning fork parabola temperature curve with a 25°C turnover point, SiT1552 temperature coefficient is factory calibrated and corrected over multiple temperature points using an active temperature correction circuit to ensure extremely tight frequency variation (i.e., ±5ppm) over the -40°C to +85°C temperature range (See Figure 4-18).

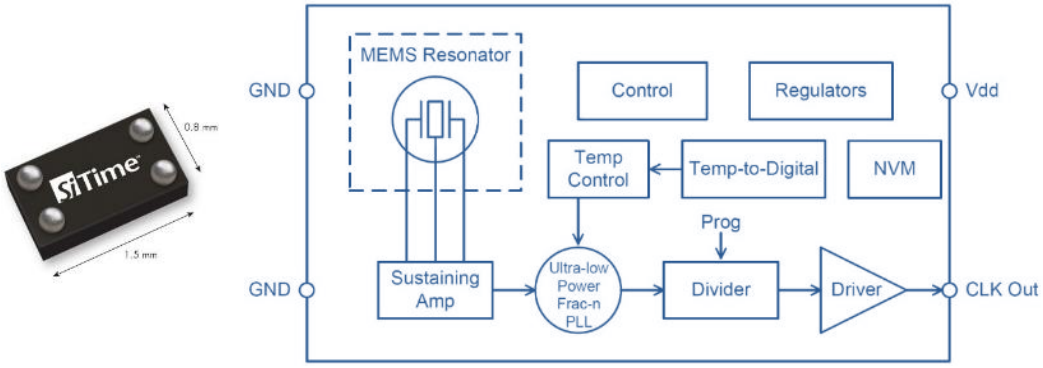

Figure 4-17 SiT1552 MEMS TCXO block diagram

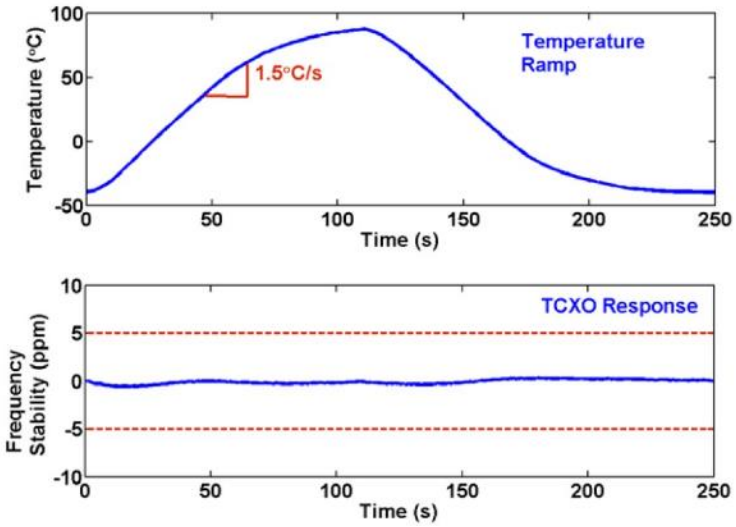

Figure 4-18 SiT1552 stability over temperature

Using SiT1552 will significantly improve 32Khz$_{osc}$ output stability with ±5ppm frequency tolerance over the -40°C to +85°C temperature range. However, ±5ppm can be reduced to 0.9537ppm by employing the STM32L0 MCU *Digital Smooth Calibration* feature in *i*VCCS$_{G2}$.

The STM32L0 MCU series implement an RTC calibration register (i.e., CALP-CALM) that can be used to increase or decrease the RTC clock (i.e., 32768Hz) with a fine resolution of 0.954ppm. An offset ranging from -511 to +512 RTC clock cycles can be added within 32-second cycle (i.e., 2^{22}) calibration window, which can be translated to a -487.1ppm to +488.5ppm calibration range. Hence, after RTC phase is aligned using GPS, all nodes can be kept synchronized by calculating RTC clock error when temperature is changed, and then adjusting RTC calibration registers instead of

accumulating $\xi_{RTC}^{(T_{osc})}$ to the timestamp itself. For a given $f_{CLK\_IN}^{(RTC)}$, RTC input clock, Eq. 4-26 can be used to calculate effective calibrated frequency $f_{CAL}^{(RTC)}$.

$$f_{CAL}^{(RTC)} = f_{CLK\_IN}^{(RTC)} 1 + \frac{(CALP \times 512) - CALM}{2^{20} + (CALM - CALP) \times 512} \qquad \textbf{Eq. 4-26}$$

4.4.2 Timestamps Matching Issues

As reported earlier, vehicle arrival and departure timestamps ($T_A^{(N_i)}$and $T_D^{(N_i)}$) are sent by each sensor node to an associated *i*AP for vehicle speed and length estimation, as well as, classification. In some cases, due to an interfering from other technologies operating in the ISM band or a heavy truck passing the sensor's detection zone—the radio channel might be degraded, resulting in delayed events (i.e., $T_A^{(N_i)}$and/or $T_D^{(N_i)}$).

Furthermore, a miscalibration in MAG baseline might cause a missing, delayed $T_D^{(N_i)}$, or unreasonable events. The issue of delayed events was solved by assigning a unique ID for each sensor node and combining $T_A^{(N_i)}$and $T_D^{(N_i)}$ timestamps with identification characters that are sent to the *i*AP at each event. Also, since sensor nodes *N1* and *N2* are placed at close proximity (6~10 meter apart), the probability of error due to a delayed event is very slim to none. In the case of missing $T_A^{(N_i)}$or $T_D^{(N_i)}$ timestamp, the corresponding $T_A^{(N_i)}$or $T_D^{(N_i)}$ event will be dropped.

4.5 Real-Time Vehicle Magnetic Length Estimation

Vehicle length is important for vehicle classification [12]. Vehicle magnetic length (VML) is defined as a disturbance in the Earth's magnetic field caused by a vehicle structure. VML is estimated from the product of vehicle speed and sensor occupancy time $T_{Occ}^{(N_i)}$, as shown in Eq. 4-27. A $T_{Occ}^{(N_i)}$ is defined as the difference between vehicle departure and arrival times at a designated detection point; both are influenced by magnetic field detection threshold.

$$\overline{VML} = \bar{v} \times T_{Occ}^{(N_i)} = \bar{v} \times \left(T_D^{(N_i)} - T_A^{(N_i)}\right) = \bar{v} \times \frac{T_D^{(N_A)} - T_A^{(N_A)} + T_D^{(N_B)} - T_A^{(N_B)}}{2} \quad \textbf{Eq. 4-27}$$

Because disturbance level to the Earth's magnetic field depends on vehicle composition of ferrous materials, VML can theoretically be longer than its actual physical length (i.e., bumper-to-bumper length).

Nevertheless, under assumptions that 1) symmetrical detection zone and 2) sensor sensitivity are independent of vehicle structure, vehicle physical length can be estimated using Eq. 4-28, where l_{DZ} is the estimated length of sensor's detection zone (Figure 4-10).

$$\bar{l}_V = l_M - \bar{l}_{DZ}^{(Ni)}; \qquad \widehat{l_{DZ}^{(Ni)}} \approx \bar{v}_i \left[T_D^{(N_B)} - T_A^{(N_A)}\right] - d^{N_A \to N_B} \quad \textbf{Eq. 4-28}$$

4.6 Real-Time Magnetic Length-based Vehicle Classification

In this section, the implementation algorithm for several LBVC schemes for MAG will be discussed. However, scheme development including field testing and data collection, as well as extensive data analysis will be introduced in Chapter 5 and 6.

Three distinctive LVBC schemes were developed as illustrated in Figure 4-19. Vehicles were grouped in each bin based on structural similarity and statistical data, which are discussed in Chapter 6. The PV group includes passenger cars, pickups, and SUVs. Short-trailer group (ST) includes busses, light-trucks, and single-unit-trucks. Long vehicles (L/LT) group includes single-trailer and multi-trailer trucks. The length decision boundaries for 4-G_{SX} using different thresholding methods (i.e., ϑ, α_T, and α_E) are shown in Table 4-1 (Refer to Chapter 6 for more details). These boundaries can be easily

implemented in real-time using if-then condition. The implementation model for LBVC scheme using MAG is depicted in Figure 4-20.

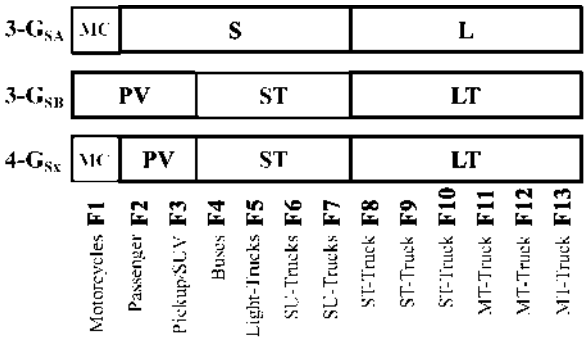

Figure 4-19 Proposed LBVC Schemes for MAG

Table 4-1 Discharge cycles and capacity as a function of charge voltage limit

		4G-S_x MAG		
Group	**FHWA-S_F**	**ϫ**	**α_T**	**α_E**
G1	F_1	0.7→2.984m	0.7→3.736m	0.7→2.9107m
G2	F_2—F_3	2.984→10.971m	3.736→7.7516m	2.912→7.427m
G3	F_4—F_7	10.971→14.727m	7.7516→14.95m	7.427→15.136m
G4	F_8—F_{13}	>14.727m	>14.95m	>15.136m

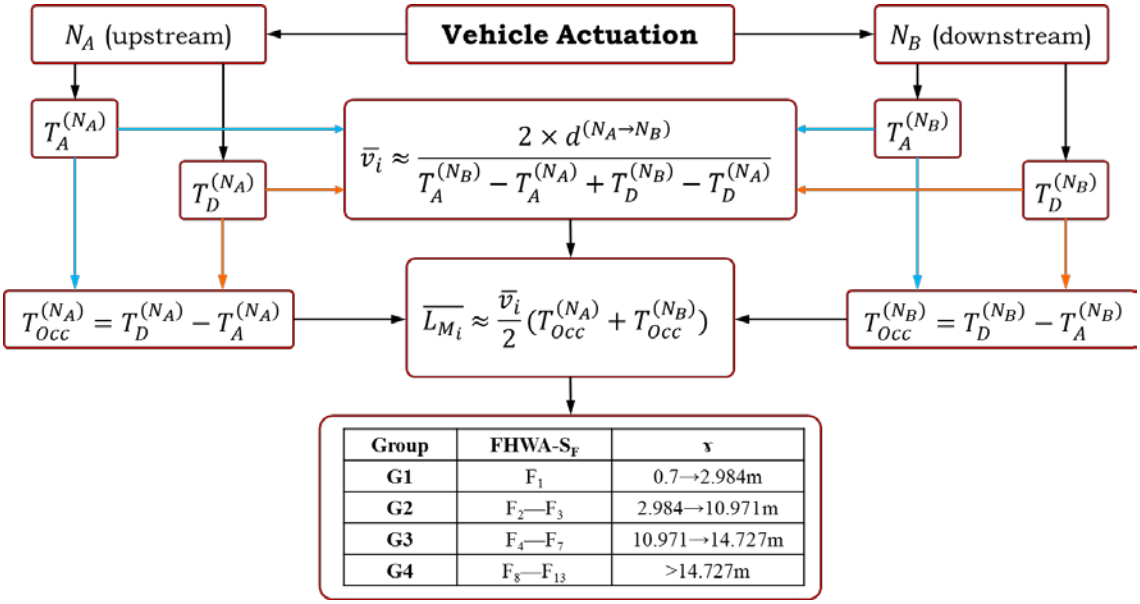

Figure 4-20 Implementation model for LBVC Scheme using MAG

Chapter 5: FIELD TESTING & DATA COLLECTION

Several field studies and tests were conducted during this research—many of which were in parking lots at *The University of Oklahoma-Tulsa Campus*. Additionally, eight major field tests were conducted on *highways* and *urban roads* in the state of Oklahoma. The objectives of these studies were to test sensor hardware, validate various developed algorithms, evaluate overall sensor real-time performance, and collect data for further analysis.

5.1 Data Collection Methodology

This section will report on major field studies conducted on the following highways and roadways in the state of Oklahoma:

- *Field Test 1* to *3—U.S. 412, Chouteau, OK 74337 USA*
- *Field Test 4—S. Yale Ave., Tulsa, OK 74135 USA*
- *Field Test 5 —Lake Hefner Pkwy, U.S. 74, OK 73120 USA*
- *Field Test 6—536 W State Hwy 152, Mustang, OK 73064 USA*
- *Field Test 7—Will Rogers Expy, OKC, OK 73108 USA*
- *Field Test 8—5959 Northwest Expy, OKC, OK 73132 USA*

5.1.1 Field Test 1

The first field study was conducted March 31st, 2015, from 10:55 to 13:15 at U.S. 412, Chouteau, OK 74337 USA, to evaluate the detection algorithm. iVCCS nodes were deployed in two setups: 1) roadway surface at lane center, and 2) roadside surface adjacent to rightmost and leftmost lanes. In both setups, MAG sensor x-axis was alongside traffic direction; y-axis was perpendicular to traffic lane; and z-axis was pointing upward, perpendicular to the ground. Two iAPs were installed by the roadside. The system was configured so that each iAP sent configuration and initialization commands to its iVCCS nodes cluster. In turn, iVCCS nodes sent vehicle counts in real time to their corresponding iAP. Two video cameras were used as ground-truth for data validation and performance evaluation. Vehicles class and count were manually extracted from video images by counting number of axles, according to FHWA Scheme F with 13 classes. To reduce human error factor, the extraction process was validated by

comparing extracted classes with collected data from a nearby WIM site. Even though video-based validation is considered the most accurate ground-truth, this method requires intensive labor.

Although only one *i*VCCS node is needed in each lane for vehicle detection, six nodes were deployed in each lane to study detection algorithm portability, as well as repeatability of vehicle magnetic signature. Cameras, *i*VCCS nodes, and *i*APs were synchronized using GPS-based clock to aid in data analysis and validation. Deployment setup is depicted in Figure 5-1.

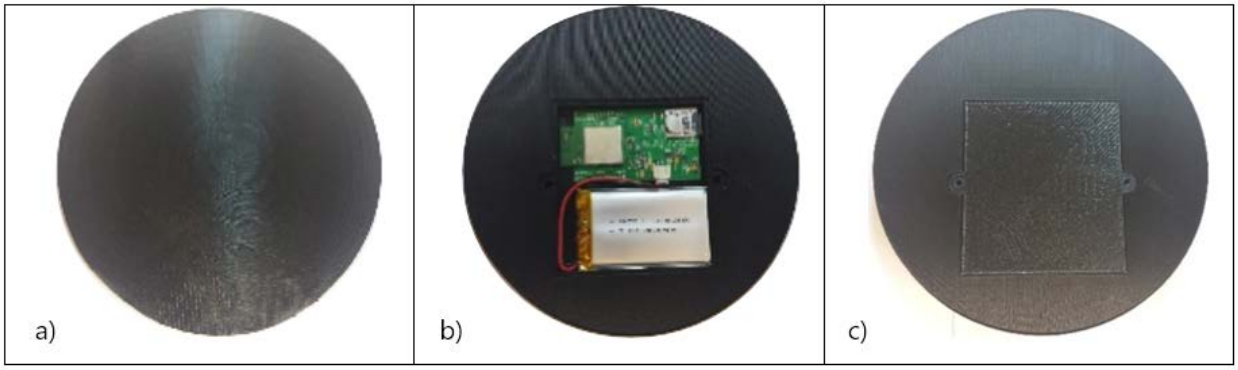

Figure 5-2 shows the initial prototype enclosure for *i*VCCS node, where *a* is top view, and *b* and *c* are bottom view. Enclosure size was 15.24(L)×15.24(W)×2.54(H) cm. The prototype was printed on a desktop 3D printer using PVC materials. Many nodes were cracked during the test as a result of enormous dynamic load caused by heavily loaded trucks traveling at 70mph speed. Figure 5-3 shows the placement of *i*VCCS nodes, *i*AP, and cameras at the deployment site. The objectives of this field test were to:

- Evaluate hardware reliability and system performance in a real life scenario.
- Evaluate the detection algorithm.
- Evaluate the initial enclosure prototype.
- Collect vehicle signature data for further analysis.

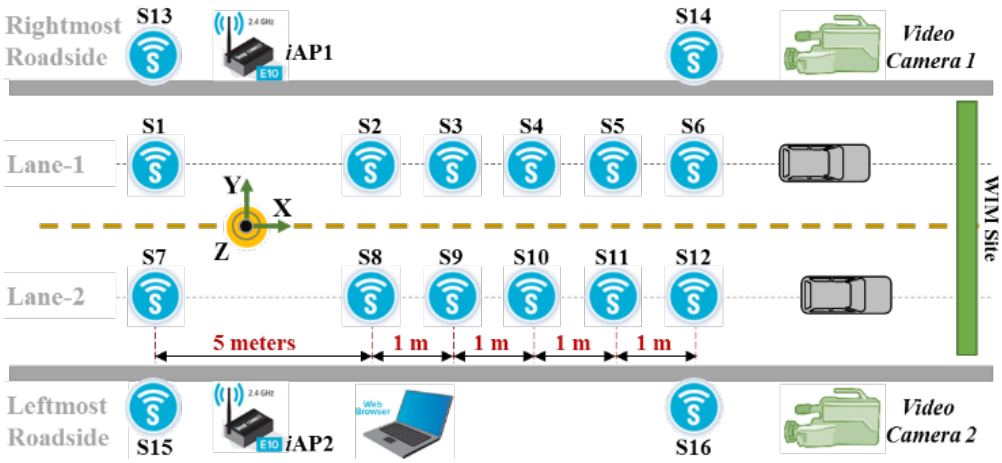

Figure 5-1 System setup layout on roadways (S1–S12) and roadsides (S13–S16)

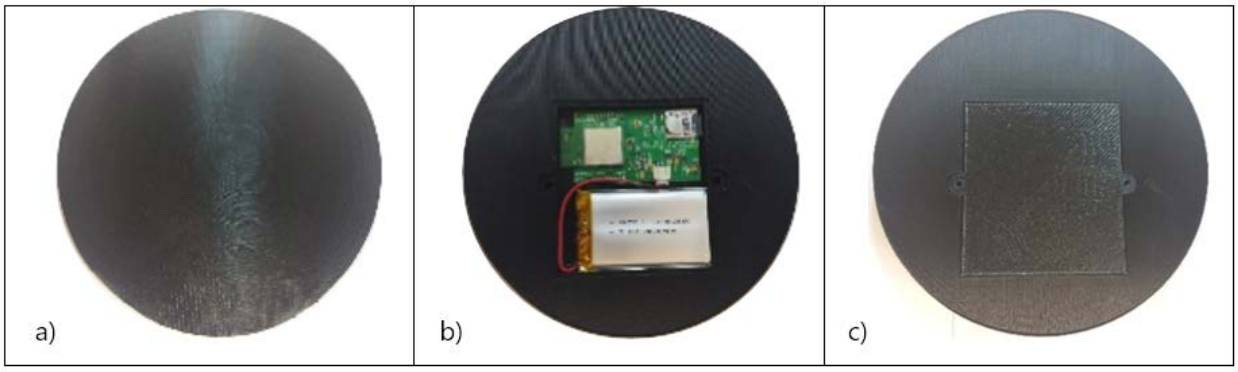

Figure 5-2 *i*VCCS enclosure—1st prototype

Figure 5-3 Field Test 1 deployment site

5.1.2 Field Test 2

A second field study was conducted August 3, 2015, from 8:50 to 12:50 at *U.S. 412 near Chouteau, OK, 74337 USA*. The overall purpose was to evaluate detection, synchronization, and speed estimation algorithms in two scenarios. Several *i*VCC nodes

were installed on *roadway surface* at the left lane center and adjacent to the left lane. The right lane was blocked using a closure so that traffic was forced to travel on only the left lane. All nodes for MAG axis (i.e., *x*, *y*, and *z*) were positioned identical to those in Field Test 1. The system was configured so that *i*VCC nodes report vehicle count and timestamp to a corresponding *i*AP in real-time. A video camera, as well as *Road Runner 3 Kit* [105] from Diamond Traffic, were used as ground-truth for data validation and performance evaluation. The *Road Runner kit* is a road tube-based vehicle counting and classification device. The kit reports 2-channel event timestamp data at a resolution of 30.5μs. Vehicles classes were manually extracted from video images by counting the number of axles for each vehicle. Effect of human error related to the extraction process was significantly reduced by comparing extracted classes from video with number of axels counted by *Road Runner*. Estimated speed and length from the *Road Runner* device were used to validate estimated speed and length reported by *i*VCCS.

Cameras, *Road Runner kit*, *i*VCCS nodes, and *i*APs were synchronized using a GPS-based clock. The deployment setup is depicted in Figure 5-4.

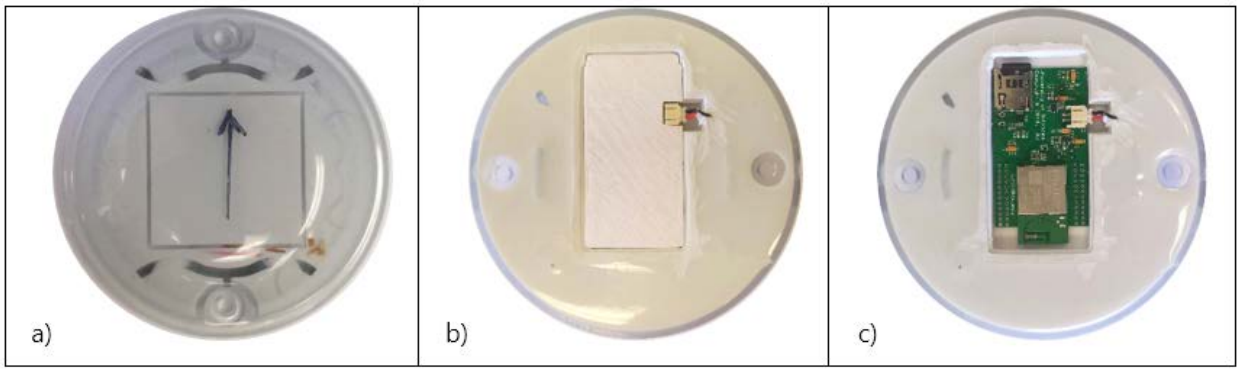

Figure 5-5 shows the second prototype enclosure for *i*VCCS node; *a* is the top view, and *b* and *c* are the bottom view. Enclosure size is 12.5(L)×12.5(W)×2.54(H) cm. Prototype shells were imported from China. A bucket to house the sensor PCB inside the shell was designed and printed on a desktop 3D printer. The shell was filled with epoxy after installing the battery and sensor bucket. Unfortunately, some nodes were cracked during the test, primarily because the epoxy material was not hard enough to withstand the dynamic load of heavy-loaded trucks. Figure 5-6 depicts the deployment site.

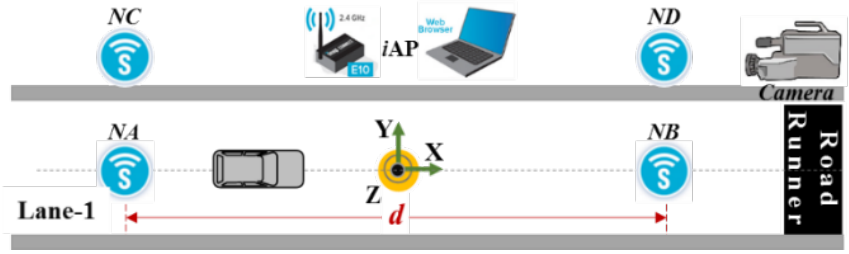

Figure 5-4 System setup layout on roadways (NA–NB) and roadsides (NC–ND)

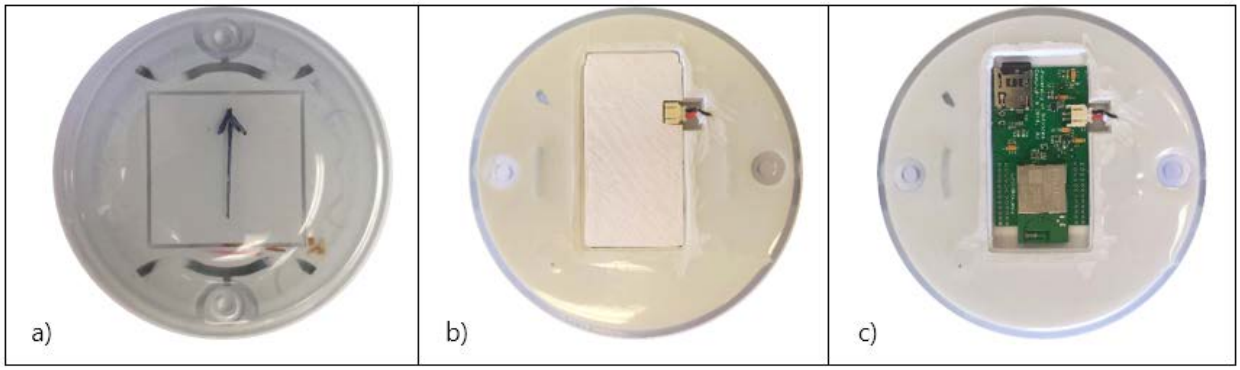

Figure 5-5 *i*VCCS node enclosure—2nd prototype

Figure 5-6 Field test 2 deployment site

The objective of field test 2 was to evaluate the following improvements:

- Holdover de-bounce time was based on the developed statistical modeling for detection error.

- An adaptive algorithm for geomagnetic baseline drift compensation was implemented to compensate for any drift resulting from variations in temperature, vibrations, and aging.
- An algorithm for time synchronization using the on-board embedded GPS module and RTC unit was implemented to estimate speed.
- In this test, each sensor node maintained its own independent local clock that was globally synchronized to a PPS (pulse-per-second) signal generated by the on-board GPS module.

5.1.3 Field Test 3

The third field study was conducted October 8, 2015, from 8:22 to 14:00 at *U.S. 412, Chouteau, OK 74337, USA*. In this test, an incredibly hard epoxy-filling material was used for q more durable enclosure. The left lane center was populated with six nodes (S_A, S_B, S_C, S_D, S_E, and S_F) installed on the *roadway surface* and separated by 2 meters. Six additional nodes (S_H, S_Q, S_L, S_G, S_I, and S_K) were installed on the roadway surface of left lane sides. Two nodes (S_M, and S_N) were also installed between left lane center and the edge for a vehicle magnetic signature diversity study. The right lane was blocked using a closure, and traffic was forced to only use the left lane. A single node (S_O) was deployed in right lane center to study interference from the adjacent lane. All nodes were positioning the same as MAG axis in first field test. Nodes were operated by three *i*AP installed on road shoulder at a separation distance of 10 meters. Sensors were configured to report vehicle count and timestamp to a corresponding *i*AP in real-time. A video camera, speed radar, and *Road Runner 3 Kit* were used as ground-truth for data validation and performance evaluation. Vehicles class was manually extracted from video images by counting number of axles for each vehicle. Estimated speeds and vehicle lengths reported from the *Road Runner Kit* were used to validate *i*VCCS data. The deployment setup layout is depicted in Figure 5-7. Figure 5-8 pictures field test 3 deployment site, installed sensors, and equipment.

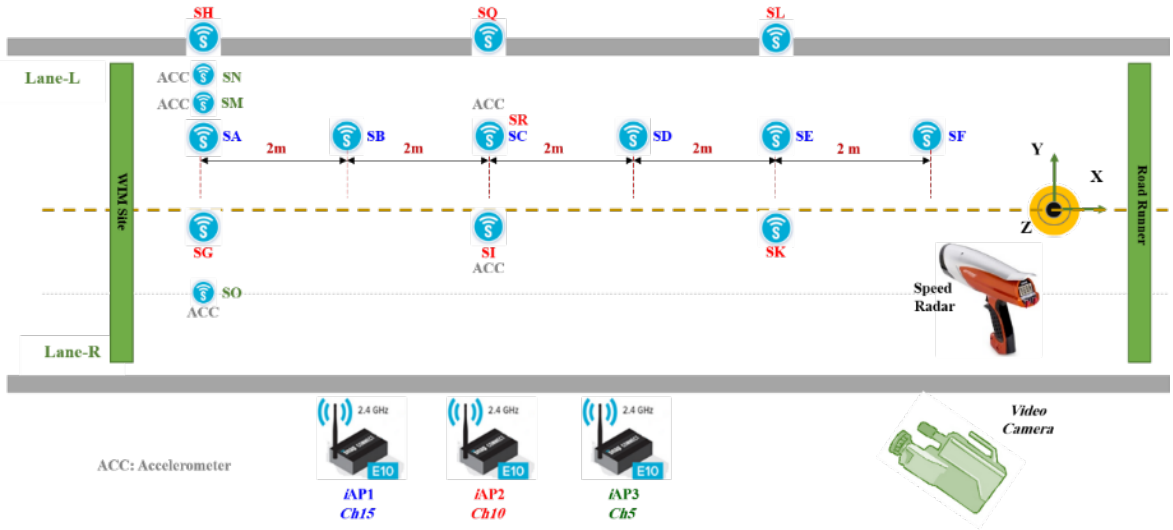

Figure 5-7 Field test 3 system setup layout

The objective of field test 3 was to collect additional data about various classes for a vehicle classification analysis study and to evaluate the following improvements:

- An optimization programming was applied to improve detection algorithm performance at higher sampling rate (400Hz and 800Hz).
- An algorithm for adaptive compensation of RTC frequency drift resulting from temperature variations was develop and implemented.
- T-synch algorithm was improved to correct residual errors.
- Arrival- and departure-detection time stamp procedures were optimized and improved for more accurate and consistent timestamping.
- On-board ACCEL was activated to collect vehicle axle data for future vehicle classification and axle detection data analysis.

Figure 5-8 Field test 3 deployment site

5.1.4 Field Test 4

Field study 4 was conducted October 15, 2015, from 9:30 to 17:30 on an urban road at *41st South Yale Ave, Tulsa, OK 74135 USA*. Eight *i*VCC nodes were installed— six nodes (S_A, S_E, S_F, S_G, S_H, and S_I) on the *roadway surface* center of each lane and two nodes (S_B, and S_K) on *roadsides surface* adjacent to the right lane. All nodes were operated using a single *i*AP. A video camera and *Road Runner Kit* were employed as ground truth for data validation and performance evaluation. Vehicles class was manually extracted from video images by counting number of axles for each vehicle. The same testing methodology was followed for this test as was in the first three tests. Deployment setup layout is depicted in Figure 5-9. Figure 5-10 pictures field test 4 deployment site, as well as installed sensors and equipment. The objective of this test was to evaluate sensors performance and accuracy at traffic signals on an urban road.

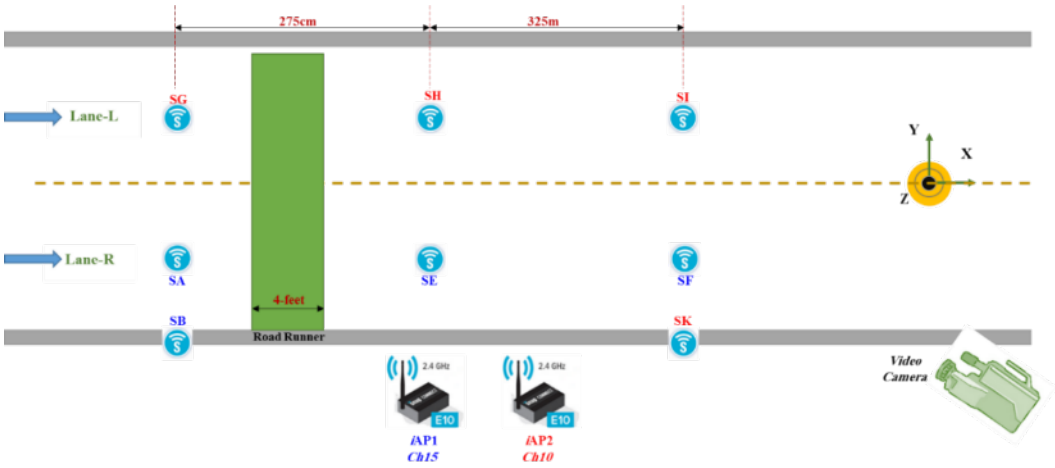

Figure 5-9 System setup layout on roadways and roadsides

Figure 5-10 Eight *i*VCCS nodes deployed on an urban road

5.1.5 Field Test 5

Field test 5 was conducted April 21, 2016, from 10:52 to 13:23 at *Britton bridge* on *Lake Hefner Pkwy, U.S. 74, OK 73120*. Several *i*VCC nodes were deployed on the north side of the highway. A video camera was installed on the shoulder and employed as ground truth for data validation and performance evaluation (See Figure 5-11).

The primary objective of this study was to collect VMS sampled using MAG and IDL for a post-processing analysis aimed at identifying the differences between the two VMS

sampled using MAG vs. IDL. The deployment location had been recently equipped by IDLs connected to a *Phoenix Traffic Classifier* from Diamond Traffic Products, Inc. This classifier device is able to sample VMS from IDL at a sampling rate of 1KHz.

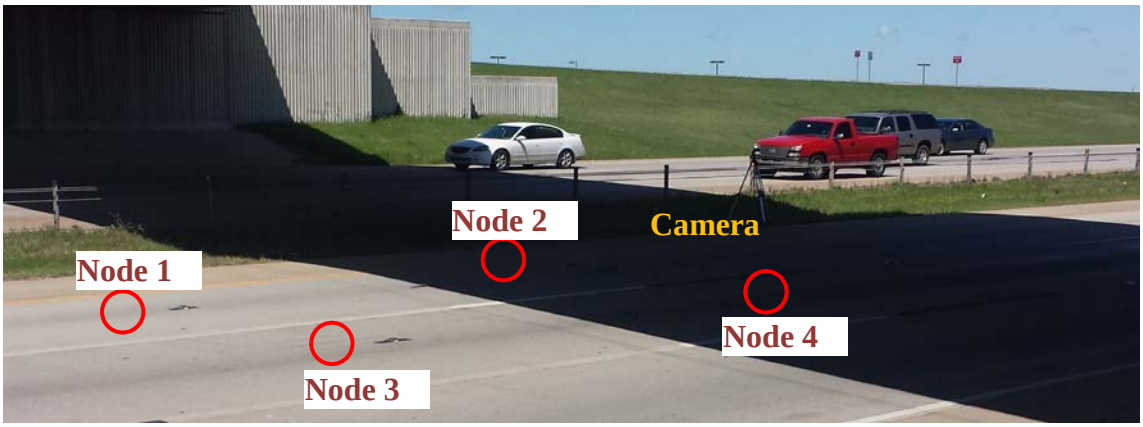

Figure 5-11 Field test 5 deployment site

5.1.6 Field Test 6

Field test 6 was conducted June 06, 2016, from 14:00 to 15:00 at *536 W State Hwy 152, Mustang, OK 73064 USA*. Several *i*VCC nodes were deployed to measure traffic traveling in both directions on the highway (See Figure 5-12). A tubes counter was also installed 20 feet from the sensors. A nearby AVC station was also employed in the study. ODOT personnel used a manual counter as ground truth for performance evaluation.

The objective of this study was comparing tubes count, AVC station count, and *i*VCC count performance with manual count. Initial data analysis was conducted by ODOT.

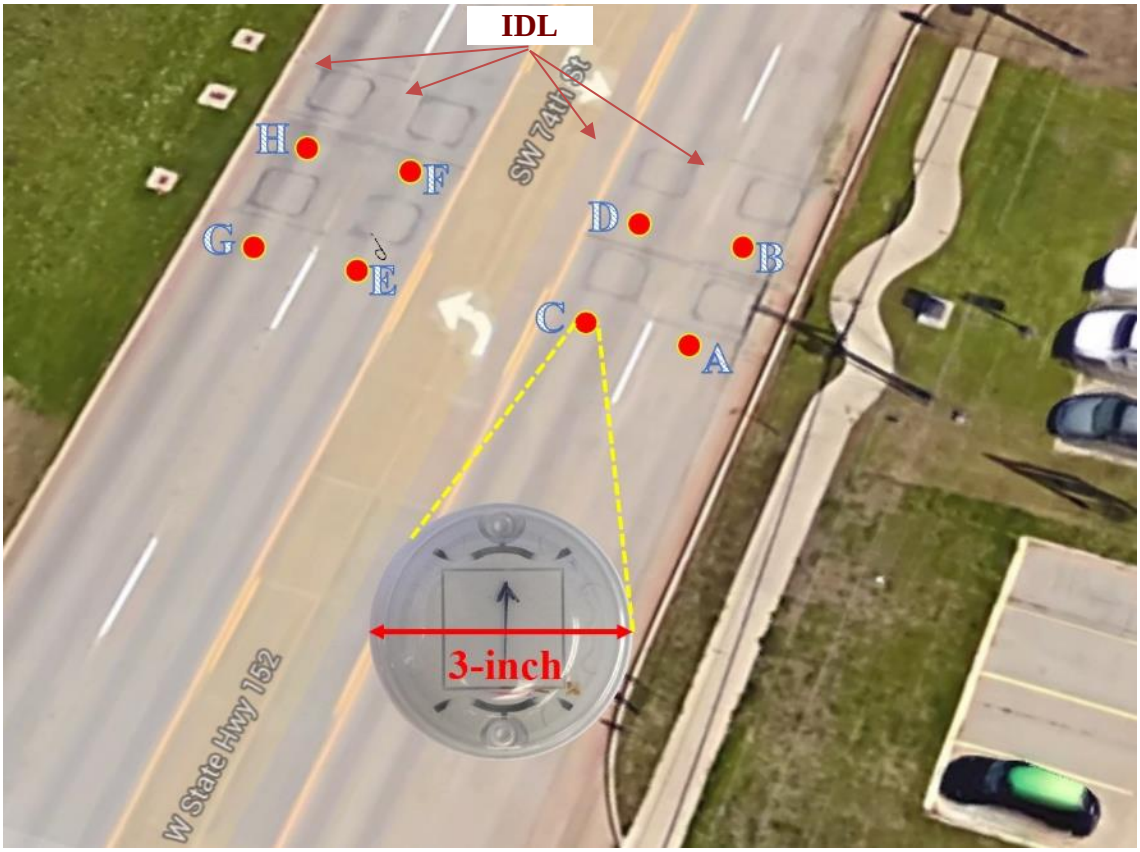

Figure 5-12 Field test 6 deployment site

5.1.7 Field Test 7

Field test 7 was conducted in June 06, 2016, from 09:00 to 10:00 at *Will Rogers Expy, OKC, OK 73108 USA*. A single *i*VCC node was placed on the far most left lane without traffic interruption (See Figure 5-13). A video camera deployed for an ODOT contractor was installed on the shoulder. A nearby AVC station was also employed in the study. ODOT personnel used a manual counter as ground truth for performance evaluation. The objective of this study was to compare performance between deployed technologies and manual count—ground truth data.

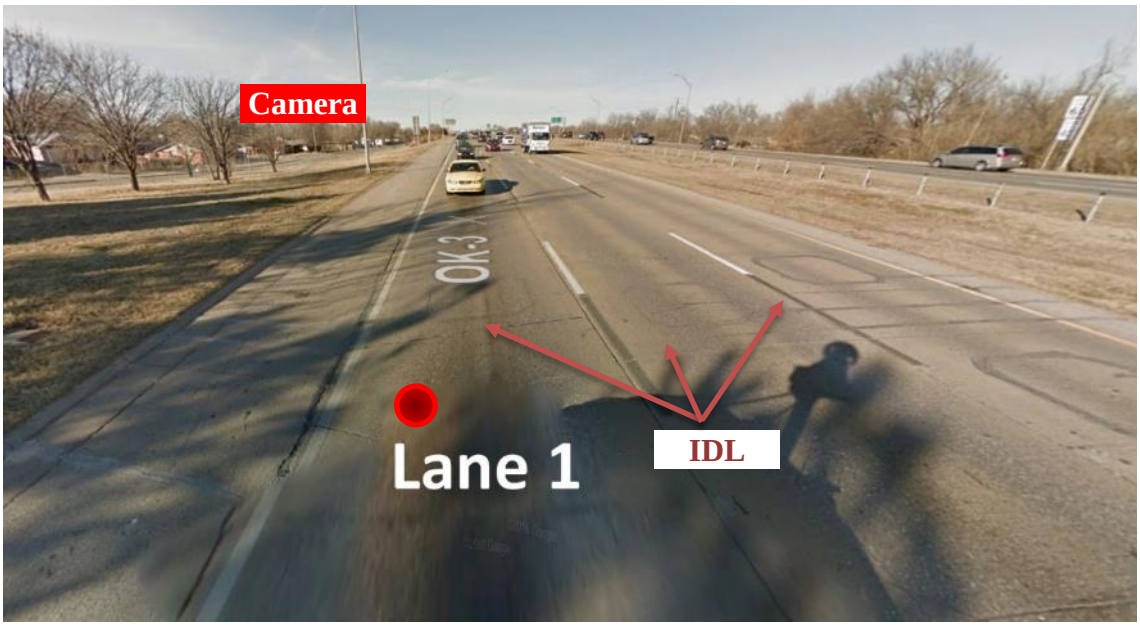

Figure 5-13 Field test 7 deployment site

5.1.8 Field Test 8

Field test 8 was conducted June 06, 2016, from 11:00 to 12:00 at *5959 Northwest Expy, OKC, OK 73132 USA*. Three *i*VCC nodes (A, B, C) were deployed at three points in the intersection (See Figure 5-14). A video camera for an ODOT contractor was installed on the shoulder, referenced to point A. A nearby AVC station that was also employed in field test 8. A tube counter was installed 10 feet apart from the sensors at point B and C. ODOT personnel used a manual counter as ground truth for performance evaluation. The objective of this study was to compare the performance of employed technologies at intersection with the manual count of the ground truth.

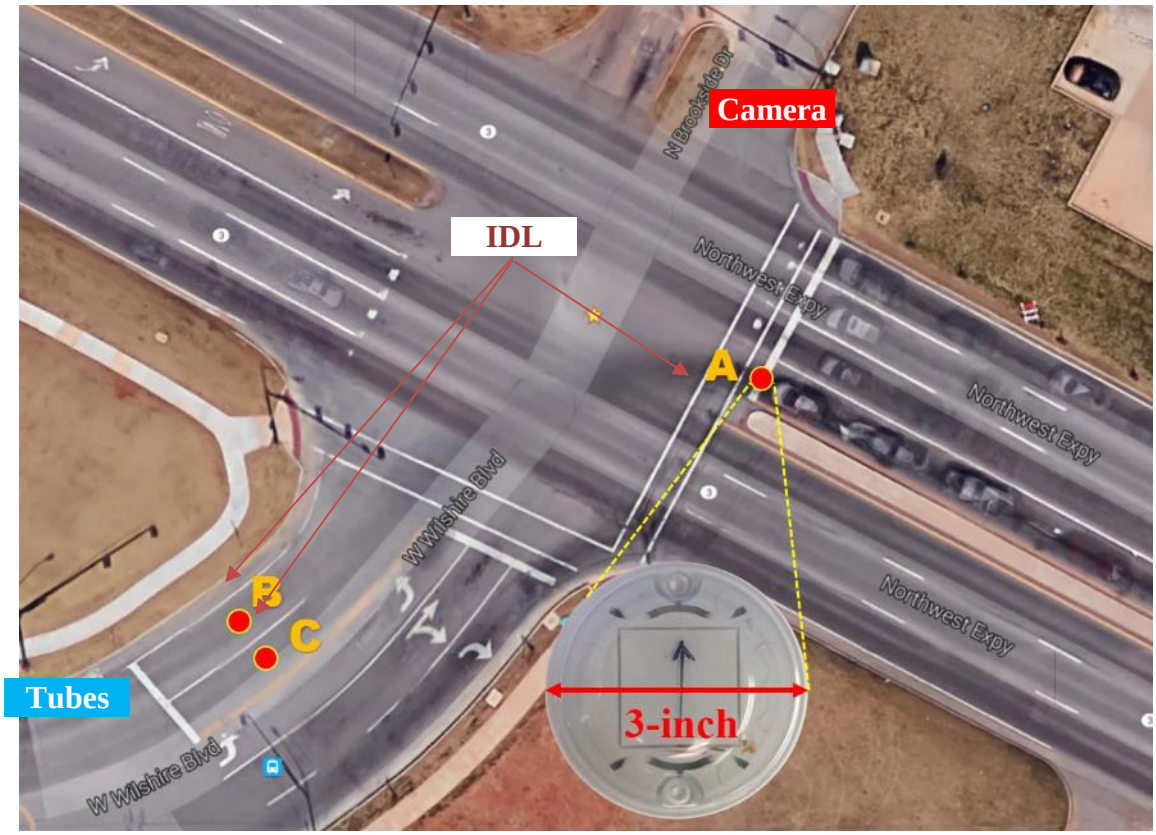

Figure 5-14 Field test 8 deployment site

5.2 Log Data File Format and Structure

The data logging unit stored raw data on the microSD card using either an *ASCII* (American Standard Code for Information Interchange) or *Binary* format. *ASCII* format is a text-based representation of data, which is more intuitive and easy to read by us. However, *ASCII* is memory consuming technique, as each single digit requires one byte in memory (e.g., the value 123 is represented in ASCII format using three bytes). The Binary format is a file that is not a text. However, it may include any type of data encoded in a binary representation (e.g., the value 123 is represented in Binary format using one byte). Besides efficient data storage, *Binary* format allows to transfer raw data over the wireless link for minimum energy. One disadvantage of Binary format is that data files require processing (i.e., format conversion) before it can be read as a text.

5.2.1 ASCII Log File Structure

An *ASCII* log file consists of a header, body, and end of file (EOF) line. The header includes information about data log time and data, node ID, and sensor configuration

settings. The body includes raw MAG (*Bx, By, Bz*) and ACCEL (*Ax, Ay, Az*) data, timestamps (i.e., vehicles arrival and departure times), instantaneous vehicle count, and reference timestamp (logged each minute). Table 5-1 illustrates ASCII file fields and corresponding values range. The MAG/ACC setting field indicates which sensor is active—"1" MAG only, "2" ACCEL only, "3" MAG and ACCEL are active. Given that MAG/ACC=1, only *Bx, By,* and *Bz* are logged. For MAG/ACC=2, only *Ax, Ay,* and *Az* will be logged. The ALL/VDT field indicates whether raw data are continually stored (ALL/VDT = 1) or only vehicle signature or/and acceleration data (i.e., vehicle detection) are stored (ALL/VDT=2). At midnight (i.e., 00:00:00), the current file will automatically close and a new file will be created. Two examples of an ASCII data log file are shown below.

Table 5-1 Log file structure in ASCII format

	Field	***Format***						***Value***
Header	Open Log File Time-Data	[hh:mm:ss dd\mm\yy]						
	Senor's ID	[ID-Nx]						x≫ [A…Z]or[a…z]
	Settings	[ODR = xxxHz] [MAG/ACC = x] [ALL/VDT = x]						xxx≫ [12.5…800] x≫ [1,2,or 3] x≫ [1 or 2]
Body	MAG *Bx By Bz* ACCEL *Ax Ay Az*	sxxxx	sxxxx	sxxxx	sxxxx	sxxxx	sxxxx	*Bx By Bz Ax Ay Az* s:±,xxxxx:0…16384
	Vehicle Arrival Time	[Nx_TA@secofday.RTCreg]						Secofday:0…86399 RTCreg: 0…32767
	Vehicle Departure Time	[Nx_TD@secofday.RTCreg]						
	Vehicle Number	[Nx_N#xxxxxxxxx]						[1…4294967295]
	Reference Timestamp	[t@hh:mm:ss]						
EOF	Close Log File Time-Data	[hh:mm:ss dd\mm\yy]						
	Total Number of Vehicles	[Nx_NT#xxxxxxxxx]						[1…4294967295]

[10:44:02 10\15\15]	**[00:00:00 10\15\15]**
ID-NK, ODR=400Hz, MAG/ACC=**1**, ALL/VDT=1	ID-NK, ODR=400Hz, MAG/ACC=**3**, ALL/VDT=1
-10 3 -1	-10 3 -1 -3 9 -4
⋮	⋮
NK_TA@38828.10391	**NK_TA@107.581**
⋮	⋮
30 -32 57	30 -32 57 2 5 8
⋮	⋮
NK_TD@38828.21667	**NK_TD@107.17633**
NK_N#1	**NK_N#1**
-3 -6 -8	-3 -6 -8 7 5 -4
⋮	⋮
2 5 8	-9 5 -7 -2 -5 8
t@10:48:00	**t@16:30:00**
-1 8 -4	-8 7 -4 -3 9 -4
⋮	⋮
-3 9 -4	-3 9 -4 1 10 -9
[17:33:00 10\15\15]	**[23:59:59 10\15\15]**
NK_VC#1352	**NK_VC#18109**

Example of ASCII data log file

5.2.2 Binary Log File Structure

In general, the binary file structure is similar to the ASCII file structure—both contain header, body and EOF sections. Binary file format lacks control characters (e.g., CR) to separate data lines; thus, prefix [**P**] and suffix [**S**] binary values are used to differentiate between various data values. For data format of type *Word* or *Integer*, the order is always [MSB] then [LSB]. The sign is assigned as the last bit of the MSB byte; a '0' indicates positive number and '1' indicates negative number. The ODR is assigned a values from 1 to 7 as a reference to 25, 50, 100, 200, 400, 800, or 1600Hz, respectively. The header section starts with a prefix value [00] and ends with a suffix value [00]. The number of bytes in the header is fixed to 50 bytes, 40 bytes are reserved for future development purpose. Table 5-2 illustrates the structure of Binary file format.

Table 5-2 Log file structure in Binary format

	Field	*Format*	*Value*	*bytes*
Header	*Open Log File Time-Data*	[00]**[-]…[-]**	hhmmssDDMMYY	06
	Senor's ID	**[-]**	ID≫(01…99)	01
	ODR	**[-]**	[01…06]	01
	MAG/ACC	**[-]**	[01,02, or 03]	01
	ALL/VDT	**[-]**[00]	[01 or 02]	01
	Reserved	**[-]…[-]**	R[255]	40
Body	*MAG Bx By Bz* *ACCEL Ax Ay Az*	**[-]…[-]** **[-]…[-]** [FF][FF]	$[MSB_x][LSB_x]…[MSB_z][LSB_z]$ $[sFFF]_{MSB}$≫ $s^+=0, s^-=1$	6/12
	Vehicle Arrival Time	[FA]**[-]…[-]**[FB][FF]	Secofday(0…86399)≫3-bytes RTCreg(0…32767)≫2-bytes	5
	Vehicle Departure Time	[FC]**[-]…[-]**[FD][FF]		
	Vehicle Number	[FE]**[-][-]**[FE][FF]	VN≫(1…65536)	2
	Reference Timestamp	[F8]**[-]…[-]**[F9][FF]	Secofday(0…86399)≫3-bytes	3
EOF	*Close Log File Time-Data*	[F6]**[-]…[-]**[F7][FF]	Secofday(0…86399)≫3-bytes	3
	Total Number of Vehicles	[F4]**[-][-]**[F5][FF]	TVN≫(1…65536)	2

An example shows the order of data bytes in Binary format for MAG/ACC = **1** is as follows:

[0x00][hh][mm][ss][DD][MM][YY][ODR][MAG/ACC][ALL/VDT][0x00][40 reserved byte… 0xFF][MSB_x][LSB_x][MSB_y][LSB_y][MSB_z][LSB_z]
[0xFF][0xFF][MSB_x][LSB_x][MSB_y][LSB_y][MSB_z][LSB_z][0xFF][0xFF]……[0xFA][$MSB^H_{Secofday}$][$MSB^L_{Secofday}$][$LSB_{Secofday}$][MSB_{RTCreg}][LSB_{RTCreg}][0xFB][0xFF][MSB_x][LSB_x][MSB_y][LSB_y][MSB_z][LSB_z][0xFF][0xFF]……[0xFC][$MSB^H_{Secofday}$][$MSB^L_{Secofday}$][$LSB_{Secofday}$][MSB_{RTCreg}][LSB_{RTCreg}][0xFD][0xFF][xFE][MSB_{VN}][LSB_{VN}][0xFE][0xFF][MSB_x][LSB_x][MSB_y][LSB_y][MSB_z][LSB_z][0xFF][0xFF]……[0xF6][$MSB^H_{Secofday}$][$MSB^L_{Secofday}$][$LSB_{Secofday}$][MSB_{RTCreg}][LSB_{RTCreg}][0xF7][0xFF][0xF4][MSB_{TVN}][LSB_{TVN}][0xF5][0xFF]

An example shows the order of data bytes in Binary format for MAG/ACC = **3** is as follows:

[0x00][hh][mm][ss][DD][MM][YY][ODR][MAG/ACC][ALL/VDT][0x00][40 reserved byte 0xFF][MSB^M_x][LSB^M_x][MSB^M_y][LSB^M_y][MSB^M_z]
[LSB^M_z][MSB^A_x][LSB^A_x][MSB^A_y][LSB^A_y][MSB^A_z][LSB^A_z][0xFF][0xFF][MSB^M_x][LSB^M_x][MSB^M_y][LSB^M_y][MSB^M_z][LSB^M_z][MSB^A_x][LSB^A_x][MSB^A_y][LSB^A_y][MSB^A_z][LSB^A_z][0xFF][0xFF]…[0xFA][$MSB^H_{Secofday}$][$MSB^L_{Secofday}$][$LSB_{Secofday}$][MSB_{RTCreg}][LSB_{RTCreg}][0xFB][0xFF][MSB^M_x][LSB^M_x][MSB^M_y][LSB^M_y][MSB^M_z][LSB^M_z][MSB^A_x][LSB^A_x][MSB^A_y][LSB^A_y][MSB^A_z][LSB^A_z][0xFF][0xFF]…[0xFC][$MSB^H_{Secofday}$][$MSB^L_{Secofday}$][$LSB_{Secofday}$][MSB_{RTCreg}][LSB_{RTCreg}][0xFD][0xFF][xFE][MSB_{VN}][LSB_{VN}][0xFE]
[0xFF][MSB_x][MSB^M_x][LSB^M_x][MSB^M_y][LSB^M_y][MSB^M_z][LSB^M_z][MSB^A_x][LSB^A_x][MSB^A_y][LSB^A_y][MSB^A_z][LSB^A_z][0xFF][0xFF]……[0xF6][$MSB^H_{Secofday}$][$MSB^L_{Secofday}$]
[$LSB_{Secofday}$][MSB_{RTCreg}][LSB_{RTCreg}][0xF7][0xFF][0xF4][MSB_{TVN}][LSB_{TVN}][0xF5][0xFF]

Chapter 6: MODELING AND OPTIMIZATION

6.1 Overview

This chapter introduces an optimization study and analytical analysis of detection error in vehicle detection algorithms used by MAG. Two types of errors were identified based on their relationship to the implemented "de-bounce" time. A probabilistic model was established to describe the relationship between detection error and chosen "de-bounce" time. The resulting model was numerically solved to find an optimal de-bounce time that achieves the best detection performance according to traffic characteristics at the measuring site. Using the optimal de-bounce time to enhance detection resulted in a 0% error in detecting 416 vehicles.

6.2 Analysis of iVCCS Detection Algorithm

Vehicle detection is the most basic and yet the most important feature of an ITS system. The accuracy of speed estimation, vehicle classification, traffic volume analysis, and highway modeling are dependent on the accuracy of vehicle detection. Magnetometer based traffic monitoring systems [17], [38], [72], [106], [107] implement simple detection algorithms to accurately count passing vehicles.

Vehicle's presence detection algorithms in general compare flux magnitude amplitude to a preset threshold that is determined based on statistical characteristics of sensor's output noise when no ferromagnetic object exists within its detection region. This threshold is used to distinguish a vehicle's presence within the sensor's detection zone from environment noise. However, these algorithms may falsely detect a single vehicle as multiple vehicles if spikes or transient events that cause the signal to drop below the threshold for a brief period of time that occur while the vehicle stills in the detection region. Vehicle's presence detection algorithms implement de-bounce timers to overcome this issue. A de-bounce timer guarantees the signal level is below the detection threshold longer to decide that no vehicle is present any longer. Figure 6-1 depicts an example of vehicle false detection when no de-bounce timers are implemented.

Using de-bounce timers improves vehicles detection accuracy. Figure 6-2 illustrates a simplified version of the implemented detection algorithm [72]. It uses two thresholds; arrival threshold, and departure threshold. The latter is set slightly lower than the former to increase immunity against noise.

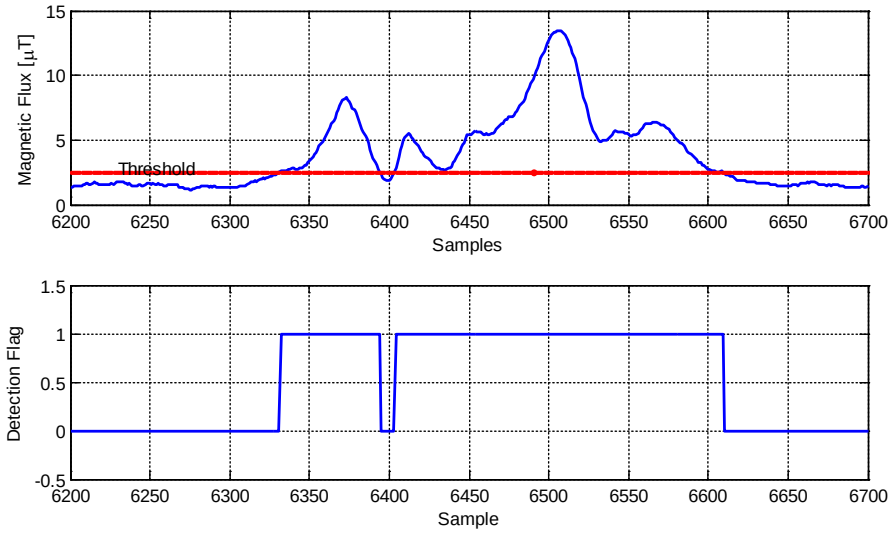

Figure 6-1 False vehicle detection due to transient event

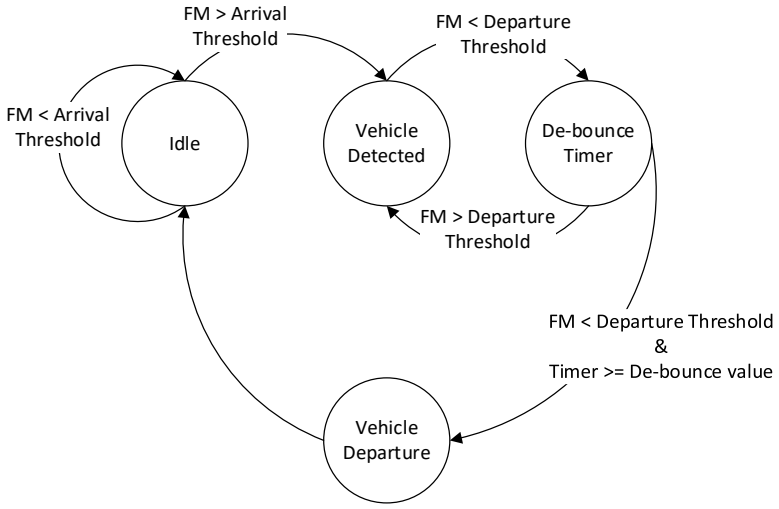

Figure 6-2 Simplified version of detection algorithm state machine

This algorithm fails in two cases. The first case (misdetection) occurs when the time separating consecutive vehicles arrival is less than the chosen de-bounce time, resulting in two vehicles counted as one. The second case (false detection) is observed in large trucks with single or double trailers. These trucks can be falsely detected as two vehicles

instead of one. This is attributed to the truck's unique structure that consists, from a magnetic point of view, of three separate sections, as shown in Figure 6-3.

Section 1—engine and first three axles—contains the majority of the truck's ferromagnetic mass. Ferromagnetic mass in Section 2 is relatively small because trailers are typically either empty or loaded with non-ferromagnetic materials. As a result, the magnetic disturbance caused by Section 1 is considerably higher than its counterpart in Section 2.

If signal magnitude corresponding to section 2 stays below the preset detection threshold for a duration longer than the de-bounce time, the magnetometer detects section 3 as a separate vehicle. This phenomenon is referred to in literature as "pulse break-up" [108]–[112]. Figure 6-4 illustrates pulse break-up in a single trailer truck. The truck's signature drops below departure threshold longer than the de-bounce time which is set to 200 milliseconds in this case.

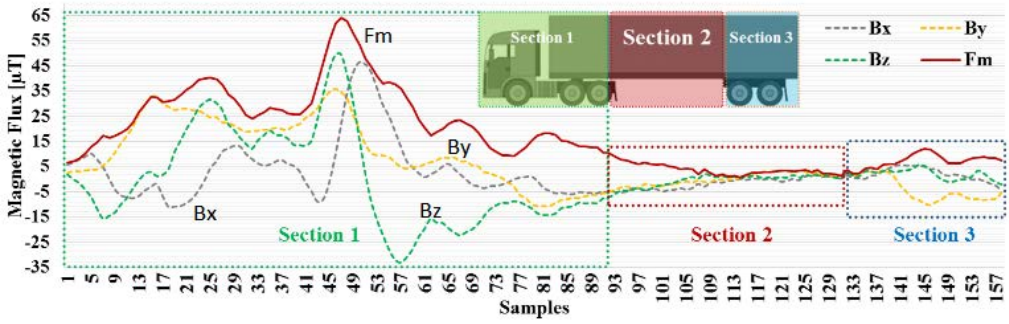

Figure 6-3 Magnetic Flux and Sections of a class 9 vehicle

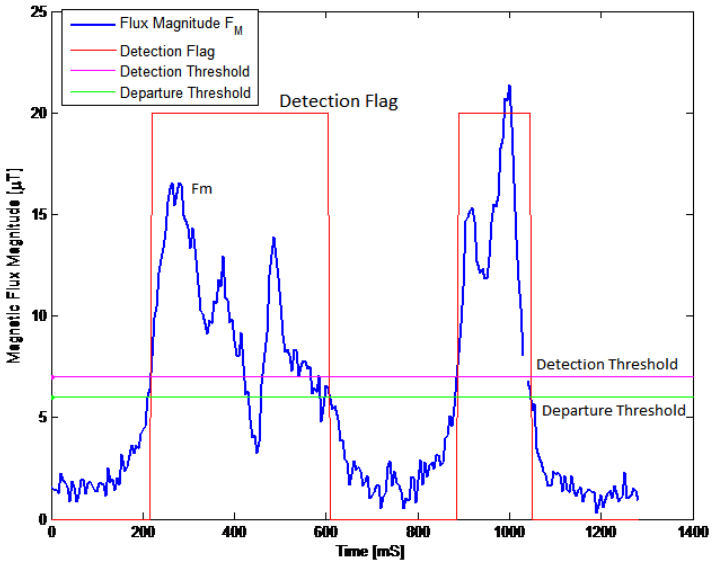

Figure 6-4 Magnetic signature corresponding to a class 9 truck

6.3 Earlier Studies and Solutions

Pulse break-up and detector errors have been heavily studied for systems based on inductive loops. However, same concepts apply to magnetometers because they are similar to loops from operational point view. The only difference between them is that loops are active sensors. They produce their own magnetic field and detect vehicles by measuring the eddy currents induced by a ferromagnetic object within its detection zone.

Identification and correction of pulse break-up and other errors has been studied at both macroscopic and microscopic levels. Macroscopic methods [113]–[116] use statistical tests to detect anomalies in aggregate detector data within a determined interval. The objective of these methods is not detecting individual erroneous records, but correcting statistical parameters affected by these errors. This is done by evaluating detector statistics against preset thresholds. Threshold values are determined according to traffic theory principles and traffic models observed in the site being studied. Macroscopic methods lack the ability to identify errors at the vehicle level, and will not perform well in homogeneous traffic where traffic models are not well defined. On the other hand, microscopic methods examine individual vehicle actuations and are capable of detecting and correcting errors in real-time. L. Chen and A. May [109] developed a microscopic method to identify pulse break-ups in loop detectors. They first obtain on-

time[1] distribution. The off-time between two pulses is then compared to a threshold preset according to the aforementioned distribution. P. Cheevarunothai, Y. Wang, and N. Nihan [112] developed an algorithm to enhance truck detection using dual loop configurations. The algorithm combines two detections if their headway[2] is less than 0.63 seconds at either loop. Figure 6-5 showcases few examples when this algorithm would identify a break-up. The algorithm decreased average detection error by 31.75%. B. Coifman [110] proposed an off-line approach to identify hardware and crosstalk errors in dual loop detectors. The method matches pulses detected at upstream and downstream loops and analyses difference between occupancy times at both of them. If the difference is larger than a certain threshold, an error will be reported. The threshold value is set based on statistical analyses of occupancy times obtained in free flow conditions. The analysis did not include congested traffic.

The most notable work addressing identification and correction of detector errors is the algorithm H. Lee and B. Coifman developed in [108]. Their algorithm identifies pulse break-ups through multiple heuristic tests. The tests were designed to be adaptable to changing traffic patterns. Authors found that using the ratio of following to preceding on-times, ratio of off-time to preceding on-time, and twentieth percentile of the last 41 off-times is less sensitive to speed changes compared to absolute on-time tests. Figure 6-6 depicts a step by step description of the algorithm. Results show a 92% success rate in identifying pulse break-ups in free flow and congested traffic. However, false positive rate in case of congestion is alarmingly high, hence authors recommend disabling the algorithm in congested sites.

All of the above work attempted to improve inductive loops data quality by implementing high level heuristic tests. These tests attempt to identify detection errors and devise corrections based on the type of error. However, no effort was made to address the problem's root cause and prevent pulse break-up or tailgating errors from happening in the first place. Moreover, most proposed methods perform poorly when

[1] On-time is the time when the detector indicates the presence of a vehicle (detection flag is set to On)
[2] Headway is the time separating the arrival of two consecutive events

traffic patterns change from free low to congestion. Addressing these issues requires a low level analysis of the underlying detection algorithm and redesigning it in a way that minimizes the probability of such errors.

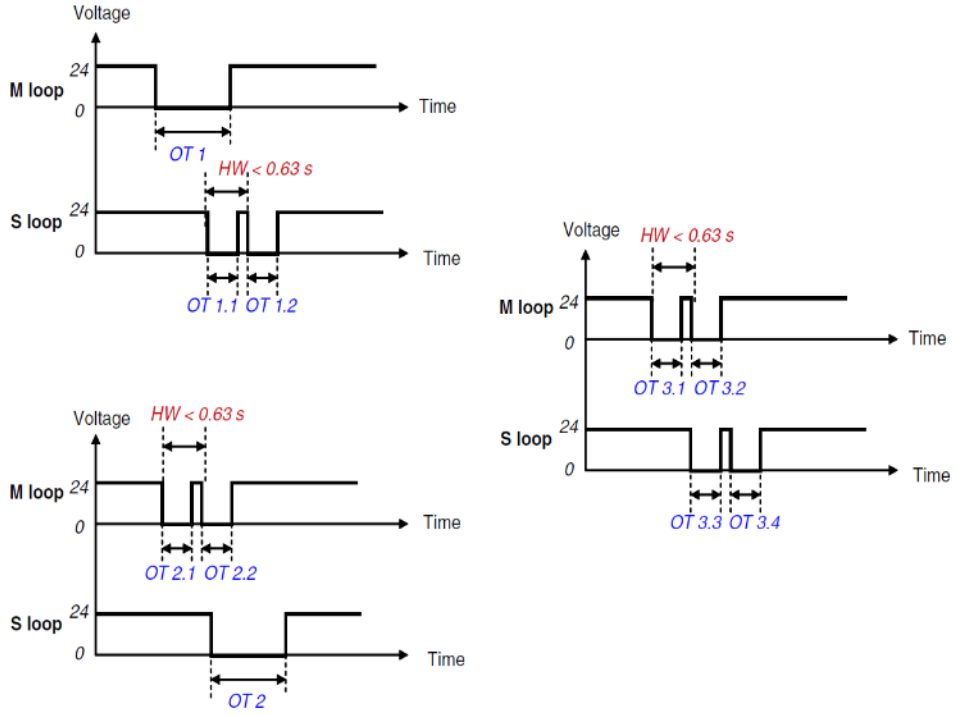

Figure 6-5 Pulse breakup detection and correction in dual loop sets [112]**.**

Based on the background study, the research team explored the following two ideas to prevent miss-detection of trucks:

1) Statistically analyze the inter-arrival times of consecutive vehicles and adjust the detection de-bounce time to accommodate magnitude decrease resulting from a truck's section 2.
2) Identifying whether two consecutive detections that happen within a short timeframe belong to the same class 9 vehicle or two smaller vehicles.
3) Develop a probabilistic model to identify the optimal debounce time value.

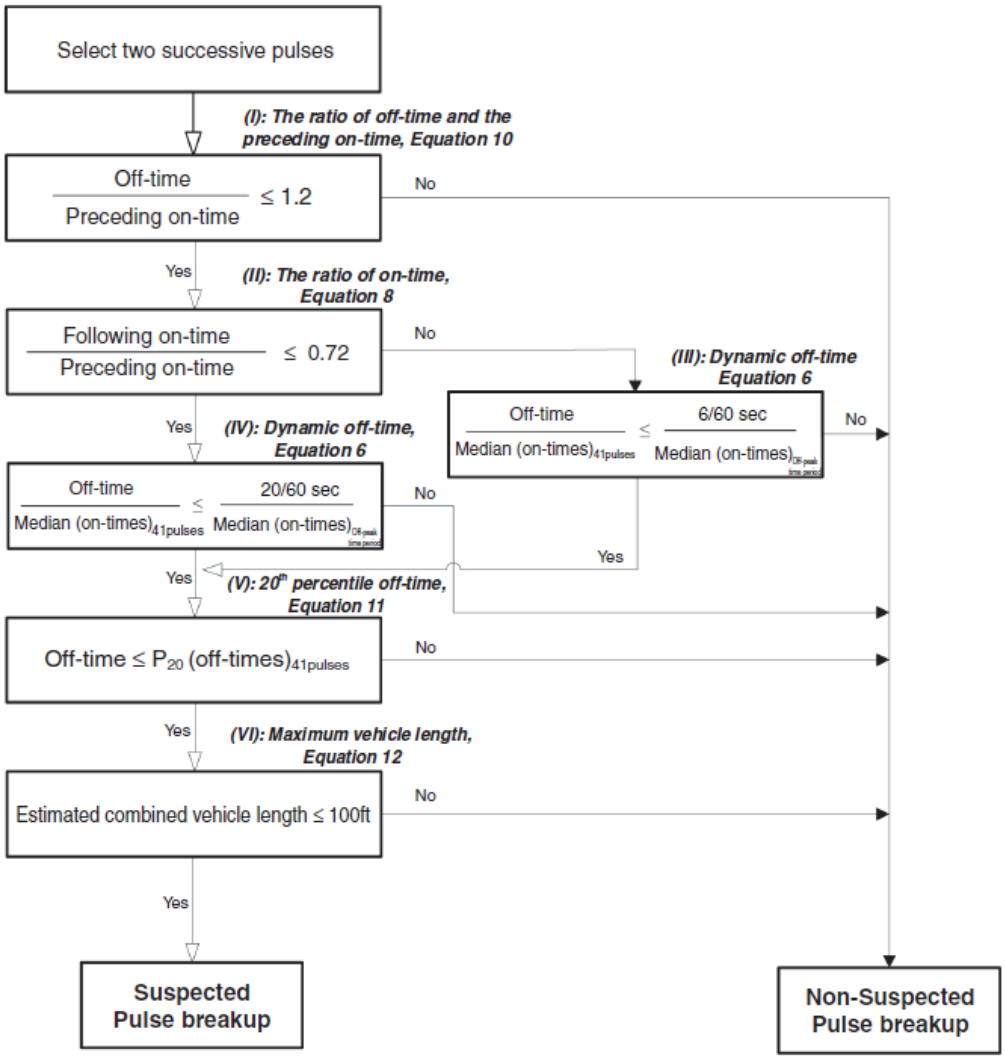

Figure 6-6 Pulse break-up detection algorithm [108]**.**

6.4 Statistically analyze vehicles inter-arrival times

Class 9 miss-detection can be simply prevented by increasing the de-bounce time used to prevent glitches and spikes from being counted as vehicles. Although this approach would decrease the probability of error in detecting long trucks, it would also increase the probability of fusing two small vehicles travelling very close to each other into one count.

In order to find the optimal value of the de-bounce time, the team calculated the cumulative distribution function (CDF) of "following time", i.e. the time between detecting two consecutive vehicles using historical data collected at ODOT's WIM16 site. The dataset included about 12500 vehicles with a following time equal to or less than 5

seconds. We can deduct from the CDF in Figure 6-7 that the probability of detecting two consecutive vehicles within 300ms is about 7%. As a result, using a de-bounce time of 300ms instead of 150ms can enhance detection accuracy for long trucks at the expense of an $7/2 = 3.5\%$ error in detecting smaller vehicles.

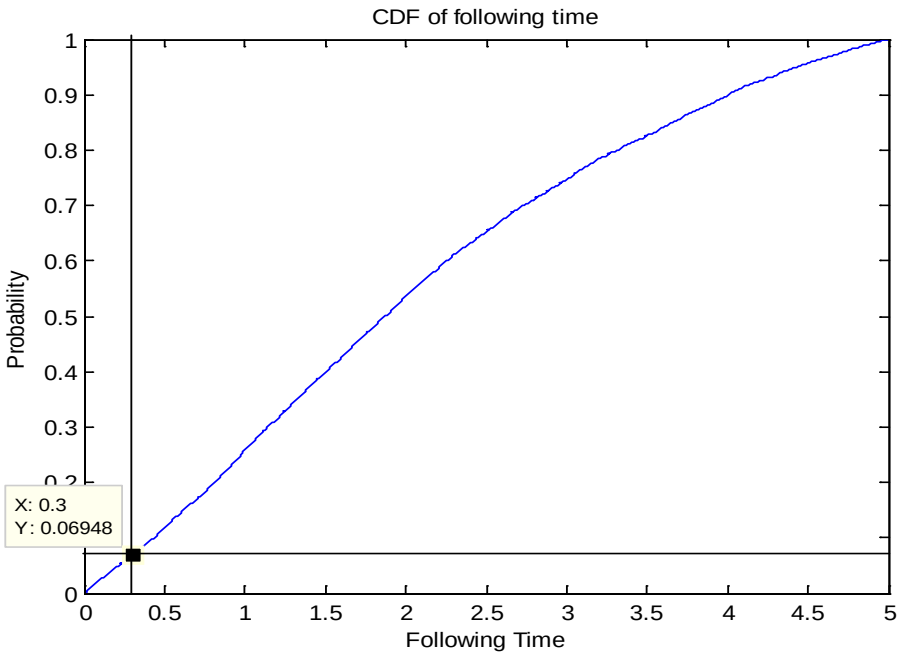

Figure 6-7 Cumulative distribution function of inter-arrival times for 12500 vehicles

6.5 Class 9 vehicle identification

A more subtle approach to overcoming trucks miss-detection is to identify whether the detected signature belongs to a single truck or two consecutive vehicles. This requires probing magnetic signatures for distinctive features that contribute to reducing uncertainty about the nature of the detected vehicle.

On that account, the research team examined the magnetic signatures of three class 9 vehicles looking for a repetitive pattern. Consequently, we found two main features that distinguish class 9 vehicles from others. These features are:

1. The ratio of the peak amplitude resulting from the tail of the vehicle to the peak amplitude resulting from its head: Clearly the disturbance caused by the tail of a class 9 truck will be considerably smaller than the disturbance caused by the head of a smaller vehicle.

2. The rate of change of magnetic signature in section 2 of a truck: The air gap between two small vehicles will produce sudden magnitude changes at a rate faster than the changes produced by a truck's trailer which still causes a relatively small disturbance

Figure 6-8 depicts the difference between the features values in both cases.

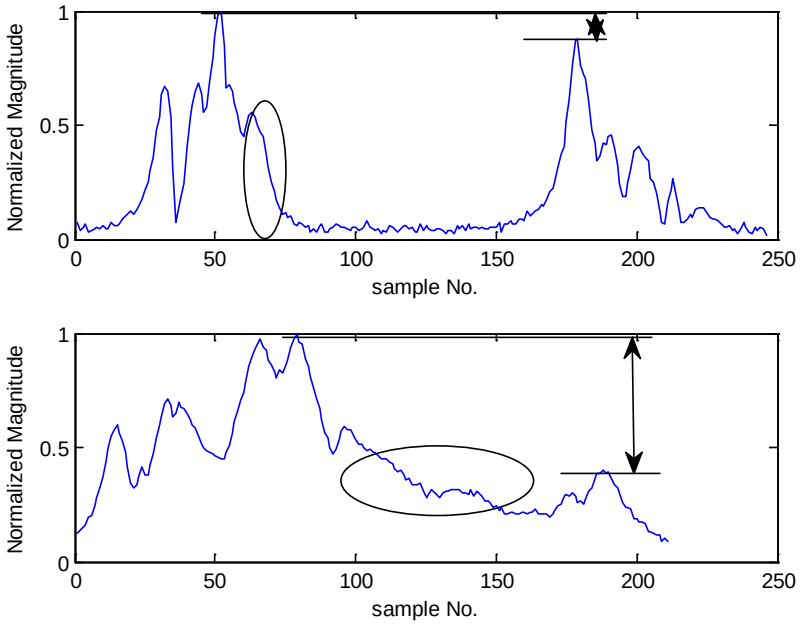

Figure 6-8 Features values in case of two small vehicles (top) and a truck (bottom)

The second feature was calculated by fitting the part of signature after the peak to the linear model in **Eq. 6-1** where a represents the rate of change:

$$f(x) = a * x + b \qquad \textbf{Eq. 6-1}$$

Using least mean square error method to find a and b we got $a \approx -0.0435$ for two consecutive vehicles and $a \approx -0.005$ for class 9 trucks. The slope in the first case is about ten times larger than the second. Thus, this feature can play an important role in distinguishing trucks.

Finally, the team approximated the sensor's response to class 9 vehicles by a fourth degree polynomial as in **Eq. 6-2**. Figure 6-9 shows a class 9 truck signature and its corresponding model.

$$f(x) = p_1 * x^4 + p_2 * x^3 + p_3 * x^2 + p_1 * x + p_5 \qquad \textbf{Eq. 6-2}$$

Consequently, the correlation between a measured signature and the previous model can also be used to decrease decision uncertainty. Figure 6-10 depicts the cross-correlation functions in both cases; a truck and separate consecutive vehicles where class 9 vehicles are highly correlated with the model compared to the other case.

These features can be fed to a learning algorithm, e.g. logistic regression and Bayesian classifiers, to create a probabilistic model of feature distribution across different classes and enhance detection accuracy. However, more data should be collected and further analyzed to validate the accuracy of our model and the efficiency of the extracted features in distinguishing all cases. Figure 6-11 shows a flow diagram of a suggested implementation of the intelligent truck identification algorithm.

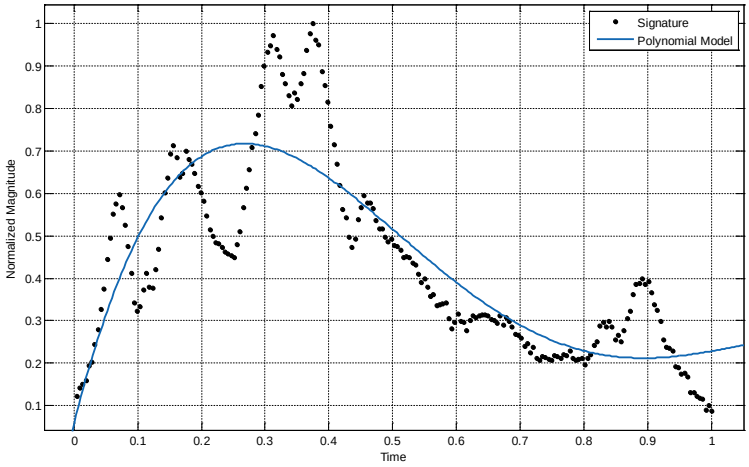

Figure 6-9 Modeling of class 9 signature

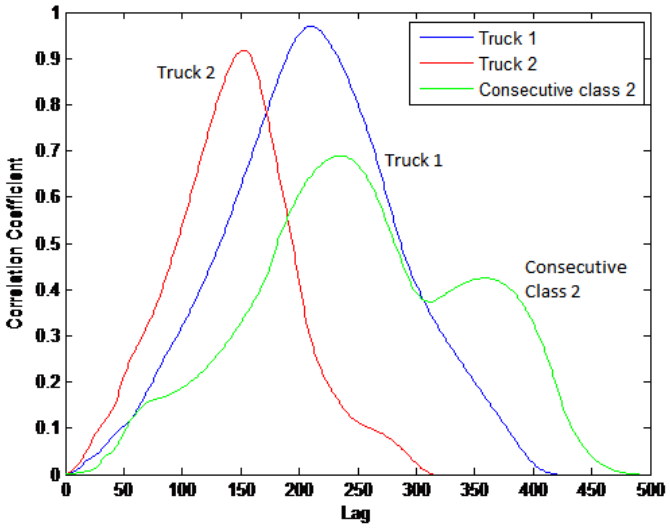

Figure 6-10 Correlation with the polynomial model

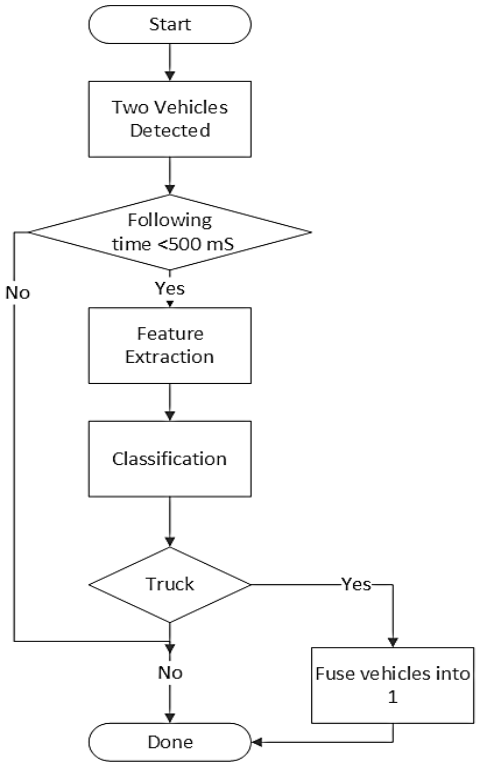

Figure 6-11 Flow chart of intelligent truck identification algorithm

6.6 Probabilistic modeling of detection errors

Pulse break-up can be avoided by increasing the de-bounce time T_d. However, a longer T_d increases the probability of two consecutive vehicles being counted as one if their inter-arrival time is less than T_d. Hence, increasing the probability of misdetection. This tradeoff between misdetection and false detection as a function of T_d implies the existence of an optimal de-bounce time $d_{optimal}$ that minimizes total detection errors in both cases. Furthermore, a de-bounce time that is suitable for free flow traffic will not perform well in congestion. Hence, detection parameters should be manually re-configured according to traffic patterns and average speed in deployment site.

The probability of detection error as a function of (d) can be derived by individually analyzing the probability of the two cases explained in section II. The probability of error is the sum of those individual components. We first define the following events in order to derive their probabilities:

- Misdetection: if two consecutive vehicles travelling close to each other are detected as one vehicle.

- False detection: when the detection algorithm falsely counts a large truck (classes 9 to 13) twice as explained in section II.

Accordingly, the total error probability is given by Eq. 6-3 Where P_r(truck) is the percentage of large trucks of total traffic.

$$P_r(\text{error}) = P_r(\text{misdetection}) + P_r(\text{truck}) \times P_r(\text{false detection}) \quad \textbf{Eq. 6-3}$$

6.6.1 Probability of misdetection:

A misdetection occurs when the inter-arrival time separating two consecutive vehicles (T_i) is less than the de-bounce time (d) causing the sensor to think they belong to the same vehicle. Therefore, the probability of miss detection can be calculated by Eq. 6-4 where $f(T_i)$ is the probability distribution of T_i

$$P_r(\text{miss detection}) = P_r(T_i < d) = \int_0^d f(T_i).dT_i \quad \textbf{Eq. 6-4}$$

Vehicles arrival to a point on a highway is usually modeled in literature [1] [2] as a Poisson process with average vehicle arrival rate λ. The probability of k vehicles arriving to the sensor's detection zone within time unit t is as in Eq. 6-5.

$$P_r(X=k) = \frac{(\lambda t)^k e^{-\lambda t}}{k!} \quad \textbf{Eq. 6-5}$$

T_i represents the length of time until the first arrival since the last arrival, according to the memoryless property of Poisson processes. Hence, $f(T_i)$ can be found by first finding its CDF $F(T_i)$ using Eq. 6-6, Eq. 6-7, and Eq. 6-8. $f(T_i)$ corresponds to a Gamma distribution with a shape parameter $\alpha = 2$ and rate λ, where Gamma distribution is given by Eq. 6-9 and Eq. 6-10.

$$F(T_i) = P_r(t < T_i) = 1 - P_r(t > T_i) = 1 - P_r(X \leq 1) \quad \textbf{Eq. 6-6}$$

$$F(T_i) = 1 - e^{-\lambda T_i} \sum_{X=0}^{X=1} \frac{(\lambda T_i)^X}{X!} \quad \textbf{Eq. 6-7}$$

$$f(T_i) = F'(T_i) = \lambda^2 T_i e^{-\lambda T_i} \quad \textbf{Eq. 6-8}$$

$$F(T_i) = P_r(t < T_i) = 1 - P_r(t > T_i) = 1 - P_r(X \leq 1) \quad \textbf{Eq. 6-6}$$

$$f(x,\alpha,\lambda) = \frac{\lambda^{\alpha} x^{\alpha-1} e^{-\lambda x}}{\Gamma(\alpha)} \quad \textbf{Eq. 6-9}$$

$$\Gamma(\alpha) = (\alpha - 1)! \quad \textbf{Eq. 6-10}$$

$$P_r(\text{misdetection}) = P_r(Ti < d) = F(d) = 1 - \lambda\left[e^{-\lambda d}\left(d + \frac{1}{\lambda}\right)\right] \quad \textbf{Eq. 6-11}$$

Where:

This Gamma distribution is used literature to model waiting times between Poisson distributed events—(mathworld.wol-fram.com/GammaDistribution.html). Substituting $f(T_i)$ in Eq. 6-4 gives Eq. 6-11.

Figure 6-12 shows the probability of misdetection as a function of d for different vehicle arrival rates λ. It is obvious that the probability of misdetection increases as λ increases. It also increases with (d) for a fixed arrival rate because more vehicles will arrive consecutively before the de-bounce time runs out.

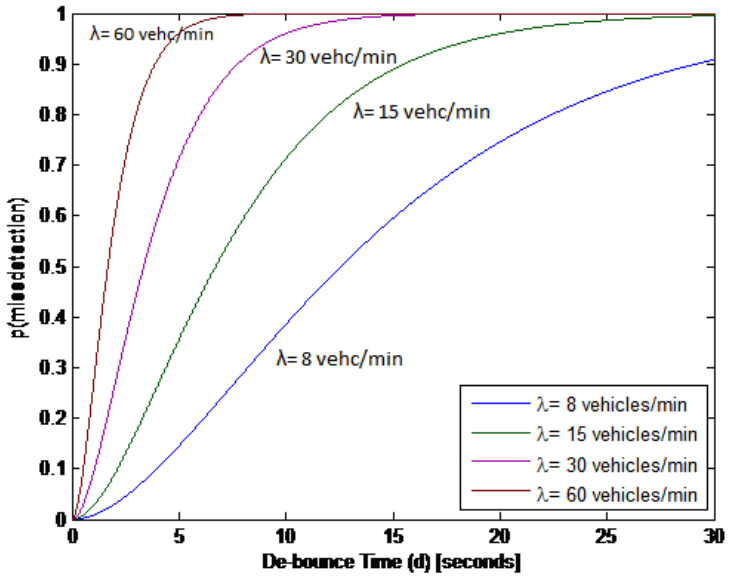

Figure 6-12 Probability of misdetection

6.6.2 Probability of false detection:

The problem of truck false detection was introduced in Section II. In this case the relatively low magnetic field corresponding to the part of trailer lying between axles three and four causes a false detection if the truck is travelling slow enough to keep magnetic disturbance below detection threshold for more than (d). Therefore, the following assumptions were made in order to calculate the probability of false detection:

- All the samples in a truck's section 2 magnetic signature fall below the detection threshold except a number of samples that correspond to the radius of the sensor's detection zone (worst case scenario).
- Section 2 length, which is assumed equal to the spacing between axles 3 and 4 minus twice the radius of sensor's detection zone, is normally distributed with mean μ_l and standard deviation σ_l.
- Vehicles speed is normally distributed with mean μ_s and standard deviation σ_s.

The radius of detection zone [r] was subtracted from axles 3-4 spacing because the magnetic field of a vehicle's part stays above the threshold until this part is [r] meters away from the sensor [72]. Therefore, the magnetic field of section 1 will keep the disturbance above the threshold level for [r] meters into section 2, and section 3 will start showing [r] meters before it is centered over the sensor.

Assumptions 2 and 3 were validated via analyzing the data collected by a calibrated Weigh in Motion station that employs piezoelectric and loop detectors and deployed on an interstate highway whose speed limit is 70 Mph. Figure 6-13 shows the distribution of axles 3-4 spacing and speed collected from the WIM station.

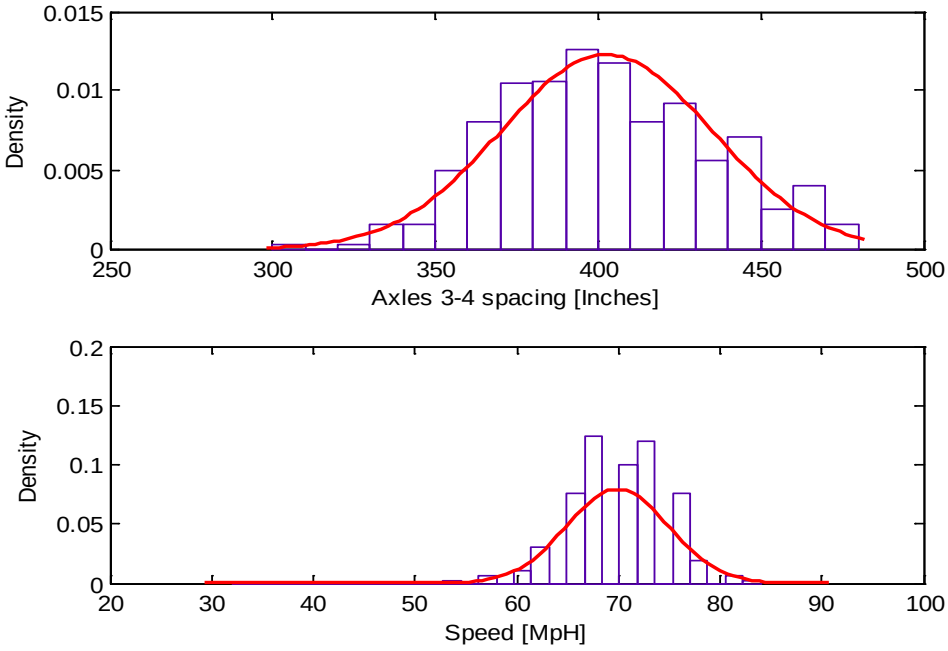

Figure 6-13 Distribution of axle 3-4 spacing (top) and speed (bottom).

A false detection takes place when the duration a truck's section 2 stays within the detection range of the sensor T_{span} is longer than the de-bounce time. T_{span} can be calculated using Eq. 6-12 where A_{34} is the spacing between axles 3 and 4, and S is vehicle's speed.

$$T_{span} = \frac{A_{34} - 2*(\text{detection zone radius}) \text{ [meters]}}{S \left[\frac{\text{meters}}{\text{second}}\right]} \qquad \textbf{Eq. 6-12}$$

Since A_{34} and S are both normally distributed, T_{span} is distributed according to the ratio distribution [117]. D. V. Hinkley derives in [117] a closed form formula for the PDF and CDF of the ratio distribution $W = \frac{X_1}{X_2}$. Hinkley also provides an approximation formula that is viable when $P(X_2 > 0) \rightarrow 1$, which applies to our case because a vehicle's speed can't be negative. The approximate CDF of ratio distribution provided in [117] is given by Eq. 6-13, Eq. 6-14, Eq. 6-15, and Eq. 6-16.

$$F(w) = \Phi\left\{\frac{\mu_2 w - \mu_1}{\sigma_1 \sigma_2 a(w)}\right\} \qquad \textbf{Eq. 6-13}$$

$$a(w) = \left(\frac{w^2}{\sigma_1^2} - \frac{2\rho w}{\sigma_1 \sigma_2} + \frac{1}{\sigma_2^2}\right)^{\frac{1}{2}} \qquad \textbf{Eq. 6-14}$$

$$F(w) = \Phi\left\{\frac{\mu_2 w - \mu_1}{\sigma_1 \sigma_2 a(w)}\right\} \quad \textbf{Eq. 6-13}$$

$$\Phi(y) = \int_{-\infty}^{y} \phi(x)dx \quad \textbf{Eq. 6-15}$$

$$\phi(x) = \frac{1}{\sqrt{2\pi}} e^{-\frac{1}{2}x^2} \quad \textbf{Eq. 6-16}$$

μ_1,μ_2,σ_1, and σ_2 are the mean and standard deviation of X_1 and X_2 respectively, and ρ is the correlation coefficient between X_1 and X_2. The probability of false detection is obtained using Eq. 6-17.

$$P_r(\text{false detection}) = P_r(T_{span} > d) = 1 - P_r(T_{span} < d) = 1 - F(d) \quad \textbf{Eq. 6-17}$$

Substituting μ_l,σ_l,μ_s,σ_s and ρ = 0 (Speed and Axles 3-4 spacing are assumed non-correlated) we get Eq. 6-18, Eq. 6-19, and Eq. 6-20. Equation Eq. 6-21 represents the probability of false detection that occurs in large trucks out of the total number of these vehicles.

$$P_r(\text{false detection}) = 1 - \Phi\left\{\frac{\mu_s d - \mu_l}{\sigma_l \sigma_s a(d)}\right\} \quad \textbf{Eq. 6-18}$$

$$a(d) = \left(\frac{d^2}{\sigma_l^2} + \frac{1}{\sigma_s^2}\right)^{\frac{1}{2}} \quad \textbf{Eq. 6-19}$$

$$P_r(\text{false detection}) = 1 - \frac{1}{\sqrt{2\pi}} \int_{-\infty}^{\frac{\mu_s d - \mu_l}{\sigma_l \sigma_s a(d)}} e^{-\frac{1}{2}x^2} dx. \quad \textbf{Eq. 6-20}$$

$$P_r(\text{false detection}) = 1 - \frac{1}{2}\left[1 + \text{erf}\left(\frac{\mu_s d - \mu_l}{\sigma_l \sigma_s \sqrt{2\left(\frac{d^2}{\sigma_l^2} + \frac{1}{\sigma_s^2}\right)}}\right)\right] \quad \textbf{Eq. 6-21}$$

Figure 6-14 shows the probability of false detection as a function of de-bounce time (d). Where μ_s,σ_s,μ_l,σ_l where estimated from the histograms in Figure 6-13. It is clear that the higher the debounce time the lower is the probability of false detection due to

the fact that when (d) is very high it's very improbable that the magnetic disturbance corresponding to a truck's section 2 will last more than the (d).

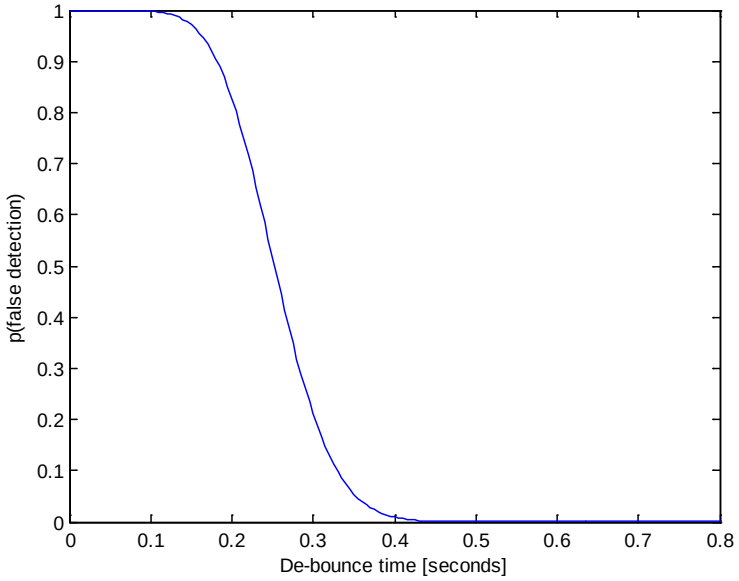

Figure 6-14 Probability of falsely detecting a truck

6.6.3 Total detection error and optimal de-bounce time:

Substituting Eq. 6-11 and Eq. 6-21 in Eq. 6-1gives Eq. 6-22 the total detection error as a function of de-bounce time.

$$P_r(error)_d = 1 - \lambda\left[e^{-\lambda d}\left(d + \frac{1}{\lambda}\right)\right] + P_r(truck) * \left\{1 - \frac{1}{2}\left[1 + \text{erf}\left(\frac{\mu_s d - \mu_l}{\sigma_l \sigma_s \sqrt{2\left(\frac{d^2}{\sigma_l^2} + \frac{1}{\sigma_s^2}\right)}}\right)\right]\right\} \quad \textbf{Eq. 6-22}$$

$P_r(truck)$ can be estimated as the percentage of large trucks out of the total traffic. A typical value is within the range 5% to 10% and it varies between urban roads and interstate highways.

As previously illustrated in Figure 6-13, μ_s is approximately equal to the road's speed limit. σ_s was estimated for a total of 13466 trucks and it varied within the range

[4.36 – 4.89]. μ_l and σ_l were also estimated for the same number of trucks; μ_l=7.9 [meters] and σ_l=1.504.

The average vehicle arrival rate λ can be estimated using Eq. 6-23.

$$\lambda\left[\frac{vehicles}{sec}\right] = average\ speed\left[\frac{meters}{sec}\right] * average\ spatial\ density\left[\frac{vehicles}{meter}\right] \quad \textbf{Eq. 6-23}$$

Figure 6-15 shows the probability of error as a function of d for different values of λ, and p(truck) = 0.1. It is clear that there is an optimum value for the de-bounce time $d_{optimum}$ that minimizes the total error.

To find $d_{optimum}$ we first find the points at which $\frac{dP(error)_d}{d(d)}$ =0 (Eq. 6-24):

$$\frac{dP_r(error)_d}{d(d)} = \lambda^2 d e^{-\lambda d} - \frac{1}{\sqrt{2\pi}} . P_r(truck) \left\{ \exp\left[-\frac{(\mu_s d - \mu_l)^2}{2\sigma_l^2\sigma_s^2\left(\frac{d^2}{\sigma_l^2} + \frac{1}{\sigma_s^2}\right)} \right] . \frac{\mu_l\sigma_s^2 d + \mu_s\sigma_l}{\sqrt{2\sigma_l}(\sigma_l + \sigma_s^2 d^2)^{\frac{3}{2}}} \right\} \quad \textbf{Eq. 6-24}$$

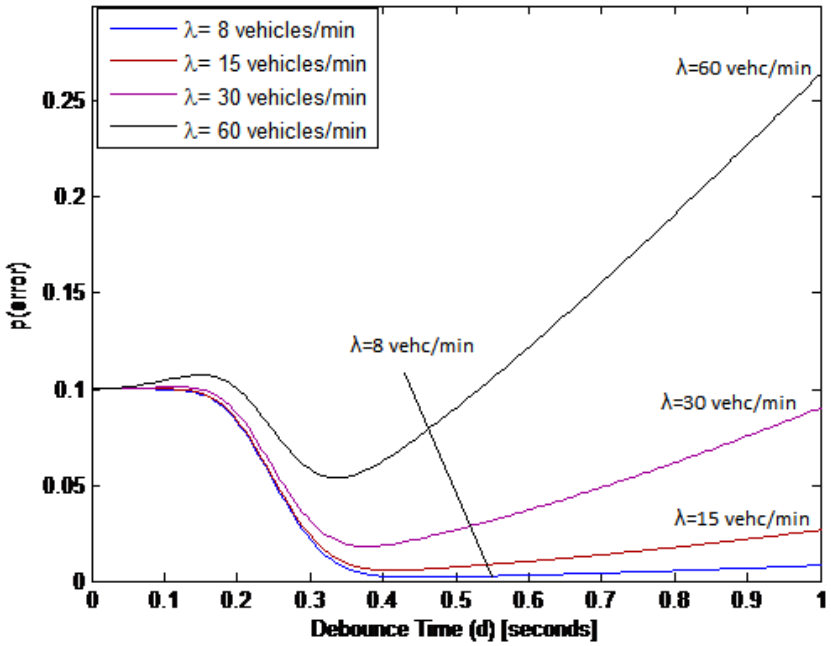

Figure 6-15 Probability of detection error

Since Eq. 6-24 is an exponential function, it is easier to use numerical methods to find its solutions. For this purpose, golden section search algorithm was used, and the result $d_{optimum}$=440 mS for λ=8 vehicles/min was obtained with only 30 iterations.

Eq. 6-23 and Golden Section search can be implemented in the main controller of the vehicle detection system.

The system will update the de-bounce time according to the changes in traffic flow characteristics such as average arrival rate λ and average speed μ_s. For example, at rush hour average arrival rate λ will be higher compared to regular hours. System controller will update the value of λ based on the number of detections every ten minutes. When $|\lambda_{new}-\lambda_{old}| \geq M$, M defines a threshold for de-bounce time re-calibration, the system controller runs golden section search to calculate the new value of de-bounce time based on Eq. 6-23.

6.7 Experimental Results

The detection algorithm was applied several times on the raw magnetic signature of 416 vehicles (72 class 9 vehicles and the rest vary between classes 2, 3, 5, and 8) recorded on I-44 interstate highway near Tulsa, Oklahoma. The de-bounce time was changed from 200ms, 440ms, to 600ms. Table 6-1 contains the detection error for different values of de-bounce time, where the average arrival rate was estimated about λ=8 vehicles/min.

Table 6-1 Results of detection algorithm at different de-bounce values

De-Bounce Time (d)	200ms	440ms	600ms
No. misdetections	0	0	3
No. false detections	11	0	0

Clearly, the best performance is obtained when d is close to its optimum value which was calculated earlier, $d_{optimal}$=440ms.

Chapter 7: DATA ANALYSIS & PERFORMANCE EVALUATION

7.1 Overview

This chapter provides detailed information about various statistical data analysis studies applied on field test data reported in chapter 5 that were collected using MAG sensors. Additionally, performance evaluation of developed algorithms—including field test results—will be presented. Both data analysis and performance evaluation is illustrated in Figure 7-1.

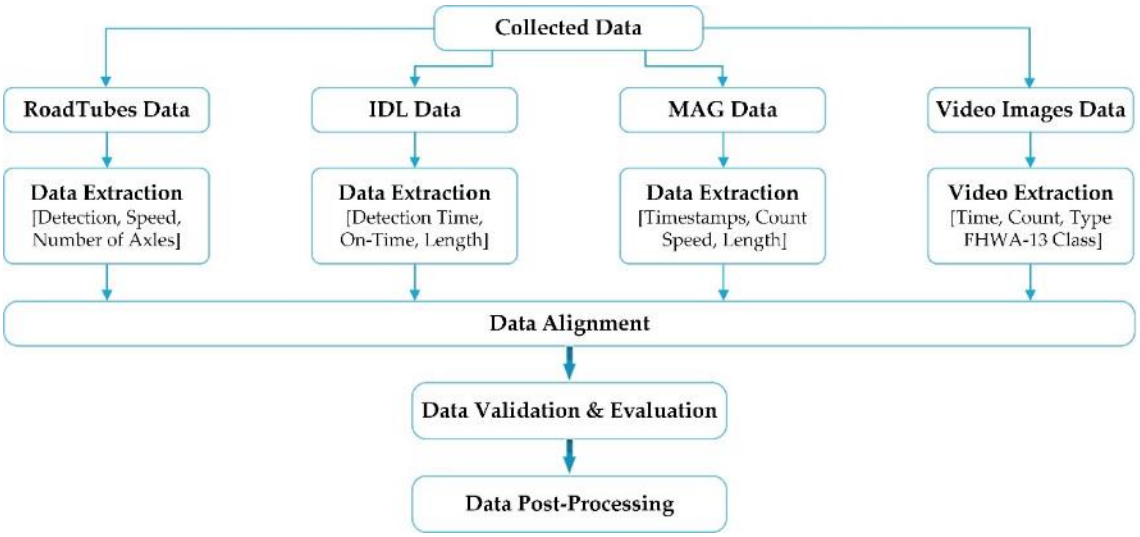

Figure 7-1 Flow diagram for data validation and performance evaluation

Data collected using MAG sensors, as well as ground truth data from *Road Runner Kit* and video cameras, was pre-processed to extract detection information (e.g., count, speed, length, detection time). The information had been aligned together—sample by sample—into a reference detection timestamp extracted from video data.

7.2 Magnetometer Sensor Characterization Analysis

7.2.1 Sampling Rate in Active Detection

Fixed sampling rates, ranging from 8Hz to 200Hz, for vehicle detection using MAG have been reported in literature [39], [42], [48], [118], [119]. Unlike other platforms, *i*VCCS, sampling rate can be configured on-the-fly within a range 1.562Hz~800KHz to best-fit application functionalities and power constraints. Increasing sampling rate will

increase resolution of sampled VMS. Notably, sensor noise output and power consumption will also increase. FXOS8700CQ has an output noise range 0.3~1.5μT-rms@1.56~800Hz. In term of power consumption vs. sampling rate, FXOS8700CQ requires 40~575μA@12.5~400Hz.

7.2.2 MAG Output Noise Characterization

Knowledge about the distribution of MAG output noise at different sampling rates is important for setting MAG reference level and *Baseline threshold* (R_{TH}).

MAG noise characteristics defined in earlier do not reflect the effect of additional components on PCB. An experimental test was conducted to and to define noise characteristics and to gain better understanding of MAG at various sampling rates in the presence of other active components on *i*VCCS board.

An *i*VCCS was tightly fixed on a wooden table in the absence of any ferrous objects. Eight sampling rates, beginning at 1.56Hz and increasing up to 800Hz, were tested. Each test was 50000 samples; each sample was 3×16-bit. Flux magnitude (F_M) was calculated from geomagnetic field components to find histogram and standard deviation (STD) of F_M. Table 7-1 and Figure 7-2 show that noise mean at 400Hz sampling rate was approximately 30, with peak noise at 55. Hence, if 400Hz was set, *Baseline threshold* (R_{TH}) should consider a value higher than noise peak.

Table 7-1 Field Magnitude STD for Different Sampling Rates

Sampling Rate	STD	Sampling Rate	STD
1.5625	2.58	**100**	5.57
6.25	3.39	**200**	7.46
12.5	3.51	**400**	9.88
50	4.63	**800**	13.04

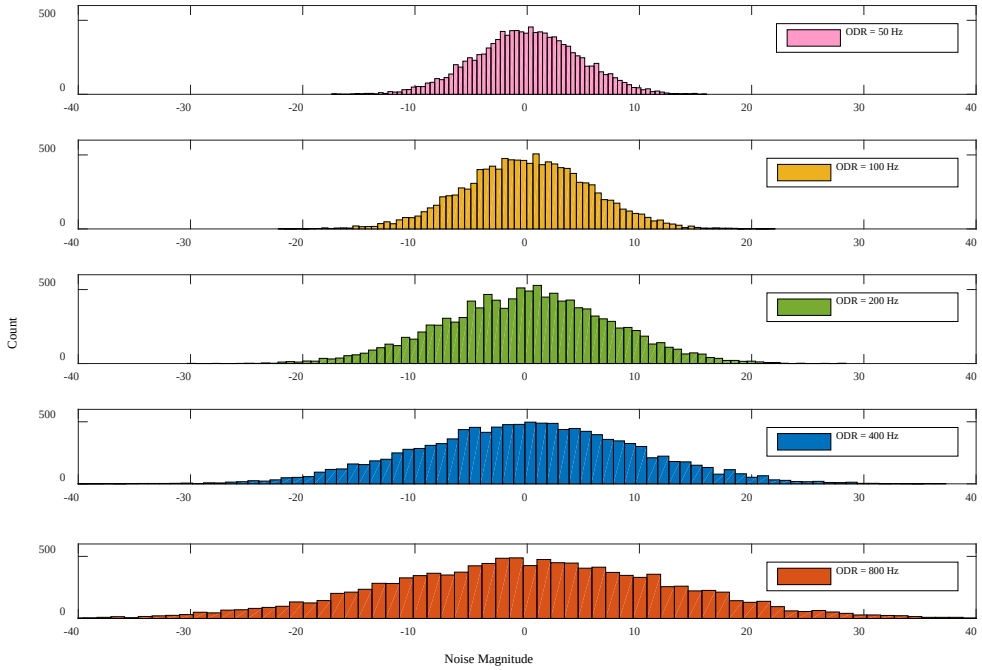

Figure 7-2 Field magnitude histogram at different sampling rates

7.2.3 MAG Sampling Rate Setting

To answer the question What is the optimal sampling rate for a particular application?, let's assume a vehicle travels on a highway at a maximum speed of 140kmh and that the number of samples represents the vehicle's magnetic signature S_{VMS} for a given sampling rate f_s and vehicle length l_V, as in Eq. 7-1.

$$S_{VMS} = 3.6 \times \left(\frac{l_{lde} + l_{tde} + l_V}{v} \right) \times f_s \times \alpha \qquad \textbf{Eq. 7-1}$$

VMS is subject not only to the disturbance in the Earth's magnetic field caused by a passing vehicle structure, but also to the sensor's detection zone. The leading and trailing detection edge of this zone is denoted as l_{lde}, l_{tde}, respectively. A correction factor is denoted by α. Assuming that l_V = 5 meters; f_s = 200Hz; l_{lde}=1.1 m; and l_{tde}= 1.1 m, by substituting in Eq. 7-1, S_{VSL} = 37 Samples.

Although knowing minimum number of S_{VSL} and low f_s (e.g., 100Hz) might be sufficient for vehicle detection applications, a higher sampling rate is needed for accurate estimation and unique features extraction is needed for speed estimation,

vehicle classification or re-identification applications based on magnetic signature or magnetic length.

7.2.4 Effect of MAG Rotation Around z-axis

Vehicles can be modeled magnetically as an infinitely large number of magnetic dipoles, each with its own moment and direction in a three-dimensional space. MAG measures geometric sum of all dipoles on x, y, and z-axes. As a result, a vehicle can be considered a single dipole with a moment equal to geometric sum of all dipoles. Hence, F_M will be the same regardless of sensor orientation. However, B_X, B_Y, and B_Z will be different for rotation angle θ. If θ is known, component values can be calculated before and after rotating sensor θ radians around z-axis using Eq. 7-2.

$$\begin{bmatrix} B_x' \\ B_y' \\ B_z' \end{bmatrix} = \begin{bmatrix} \cos\theta & \sin\theta & 0 \\ \sin\theta & \cos\theta & 0 \\ 0 & 0 & 1 \end{bmatrix} \begin{bmatrix} B_x \\ B_y \\ B_z \end{bmatrix} \qquad \textbf{Eq. 7-2}$$

Figure 7-3 illustrates the test setup where nine *i*VCCS nodes were rotated around z-axis and the rotation of first node (θ=0°) components by 135°, compared to original node at 135°.

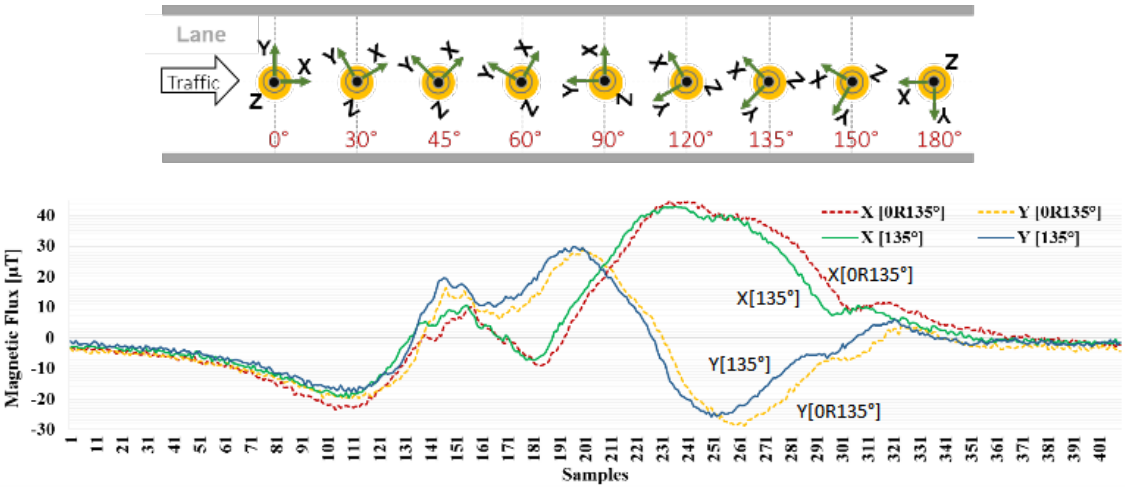

Figure 7-3 Orientation setup and *Bx* and *By* with θ=0° were rotated by 135°

7.2.5 Repeatability of VMS and MAG Sensors Output

The objective of this analysis was finding degree of similarity of several magnetic signatures produced by multiple MAG sensors for the same vehicle under identical testing condition.

Data collected in The objective of field test 2 was to evaluate the following improvements:

- Holdover de-bounce time was based on the developed statistical modeling for detection error.
- An adaptive algorithm for geomagnetic baseline drift compensation was implemented to compensate for any drift resulting from variations in temperature, vibrations, and aging.
- An algorithm for time synchronization using the on-board embedded GPS module and RTC unit was implemented to estimate speed.
- In this test, each sensor node maintained its own independent local clock that was globally synchronized to a PPS (pulse-per-second) signal generated by the on-board GPS module.

Field Test 3 was used to verify MAG output consistency. Data from only the first four sensor nodes, namely S_A, S_B, S_C, and S_D—each separated by 2m (See Figure 5-7)—were used in this analysis. The dataset included 1655 vehicles, ranging from class 1 to 10. Cross-correlation data analysis was used to find statistical relationship of generated signatures between four aligned sensors

This method can be used to measure the similarity of two waveforms as a function of a time lag applied to either. Correlation between signals can be linear (e.g., impulses signals) or circular (e.g., periodic signals). A correlation coefficient R was used to express correlation strength between signals. Pearson's correlation coefficient is the most common measure of linear dependence between two random variables, A and B, as defined in Eq. 7-3. A μ_A and σ_A are mean and STD of A, and μ_B and σ_B are mean and STD of B.

$$\rho(A,B) = \frac{cov(A,B)}{\sigma_A \sigma_B} = \frac{1}{N-1}\sum_{i=1}^{N}\frac{(A_i - \mu_A)(B_i - \mu_B)}{\sigma_A \sigma_B} \qquad \textbf{Eq. 7-3}$$

Given that our investigation had four sensors, *R* for pairwise signals was first found using Eq. 7-3, and then the correlation coefficient matrix for all signals was found by combining the *R*s of all pairwise variable, as in Eq. 7-4. Diagonal entries are always equal to 1, as all signals are directly correlated to themselves.

$$R = \begin{pmatrix} \rho(N_A,N_A) & \rho(N_A,N_B) & \rho(N_A,N_C) & \rho(N_A,N_D) \\ \rho(N_B,N_A) & \rho(N_B,N_B) & \rho(N_B,N_C) & \rho(N_B,N_D) \\ \rho(N_C,N_A) & \rho(N_C,N_B) & \rho(N_C,N_C) & \rho(N_C,N_D) \\ \rho(N_D,N_A) & \rho(N_D,N_B) & \rho(N_D,N_C) & \rho(N_D,N_D) \end{pmatrix} \qquad \textbf{Eq. 7-4}$$

$$R = \begin{pmatrix} 1 & \rho(F_M^{(N_A)},F_M^{(N_B)}) & \rho(F_M^{(N_A)},F_M^{(N_C)}) & \rho(F_M^{(N_A)},F_M^{(N_D)}) \\ \rho(F_M^{(N_B)},F_M^{(N_A)}) & 1 & \rho(F_M^{(N_B)},F_M^{(N_C)}) & \rho(F_M^{(N_B)},F_M^{(N_D)}) \\ \rho(F_M^{(N_C)},F_M^{(N_A)}) & \rho(F_M^{(N_C)},F_M^{(N_B)}) & 1 & \rho(F_M^{(N_C)},F_M^{(N_D)}) \\ \rho(F_M^{(N_D)},F_M^{(N_A)}) & \rho(F_M^{(N_D)},F_M^{(N_B)}) & \rho(F_M^{(N_D)},F_M^{(N_C)}) & 1 \end{pmatrix} \qquad \textbf{Eq. 7-5}$$

Initially, correlation coefficients matrix of magnetic magnitudes F_M (see Eq. 4-5) obtained from the four sensor nodes were found, as in Eq. 7-5. Histograms for the first three pairwise signals, *N_A-vs-N_B*, *N_A-vs-N_C*, and *N_B-vs-N_C*, are shown in Figure 7-4, Figure 7-5, and Figure 7-6, respectively. The CDF for all pairwise combinations is shown in Figure 7-7. The histogram shows that most correlation coefficients range between 0.9 and 1 (i.e., 1462 out of 1655 values), indicating high similarity between sensor output across multiple nodes (See Figure 7-8). The p-values matrix was also found for all pairwise combination. The matrix returned noticeably small p-values (e.g., 2e-138), rejecting the null hypothesis and identifying significant correlations.

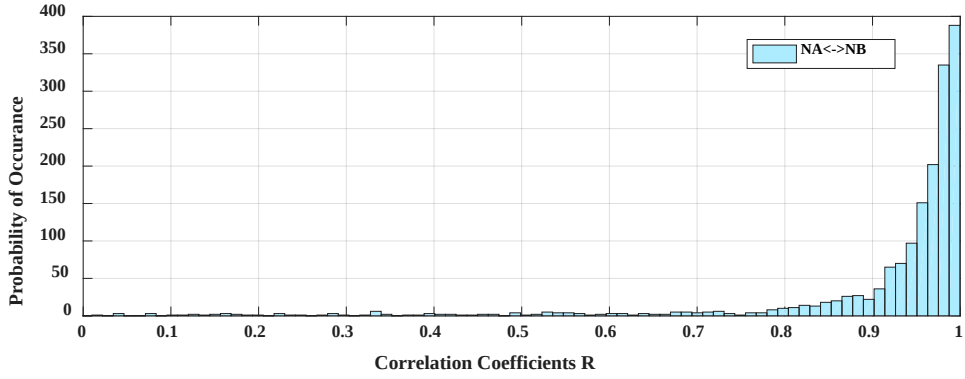

Figure 7-4 Histogram of R between magnetic magnitudes of Node-A and B

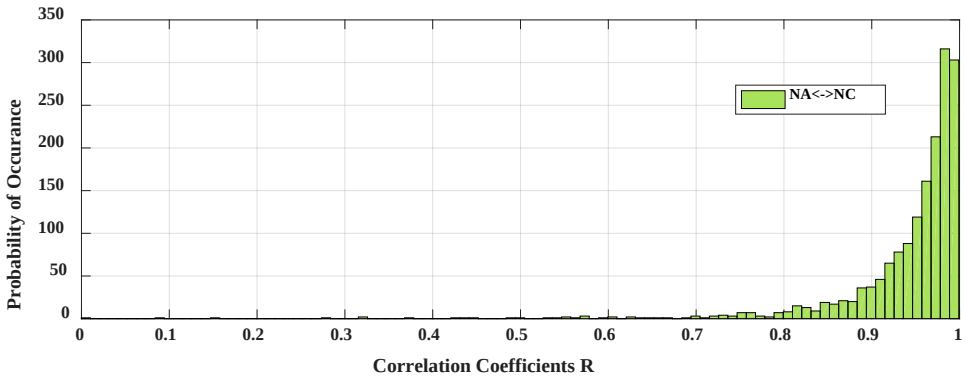

Figure 7-5 Histogram of R between magnetic magnitudes of Node-A and C

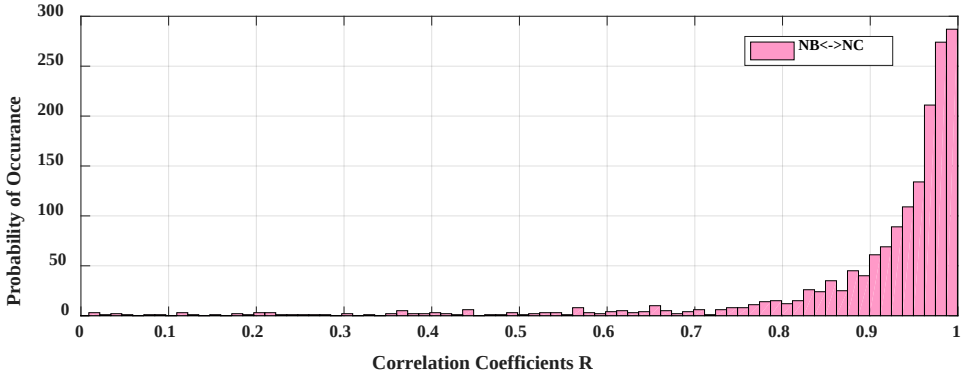

Figure 7-6 Histogram of R between magnetic magnitudes of Node-B and C

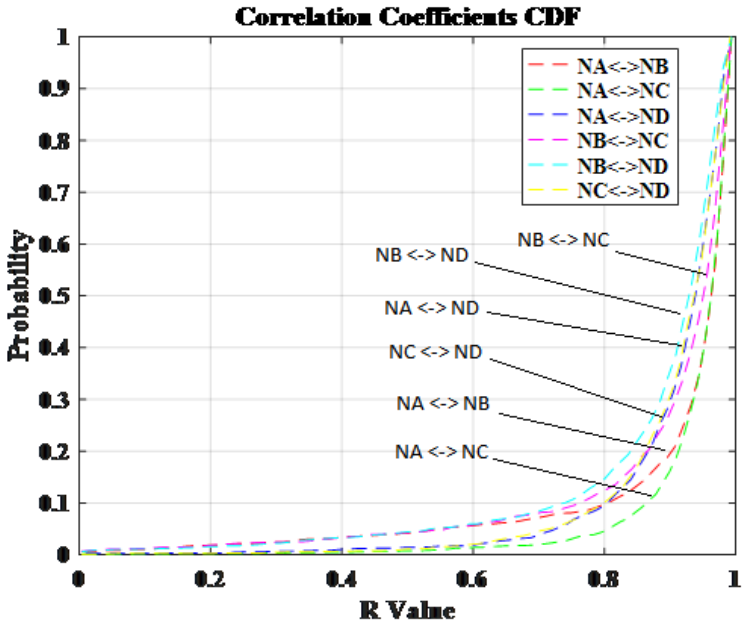

Figure 7-7 CDF of correlation coefficients for all pairwise signals

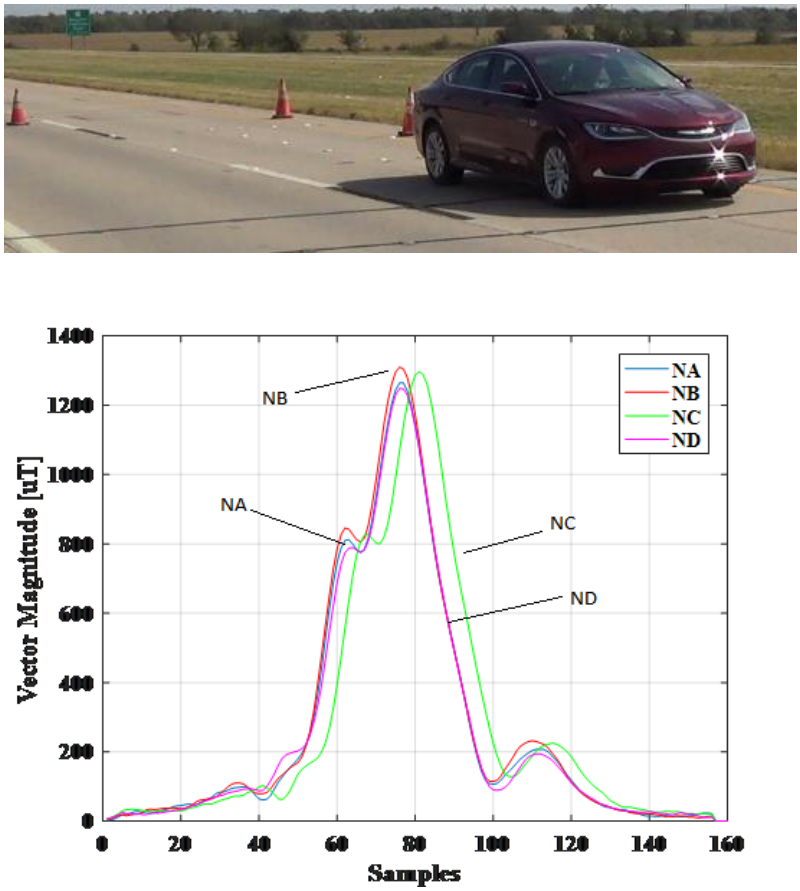

Figure 7-8 Magnetic magnitudes for class 2 vehicle obtained from all Nodes

Alternatively, approximately 11% of magnetic signatures had $R < 0.9$ (i.e., 193 out of 1655 values). In a real-world environment (e.g. highway), multiple factors could prevent repeatable results. Including pavement temperature, changes in vehicle trajectory during passage, traffic interference from adjacent lanes, and data loss due to jittery sampling rate, are among the most significant factors. A sample set of vehicle signatures with low correlation coefficient value was visually inspected and compared to identify the cause for 11% degradation in sensors output similarity. Primary causes for sensor output variations proved to be 1) running over the sensors, creating significant vibrations and, in some rare cases, data loss in sensors output, and 2) changing vehicle trajectory during passage time. Figure 7-9 shows a class 3 vehicle traveling at 72mph ran over the edge of all four sensors. Data loss and noisy signal was observed in sensor N_B.

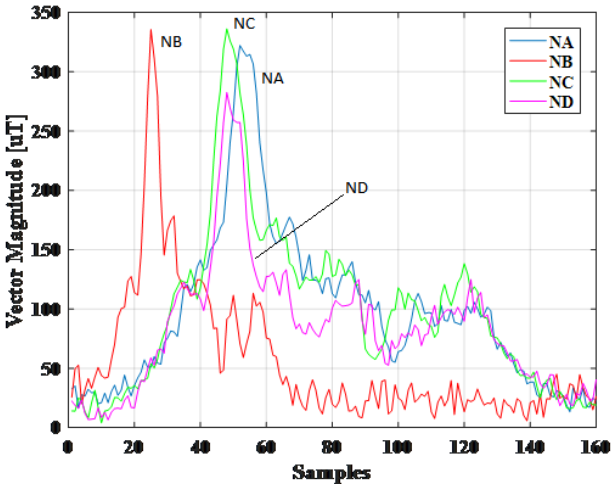

Figure 7-9 Magnetic magnitudes for class 3 vehicle driving over all sensors

Figure 7-10 depicts correlation coefficient CDFs for *X*, *Y*, and *Z-axis*, respectively. Clearly, the *Y* component (i.e., B_Y) demonstrates the highest consistency among the three axis; *X* and *Z* components (i.e., B_X, B_Z) diverge and spread over many lower values. This phenomenon confirms that the major contributor for inconsistency is running over the sensor, which creates a huge vertical acceleration and random magnetic distortion on *X* and *Z*-axis. Higher correlation coefficients for F_M were observed, when compared with correlation coefficients for B_X, B_Y, and B_Z individually.

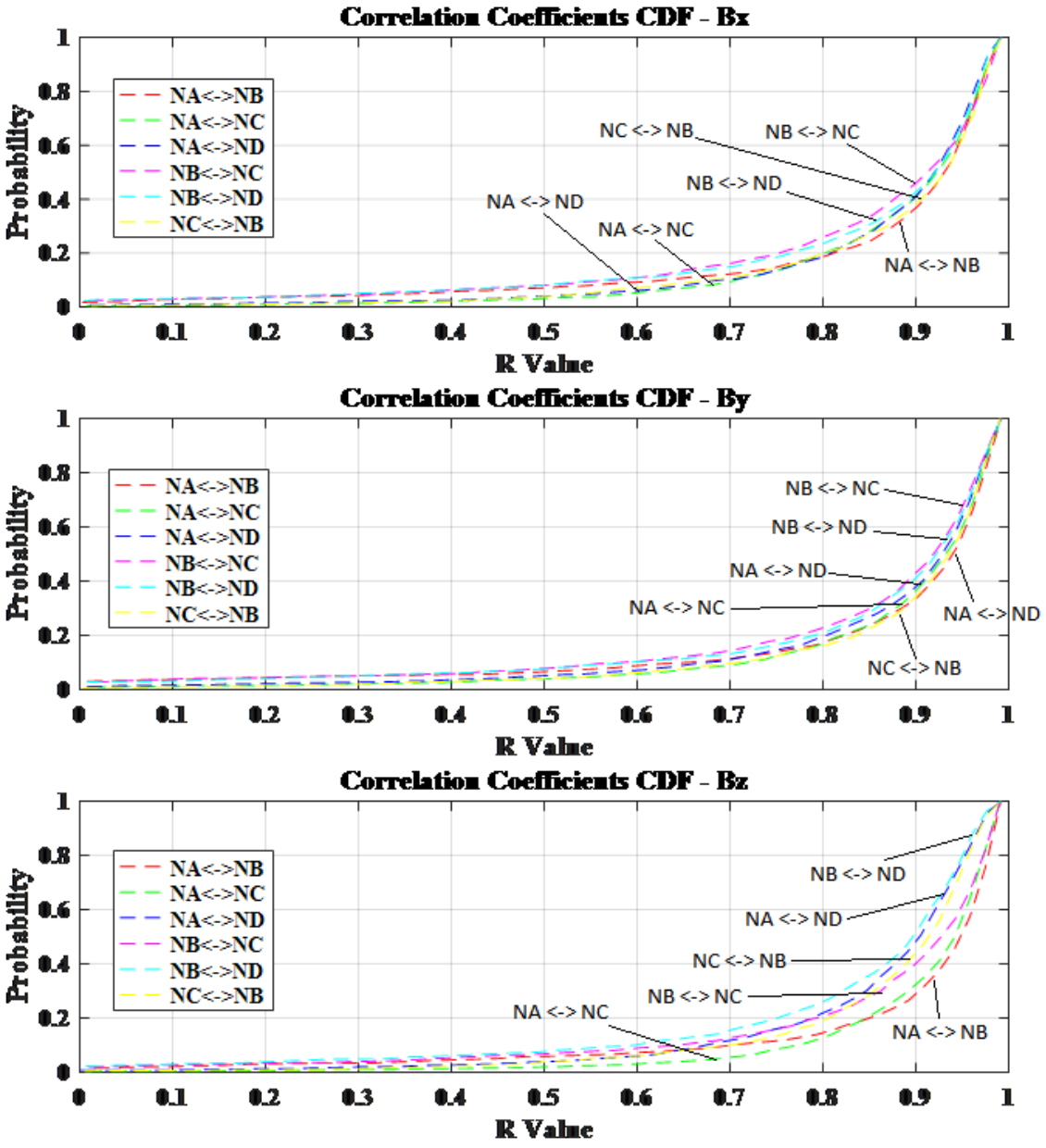

Figure 7-10 Correlation coefficients CDFs for all pairs on x, y, and z-axis

Small variations between different sensors output are considered a noise source with minimal effect on detection accuracy.

In conclusion, CDF for all pairwise combinations revealed that most *R* values are between 0.9 and 1, indicating high similarity in sensor output across multiple nodes. Furthermore, the p-value matrix returned insignificant p-values (i.e., 2e-138), which

reject the null hypothesis and indicate significant correlations. Hence, each vehicle has a unique magnetic signature that can be utilized for vehicle re-identification applications.

7.3 Vehicle Detection

7.3.1 Optimal Detection Thresholds Analysis

F_M measurements for 12000 vehicles classified among various FHWA F scheme classes [13] via *i*VCCS on highway and urban roads, were statistically analyzed to determine optimal O_{TH}, H_{TH}, and R_{TH} values—defined by Eq. 4-2, Eq. 4-3, and Eq. 4-4, thus guaranteeing best detection performance.

F_M measurements are normally distributed with a mean μ and STD σ—$F_M \propto N(\mu, \sigma)$. F_M measurements can be represented as two Gaussians of a single dimension dataset—one representing noise and the other representing vehicle signatures. Since no information was provided with regard to which points belong to which distribution, a Gaussian Mixture Model (GMM) was used to separate the two distributions, assuming both are normally distributed.

GMM is a parametric probability density function (PDF) of continuous measurements represented as a weighted sum of *M* component Gaussian densities (CGD), as in Eq. 7-6, where *x* is a data vector of *d*-dimensional continuous measurements such that $x = [x^1, x^2, \dots, x^d]^T$; Σ is the covariance matrix of the Gaussian; *M* is the number of Gaussians; ω_i is the weight of Gaussian i such that $\sum_i \omega_i = 1$, $\omega_i \geq 0$, and $\mathcal{N}(x|\mu_i, \Sigma_i)$; and $i = 1 \dots M$ is the CGD given by Eq. 7-7. GMM parameters are estimated from training dataset by maximum likelihood using expectation-maximization (EM) algorithm or maximum a posteriori (MAP) estimation.

$$p(x|\lambda) = \sum_{i=1}^{M} \omega_i . \mathcal{N}(x|\mu_i, \Sigma_i) \qquad \textbf{Eq. 7-6}$$

$$\mathcal{N}(x|\mu_i, \Sigma_i) = \frac{1}{(2\pi)^{d/2}\sqrt{|\Sigma_i|}} e^{-\frac{1}{2}(x-\mu)^T \Sigma^{-1}(x-\mu)} \qquad \textbf{Eq. 7-7}$$

Since *d*=1 and *M*=2, Eq. 7-7 can be rewritten as given in Eq. 7-8 and Eq. 7-9, where x_i is a vector of F_M readings (32,905,300), μ_n, σ_n^2 and μ_s, σ_s^2 are the mean and variance of noise and vehicle signature, respectively.

These can be solved using Bayesian's role by calculating the likelihood to which Gaussian each value of F_M belongs using Eq. 7-10 and Eq. 7-11. The result is two distributions, (as shown in Figure 7-11); where μ_n=18.6; σ_n=8.24; μ_s=153.5; and σ_s=153.3. By substituting μ_n, σ_n in Eq. 4-2, Eq. 4-3, and Eq. 4-4, and considering β=5 and α=6 (i.e., 6σ represents 99.999% confidence level), we find R_{TH}=35; O_{TH}=68; and H_{TH}=60 are the optimal thresholds.

$$\mathcal{N}(x_i|\mu_s,\sigma_s^2) = \frac{1}{\sqrt{2\pi\sigma_s^2}}\exp\left\{-\frac{(x_i-\mu_s)^2}{2\sigma_s^2}\right\} \quad \textbf{Eq. 7-8}$$

$$\mathcal{N}(x_i|\mu_n,\sigma_n^2) = \frac{1}{\sqrt{2\pi\sigma_n^2}}\exp\left\{-\frac{(x_i-\mu_n)^2}{2\sigma_n^2}\right\} \quad \textbf{Eq. 7-9}$$

$$p(\mu_s,\sigma_s^2|x_i) = \frac{p(x_i|\mu_s,\sigma_s^2)p(\mu_s,\sigma_s^2)}{p(x_i|\mu_s,\sigma_s^2)p(\mu_s,\sigma_s^2)+p(x_i|\mu_n,\sigma_n^2)p(\mu_n,\sigma_n^2)} \quad \textbf{Eq. 7-10}$$

$$p(\mu_n,\sigma_n^2|x_i) = 1 - p(\mu_s,\sigma_s^2|x_i) \quad \textbf{Eq. 7-11}$$

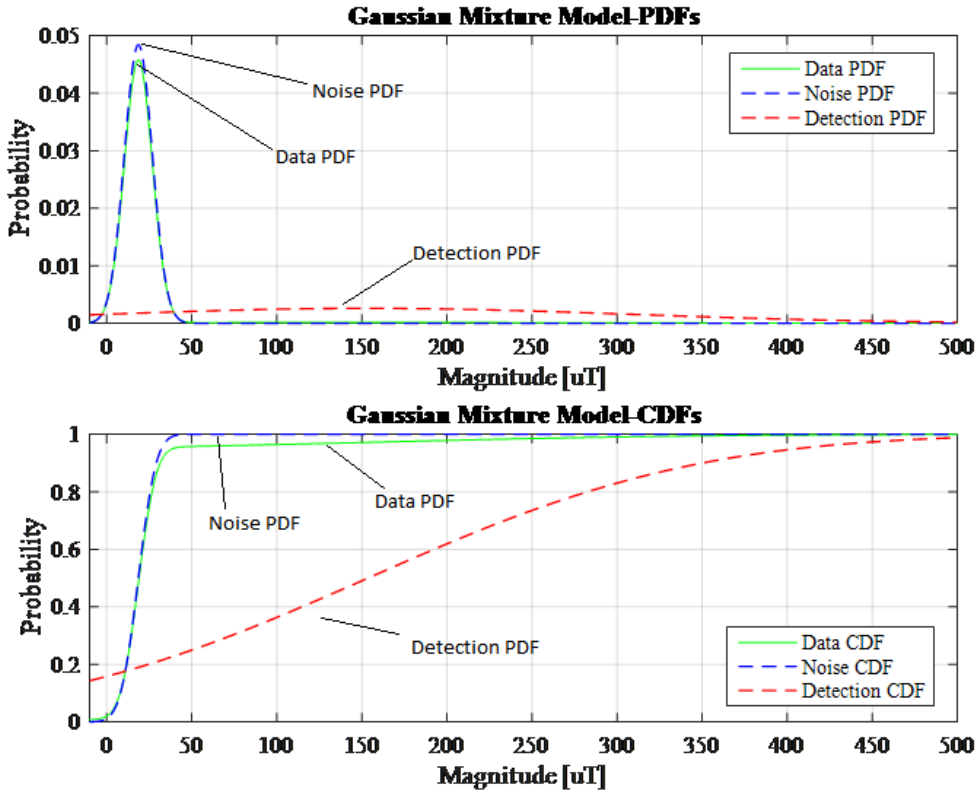

Figure 7-11 Distribution of magnetic noise and signature separated using GMM

7.3.2 Optimal Holdover Debounce-time Value

Three detection errors can be observed if MAG is used for vehicle detection

a) *Mis-detection*: Two successive vehicles at close proximity grouped as one.
b) *Double-detection*: Long vehicle with insignificant ferrous composition in the center
c) *False-detection*: Interfering from adjacent lanes caused by very large trucks.

Mis-, double-, and false-detection errors are illustrated in Figure 7-12, Figure 7-15, and Figure 7-16, respectively. Both mis-detection and double-detection errors can be eliminated using Holdover debounce timer (H_{DT}).

Mis-detection occurs when two vehicles driving at close proximity, bumper-to-bumper, are grouped as one *when* the condition $g_T < H_{DT}$ is true (See Figure 7-12), where g_T is the gap time between departure of vehicle i and arrival of vehicle $i+1$ at a designated detection point x, as depicted in Figure 7-13; and where sensor detection zone, vehicle length, headway, gap, and clearance are denoted by $l_{DZ}^{(Ni)}$, $\overline{l_V}$, $\bar{h}$, $\bar{g}$, and $\bar{c}$, respectively.

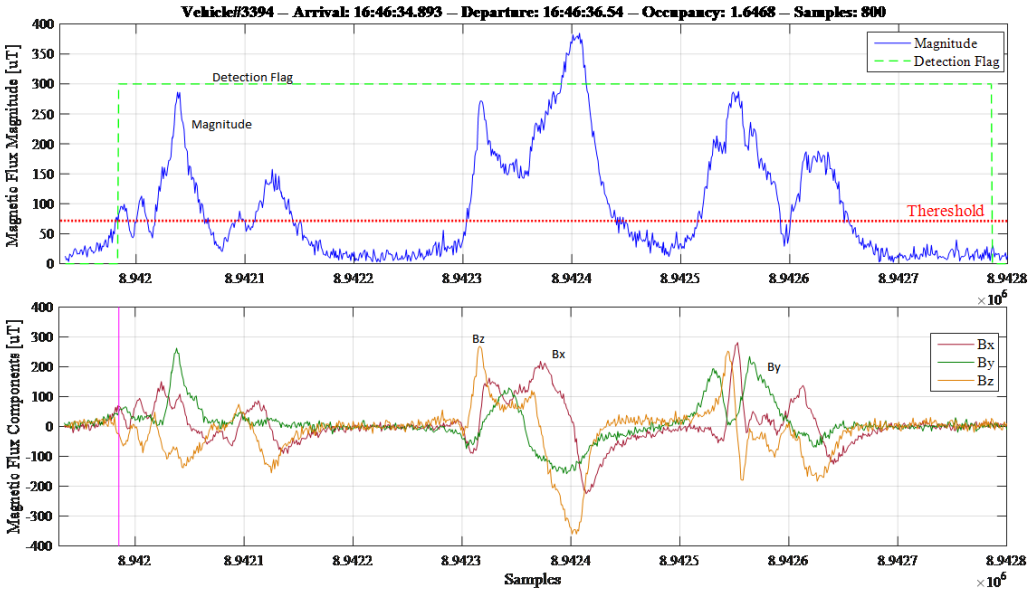

Figure 7-12 Miss-detection caused by two vehicle driving at close proximity

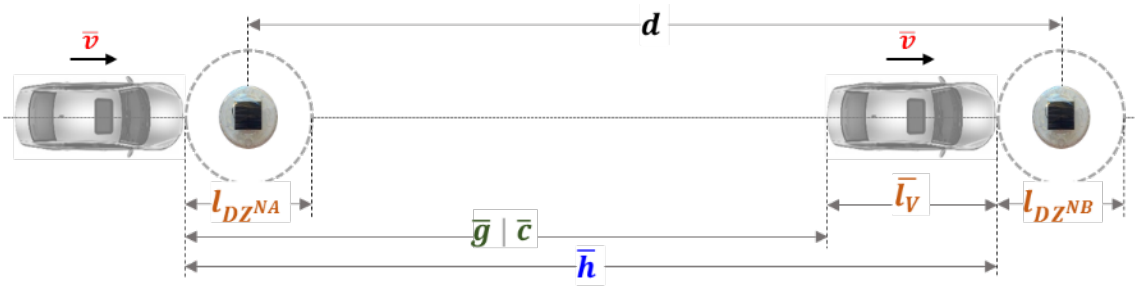

Figure 7-13 Speed estimation deployment setup

Double-detection error is observed with combination trucks (i.e., long trucks), as their structure can be magnetically divided into three sections: lead, center, and tail. Figure 7-14 illustrates the magnetic signature for a class 9 vehicle: lead section engine and first three axles, which contain the majority of the vehicle's ferromagnetic mass. The tail section includes two axles. The central section $S^{(2)}$ has a relatively small ferromagnetic mass, making $F_M(k) < H_{TH}$ true for duration $S^{(2)}_T > H_{DT}$, given truck speed is relatively slow so that the vehicle is double detected, as shown in Figure 7-15. This phenomenon is referred to in literature as *pulse break-up* [108]–[112]. Hence, to minimize mis- and double-detection errors, H_{DT} value should satisfy the condition $g_T > H_{DT} > S^2_T$.

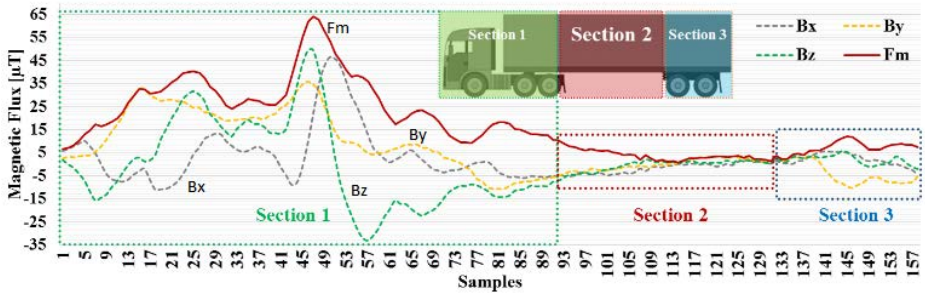

Figure 7-14 Magnetic Flux and Sections of a class 9 vehicle

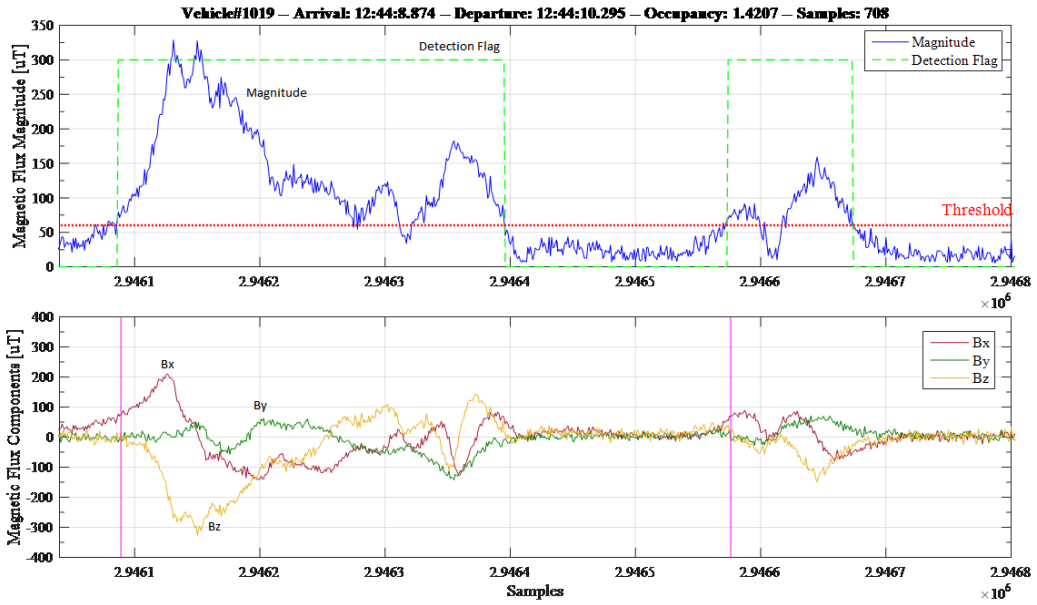

Figure 7-15 Double detection caused by class 9 vehicle

7.3.2.1 Minimizing mis-detection error

Minimizing mis-detection errors was achieved by statistically analyzing g_T, computed in Eq. 7-12. The objective was to determine optimal value of H_{DT} that minimizes mis-detection error, such that $g_T > H_{DT}$. The longer the gap time, the larger debounce time, and vice versa. g_T values were computed from historical data collected using *i*VCCS (See Chapter 5). Dataset included 13400 records collected on Oklahoma highways, in addition to 17180 records collected on urban roads in Tulsa. PDF and cumulative distribution function (CDF) were subsequently found (See Figure 7-17). CDF showed that setting H_{DT} to 370ms for highway setup and 430ms for urban road setup reduced mis-detection error to 0.1865% and 0.5065%, respectively.

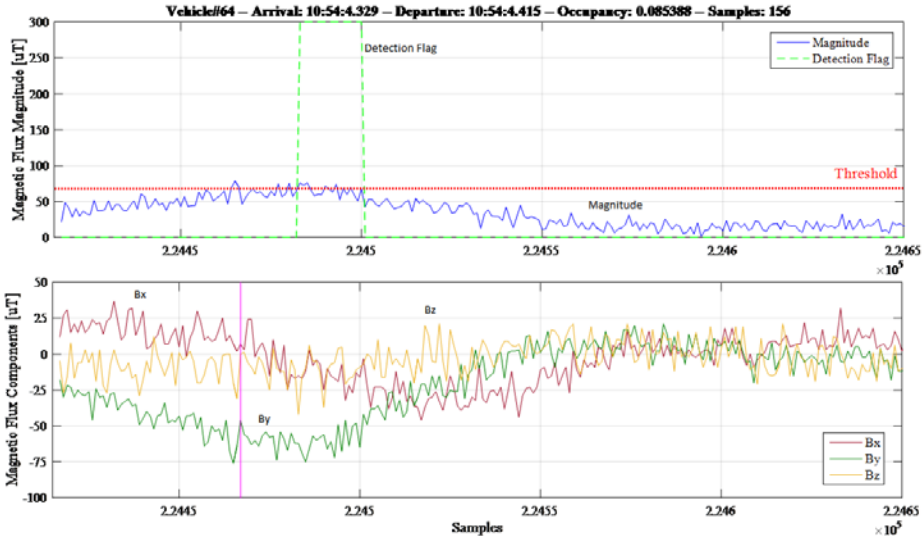

Figure 7-16 False detection caused by a vehicle passing in adjacent lane

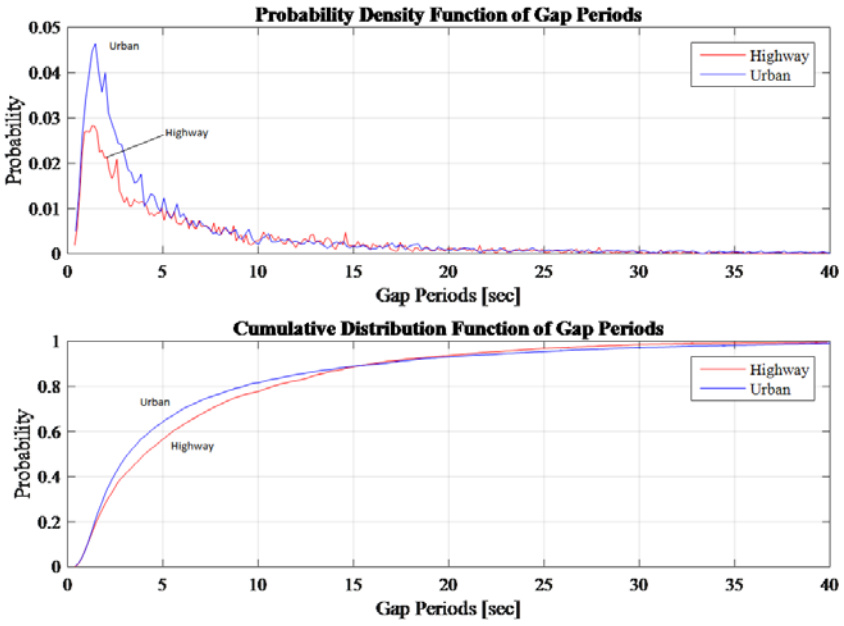

Figure 7-17 Probability distributions of Gap periods

$$g_T(k) = T_A(k+1) - T_d(k) \qquad \textbf{Eq. 7-12}$$

7.3.2.2 *Minimizing double-detection error*

To define optimal value of H_{DT} that minimizes double-detection error such that $H_{DT} > S^2_T$, PDF and CDF of $S^{(2)}_T$ for 1770 vehicle of class 8, 9, and 10 were found from data collected using *i*VCCS on highway and urban roads at speed range of 25 to 88mph. The computation process for S^2_T is depicted in Figure 7-18. CDF in Figure 7-19 indicates that the longest S^2_T is 500ms. Error probability distribution showed 0.004% and 0.005% probability of double-detection error when setting $H_{DT} \geq 400$ms and $H_{DT} \geq 370$ms, respectively (See Figure 7-20).

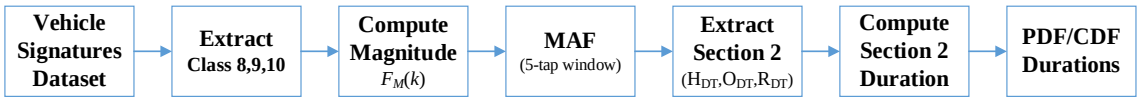

Figure 7-18 S^2_T computation process

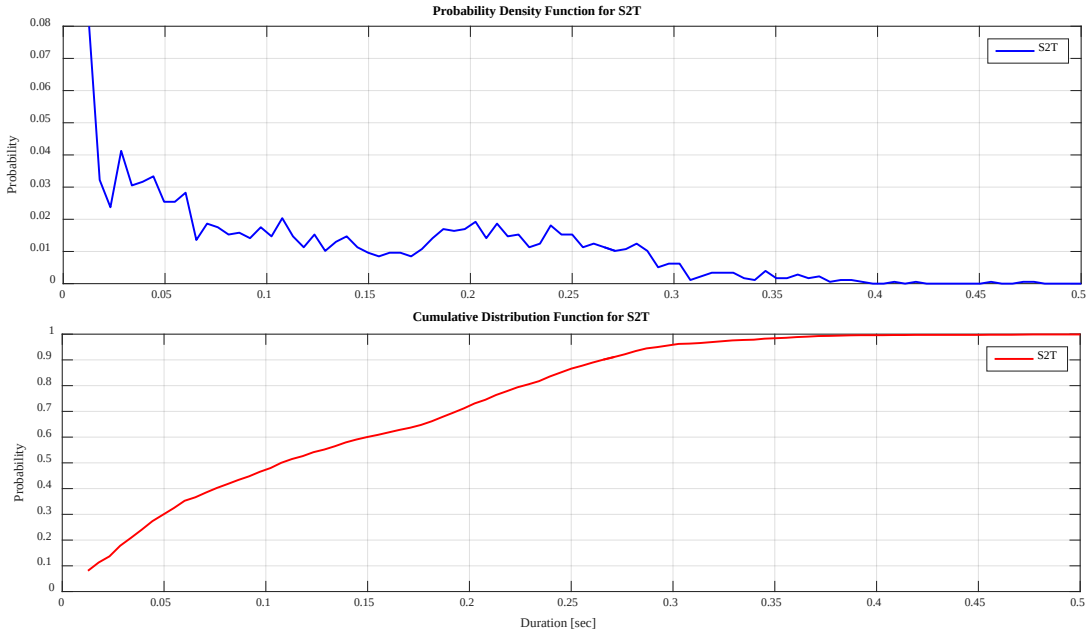

Figure 7-19 Probability distributions of Section 2 periods

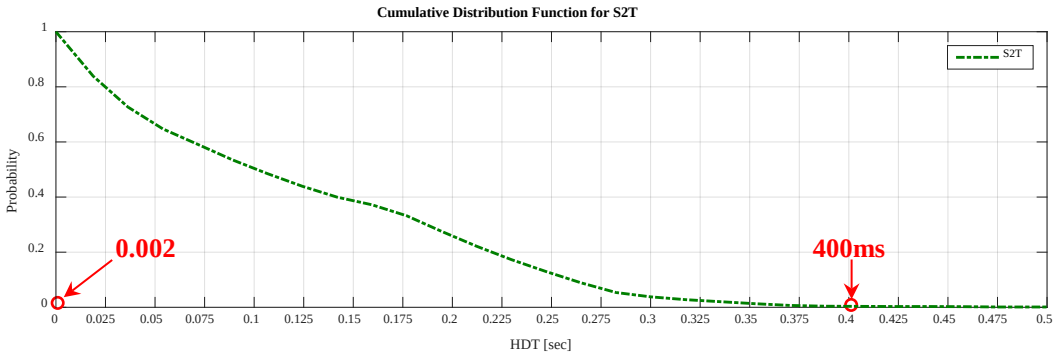

Figure 7-20 Probability of double detection for a given H_{DT}

7.3.2.3 Minimizing false-detection error

False-detection error is the result of a magnetic disturbance in the adjacent lane caused by a vehicle with high magnetic flux density traveling at the edge of lane. Such a disturbance will be detected by sensors in both lanes.

False-detection can initially be eliminated by defining sensor detection zone (*DZ*). In general, *DZ* can be defined at five detection edges (see Figure 7-21): 1) *leading*, 2) *trailing*, 3) *right-side*, 4) *left-side,* and 5) *elevation* edge. An empirical test was conducted to find the relationship between distance and magnetic disturbance magnitude. Results are illustrated in Table 7-2. Notably, the leading edge has the highest magnetic disturbance because vehicles contain the majority of ferromagnetic mass in the front section (e.g., engine).

Table 7-2 Detection zone characteristics

Leading Edge		Trailing Edge		Side sensitivity	
Distance (m)	**F_M (μT)**	**Distance (m)**	**F_M (μT)**	**Distance (m)**	**F_M (μT)**
2.50	3	2.50	1	2.00	3
2.20	4	2.20	2	1.30	7
1.25	6	1.16	4	0.90	10
1.10	7	1.10	6	0.60	18
0.90	10	0.90	7	0.30	30
0	70	0	10	0.20	40

Detection zone can be controlled by either changing MAG sensor sensitivity or changing detection thresholds, O_{TH} and H_{TH}, where α and β (See Eq. 4-2, Eq. 4-3 and

Eq. 4-4) can be calibrated to control detection zone and to eliminate interference outside the detection region.

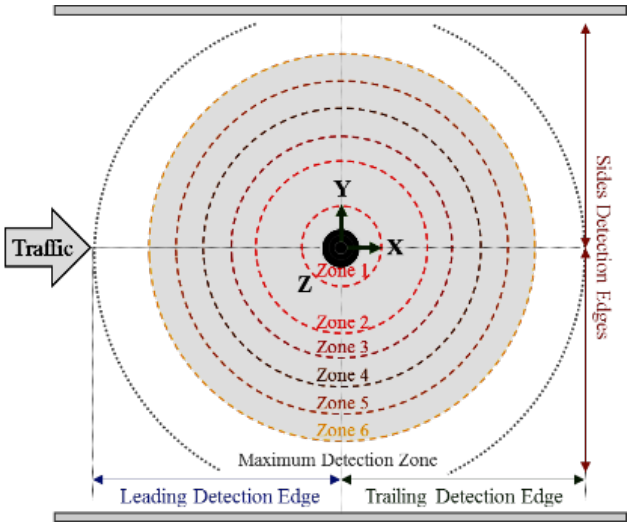

Figure 7-21 Detection zone edges was found to be symmetric

Analyzing the vehicle magnetic signatures dataset revealed that increasing O_{TH} to 9μT and H_{TH} to 6μT will prevent false-detection. However, increasing O_{TH} or H_{TH} will result in the loss of a chunk of vehicle magnetic signature, hence, render an unreliable estimation of vehicle length and loss of important features for vehicle classification. On the contrary, reducing sensitivity might cause motorcycle mis- and delayed-detection.

To solve this issue, variations in B_X, B_Y, and B_Z components were analyzed to measure vehicle effect on an adjacent lane interfering on each component. Analysis showed insignificant interfering effect on B_Z. Thus, by using 10-tap MAF, calculating $B_Z(k)$ mean—as in Eq. 7-13, and comparing μB_Z for each detected vehicle (V_n) with a threshold I_{TH}, a decision can be made whether V_n is a real detection or an interfering signal. I_{TH} =80 was statistically found from dataset.

Figure 7-22 illustrates variations in $B^{(\gamma)}$, their magnitude ($B^{(\gamma)}m$), and after MAF ($B^{(\gamma)}ma$) for class 3 with a trailer detected in right lane and the interfering vehicle in adjacent lane.

$$\mu B_Z(V_n) = \frac{1}{\mathrm{N}}\sum_{k=1}^{N}\left(\frac{1}{M}\sum_{i=0}^{M-1} B_{Zm}(k-i)\right) \geq I_{TH};\ B_{Zm}(k) = \sqrt{\left(B_Z(k) - B_{Zref}\right)^2} \quad \textbf{Eq. 7-13}$$

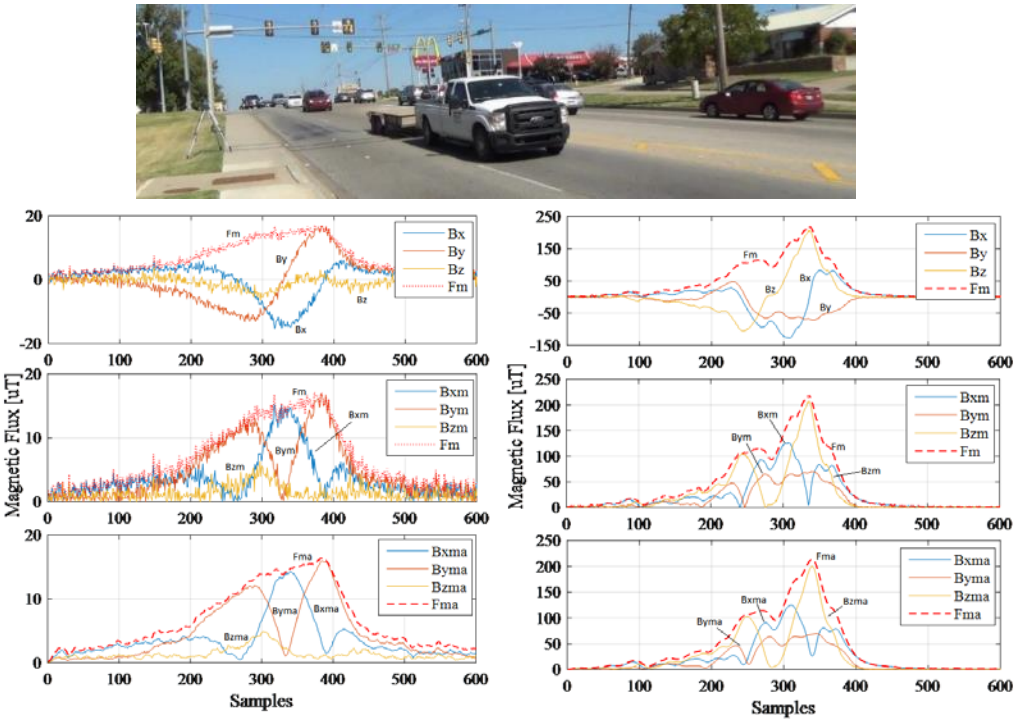

Figure 7-22 Variations in $B^{(Y)}$caused by interfering (left) and detection (right)

7.3.3 Adaptive Geomagnetic Baseline Drift Compensation Performance

To evaluate adaptive baseline drift compensation algorithm performance, a sensor node was deployed over the course of the day on pavement in the absence of any ferrous materials. Distribution of noise was found with and without the use of baseline drift compensation algorithm. Figure 7-23 shows drift in F_{Mref} over 240 minutes without (in yellow) and with (in blue) geomagnetic baseline compensation algorithm.
Figure 7-24 shows vector magnitude normalized distributions without (in yellow) and with (in blue) compensation. Given no compensation is applied, mean is μ=7.67μT and STD is σ=1.6319μT. Given the application of compensation algorithm, mean and STD are μ=1.79μT and σ=0.7μT, respectively.

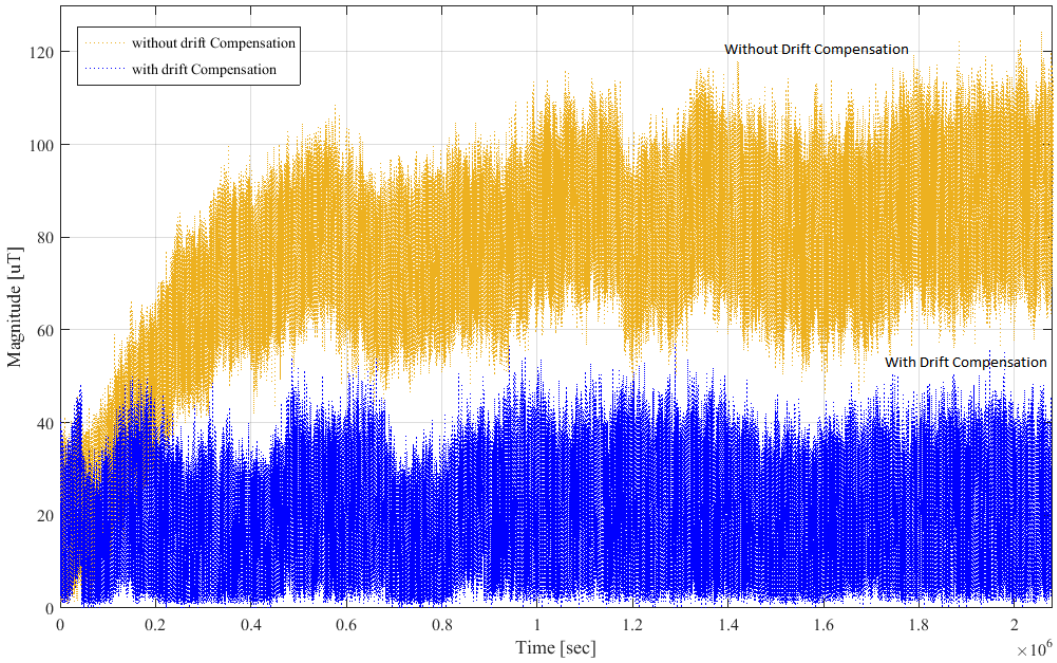

Figure 7-23 The drift in F_{Mref} with and without adaptive compensation

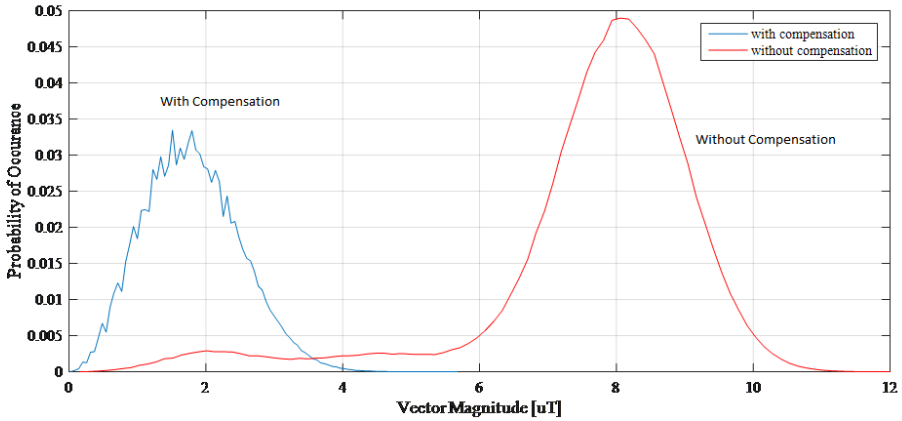

Figure 7-24 F_{Mref} distribution over 24-hour with and without compensation

7.3.4 Detection and Counting Accuracy

Counting accuracy was evaluated using the mean absolute percent error (MAPE), computed as in Eq. 7-14.

$$MAPE = \frac{1}{n}\sum_{1}^{n}\frac{|Count_{video} - Count_{iVCCS}|}{|Count_{video}|} \times 100 \qquad \textbf{Eq. 7-14}$$

Field Test 1 resulted in high detection ratio with overall 2% relative error. Dataset was limited to 463 vehicles. Classes 4, 7, 10, 11, 12, and 13 were not observed during

this test. Remaining classes were correctly detected, with the exception of class 9, which was double-detected with 9% error, as presented in Table 7-3.

Table 7-3 Detection MAPE for Roadway Setup—Field Test 1

Vehicle Class	Video Count	*i*VCCS Count	MAPE
F01	1	1	0.0%
F02	247	247	0.0%
F03	65	65	0.0%
F05	65	65	0.0%
F06	8	8	0.0%
F08	2	2	0.0%
F09	75	82	9.0%
Total	**463**	**470**	**2.0%**

Double-detection is one of three detection errors detailed in Section 7.3.2; these can be observed when using MAG for vehicle detection.

As stated earlier, double-detection occurs when signal magnitude drops below *Holdover Threshold* (H_{TH}) for duration $S^2_T > H_{DT}$ and crosses H_{TH} again while same vehicle remains in sensor detection zone. Finding optimal H_{DT} value that satisfies the condition $H_{DT} > S^2_T$ would solve this problem. Section 7.3.2 provides a detailed analysis for optimal H_{DT} value that minimizes double-detection error.

Field Test 2 had two deployment setups—roadway and roadside. *Roadway* setup resulted in 99.90% detection accuracy for dataset with 2007 vehicles. Class 1, 4, 11, 12, and 13 vehicles were not observed during this test. Unlike *Field Test 1*, all class 9 vehicles were correctly detected, primarily because a new H_{TH} value based on the analysis study in Section 7.3.2 was considered for this test. However, a mis-detection of two Class 2 vehicles occurred when two successive vehicles located within close proximity of one another were grouped as one. This could occur given that $H_{DT} > g_T$. Hence, to reduce the probability of double-detection and mis-detection, optimal H_{DT} value for satisfying the condition $g_T > H_{DT} > S^2_T$ should be found This requirement is well-detailed in Section 7.3.2.

The *Roadside* setup in *Field Test 2* confirmed 99.95% detection accuracy (See Table 7-5). Flux magnitude variations in *roadside* setup were relatively uniform when compared to *roadway* setup, which accounts for slightly better accuracy.

Table 7-4 Detection MAPE for Roadway Setup—Field Test 2

Vehicle Class	Video Count	iVCCS Count	MAPE
F02	624	622	0.32%
F03	1027	1027	0.00%
F05	97	97	0.00%
F06	32	32	0.00%
F07	1	1	0.00%
F08	8	8	0.00%
F09	213	213	0.00%
F10	5	5	0.00%
Total	2007	2005	0.099%

Table 7-5 Detection MAPE for Roadside Setup—Field Test 2

Video Count	iVCCS Count	Detection	MAPE
2044	2045	99.951%	**0.0489%**

Field Test 3 resulted in a high detection ratio with only 0.0363% MAPE. Dataset included 2754 vehicles. Class 11, 12, and 13 vehicles were absent. Detection results per class are shown in Table 7-6.

Table 7-6 Detection MAPE for Roadway Setup—Field Test 3

Vehicle Class	Video Count	Roadrunner	iVCCS Count	MAPE
1	10	10	8	10%
2	919	919	918	0.10881393%
3	1287	1287	1287	0
4	13	13	13	0
5	133	133	133	0
6	48	48	48	0
8	13	13	13	0
9	327	330	329	0.6116208%
10	4	4	4	0
Total	**2754**	**2757**	**2753**	**0.036311%**

Field Test 4 proved excellent *in-lane* detection. However, unlike the first three highway-based field tests, Field Test 4 was conducted on an urban road; this introduced a new "*false-detection*" error resulting from interfering vehicles on an adjacent lane. This error was specifically caused by the following scenarios:

1) Dissimilar lanes widths characterized by highway lanes measuring at least 12 feet (3.7 m) wide and urban road lanes measuring a width of 9 feet (2.7 m)
2) Trucks traveling at the edge of a detection lane (See Figure 7-25, Figure 7-26, and Figure 7-27) or hybrid cars traveling on an adjacent lane (See Figure 7-28).
3) Vehicles with a significant amount of steel in their structure.

Figure 7-25 Class 9 truck at the edge of lane 2, detected in both lanes

Figure 7-26 Class 6 truck on the edge of lane 2, detected in both lanes

Figure 7-27 Class 3 truck with huge trailer on edge of lane 2, detected in both lanes

Figure 7-28 Class 2 hybrid car on the edge of lane 2, detected in both lanes

Results for in-lane detection errors (i.e., errors resulting from adjacent lane interference are not considered) are illustrated in Table 7-7. All classes were detected correctly, with the exception of two class 9 vehicles and one class 8 vehicle that were double-detected when traveling at very low speeds (e.g., 10 mph). Mean Absolute Error (MAE) for per class detection is 0.25% for Lane 1 and 0% for Lane 2. MAPE is 0.058% for Lane 1 and 0% for Lane 2. Classes 7, 10, 11, 12, and 13 were not observed during this test.

Table 7-7 Number of detections In-Lane per-class—Field Test 4

Class	Video		*i*VCCS		MAPE	
	Lane 1	Lane 2	Lane 1	Lane 2	Lane 1	Lane 2
1	7	4	7	4	0	0
2	2607	2552	2607	2552	0	0
3	793	817	793	817	0	0
4	1	2	1	2	0	0
5	39	24	39	24	0	0
6	4	0	4	0	0	0
8	3	2	3	2	0	0
9	6	0	8	0	33.33%	0
Total	**3460**	**3401**	**3462**	**3401**	**0.058%**	**0%**

Table 7-8 shows overall detection error when vehicles detected from adjacent lane are considered in the error analysis. Overall MAPE is 1.676%. Out of 6976 detected by *i*VCCS on both lanes, 115 vehicles were falsely detected from adjacent-lane due to either trucks or hybrid cars bypassing the detection lane. False-detection caused by hybrid cars can be attributed to the large amount of metal located in the stack of battery elements, as well as a large magnet in the electric engine router.

Table 7-8 Total Detection Error—Field Test 4

Detection	iVCCS		Video		MAE		MARE	
	Lane 1	Lane 2	Lane 1	Lane 2	Lane 1	Lane 2	Lane 1	Lane 2
In-Lane	3462	3401	3460	3401	4.02%	6.45%	1.27%	2.088%
Adj-Lane Trucks	23	56	-	-				
Adj-Lane Hybrid	19	15	-	-				
Total	**6976**		**6861**		**5.24%**		**1.676%**	

False-detection error can be eliminated, as described in Section 7.3.2, by computing μB_Z using Eq. 7-13, and then comparing μB_Z for each detected vehicle (V_n)

with threshold I_{TH}. A decision can be made whether V_n a real detection or an interfering signal is.

Field Test 5 results (See Table 7-9) demonstrated outstanding detection performance. Notably, several Class 1 (i.e., motorcycles) were detected albeit falsely considered as false-detection (i.e., interfering from adjacent lane) by *i*VCCS because they had an insignificant ferromagnetic mass and bypassed detection zone (See Figure 7-29). Some Class 2 and 3 vehicles were not detected because *i*VCCS was in calibration state during vehicle passage. Vehicles traveling between lanes were considered false-detection by *i*VCCS sensors in both lanes.

Table 7-9 Detection MAPE—Field Test 5

Class	Video		*i*VCCS		MAPE	
	Lane 1	Lane 2	Lane 1	Lane 2	Lane 1	Lane 2
1	3	9	2	7	33.3333	22.2222
2	2062	947	2059	943	0.1454	0.42234
3	582	289	581	287	0.17186	0.6922
4	6	0	6	0	0	0
5	40	11	40	11	0	0
6	14	4	14	4	0	0
7	1	1	1	1	0	0
8	2	0	2	0	0	0
9	15	6	15	6	0	0
10	1	1	1	1	0	0
12	3	0	3	0	0	0
Total	**2729**	**1268**	**2724**	**1260**	**0.1832%**	**0.6309%**

Figure 7-29 Motorcycle considered as False-detection

Field Test 6 and *7* results were evaluated by ODOT before disclosure to other parties. ODOT-reported results are listed in Table 7-10 and Table 7-11. ODOT considered the manual count as a ground truth for evaluation. In *Field Test 6*, *i*VCCS over performed AVC and video-based counting methods with 0.639% MAPE. In *Field Test 7*, *i*VCCS achieved 98.5% detection accuracy

Table 7-10 Detection MAPE—Field Test 6

Detection Method	Manual	Video	AVC23	*i*VCCS
Total Count	**1252**	**1227**	**1263**	**1260**

Table 7-11 Detection MAPE—Field Test 7

Detection Method	Manual	Tubes	AVC04	*i*VCCS
Total Count Lane 1	314	314	307	302
Total Count Lane 2	286	292	293	289
Total Count Lane 3	228	226	225	224
Total	**828**	**832**	**825**	**815**

7.3.5 Detection in Stationary-state and Stop-and-go Scenarios

Stationary state occurs when a vehicle stops completely (e.g., parking lots) or travels in stop-and-go conditions (e.g., at traffic signals and intersections). The developed detection algorithm was tested in both scenarios. Achieved detection accuracy was 100% when sensor was deployed in *roadside* and *roadway* setups. Figure 7-30 and Figure 7-31 show go-stop-go detections for Honda Accord 2004 in both roadside and roadway setups. *R1* represents vehicle arrival; *R2* represents steady state (stop); and *R3* represents departure. Figure 7-32 shows F_M for go-stop-go scenario in both roadside and roadway setups. G_A, S_S, and G_D represent vehicle arrival section (go-in), vehicle in steady state (stop); and vehicle departure section (go-out).

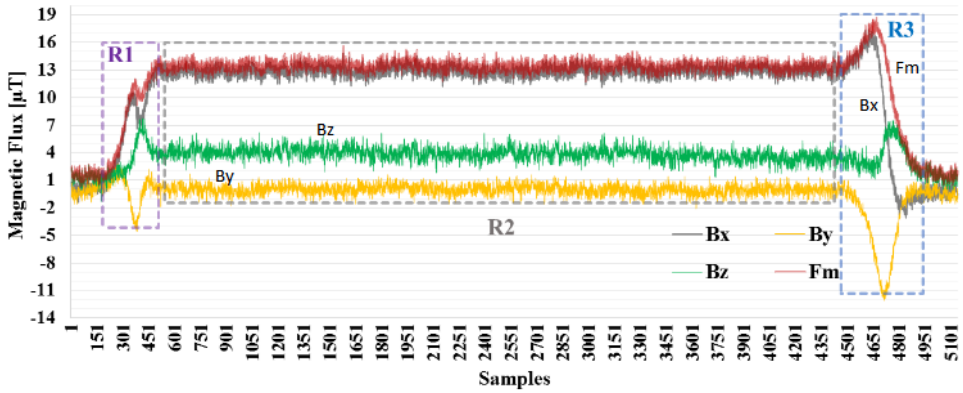

Figure 7-30 Go-Stop-Go detection using sensor in roadside setup

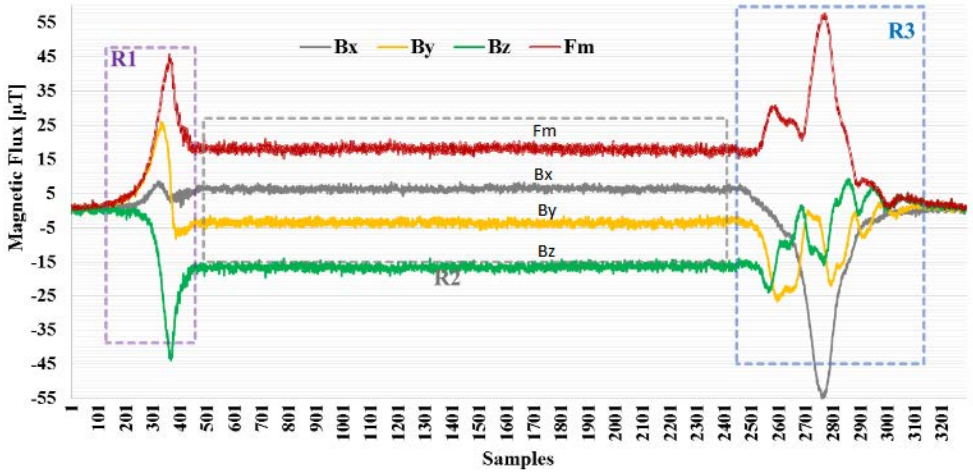

Figure 7-31 Go-Stop-Go detection using sensor in roadway setup

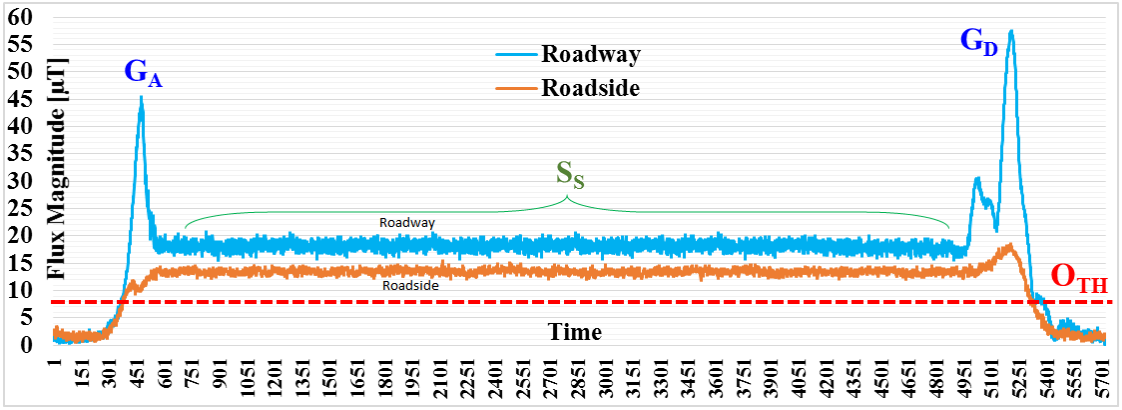

Figure 7-32 The FM and detection flag in Go-Stop-Go scenario

7.4 Time Synchronization

To assess T-Sync algorithm performance and evaluate drift error on each node, as well as over a network, the following test was conducted.

RTC-1Hz signal duration $T_{RTC}^{(MCU)} = 1/f_{RTC}^{(MCU)}$ was compared to GPS-PPS signal duration $T_{PPS}^{(GPS)} = 1/f_{PPS}^{(GPS)}$ over the course of 24 hours. Both clocks were sampled using the MCU's high frequency clock at $f_{TCLK}^{(MCU)} = 32MHz$. Measurement resolution is one-cycle of $f_{TCLK}^{(MCU)}$, which is equal to 31.25ns. $f_{TCLK}^{(MCU)}$has a tolerance ±5*ppm*; however, since both signals are measured instantaneously using the same clock, tolerance error is canceled. Differences between measured durations were logged.

This particular test was implemented instantaneously on five different *i*VCCS nodes. RTC drift for each node was calculated separately and compared statistically with other node drift to find over-network T-Sync error. Drift dataset included 86400 measurements from each sensor. Temperature measurements were also combined on q one-minute basis. Figure 7-33 shows a histogram for absolute error between RTC-1Hz and GPS-PPS signals over the course of day for three *i*VCCS Nodes—A, B, and C. Consistent drift between RTC-1Hz and GPS-PPS signals with mean 20~25µSec can be observed for all nodes. Figure 7-34 shows distribution of T-Sync error between two nodes. Drift with a mean of 2~4µSec can be observed among Nodes A, B, and C.

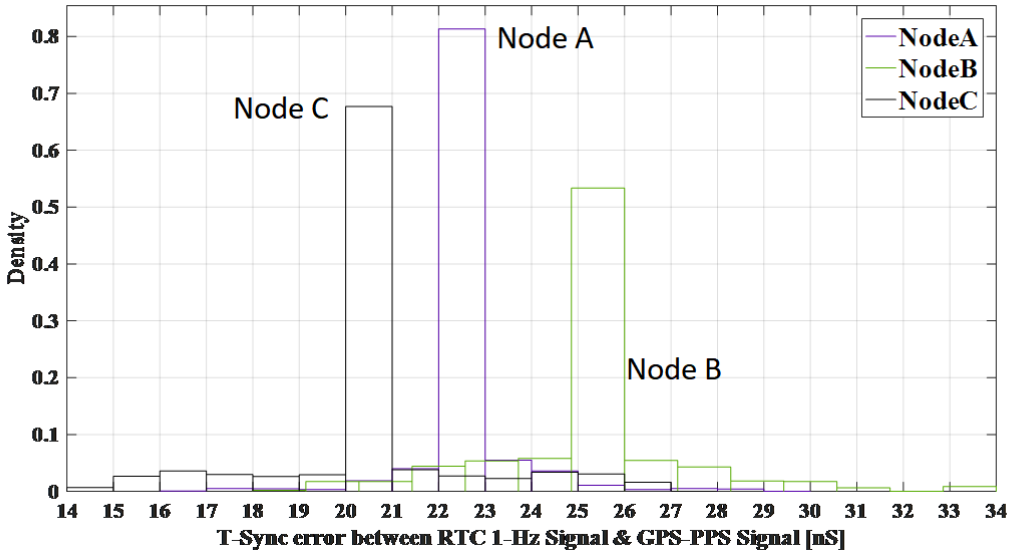

Figure 7-33 Histogram of T-Sync error between RTC and GPS

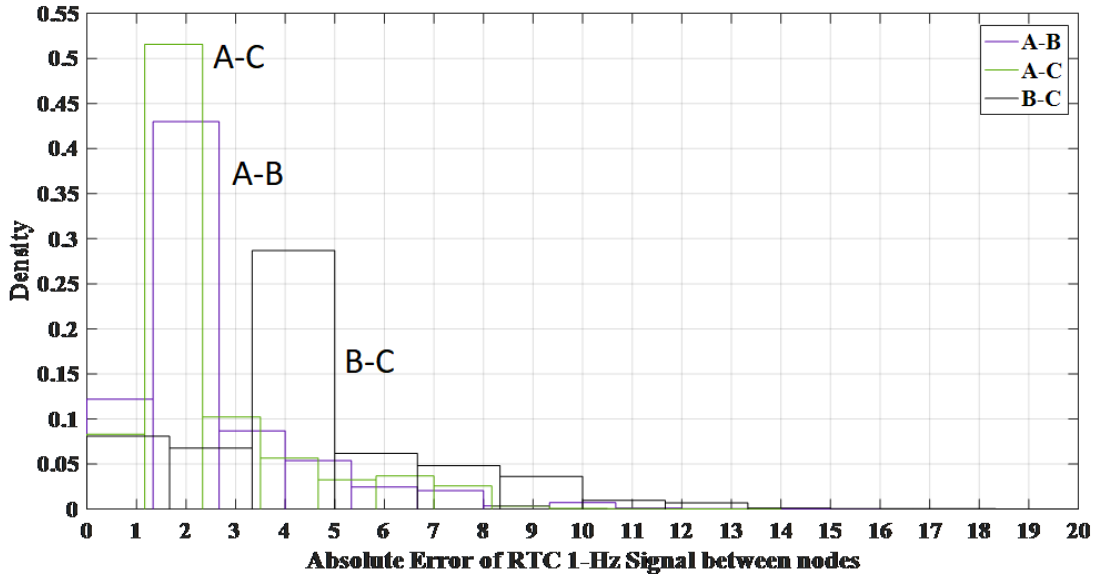

Figure 7-34 Histogram of absolute error of RTC between two nodes

7.4.1 Evaluation of Timestamps Consistency

GPS-PPS signal is used to synchronize spatially distributed sensor nodes that share a globally synchronized timestamp. However, error in arrival and departure timestamps is driven by factors other than T-Synch error (e.g., delay in MCU's interrupt routine and instruction execution).

Delay in executing arrival and departure timestamps is nondeterministic. Rather, it is subject to frequency tolerance $f_{osc\text{-}tol}$ of MCU's oscillator and task priority MCU is executing at the moment of a timestamp event. Arrival timestamp event is triggered by MAG *Magnitude Interrupt* over the MC's external interrupt *INT0*.

To evaluate the consistency and determine timestamping delay, a highly accurate signal generator was used to trigger *INT0* at consistent frequency $f_{Trigger}$. Trigger time was logged, and delay between each two consecutive triggers was calculated. The test was repeated for different $f_{Trigger}$, ranging 1~1600Hz, each with 10^8 samples. The test resulted in trivial delay (i.e., tens of nanosecond) at various $f_{Trigger}$ values.

7.5 Speed Estimation

Speed estimation accuracy was evaluated against *Road Runner 3 kit* with 30.5μs event timestamp resolution. Two statistical measurements were used: 1) Mean Absolute Percentage Error (MAPE), which measures systematic bias to error such that estimated

speed values are consistently high or low (Eq. 7-15) and 2) Root Mean Square Error (RMSE), which measures mean deviation of estimated speed values (Eq. 7-16). Speed analysis is shown in Table 7-12.

Three separations between the nodes, namely 6-, 8-, and 10-meter, were investigated. Superior results occurred when two nodes were separated by 8 meters. *Roadside* setup demonstrated a higher speed estimation error when compared to *roadway* setup. This phenomenon can be attributed to lower SNR in the roadside scenario.

$$MAPE = \frac{1}{n}\sum_{i=1}^{n}\left|\frac{True\ Speed_{(i)} - Estimated\ Speed_{(i)}}{True\ Speed_{(i)}}\right| \quad \textbf{Eq. 7-15}$$

$$RMSE = \sqrt{\frac{1}{n}\sum_{i=1}^{n}\left(True\ Speed_{(i)} - Estimated\ Speed_{(i)}\right)^2} \quad \textbf{Eq. 7-16}$$

Table 7-12 Speed Estimation Accuracy

Setup	MAPE	RMSE	Speed Accuracy
Roadside (*d*=6m)	6.4603 mph	6.5001%	93.5012%
Roadway (*d*=6m)	3.2064 mph	2.6585%	97.3415%
Roadway (*d*=8m)	2.9281 mph	2.5773%	97.4227%
Roadway (*d*=10m)	2.9867 mph	2.5218%	97.4782%

Speed estimation using MAG is subject to several inaccuracy factors (e.g., sensor sampling rate (f_S), T-Sync error, and defined vehicle detection zone, among others).

Nondeterministic error ξ_{Ts} could occur as the result of a delay in sampling the exact instant of vehicle arrival or departure. Maximum ξ_{Ts} is equal to the period of pre-defined sampling rate (e.g., if f_S=100Hz then ξ_{Ts}=10ms). Assume a vehicle with 5-meter average length travels at 90mph (i.e., 40m/s). Occupancy time on each sensor $T_{Occ} = 5/40 = 125ms$. Hence, maximum error in T_A and T_A timestamps is $2\xi_{Ts}/T_{Occ}$ = 320μs, which accounts for 0.256% error in speed estimation.

Based on data observations and statistical analysis, the following issues must be considered for more accurate speed estimation.

1) The higher the sampling rate, the higher the speed estimation accuracy.
2) All sensor nodes should implement the same detection reference thresholds (O_{TH}, H_{TH}, and R_{TH}) and debounce timers (O_{DT}, H_{DT}, and P_{DT}); any difference in thresholding between nodes will add a detection timestamp error.
3) Tolerance error in sensors sensitivity—due to environmental factors—can be reduced by using higher sampling rates; however, this error can be neglected without need for compensation.
4) Changes in vehicle trajectory at detection point might result in a T_A and T_A timestamp error; however, this error is rear, trivial, and can be neglected.

7.6 Diversity-based Speed Estimation

Diversity combining is a widely used technique in telecommunications to enhance receiver immunity against noise and channel effects. Diversity increases signal to noise ratio by coherently combining multiple copies of signals received from multiple antennas. This enhances signal to noise ratio (SNR), hence, enhances connection quality. The same principle applies to sensor networks where using multiple sensors to measure the same physical quantity leads to a more accurate characterization of the measured system.

In this section the potential of using on-board array sensors to enhance the quality magnetic field measurements is investigate. The diversity role in enhancing SNR is researched for two cases: 1) noise consists of environment effects and electronics thermal noise, 2) considers distortion produced by vehicles traveling along an adjacent lane.

7.6.1 Diversity combining in the presence of environmental noise

Improving a device's immunity against noise plays an important role in enhancing its measurements quality. Equipment manufacturers spend considerable efforts immunizing their systems against noise. Diversity combining is one of the techniques frequently used to achieve this objective. It uses multiple sensors, placed within close proximity from each other, to capture multiple copies of the same physical event (e.g. vehicle detection). Different sensors will have different SNR, but the weighted sum of output signals, as shown in Figure 7-35, produces a new signal with higher SNR than each individual signal.

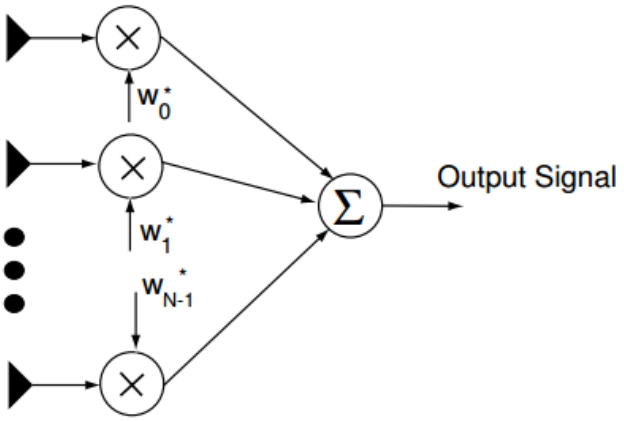

Figure 7-35 Diversity combining principle

Enhancing SNR in the Intelligent Vehicle Counter and Classifier (iVCCS) is beneficial in improving vehicles detection and classification accuracy. The team conducted a test setup to study the efficiency of diversity in enhancing measurements SNR. Three sensors were used to collect magnetic signatures of a sedan vehicle. The sensors were placed as shown in Figure 7-36 with 4 centimeters separation between neighboring units.

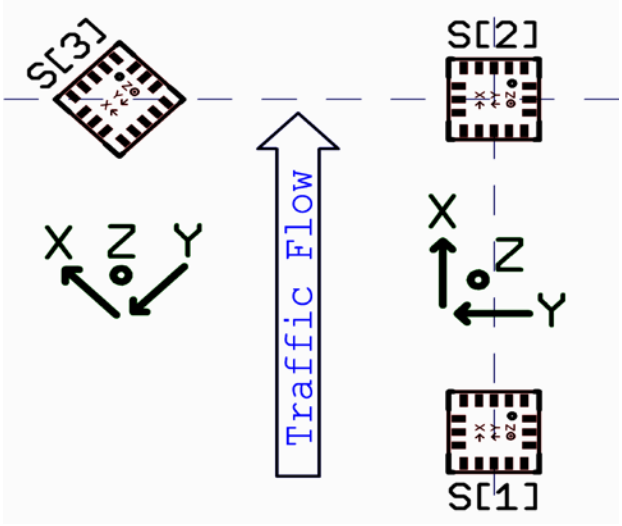

Figure 7-36 Test setup

Two combining schemes were studied. The first is called equal-gain combining (EGC) in which signals are multiplied by equal weights $W_0 = W_1 = \cdots = W_{N-1}$ and added coherently. Table 7-13 reports SNR before and after EGC combining.

Table 7-13. SNR using EGC combining

Signals	S1	S2	S3	Combined Signal
SNR	18.85 dB	19.87 dB	19.27 dB	19.72 dB

In the second combination scheme, signals were multiplied by weights that are proportional to their SNR. The signal with the highest SNR had the highest weight and vice versa. This combination technique is called maximal-ratio combining (MRC). Table 7-14 shows signals SNR before and after MRC.

Table 7-14. SNR using MRC combining

Signals	S1	S2	S3	Combined Signal
SNR	18.85 dB	19.87 dB	19.27 dB	20.1 dB

Results show that SNR enhancement was less than 1 dB for both techniques. This is attributed to the fact that signals from individual sensors are highly correlated if they are placed close to each other. Figure 3 shows a correlation coefficient close to one between signatures recorded by two of the sensors. Diversity combining does not provide considerable enhancement unless individual signals are not correlated. Therefore, the team repeated the same test after increasing separation to 10 centimeters. Table 7-15 shows new SNR values after increasing separation.

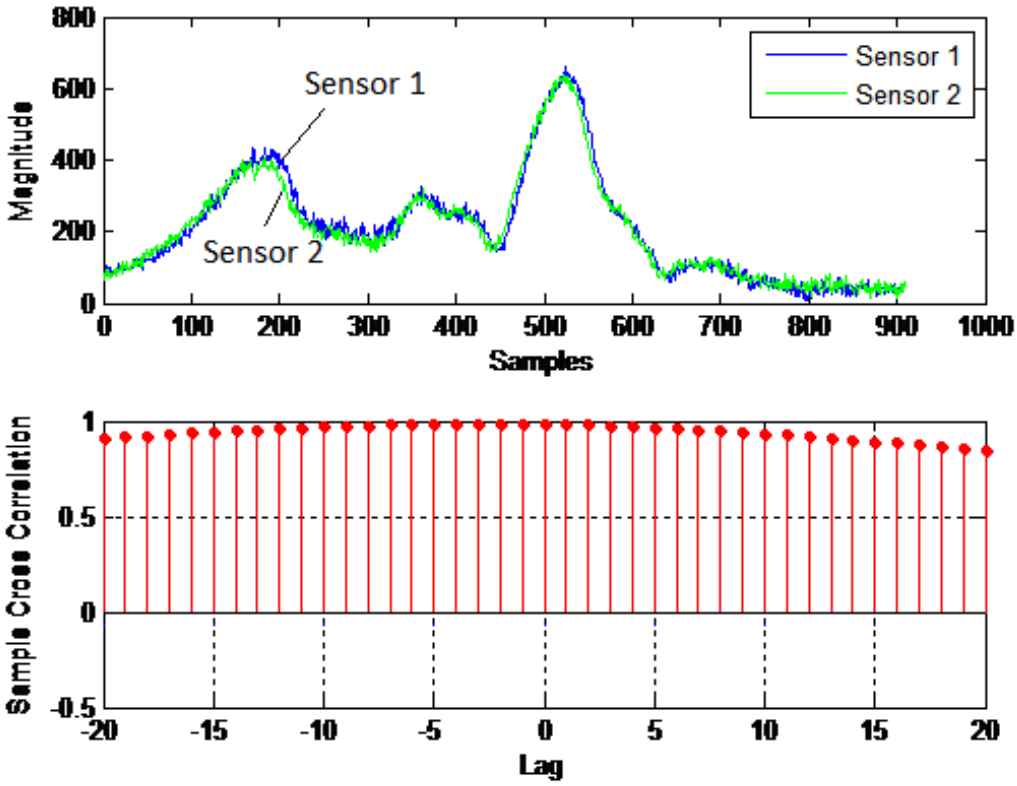

Figure 7-37 Correlation between signatures recorded by separate sensors

Table 7-15. SNR using EGC and MRC after increasing separation.

	S1	S2	S3	EGC Combining	MRC Combining
SNR	25.34 dB	19.22 dB	15.62dB	19.8 dB	22.48

The results in Table 7-15 show a notably large variance in SNR values between sensors. Therefore, it is better, in this case, to select the signal with the highest SNR instead of combining all signals. This variation in SNR is attributed to a lower correlation between individual signals compared to what it was at 4 Cm separation.

7.6.2 Diversity combining in the presence of adjacent-lane noise

Figure 7-38 depicts an experiment the team did to test the diversity's role in canceling noise from vehicles traveling along adjacent lanes. Both vehicles drove adjacent to each other at the same time. The signature of the vehicle on lane 2 adds

noise to the vehicle's signature on lane 1. This noise can lead to false detections and decrease classification certainty.

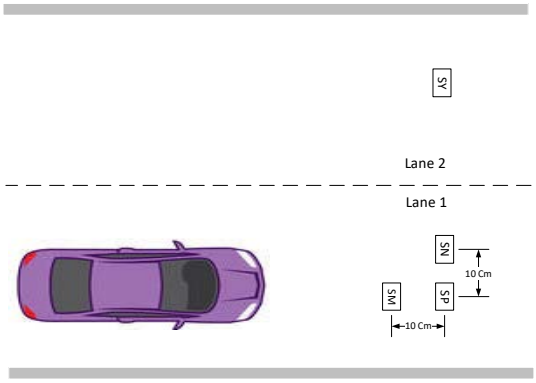

Figure 7-38 Test setup to study adjacent lane distortion.

Figure 7-39 shows the signatures of the vehicle on Lane with and without adjacent lane noise. Obviously, adjacent lane noise distorts vehicles signatures. This distortion might hinder the accuracy of advanced applications such as vehicle classification and re-identification. Furthermore, if distortion level is high enough, the sensors might falsely count a vehicle on adjacent lanes. Combining the signals of multiple sensors deployed on the same lane plays a role in reducing adjacent lane distortion. In Figure 7-38, distortion will be higher at SN than that at SM and SP because SN is placed closer to the adjacent lane. Therefore, combining the signals of the 3 sensors has the effect of reducing discrepancies between signatures, due to the fact that equal gain combining acts as an averaging filter. Figure 7-40 illustrates the role of diversity combining in removing adjacent lane distortion. Distortion is more pronounced in SN compared to other sensors because it is closer to the adjacent lane. Equal gain combining produces a signature that emphasizes similarities between signatures and reduces discrepancies resulting from both environmental noise and adjacent lane distortion.

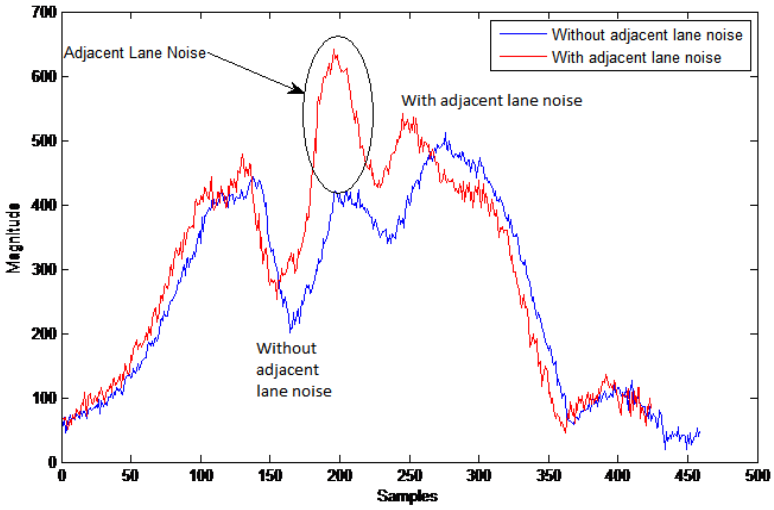

Figure 7-39 Distortion produced by adjacent lane traffic.

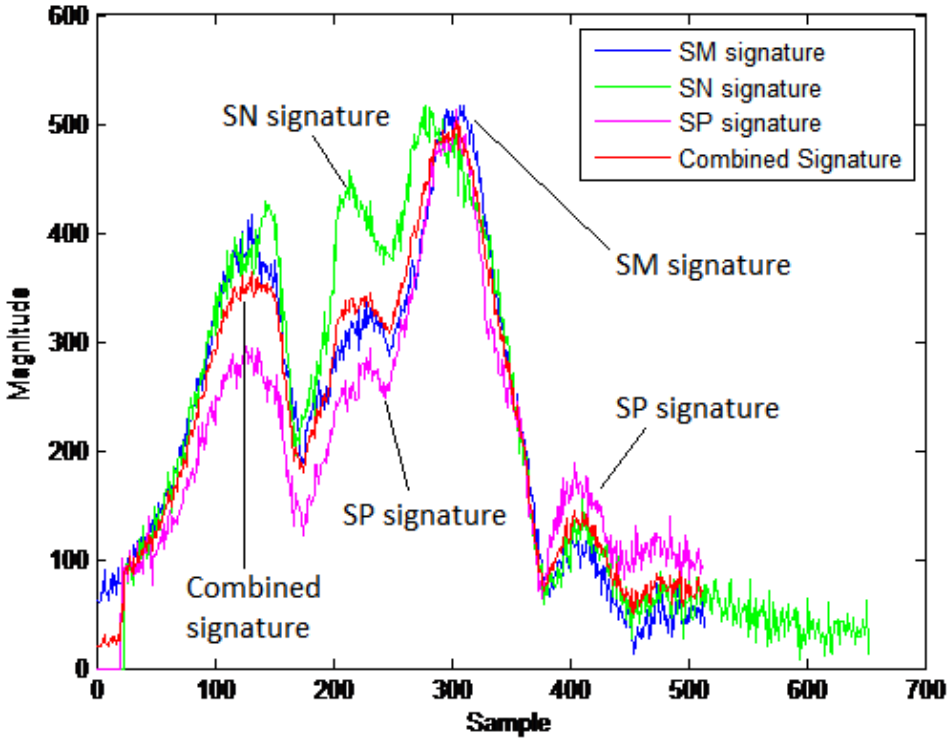

Figure 7-40 Diversity's role in canceling adjacent lane distortion.

7.7 Vehicle Length Estimation

VML is estimated from the product of vehicle estimated speed and occupancy time using Eq. 4-27. The highway dataset includes 4178 VML measurements; urban road

dataset includes 6856 VML measurements. Figure 7-41 and Figure 7-42 show the distribution of VML by FHWA F Scheme with 13 classes for tests conducted on highway and urban roads, respectively. Combined distribution is shown in Figure 7-43.

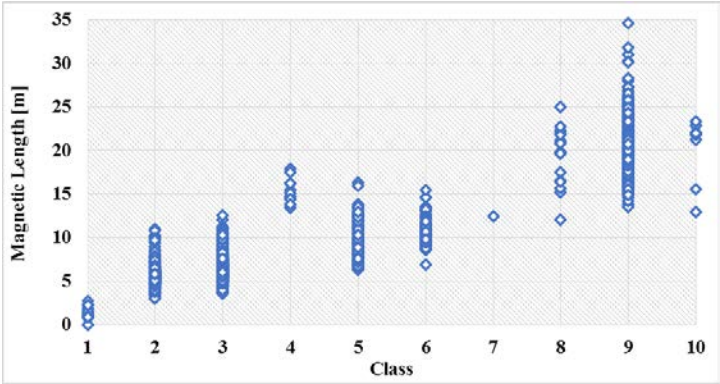

Figure 7-41 VML by FHWA F Scheme – Highway Data

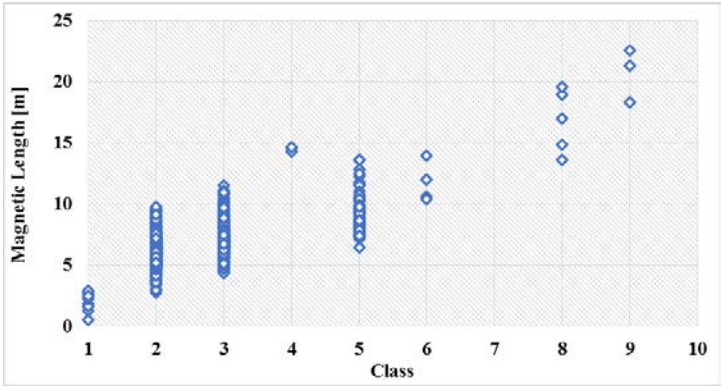

Figure 7-42 VML by FHWA F Scheme – Urban Data

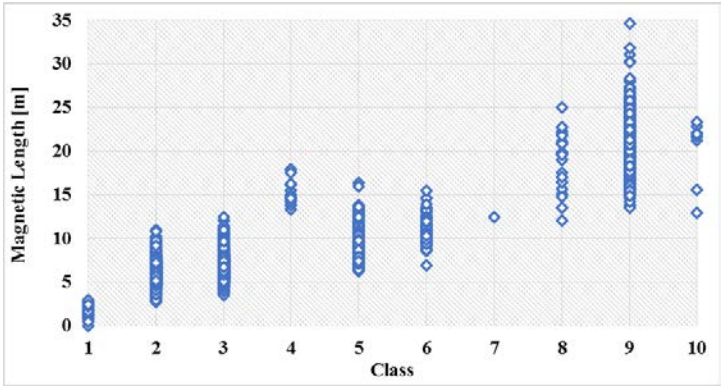

Figure 7-43 VML by FHWA F Scheme – Combined

7.8 Vehicle Classification

In this section, two methods for vehicle classification using MAG, namely Length-Based Vehicle Classification (LBVC) and Magnetic Signature-based Vehicle Classification (SBVC), are discussed in detail.

7.8.1 Real-Time Magnetic Length-based Vehicle Classification

LBVC algorithm using two timely, synchronized MAG nodes was developed and implemented by means of ML and probabilistic modeling. Several classification schemes are proposed. The developed algorithm enables real-time, computationally efficient vehicle classification based on VML.

Classification based on VML requires precise vehicle detection and highly accurate speed estimation. Precise detection demands a consistent baseline (i.e., localized geomagnetic field) and coherent sampling rate. Speed estimation accuracy relies on the precision of time-stamping (i.e., vehicle arrival and departure time), which is dependent upon the accuracy of time synchronization algorithm. All algorithms are well detailed in companion publications [72]–[74].

7.8.1.1 Vehicle Magnetic Length

Before developing any classification scheme that bins multiple classes, it is important to understand the underlying statistical distribution of each class, as well as overlap among various classes. Classes that show significant overlapping should be grouped into the same bin. Significant overlap between two groups will result in a high mis-classification rate.

In this study, the combined VML dataset (11034 sample) was considered for data analysis and classification study. Vehicles in Classes 11, 12, and 13 were missing from dataset, as they were not observed during the field study. Figure 7-44 shows VML scatter plots for the dataset used to develop LBVC schemes. Table 7-16 presents five essential statistical measurements for each class, namely mean, standard deviation (STD), and variance (Var), as well as maximum and minimum values. Notably, a significant overlap is observed among classes 2 and 3, classes 5 through 7, and classes 8 through 13. Additionally, significant variations in VML per class are attributed to differences in the amount of permeable ferrous materials in each vehicle structure. Vehicles with a large amount of steel in their structure can be detected from a longer

distance; hence, their magnetic length will be longer. There is no way to find a general dipole model for all vehicles, even for those within the same class. Figure 7-45 illustrates the histograms of VML by FHWA Scheme F with 13 classes.

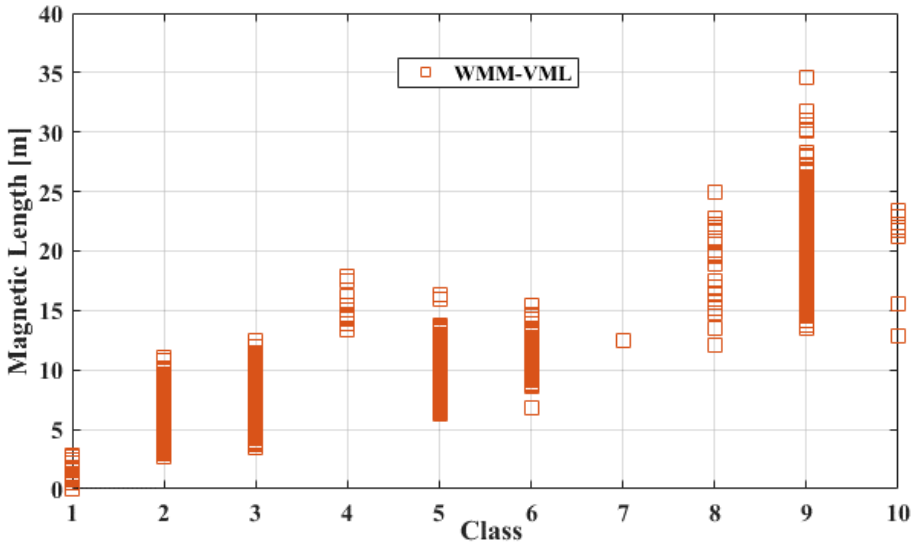

Figure 7-44 VML scatter plots for dataset that used to develop LBVC schemes

Table 7-16 VML statistical measurements

FHWA Class	Mean Length (m)	Standard Deviation	Variance	Maximum Length (m)	Minimum Length (m)
F01	1.7629	0.7156	0.5120	2.9106	0.5370
F02	5.9383	0.8190	0.6708	11.0377	2.7606
F03	6.6140	1.0713	1.1477	12.5161	3.5516
F04	15.2446	1.3782	1.8996	17.9241	13.3784
F05	9.2552	1.9270	3.7132	16.3884	6.2894
F06	10.9073	1.6149	2.6078	15.4366	6.8855
F07	12.4458	NA	NA	12.4458	12.4458
F08	18.8185	3.2396	10.4950	25.0102	12.0606
F09	21.3425	2.9298	8.5840	34.6607	13.5164
F10	20.3949	3.5930	12.9097	23.3700	12.9307

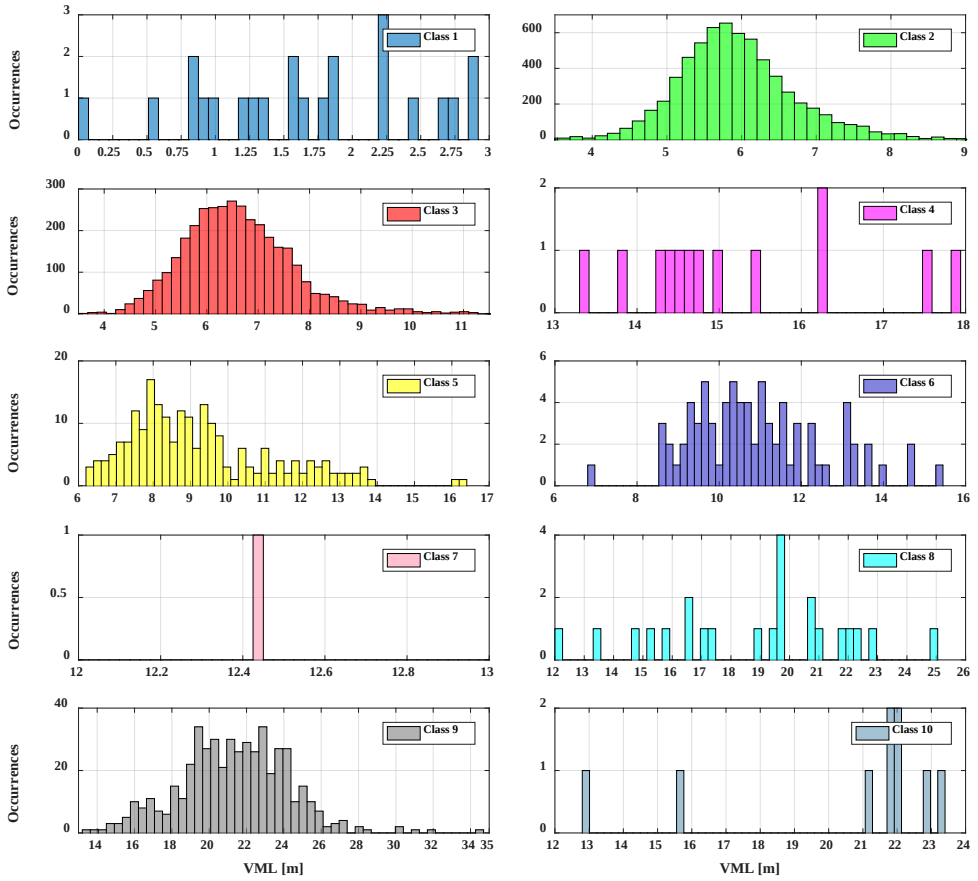

Figure 7-45 Histograms of VML by FHWA F Scheme Classes

7.8.1.2 Proposed Classification Schemes

According to the FHWA's traffic monitoring guide, "*If length-based classification is used, it should accommodate motorcycle identification as one of the groups*" [13]. Based on a) visual observation of VML data shown in Figure 7-44 and Figure 7-45, b) statistical measurements presented in Table 7-16, as well as c) structural similarity of vehicles, three distinctive LBVC schemes are proposed, as shown in Figure 7-46.

MC group includes only motorcycles. PV group includes passenger cars, pickups, and SUVs. Short-trailer group (ST) includes buses, light-trucks, and single-unit-trucks. Long vehicles (L/LT) group includes single-trailer and multi-trailer trucks.

The main objective of the *Three Groups LBVC Scheme A* (3-G_{SA}) is providing a general distinction of long and heavy commercial vehicles, which includes buses, semi-trailer (ST) trucks, and multi-trailer (MT) trucks. The 3-G_{SB} and 4-G_{SX} provide further distinction between Passenger Vehicles (PV) and Single-Unit Trucks (SU).

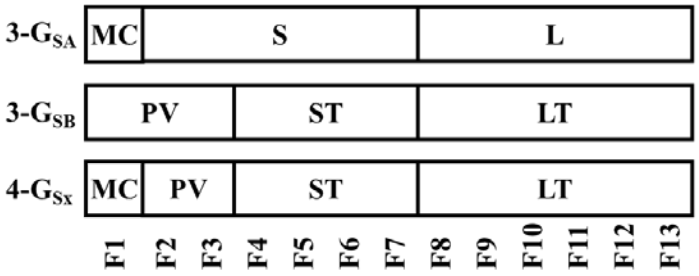

Figure 7-46 Recommended Classification Schemes

Scatter plots for datasets based on proposed LBVC schemes are shown in Figure 7-47. A histogram and statistical measurements for 3-G_{SA} are illustrated in Figure 7-48 and Table 7-17, respectively. Statistical measurements for 3-G_{SB} are illustrated in Table 7-18. A histogram and statistical measurements for 4-G_{Sx} are illustrated in Figure 7-49 and Table 7-19, respectively.

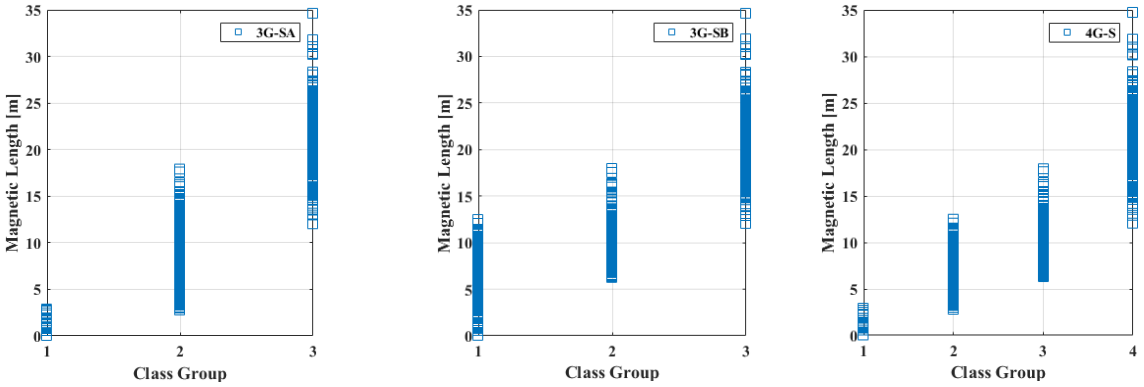

Figure 7-47 Dataset scatter plots for 3-G_{SA}; 3-G_{SB}; and 4-G_{Sx}

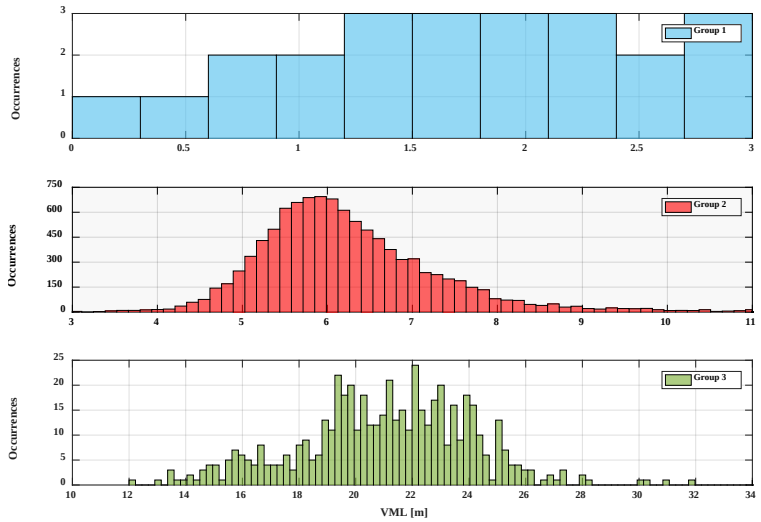

Figure 7-48 Histograms of VML by 3-G_{SA}

Table 7-17 VML statistical measurements for 3-G_{SA}

Group Number	Mean Length (m)	Standard Deviation	Variance	Maximum Length (m)	Minimum Length (m)
G1	1.6863	0.7899	0.6239	2.9106	0.8112
G2	6.2912	1.2165	1.4799	17.9241	2.7606
G3	21.2157	2.9961	8.9765	34.6607	12.0606

Table 7-18 VML statistical measurements for 3-G_{SB}

Group Number	Mean Length (m)	Standard Deviation	Variance	Maximum Length (m)	Minimum Length (m)
G1	6.1681	0.9949	0.9898	12.5161	0.8112
G2	9.9333	2.2571	5.0944	17.9241	6.2894
G3	21.2157	2.9961	8.9765	34.6607	12.0606

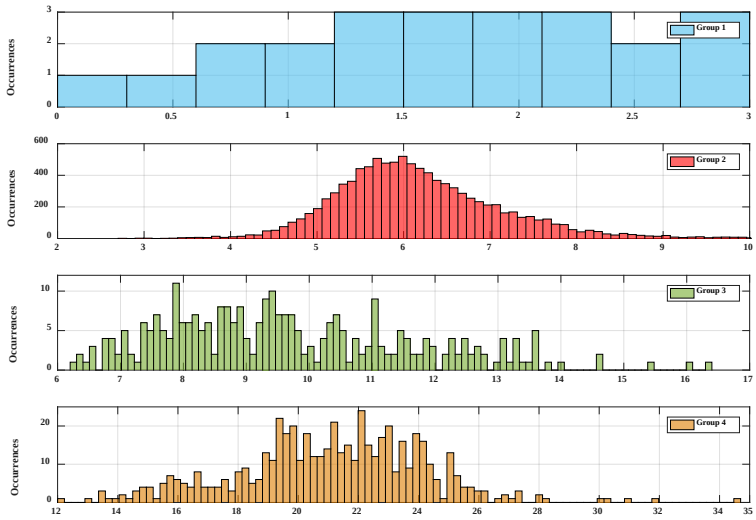

Figure 7-49 Histograms of VML by 4-G_{Sx}

Table 7-19 VML statistical measurements for 4-G_{Sx}

Group Number	Mean Length (m)	Standard Deviation	Variance	Maximum Length (m)	Minimum Length (m)
G1	1.6863	0.7899	0.6239	2.9106	0.8112
G2	6.1783	0.9720	0.9447	12.5161	2.7606
G3	9.9333	2.2571	5.0944	17.9241	6.2894
G4	21.2157	2.9961	8.9765	34.6607	12.0606

7.8.1.3 LBVC Model using Machine Learning

Intelligent classification algorithms learn to classify vehicles into predefined classes by statistically modeling the relationship between vehicle class and probabilistic distribution of features set (or predictors) extracted from VMS. Several ML classification methods (e.g., Decision Trees [DT], Support Vector Machine [SVM], *k*-Nearest Neighbor [*k*NN], and Naïve Bayes Classifier [NBC]) were evaluated investigating best practices to build a system classification model and to infer optimal length boundaries of a real-time LBVC using MAG or IDL.

VML dataset was divided into two subsets—training and testing. The first was used for training the intelligent classifier and the other for assessing its performance. Predictive accuracy of fitted models was examined using 10-fold cross-validation. This method builds *k*-different test sets from the same training set; trains all models based on the remaining training dataset; and utilizes best performing hypothesis on average to avoid over-fitting.

All classification methods attempt to maximize total classification accuracy. However, each method implements different techniques. ML methods and their techniques are not the focus of this paper; interested readers can review details in [120]. Greatly important is that RBF kernel SVM outperformed other kernel types. Since SVM is a binary classifier, a one-vs-all approach was used. This means that *m-class* models are fitted to the training data—one model for every class. When fitting the model for the *mth* class, training dataset labels are changed. Thus, the model is fitted to distinguish among two classes at once. During validation with the test dataset, *m*-individual scores are estimated—one for every model. Class with the highest score is chosen as the predicted class. For DT, a J84 version was implemented. This algorithm optimizes the

tree size using "pruning"—cease splitting if the number of objects in a branch is smaller than a predefined value. Optimal values for other parameters (e.g., *k*-value in *k*NN; size of the tree and number of leaves in DT; C and gamma in SVM) were found using hyper-parameter optimization algorithms.

Classifier performance was assisted using 10 commonly-used metrics (See Table 7-20), namely, classification rate (C_R), MAPE, RMSE, root relative squared error (*RRSE*), true positive rate (*TPR*), false positive rate (*FPR*), F-measure (*F1*), Matthews's correlation coefficient (*MCC*), area under ROC curve (*AUC*), and confusion matrix (*CM*), denoting the *True Class* as c^* and *Predicted Class* as $\hat{c}$. C_R indicates the efficacy of classifier to assign a correct vehicle class, where *N* is the number of classified vehicles and $\delta_n(\hat{c}_n)$ is a binary indicator function. *MAE* is a linear average of classification error magnitude. *RMSE* measures the distance from $\hat{c}$ to c^*. *RRSE* reports the relative amount a predicted class differs from itself. *TPR* indicates the number of vehicles correctly classified. *FPR* is an indicator of how many vehicles were classified incorrectly. *F1* measures harmonic mean of the precision or positive prediction value (*PPV*) and *FPR*. *MCC* is an important balanced measure of classification quality even if classes are imbalanced. *AUC* measures overall classifier quality. *CM* includes *True Classes* in rows and *Predicted Classes* in columns. *CM* diagonal shows the match between *true class* and *predicted class*; values outside the diagonal indicate a misclassification. *TPR*, *FPR*, *F1*, *MCC*, and *ROC* will be reported from this point as a weighted average score instead of per-class score.

Table 7-20 Performance metrics used to evaluate built classification models

Metric	Formula	
C_R	$C_R = \frac{1}{N}\sum_{n=1}^{N}\delta_n(\hat{c}_n);\quad \delta_n(\hat{c}_n) = \begin{cases}1, & \hat{c}_n = c_n^* \\ 0, & \hat{c}_n \neq c_n^*\end{cases}$	**Eq. 7-17**
MAPE	$MAE = \frac{1}{N}\sum_{n=1}^{N}\lvert\hat{c}_n - c_n^*\rvert$	**Eq. 7-18**
RMSE	$MSE = \sqrt{\frac{1}{N}\sum_{n=1}^{N}(\hat{c}_n - c_n^*)^2}$	**Eq. 7-19**
RRSE	$RSE = \sqrt{\frac{\sum_{n=1}^{N}(\hat{c}_n - c_n^*)^2}{\sum_{n=1}^{N}(\bar{c}_n - c_n^*)^2}}$	**Eq. 7-20**
TPR	$TPR = \frac{TP}{TP + FN}$	**Eq. 7-21**
FPR	$FPR = \frac{FP}{FP + TN}$	**Eq. 7-22**
F1	$F1 = 2\frac{\mathrm{PPV} \times FPR}{\mathrm{PPV} + FPR};\quad PPV = \frac{TP}{TP + FP}$	**Eq. 7-23**
MCC	$MCC = \frac{(TP \times TN) - (FP \times FN)}{\sqrt{(TP + FP)(TP \times FN)(TN + FP)(TN \times FN)}}$	**Eq. 7-24**

Table 7-21 presents performance results of all classification methods applied on the proposed LBVC schemes using the MAG dataset. Notably, all classification methods showed comparable accuracy when correctly assigning vehicle to a class. Results can be attributed to parameter optimization (i.e., hyper-parameter optimization), which was conducted for each ML classification method. DT models were adopted primarily to identify length boundaries using a generated decision tree, primarily because it is quite easy to implement and it is very memory efficient. 3G-S_A slightly outperformed 3G-S_B, as

the later had more overlap between group 1 and group 2. 3G-S_A provides a general distinction of long- and heavy-commercial vehicles from other small and medium vehicles. 3G-S_B, on the other hand, provides further distinction between PV, pickups, and SUVs in one group, and SU trucks and buses in another group. 4G-S_x provides an important distinction for motorcycles and outperforms 3G-S_B due to the fact there is no overlap between group 1 and group 2.

Table 7-21 LBVC Schemes performance results for MAG Dataset

		Classification Method & Classification Scheme											
Criteria		DT			*k*-NN			C-SVM			NBC		
		3G-S_A	3G-S_B	4G-S_x	3G-S_A	3G-S_B	4G-S_x	3G-S_A	3G-S_B	4G-S_x	3G-S_A	3G-S_B	4G-S_x
Average	C_R	99.82%	97.70%	97.69%	99.82%	97.80%	97.79%	99.83%	97.83%	97.78%	99.83%	97.59%	97.75%
	MAE	0.0022	0.0274	0.022	0.0021	0.0226	0.0171	0.0012	0.0145	0.0111	0.0025	0.022	0.0173
	RMSE	0.0342	0.1185	0.1057	0.0338	0.1082	0.0963	0.034	0.1202	0.1054	0.0323	0.117	0.0932
	RRSE	19.19%	54.07%	54.94%	18.94%	49.35%	50.08%	19.08%	54.84%	54.80%	18.12%	53.35%	48.47%
Weighted Average	TPR	0.998	0.977	0.977	0.998	0.978	0.978	0.998	0.978	0.978	0.998	0.976	0.977
	FPR	0.016	0.220	0.238	0.017	0.199	0.195	0.016	0.209	0.206	0.012	0.144	0.204
	PPV	0.998	0.973	0.974	0.998	0.975	0.975	0.998	0.975	0.974	0.998	0.975	0.974
	F1	0.998	0.973	0.971	0.998	0.975	0.975	0.998	0.975	0.974	0.998	0.975	0.974
	MCC	0.981	0.841	0.838	0.981	0.846	0.849	0.982	0.847	0.848	0.983	0.838	0.846
	AUC	0.997	0.912	0.864	0.999	0.967	0.963	0.991	0.885	0.886	0.999	0.987	0.987

Length boundaries (ɣ) found by DT models for all LBVC schemes are presented in Table 7-22 relative to corresponding FHWA Scheme F classes.

Table 7-22 Decision boundaries for proposed LBVC Schemes—unites are in meter

Group	3G-S_A		3G-S_B		4G-S_x	
	FHWA	ɣ-MAG	FHWA	ɣ-MAG	FHWA	ɣ-MAG
G1	F_1	0.7→2.984	F_1—F_3	0.7→10.971	F_1	0.7→2.984
G2	F_2—F_7	2.984→14.727	F_4—F_7	10.971→14.727	F_2—F_3	2.984→10.971
G3	F_8—F_{13}	>14.727	F_8—F_{13}	>14.727	F_4—F_7	10.971→14.727
G4	—	—	—	—	F_8—F_{13}	>14.727

One important observation from Table 7-21 is that MCC for 3G-S_B and 4G-S_x was slightly degraded in all classifiers. As stated earlier, MCC is a balance measure of statistical correlation between a true class and predicted class. A correlation coefficient of '+1' represents perfect agreement between prediction and observation; a '0' indicates

nothing but random prediction; and '−1' indicates total disagreement between prediction and observation. Declining MCC value, notwithstanding extremely high classification rate, is attributed to class imbalance in the training set, as clearly visible in the confusion matrix for each DT classifier (See Figure 7-50). CM for 3G-S_B illustrates 32.7% classification accuracy for group 2 compared to 99.75% classification accuracy for group 1 and 97.15% for group 3. The same can be seen in 4G-Sx CM. The primary problem with ML algorithms is that they maximize total classification accuracy while imbalanced class distributions increase sensitivity of ML algorithms towards overrepresented class [121].

3GS A/WMM		Predicted Class					
		C1	C2	C3	FNR	TPR	Total
Ture Class	C1	**21**	2	0	2	21	23
	C2	1	**10374**	10	11	10374	10385
	C3	0	7	**518**	7	518	525

3GS B/WMM		Predicted Class					
		C1	C2	C3	FNR	TPR	Total
Ture Class	C1	**10070**	26	0	26	10070	10096
	C2	199	**102**	11	210	102	312
	C3	0	15	**510**	15	510	525

4GS /WMM		Predicted Class						
		C1	C2	C3	C4	FNR	TPR	Total
Ture Class	C1	**21**	2	0	0	2	21	23
	C2	1	**10060**	12	0	13	10060	10073
	C3	0	220	**82**	10	230	82	312
	C4	0	0	7	**518**	7	518	525

Figure 7-50 DT Confusion Matrixes for all LVBC schemes

Imbalanced data is very common in ML. A powerful method to accommodate strongly imbalanced data is leveraging algorithms that combine boosting and data sampling, such as RUSBoost and SMOTEBoost [121]. SMOTEBoost (Synthetic Minority Oversampling Technique) works in direct contrast to RUSBoost (Random Under-sampling). However, both techniques implement multiple learners to produce a more intelligent classifier. In this study, RUSBoost was investigated. This method creates a model, examines instances misclassified, assigns more weight, under-samples the overrepresented class, and produces a revised model iteratively. After all iterations are complete, all trained models vote on which class each observation should belong to, and the predicted outputs are based on a weighted majority.

91% classification accuracy was obtained when using the RUSBoost technique with 4G-S, as opposed to 97.7% classification accuracy using DT. MCC for RUSBoost was 0.93, showing a more balanced measure compared to 0.83 with DT. A 0.9119 TPR and 0.0322 FPR were observed using RUSBoost. Figure 7-51 presents CM for RUSBoost using 4G-Sx dataset. Class 1 was correctly classified with 100% TPR. Although 91% of observations in

Class 2 where correctly classified, 30 observations were misclassified as Class 1 and 894 observations where misclassified as Class 3.

4GS/WMM RUSBoost		Predicted Class								
		C1	C2	C3	C4	FNR	TPR	Total	FNR	TPR
Ture Class	C1	**23**	0	0	0	0	**23**	23	**0%**	**100%**
	C2	30	**9149**	894	0	879	**9149**	10073	**9%**	**91%**
	C3	0	46	**248**	5	51	**165**	299	**17%**	**83%**
	C4	0	0	7	**531**	7	**531**	538	**1%**	**99%**

Figure 7-51 Confusion Matrix for RUSBoost using 4G-S/MAG dataset

Classification error for Class 3 dropped to 17% compared to 74% using DT, indicating a classification balance between groups. However, this method is computationally inefficient—requiring10 learners, each composed of a decision tree with 11 split, to implement the intelligent classifier. In such case, probabilistic modeling is proposed to achieve optimal solutions, as presented in the next section.

The fact that vehicle class distributions are imbalanced is not unique to Oklahoma, where more than 97% of vehicles belong to classes 2, 3, 5, 6, 8, and 9, as seen in our vehicle data collection (See Figure 7-52) and in another dataset collected over three months from IDL. Similar results can be found in [12], [38], [48], [54], [122]–[126], although none considers this fact and most studies reported classification rate only as an overall measure of classifier performance.

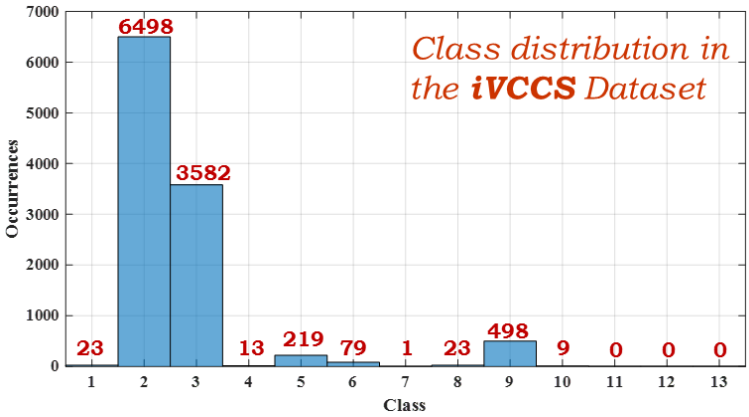

Figure 7-52 Class distribution in Dataset collected using MAG

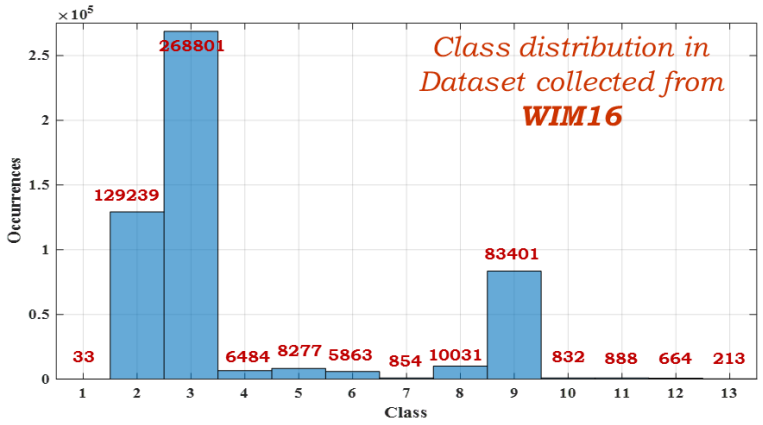

Figure 7-53 Class distribution in Dataset collected from IDL

7.8.1.4 LBVC Model using Probabilistic Modeling

Separating two neighboring classes from each other can be treated as a binary problem. As such, probabilistic models can be employed to determine optimal boundary decisions to separate neighboring classes whose vehicles have overlapping lengths. These methods can be implemented in real-time, require no training sets, and improve classification accuracy by minimizing classification errors. This section describes the implementation of probabilistic models and optimization theory.

Let x be the vehicle magnetic length, and C_1 and C_2 represent two vehicle classes. The probability of error between two distributions, as shown in Figure 7-54, include $P(C_1|C_2)$ and $P(C_2|C_1)$, given in Eq. 7-25 and representing probability of error for classifying C_2 as C_1 and C_1 as C_2.

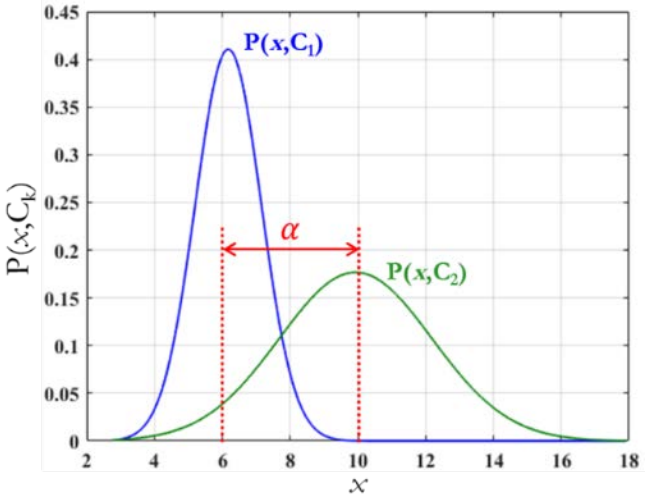

Figure 7-54 Two overlapped Gaussian distributions with an unknown decision threshold α

$$P(error) = \int_{-\infty}^{\alpha} P(x|C_2)P(C_1)dx + \int_{\alpha}^{+\infty} P(x|C_1)P(C_2)dx \qquad \textbf{Eq. 7-25}$$

Distributions $P(x, C_1)$ and $P(x, C_2)$, shown in Figure 7-54, statistically describe random variable, x, corresponding to VML for vehicles traveling on Oklahoma roadways. In accordance with central limit theorem and law of large numbers, these distributions can be approximated as Gaussian distribution models, per Eq. 7-26, Eq. 7-27, and Eq. 7-28, where k is the class number.

$$X_k \propto \mathcal{N}\left(\mu_{C_k}, \sigma_{C_k}\right) \rightarrow \; p\left(x|\mu_{C_k}, \sigma_{C_k}\right) = \frac{1}{\sigma_{C_k}\sqrt{2\pi}} e^{-\frac{\left(x-\mu_{C_k}\right)^2}{2\sigma_{C_k}^2}} \qquad \textbf{Eq. 7-26}$$

$$\mu_{C_k} = \frac{1}{n}\sum_{i=1}^{n} x_i \;\; , \;\; \sigma_{C_k} = \sqrt{\frac{1}{n}\sum_{i=1}^{n}\left(x_i - \mu_{C_k}\right)^2} \qquad \textbf{Eq. 7-27}$$

$$P(error) = P(C_1)\int_{-\infty}^{\alpha_T} \frac{1}{\sigma_{C2}\sqrt{2\pi}} e^{-\frac{(x-\mu_{C2})^2}{2\sigma_{C2}^2}}.dx + P(C_2)\int_{\alpha_T}^{+\infty} \frac{1}{\sigma_{C1}\sqrt{2\pi}} e^{-\frac{(x-\mu_{C1})^2}{2\sigma_{C1}^2}}.dx \qquad \textbf{Eq. 7-28}$$

The integration of a probability distribution function (PDF) is a cumulative distribution function (CDF) represented by the error function *erf*, as given in Eq. 7-29.

$$P(error) = P(C_1)\frac{1}{2}\left[1 + erf\left\{\frac{\alpha_T - \mu_{C2}}{\sigma_{C2}\sqrt{2}}\right\}\right] + P(C_2)\left(1 - \left(\frac{1}{2}\left[1 + erf\left\{\frac{\alpha_T - \mu_{C1}}{\sigma_{C1}\sqrt{2}}\right\}\right]\right)\right) \quad \textbf{Eq. 7-29}$$

Optimal threshold α_T can be found by taking the derivative of Eq. 7-29 and equating the outcome to 0, as presented in Eq. 7-30.

To ensure classification error will not change at various times when new values are added to either group—as not all groups have the same number of vehicle instances per unit of time—weights, $P(C_1)$ and $P(C_2)$, that are proportional to number of instances in each class group are calculated, as in Eq. 7-31. It is worth mentioning that optimal threshold found by solving Eq. 7-30 is global minima, which can be verified using the second derivative test, as in Eq. 7-32, such that $\alpha_T > 0$.

$$\frac{dP(error)}{d\alpha_T} = 0 \rightarrow \frac{P(C_1)}{\sigma_{C2}\sqrt{2\pi}} e^{-\frac{(\alpha_T - \mu_{C2})^2}{2\sigma_{C2}^2}} - \frac{P(C_2)}{\sigma_{C1}\sqrt{2\pi}} e^{-\frac{(\alpha_T - \mu_{C1})^2}{2\sigma_{C1}^2}} = 0 \quad \textbf{Eq. 7-30}$$

$$P(C_1) = \frac{Length(C_1)}{Length(C_1 + C_2)} \quad ; \quad P(C_2) = \frac{Length(C_2)}{Length(C_1 + C_2)} \quad \textbf{Eq. 7-31}$$

$$\frac{d2P(error)}{d\alpha_T^2} = 0$$

$$\rightarrow P(C_1)\frac{(\mu_{C2} - \alpha_T)}{\sigma_{C2}^3\sqrt{2\pi}} e^{-\frac{(\alpha_T - \mu_{C2})^2}{2\sigma_{C2}^2}} \quad \textbf{Eq. 7-32}$$

$$- P(C_2)\frac{(\mu_{C1} - \alpha_T)}{\sigma_{C1}^3\sqrt{2\pi}} e^{-\frac{(\alpha_T - \mu_{C1})^2}{2\sigma_{C1}^2}} = 0$$

The α_E uses equal weights ($P(C_1) = P(C_2)$) but implements a classification error minimization algorithm among groups. In other words, α_E is found by solving Eq. 7-33 such that probability of error for C_1 classified as C_2 is equal to probability of error for C_2 classified as C_1; ε is a precision value (e.g., 0.001). Equating classification errors would result in a decreased classification error for one particular group (i.e., the one with fewer

instances), but will increase classification error for the second group (i.e., the one with more instances), and hence, increase overall system classification error.

$$P(\alpha_E, C_1) - P(\alpha_E, C_2) \leq \varepsilon \qquad \textbf{Eq. 7-33}$$

Developed models can now be applied on all overlapping problematic LBVC schemes (e.g., 4G-S_x and 3G-S_B) that have imbalanced data, as well as high overlap ratio among neighbored groups.

1) Decision Boundaries for 3G-S_B:

Figure 7-55 shows the fitted Gaussian distribution models and found decision thresholds for MAG 3G-S_B dataset. Misclassification occur between problematic groups G1 and G2, as high overlapping is observed.

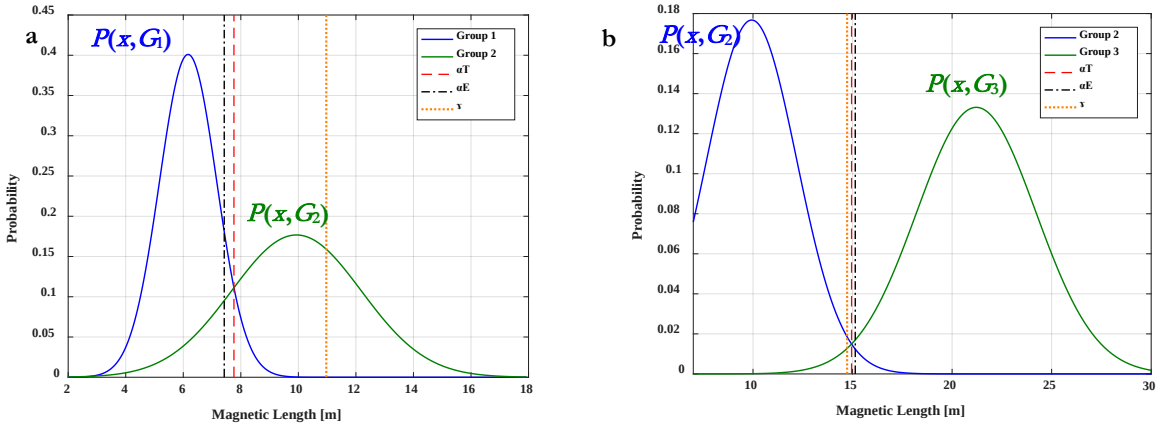

Figure 7-55 Gaussian distribution models and decision thresholds for MAG *3G-S_B*

Table 7-23 presents a comparison between decision boundaries found by various proposed thresholding methods for *3G-S_B* dataset. Corresponding classification rates in each group (i.e., how many where correctly classified as G_X out of the total number of instances in G_X) and classification errors between groups (i.e., how many where incorrectly classified out of the total number of instances in both groups) for pairwise overlapped groups are shown in Table 7-24. Table 7-25 presents a comparison between classification rates for different thresholding schemes applied onto the 3G-S_B dataset.

Decision threshold, γ, found using ML methods, was 10.97m, which maximizes total classification accuracy at the expense of misclassifying more instances in G2. Optimal threshold for achieving balance among groups—regardless of instances in each group,

α_T—was set at 7.76m, which significantly reduces G2 misclassification error at the expense of decreasing accurate classification rate for G1. See Table 11 ($C_{R\text{-}G1\text{-}vs\text{-}G2}$). Because the number of instances in G_1 is considerably larger than G_2—see Figure 7-44, overall classification accuracy was decreased—see Table 7-25. Optimal threshold for equal error among overlapping groups' scenario, α_E, was 7.43m, which rendered an equal classification rate $C_{R\text{-}G1\text{-}vs\text{-}G2}$ at the expense of reducing overall classification accuracy to 90.2314%, compared to 99.70% and 93.8077% for γ and α_T, respectively. For classification rates between G2 and G3 ($C_{R\text{-}G2\text{-}vs\text{-}G3}$), all scenarios achieved comparable performance primarily because a minimum overlapping can be observed.

Table 7-23 Decision boundaries found by thresholding methods for 3G-S_B

		3G-S_B MAG		
Group	**FHWA-S_F**	**ɣ**	**α_T**	**α_E**
G1	F_1—F_3	0.81→10.971m	0.81→7.761m	0.81→7.4286m
G2	F_4—F_7	10.971→14.727m	7.761→14.9504m	7.427→15.136m
G3	F_8—F_{13}	>14.727m	>14.9504m	>15.136m

Table 7-24 Pairwise classification rates and errors for different decision boundaries applied on 3G-S_B dataset

	3G-S_B MAG	
Threshold	**$C_{R\text{-}G1\text{-}vs\text{-}G2}$ /C_{Err}** (%)	**$C_{R\text{-}G2\text{-}vs\text{-}G3}$ /C_{Err}** (%)
ɣ	99.9109 vs. 29.8077 / 2.1906	96.7949 vs. 98.6667 / 2.0311
α_T	93.9778 vs. 83.9744 / 6.3221	97.1154 vs. 98.0952 / 2.2700
α_E	89.9366 vs. 90.0641 / 10.059	97.4359 vs. 97.5238 / 2.5090

Table 7-25 Comparison between classification rates by different thresholding methods for 3G-S_B LBVC

		3G-S_B MAG		
Group	**FHWA-S_F**	**ɣ**	**α_T**	**α_E**
G1	F_1—F_3	99.70%	93.9778%	89.9366%
G2	F_4—F_7	32.70%	81.0897%	87.5000%
G3	F_8—F_{13}	97.10%	98.0952%	97.5238%

	3G-S_B MAG		
Overall C_R	**97.70%**	**93.8077%**	**90.2314%**

2) Decision Boundaries for 4G-Sx:

Figure 7-56 illustrates fitted Gaussian distribution models and decision thresholds for MAG 4G-S_x dataset.

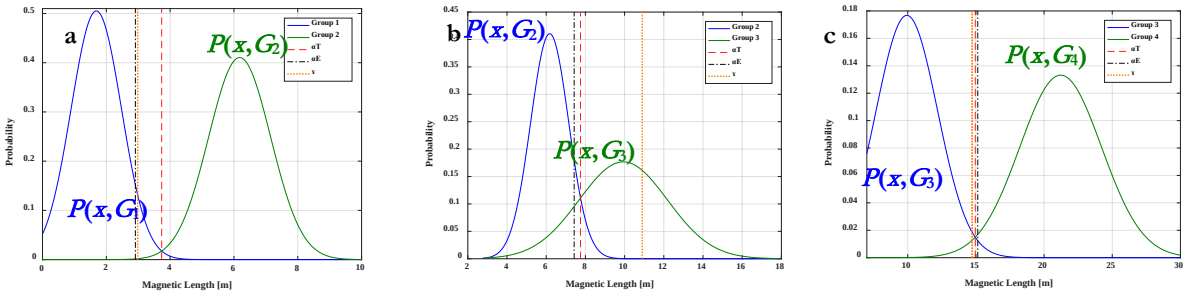

Figure 7-56 Gaussian distribution models and decision thresholds for the MAG *4G-S_x* dataset

Problematic groups in *4G-S_x* are G2 and G3, which have more significant overlap in MAG dataset when compared to IDL dataset, as seen in Figure 7-56b. Table 7-26 presents a comparison between decision boundaries determined by various proposed thresholding methods for MAG and IDL *4G-S_x* datasets.

Table 7-27 presents the corresponding classification rates and errors for pairwise overlapping groups. A comparison between classification rates for various thresholding methods applied on the 4G-S_x dataset is presented in Table 7-28.

Table 7-26 Decision boundaries found by different thresholding methods for 4G-S_x

		4G-S_x MAG		
Group	**FHWA-S_F**	**ϑ**	**α_T**	**α_E**
G1	F_1	0.7→2.984m	0.7→3.736m	0.7→2.9107m
G2	F_2—F_3	2.984→10.971m	3.736→7.7516m	2.912→7.427m
G3	F_4—F_7	10.971→14.727m	7.7516→14.95m	7.427→15.136m
G4	F_8—F_{13}	>14.727m	>14.95m	>15.136m

Table 7-27 Pairwise classification rates and errors for different decision boundaries applied on 4G-S_x

	4G-S_x MAG		
Threshold	**$C_{R\text{-}G1\text{-}vs\text{-}G2}$ /C_{Err} (%)**	**$C_{R\text{-}G2\text{-}vs\text{-}G3}$ /C_{Err} (%)**	**$C_{R\text{-}G3\text{-}vs\text{-}G4}$ /C_{Err} (%)**
γ	100 vs. 99.98 / 0.0198	99.91 vs. 29.81 / 2.196	96.79 vs. 98.67 / 2.031
α_T	100 vs. 99.69 / 0.307	93.86 vs. 84.29 / 6.423	97.115 vs. 98.09 / 2.27
α_E	100 vs. 99.99 / 0.0099	89.90 vs. 90.06 / 10.09	97.44 vs. 97.52 / 2.509

Table 7-28 Comparison between classification rates by different thresholding methods for 4G-S_x

		4G-S_x MAG		
Group	**FHWA-S_F**	γ	α_T	α_E
G1	F_1	91.30%	100%	100%
G2	F_2—F_3	99.90%	93.557%	89.8938%
G3	F_4—F_7	26.30%	81.4103%	87.5%
G4	F_8—F_{13}	98.70%	98.0952%	97.5238%
Overall C_R		**97.6951%**	**93.4419%**	**90.2131%**

For G1 and G2, an insignificant overlapping rendered comparable high rates for all thresholding methods. However, G2 and G3 demonstrated a significant overlap, as G3 included SU (e.g., Class 5), which are highly overlapped in length with Class 3 included in G2. ML methods set γ at a value that maximizes total classification accuracy at the expense of misclassifying most instances in the other group (G3 classification error 73.7%) because the number of instances in G_2 is considerably larger than G_3. Classification error for G3 was significantly reduced to 18.5897% when using α_T. However, overall classification accuracy was decreased. Classification rate for G3 improved when using α_E to achieve balanced classification rates among all groups (See

Table 7-27) at the expense of reducing overall classification accuracy to 90.2131% when compared with 97.6951% and 93.4419% for γ and α_T, respectively. All scenarios achieved comparable classification performance for G3 and G4, as a minimum overlapping can be observed. Also, number of data points in both groups is relatively comparable.

7.8.1.5 Discussion on LBVC Models

A comparison between LBVC scheme boundaries developed for MAG for this study and alternative schemes based on IDL data developed by various states throughout the U.S. can be seen in Figure 7-57 and Figure 7-58. Observations include the following:

- Vehicle length boundaries detected in a number of states throughout the U.S. vary because vehicle and traffic characteristics differ per road type, region, state, and other factors; hence, LBVC boundaries developed in one state might require adjustment to remain applicable in another.
- Boundaries defined for MAG detectors are longer in length than those detected by IDL detectors; this is primarily due to the fact that MAG estimate VML, which is longer than the physical length.
- Defining an accurate detection zone for MAG is challenging, as disturbance to the earth's magnetic field depends upon detection; this is proportional to vehicle length, height of vehicle chasse above ground, and vehicle structure composition of ferrous materials.
- A higher overlap ratio among LBVC scheme groups was observed in MAG dataset when compared to IDL dataset; this is attributed to variations in magnetic length for vehicles from the same class.
- Analyses demonstrated the importance of investigating not only the classification rate for evaluating classification models, but also other performance metrics (e.g., CM and MCC) for identifying bias in the model as a result of imbalanced class distributions; this increases sensitivity of ML algorithms toward overrepresented classes.
- Three algorithms developed for identifying optimal length boundaries for LBVC schemes resulted in three very different sets of thresholds (γ, α_T, and α_E): 1) γ maximizes classification accuracy at the expense of minority classes; 2) α_T achieves balance among overlapped groups regardless of number of instances in each group; and 3) α_E tries to equate classification error between two overlapped groups despite group population size. The question remains as to which algorithm is suitable. The answer depends exclusively on the objective of the LBVC system. If traffic engineers are more concerned with vehicles in higher

classes (i.e., trucks that are generally highly underrepresented), then it is important to utilize a method that achieves balance among classes (i.e., α_T). However, if classification accuracy is paramount regardless of classification rate per group, then γ method would be suitable. For balanced classification error among groups, α_E should be implemented.

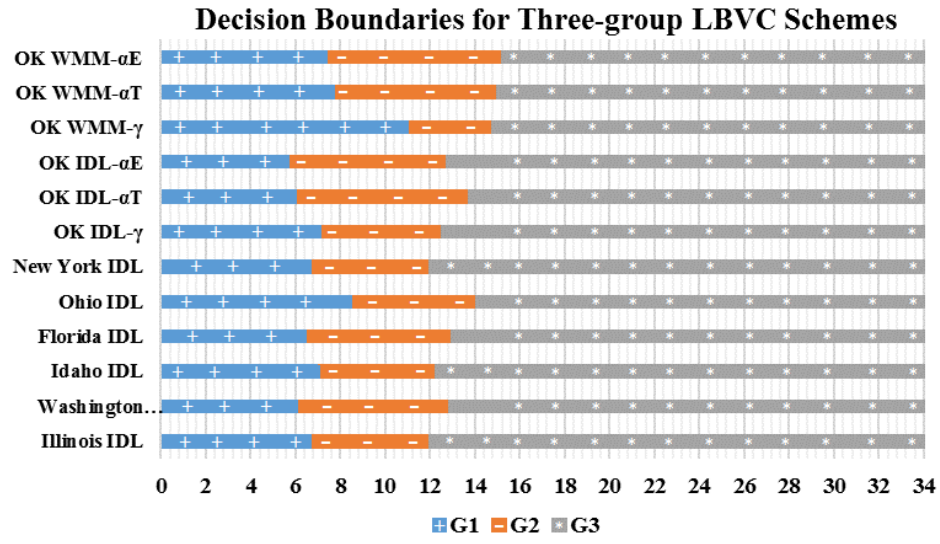

Figure 7-57 Decision boundaries for *3G-S_B* LBVC for several states

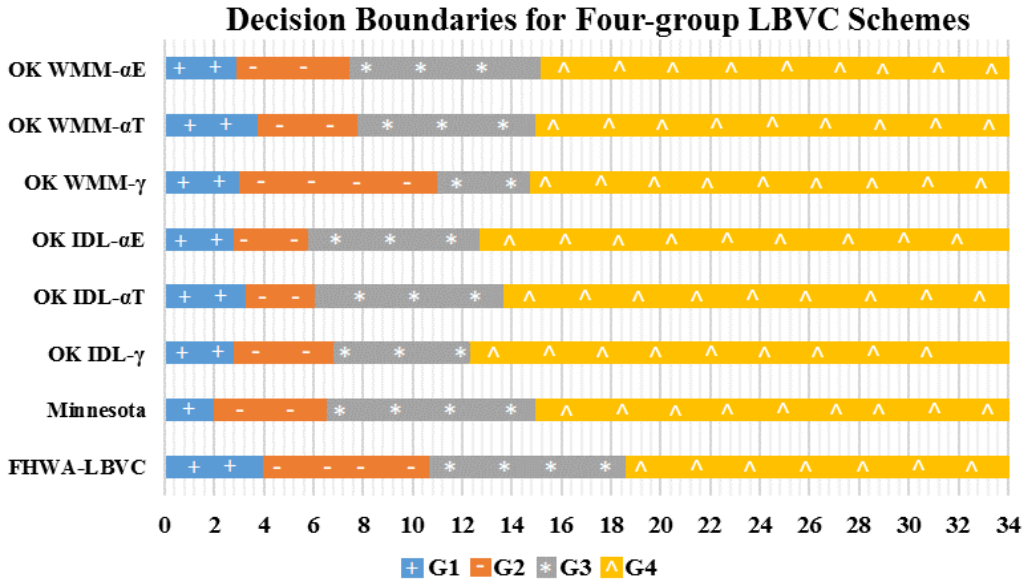

Figure 7-58 Decision boundaries for *4G-S_x* LBVC for several states

7.8.2 Magnetic Signature-based Vehicle Classification

7.8.2.1 *Vehicles Magnetic Signature Dataset*

Dataset size plays a vital role in developing an accurate vehicle classification model. Most earlier studies on vehicle classification [12], [38], [47], [48], [50], [54], [122]–[130] relied on small training sets consisting of only a few hundred vehicles—the majority of which were passenger cars—to train an intelligent classifier. Doing so profoundly limits the accuracy of any classification algorithm. Moreover, such a practice limits the number of distinguishable classes.

Several iVCCS nodes were used to collect VMS on both freeway and urban roads. Different sampling rates were tested, ranging from 200~800Hz, to identify optimal sampling rate necessary to achieve accurate classification while maintaining low power consumption. Collected signatures are used at a later time to extract distinguishable features that can be used to identify vehicle class. Video cameras were employed as a ground truth to evaluate system performance. Video images were analyzed manually and utilized to assign a class label for each signature in the training set collected via iVCCS. Images were also used to evaluate classification method performance on the testing set.

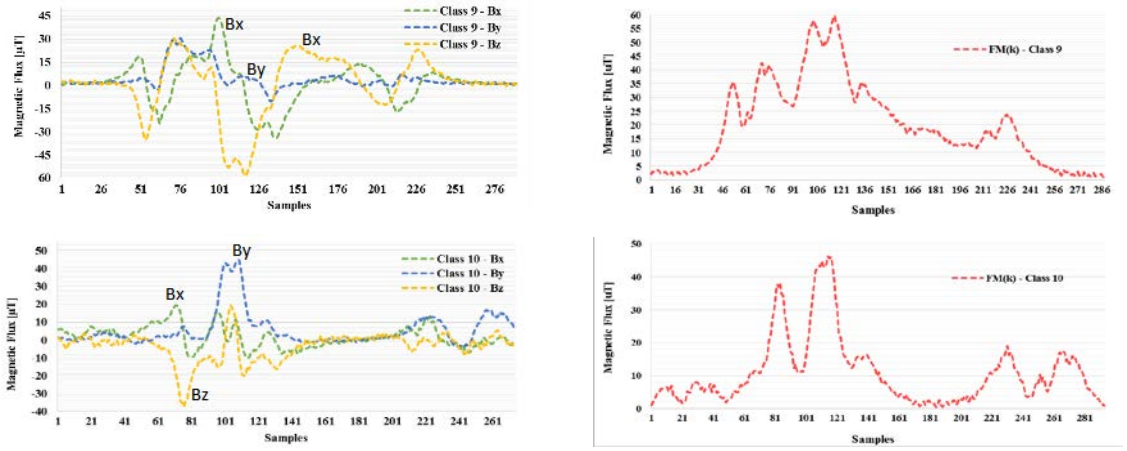

Figure 7-59 Vehicles signatures, *i*VCCS on roadway – $B^{(Y)}$ (left) and F_M (right)

Figure 7-59 to Figure 7-61 illustrate geomagnetic field components (B_X, B_Y, and B_Z) and corresponding flux magnitude (F_M) for vehicles of various classes that were collected by *i*VCCS for various speeds in roadway setup.

Figure 7-62 illustrates VMS prior to MAF with a gain coefficient provided in Eq. 4-8,for a vehicle detected by three *i*VCCS nodes deployed roadside at a distance of 30cm, 60cm, and 100cm from vehicle side. Unlike roadway setup, which produces a

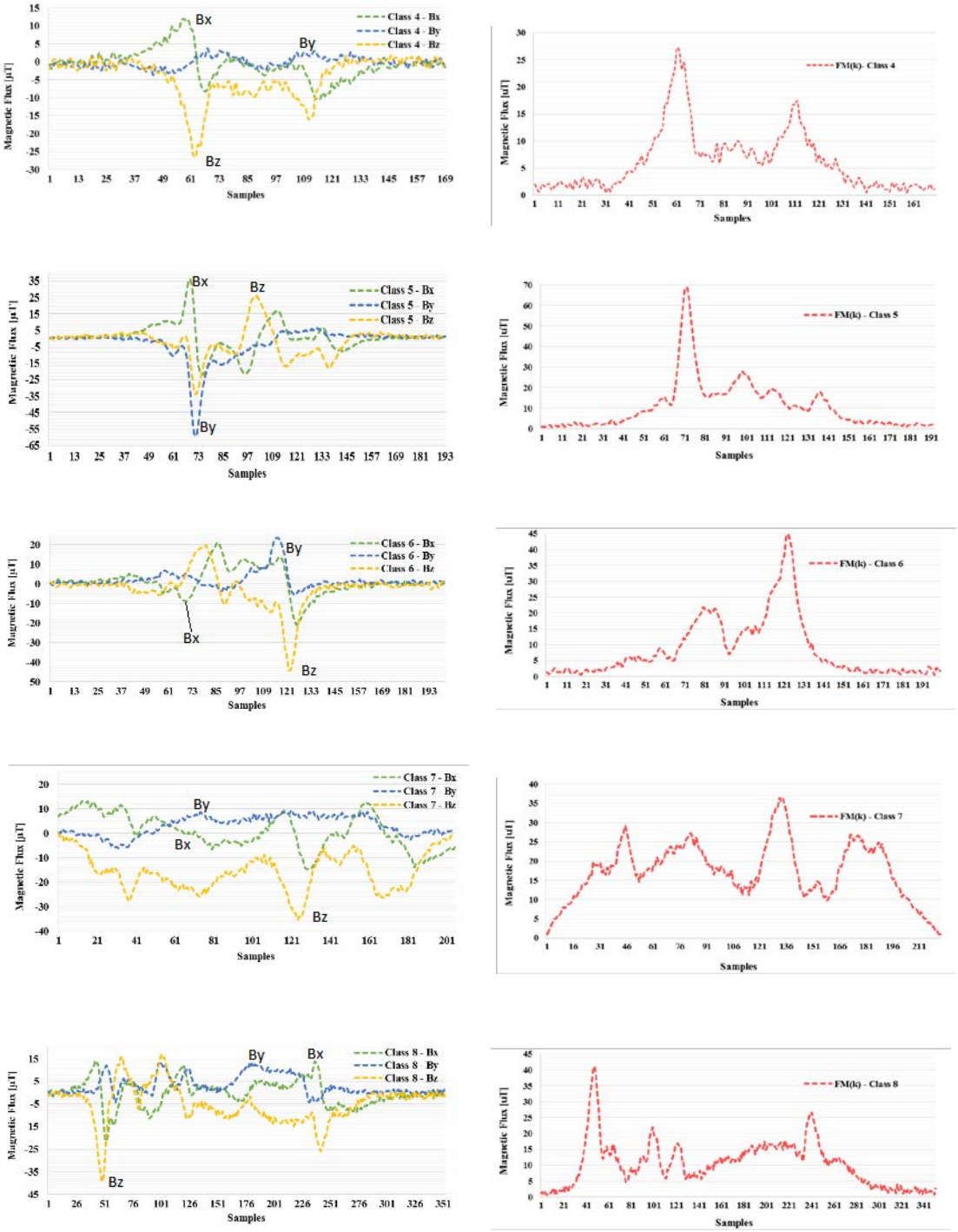

Figure 7-60 (Continued) Vehicles signatures, *i*VCCS on roadway – $B^{(\gamma)}$ (left) and F_M (right)

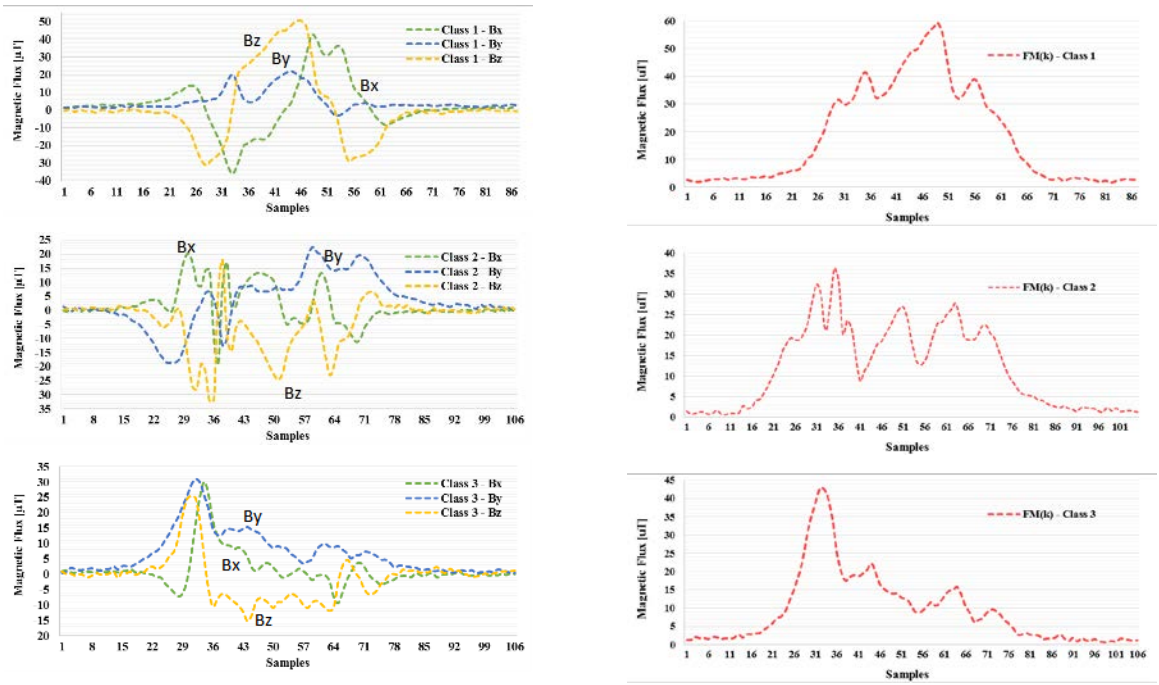

Figure 7-61 (Continued) Vehicles signatures, *i*VCCS on roadway – $B^{(\gamma)}$ (left) and F_M (right)

highly correlated signature for the same vehicle over multiple sensors, VMS characteristics in roadside setup is subject to the distance between detection point and vehicle. Moreover, vehicle trajectory can significantly influence VMS characteristics. Roadside setup using MAG for vehicle classification or re-identification based solely on identifying unique features in VMS is very challenging. Therefore, the dataset used will include only VMS sampled using roadways sensors.

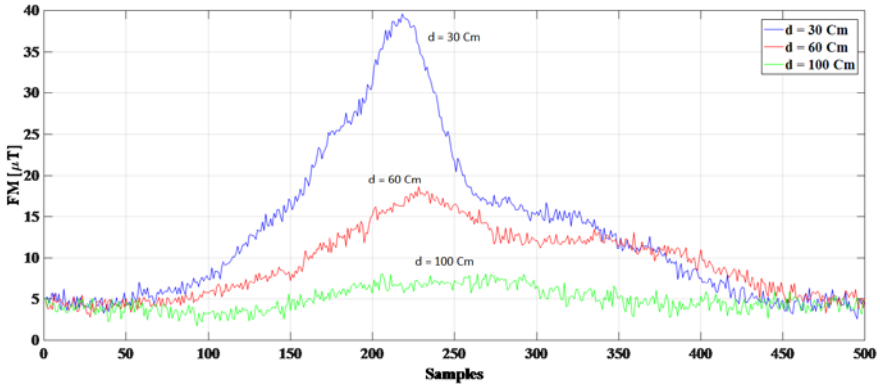

Figure 7-62 VMS for same Vehicle at different *d* using *i*VCCS on roadside

7.8.2.2 *Data Preprocessing*

Data preprocessing is an important stage for distinguishing features collected from raw data that can be extracted in the next step. Preprocessing includes 1) data cleaning for removing outliers, 2) data imputation for filling gaps, 3) vehicle signature extraction for separating vehicles signatures (in detection zone) and removing useless raw data (no detection), 4) filtering and smoothing for eliminating transient state effect and reducing fluctuations, 5) data alignment and labeling for aligning and labeling training data by means of ground truth data (i.e., video), 6) computations for magnitude (Eq. 4-5), speed (Eq. 4-12), occupancy time (Eq. 4-16), length (Eq. 4-27), headway, gap (Eq. 7-12), and finally, 7) normalization for obtaining an equal length and normalized amplitude for all VMS vectors.

As for data cleaning, assume a vehicle traveling at maximum speed limit of 85mph has minimal length l_V =1.8m (e.g., motorcycle). Using Eq. 7-1, we can calculate minimum sample number S_{VSL}= 34 samples (i.e., worst case scenario), given maximum sampling rate f_s = 400Hz. Accordingly, given that a signature is shorter than 30 data points, the vehicle will be not considered in the training or testing data sets.

Data imputation can be achieved by either finding a statistical average of surrounding values to fill any missing record or importing missing records from other aligned sensor nodes. Although several *i*VCCS nodes were installed on each lane during deployment, data from only two nodes were used in this study.

Since all sensor nodes were synchronized and both detection and speed estimation algorithms were implemented during data collection, vehicle magnetic signature S_V was simply extracted by means of arrival and departure times, as presented in Eq. 7-34, where k is number of samples; and B^γ is the geomagnetic flux magnitude sampled using MAG in three axles—*x*, *y*, and *z*.

$$S_{V_n}^{(B^\gamma)} : \left\{ k_{T_A^{(N_i)}}, \dots, k_{T_D^{(N_i)}} \right\} \; ; \; \gamma = \{x, y, z\} \in \mathbb{R}^3 \qquad \textbf{Eq. 7-34}$$

The MAG was configured to run at 400Hz sampling rate, resulting in a significant fluctuation in VMS. To achieve a more consistent signal among all nodes aligned in-lane, applying a low-pass filter on the signal, as in Eq. 7-35, is recommended to eliminate transient state effect and to reduce fluctuations. *M* is the total number of samples in a VMS.

$$S_{V_N Filtered}^{(B^\gamma)} = \frac{1}{M}\sum_{i=0}^{M-1} S_{V_N}^{(B^\gamma)}(k-i)\,; \quad \gamma = \{X, Y, Z\} \in \mathbb{R}^3 \qquad \textbf{Eq. 7-35}$$

Data alignment and labeling is necessary to train an intelligent classifier when using a supervised machine learning method. Ground-truth data (i.e., video) was used to assign class labels to the vehicle class dataset collected using MAG. Erroneous, double-detection records determined via ground truth comparison are removed from the dataset. Having to do so is rare, as *i*VCCS has demonstrated outstanding performance and precision in terms of vehicle detection and speed estimation [72]–[74].

After data was aligned and labeled, SMOTE (Synthetic Minority Oversampling Technique) [131] was employed to balance the dataset [132]. As discussed earlier in Section 7.8.1.3, imbalanced class distributions increase sensitivity of ML algorithms towards overrepresented class [121]. More than 85% of vehicles in the processed dataset belong to Class 2 and Class 3, as illustrated in Figure 7-52. Similar results can be found in [12], [38], [48], [54], [122]–[126], although none of these experiments considered this phenomenon. Most studies reported classification rate as an overall measure of classifier performance.

7.8.2.3 Normalization and Transformation

Data was collected from vehicles of various classes. Lengths ranged between 1.8-30 meter, and vehicles were traveling at various speeds, ranging between 10-90mph. Thus, extracted vehicle signature vectors (See Eq. 7-34) have varying sample number. Notably, some statistical features require signature length and/or magnitude normalization.

If vehicle speed is known and accurate, length normalization can be achieved as a time-domain multiplication of signal length by speed and sampling time T_S, as in Eq. 7-36.

$$\tilde{x}_n = v.T_s.x_n \qquad \textbf{Eq. 7-36}$$

Given VMS length normalization such that all signals have the same number of samples, interpolation and decimation processes can be applied to resample vehicle signatures at predefined signal length. Unfortunately, these processes are computationally expensive for large datasets.

Signal Interpolation is an upsampling and filtering technique applied to discrete-time signal and aimed at increasing the number of samples by factor *L* through inserting *L-1* zeros in between samples, multiplying amplitude by *L*, and smoothing interpolated signal. Interpolation is depicted in Figure 7-63 and presented in Eq. 7-37.

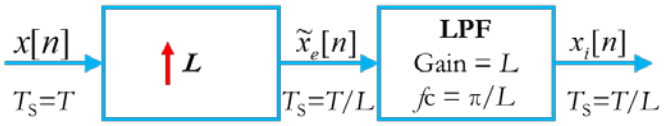

Figure 7-63 Representation of upsampling system by an integer factor *L*

$$x_i[n] = \begin{cases} x[n/L] = x\left(\frac{nT}{L}\right), & n = \{0, \pm L, \pm 2L, \dots\} \\ 0, & otherwise \end{cases} \qquad \textbf{Eq. 7-37}$$

Signal Decimation is a complementary process for interpolation achieved by filtering and downsampling a discrete-time signal. The goal is decreasing the number of samples by factor M through resampling the signal each Mth sample and discarding the remaining samples. LPF is a low pass filter used to eliminate aliasing. The decimation process is depicted in Figure 7-64 and represented using Eq. 7-38.

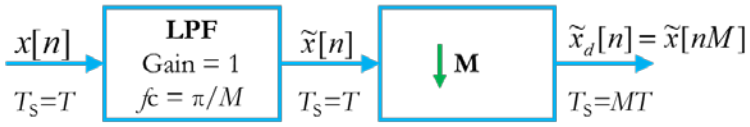

Figure 7-64 Representation of downsampling system by integer factor *M*

$$\tilde{x}_d[n] = x[nM] = x_c(nMT) \qquad \textbf{Eq. 7-38}$$

As stated earlier, the number of samples in a vehicle signature is speed- and length-dependent, ranging between S_{VSL}= 34 ~ 1000 samples at f_s = 400Hz (See Eq. 7-34). If all vehicle signatures must be normalized such that S_{VSL}= 200 samples, a resampling at non-integer factor is needed. Changing sampling rate by a non-integer factor is possible by combining both decimation and interpolation processes, such that the interpolator increases its sampling rate by a factor *L*. This is followed by a linear time-invariant LPF for eliminating signal images and a decimator in the final stage, which increases sampling rate by a factor *M*. Generated signal will have an effective sampling period of T_S = *TM/L*, where both factors *L* and *M* are integers.

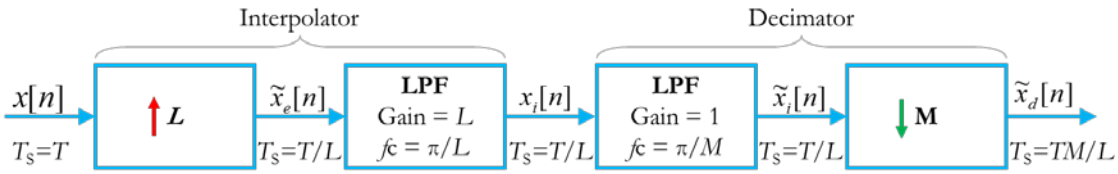

Figure 7-65 Representation of combined upsampling and downsampling systems

L and *M* factors should be chosen appropriately. A reduction in T_S happens when *M* > *L* and the opposite is true. In this work, the value of *M* was chosen experimentally, and *L* was calculated by Eq. 7-39, where T_{Occ} is sensor's occupancy time, $Length(\tilde{S}_{V_N}^{(B^Y)})$ is the normalized length of vehicle signatures.

$$L = M \times \frac{Length(\tilde{S}_{V_N}^{(B^Y)})}{Length(S_{V_N}^{(B^Y)})} = M \times \frac{f_s . \tilde{T}_{Occ}}{f_s . T_{Occ}} \qquad \textbf{Eq. 7-39}$$

To find the best normalized length, $T_{Occ}$for vehicle signature datasets collected on highway and urban roads were analyzed. Dataset included 11399 (highway) and 15853 (urban) VMS of various classes, sampled at f_s = 400Hz. The T_{Occ} histogram for both datasets is shown in Figure 7-66. $\mu T_{Occ}^{(urban)} = 0.3989\ sec$, which is equal to $0.3989 \times 400 \approx 160$ samples. $\mu T_{Occ}^{(highway)} = 0.3217\ sec$, which is equal to $0.3217 \times 400 \approx 128$ samples. Based on this analysis, $Length(\tilde{S}_{V_N}^{(B^Y)}) = 120$ samples were chosen for data normalization. Assuming $Length(S_{V_N}^{(B^Y)})$ ranges 40–1000 samples and *M*=50, *L* will range between 150–6, according to Eq. 7-39. Sampling rate conversion ratio *D* can be calculated using Eq. 7-40.

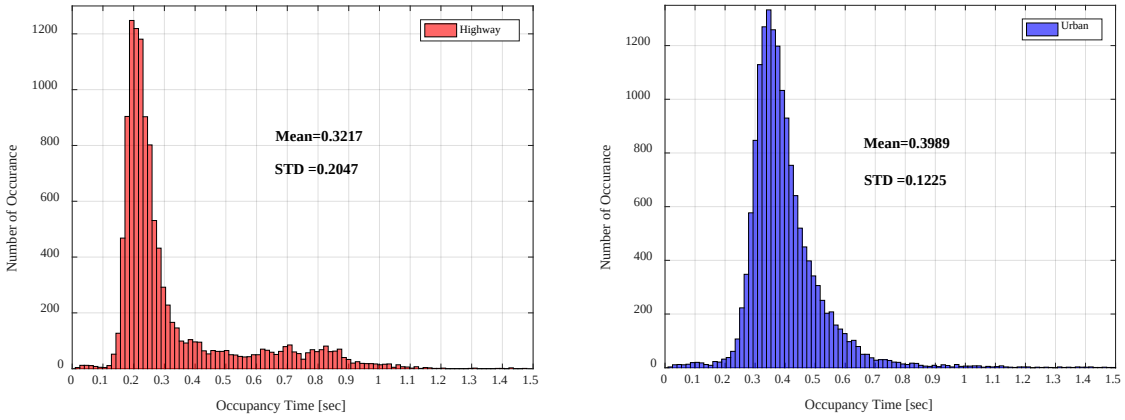

Figure 7-66 Histogram of occupancy time T_{Occ}, highway (left) and urban (right)

$$D = \frac{L}{M} = \frac{Length^{(new)}}{Length^{(original)}} \qquad \textbf{Eq. 7-40}$$

Unlike VMS produced by IDL, vehicle signatures sampled using MAG have less consistent peak magnitude due to several factors (e.g., differences in sensitivity, vehicle trajectory, and non-symmetry of detection zone). Hence, signature magnitude normalization is necessary before VMS analysis.

Figure 7-67 and Figure 7-68 illustrate an extracted signature (See Eq. 7-34) for Class 3 vehicles. The figures illustrate raw signature before and after filtering and normalization. Filtering is achieved using MAF with 5-tap (See Eq. 7-35).

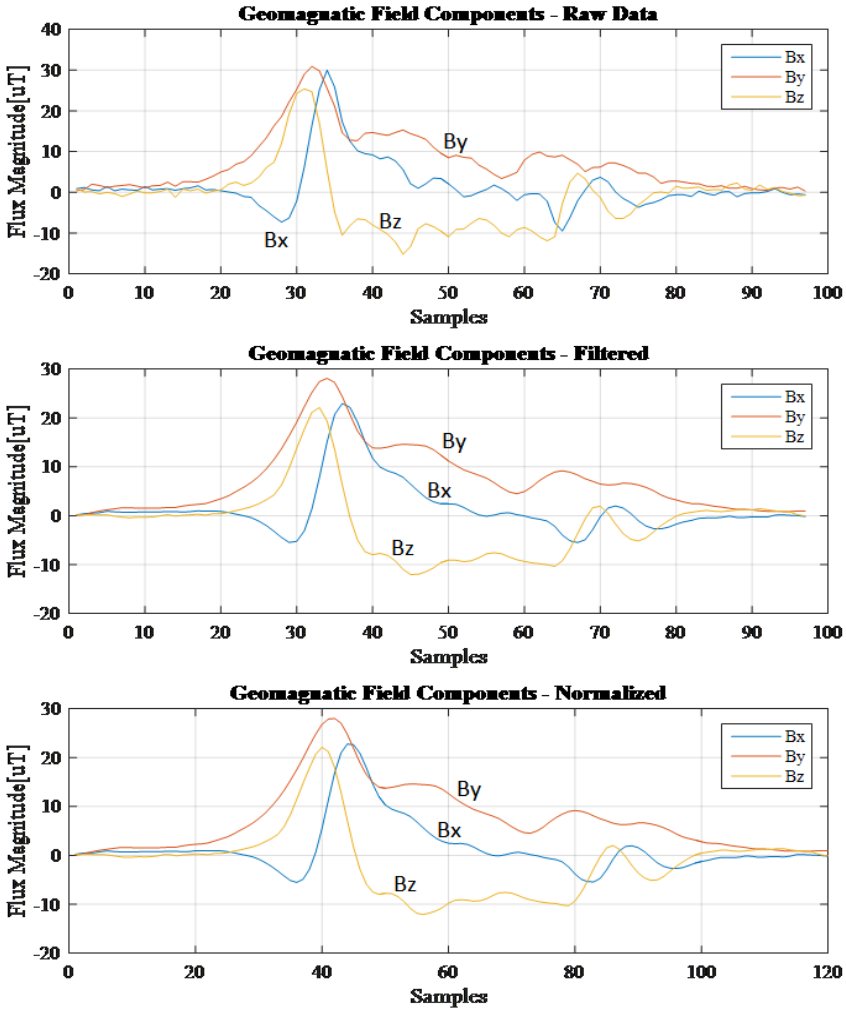

Figure 7-67 Class 3 vehicle signature before and after normalization

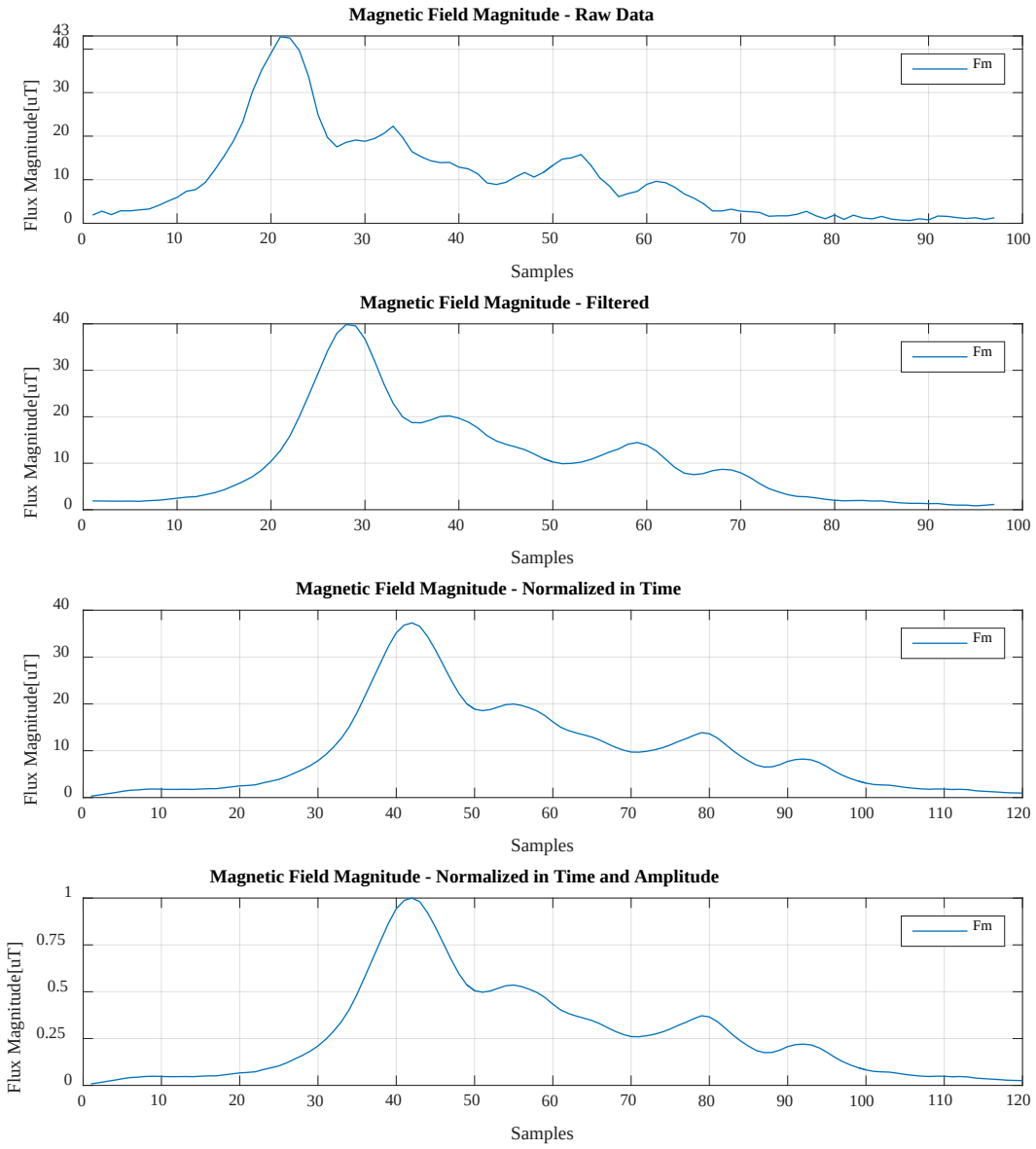

Figure 7-68 Class 3 vehicle magnitude before and after normalization

7.8.2.4 Feature Extraction

Intelligent classification algorithms learn to classify vehicles by statistically modeling the relationship between a vehicle's class and the probabilistic distributions of features extracted from the vehicle's magnetic signature. To accomplish high classification accuracy, features should be selected such that they are significantly different for various vehicle classes. Hence, chosen features will play a critical role in classifier performance. Sixty features were extracted from the VMS dataset. Features are listed in Table 7-29; additional features are depicted in Figure 7-69.

Table 7-29 Extracted features

F_{ID}	Extracted Feature
F_1	Magnetic Length
F_2	RMS of F_M
$F_{3,4,5}$	RMS of B^γ
F_6	Mean of F_M
$F_{7,8,9}$	Mean of B^γ
F_{10}	Variance of F_M
$F_{11,12,13}$	Variance of B^γ
F_{14}	STD of F_M
$F_{15,16,17}$	STD of B^γ
F_{18}	Median of F_M
$F_{19,20,21}$	Median of B^γ
F_{22}	Skewness of F_M
$F_{23,24,25}$	Skewness of B^γ
F_{26}	Kurtosis of F_M
$F_{27,28,29}$	Kurtosis of B^γ
F_{30}	F_M Shape Symmetry Ratio
F_{31}	F_M Shape Symmetry Degree
F_{32}	Peak of F_M
$F_{33,34,35}$	Peak of B^γ
F_{36}	Number of peaks of F_M
F_{37}	Number of valleys of F_M
$F_{38,39,40}$	Ratio of +/- B^γ RMS
F_{41}	Maximum Magnitude Value (F_{Mp})
$F_{42—60}$	Time derivative of F_M and B^γ

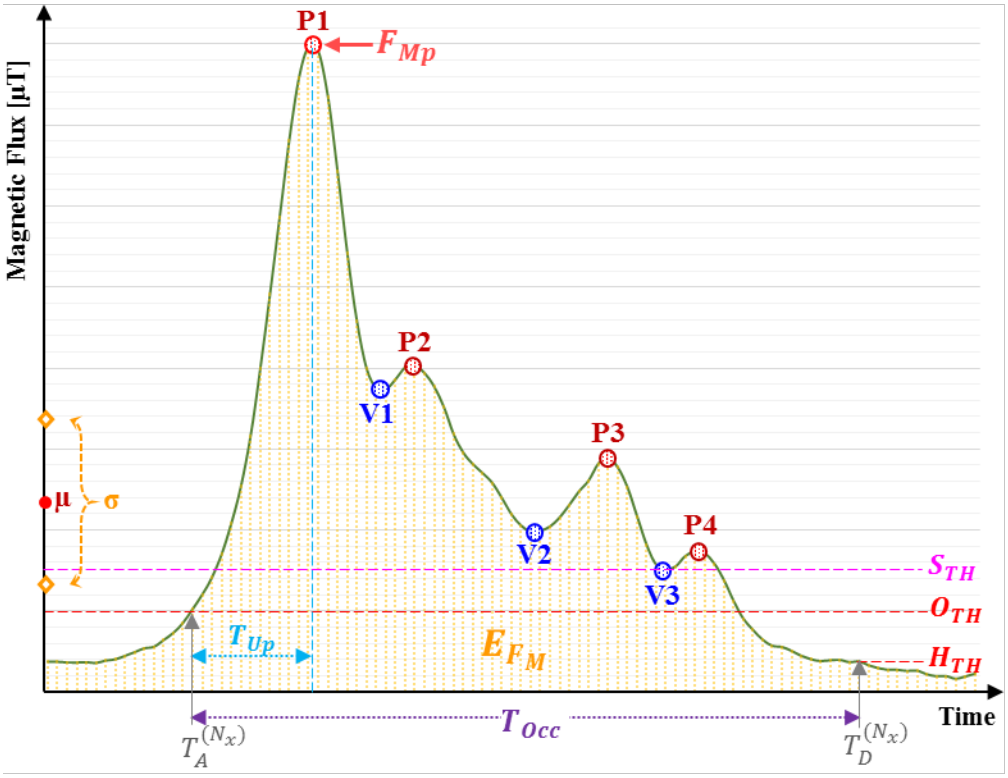

Figure 7-69 Features extraction of a vehicle magnetic signature magnitude

A. Length of Vehicle Magnetic Signature

Various vehicle classifications have different lengths with some overlap among them. In this work, vehicle magnetic length per class (discussed in section 4.5) is considered a principle feature for classification. Table 7-30 shows axle-based vehicle length ranges per class. According to [133], vehicles can initially be classified into a) single-unit vehicles, including FHWA Classes 1, 2, 3, 4, 5, 6, and 7, with length range between 3- and 35-feet and b) multi-unit vehicles, including FHWA Classes 4, 8, 9, 10, 11, 12, and 13, with length range between 36- and 78-feet.

Table 7-30 Axle vs. Length Classification

FHWA Class	Average Length (feet)	Standard Deviation	Minimum Length (feet)	Maximum Length (feet)
F01	5.38	2.23	3.14	7.61
F02	15.33	2.27	13.06	17.60
F03	18.32	4.13	14.19	22.46
F04	38.06	6.87	31.19	44.93
F05	25.14	4.91	20.24	30.05
F06	24.68	4.19	20.49	28.86
F07	31.58	2.86	28.72	34.44
F08	43.85	6.85	37.00	50.70
F09	64.51	5.69	58.81	70.20
F10	63.50	5.82	57.68	69.31
F11	68.76	2.62	66.14	71.37
F12	73.22	4.37	68.85	77.60
F13	69.02	5.74	63.28	74.77

B. Energy of Vehicle Magnetic Signature:

The energy for a given signal x, sampled over timer period *T*, can be measured in several ways: 1) total energy (Eq. 7-41); 2) square-root of total energy (Eq. 7-42); 3) average-absolute energy (Eq. 7-43); and 4) root-mean-square (RMS) value (Eq. 7-44). Total number of samples is denoted by *N*.

In this study, the normalized, discrete-time RMS value of the MAG flux magnitude (Eq. 7-45) and tree geomagnetic field components (Eq. 7-46) are considered as features. Energy values are normalized to the estimated vehicle magnetic length (See Eq. 4-27), so that all values are comparable and independent of vehicle speed and occupancy time. This feature represents overall disturbance caused by a passing vehicle, such that a larger vehicle would have more energy.

$$E_{Total} \triangleq \int_0^T |x(t)|^2 . dt \triangleq \sum_{n=0}^{N-1} |x[n]|^2 \qquad \textbf{Eq. 7-41}$$

$$E_{Total} \triangleq \sqrt{\int_{-\infty}^{+\infty} |x(t)|^2 . dt} \triangleq \sqrt{\sum_{n=0}^{N-1} |x[n]|^2} \quad \textbf{Eq. 7-42}$$

$$E_{Total} \triangleq \frac{1}{T}\int_{0}^{T} |x(t)|^2 . dt \triangleq \frac{1}{N}\sum_{n=0}^{N-1} |x[n]|^2 \quad \textbf{Eq. 7-43}$$

$$E_{Total} \triangleq \sqrt{\frac{1}{T}\int_{0}^{T} |x(t)|^2 . dt} \triangleq \sqrt{\frac{1}{N}\sum_{n=0}^{N-1} |x[n]|^2} \quad \textbf{Eq. 7-44}$$

$$E_{F_M} \triangleq \frac{\bar{v}}{f_s}\sqrt{\frac{1}{T_{Occ}}\int_{T_A}^{T_D} F_M(t)^2 . dt} \triangleq \frac{\bar{v}}{f_s}\sqrt{\frac{1}{f_s . T_{Occ}}\sum_{n=1}^{k} F_M(k)^2} \quad \textbf{Eq. 7-45}$$

$$E_{B^\gamma} \triangleq \frac{\bar{v}}{f_s}\sqrt{\frac{1}{T_{Occ}}\int_{T_A}^{T_D} |B^\gamma(t)|^2 . dt} \triangleq \frac{\bar{v}}{f_s}\sqrt{\frac{1}{f_s . T_{Occ}}\sum_{k=1}^{n} |B^\gamma(k)|^2} \; ; \; \gamma \in \mathbb{R}^3 \quad \textbf{Eq. 7-46}$$

C. Moments of Vehicle Magnetic Signature:

Moments are statistical parameters of a random variable *X* or function *f(x),* describing characteristics of the distribution of *X* or *f(x)*. Mean, variance, skewness, and kurtosis are, namely, the first, second, third, and fourth moments. In this study, the first four moments are used to characterize vehicle magnetic signature shape for classification.

The k^{th} central moment μ_k of a random variable *X* about μ is defined [134] in Eq. 7-47, where μ_k is the expectation value of *X*.

$$\mu_k = E[(X-\mu)^k] = \sum_i f(x_i).(x_i-\mu)^k \quad \textbf{Eq. 7-47}$$

The mean of $x_1, \ldots, x_n$ estimates the value around which central clustering occurs (See Eq. 7-48):

$$\mu_1 = \frac{1}{n}\sum_{i=1}^{n} x_i \quad \textbf{Eq. 7-48}$$

Variance is a measure of dispersion (or spread) around a central value, given by Eq. 7-49. STD is $\sigma = \sqrt{\sigma^2}$.

$$\sigma^2 = \mu_2 = E[X - \mu_1]^2 = \frac{1}{n-1}\sum_{i=1}^{n}(x_i - \mu_1)^2 \qquad \textbf{Eq. 7-49}$$

Skewness γ_1 characterizes the degree of asymmetry around μ_1 and is given by Eq. 7-50. Unlike the mean, variance, and STD, skewness is a non-dimensional quantity that characterizes shape only. $\gamma_1 > 0$, given that vehicle signature is more flattened to the right and vice versa.

$$\gamma_1 = \frac{\mu_3}{\sigma^3} = E\left[\left(\frac{X - \mu_1}{\sigma}\right)^3\right] = \frac{1}{n-1}\sum_{i=1}^{n}\left(\frac{x_i - \mu_1}{\bar{\sigma}}\right)^3 \qquad \textbf{Eq. 7-50}$$

Kurtosis γ_2, on the other hand, is also a non-dimensional quantity that is used to measure the relative flatness of a distribution. It is defined using Eq. 7-51, where $\bar{\sigma}$ is the estimated standard deviation and "-3" term makes the value zero for a normal distribution such that $\mathcal{N}(\mu, \sigma) \rightarrow \gamma_1 = \gamma_2 = 0$. $\gamma_2 > 0$, given that a vehicle signature has a positive excess and vice versa.

$$\gamma_2 = \frac{\mu_4}{\sigma^4} - 3 = E\left[\left(\frac{X - \mu_1}{\sigma}\right)^4\right] - 3 = \frac{1}{n-1}\sum_{i=1}^{n}\left(\frac{x_i - \mu_1}{\bar{\sigma}}\right)^4 - 3 \qquad \textbf{Eq. 7-51}$$

D. Shape Symmetry Ratio of Vehicle Magnetic Signature:

The *Shape Symmetry Ratio (SSR)* feature is defined using Eq. 7-52, where T_R is the rising time. Relative to magnetic effects, any vehicle structure can be divided into three sections—engine, center, and tail. The length of each section is proportional to total vehicle length. The engine section, unlike the other two sections, contains the majority of a vehicle's ferromagnetic mass. Hence, larger vehicles will have a unique shape ratio.

$$SSR = \frac{T_{UP}}{T_{Occ}} \qquad \textbf{Eq. 7-52}$$

E. Shape Symmetry Degree of Vehicle Magnetic Signature:

Shape Symmetry Degree (SSD) is defined in this study as the number of samples in which the magnitude of a vehicle signature $F_{M(k)}^{(V_N)}$ exceed a certain shape threshold S_{TH},

as shown in Eq. 7-53, where *N* is the number of sample per a vehicle signature, and δ_N is a binary indicator function.

$$SSD = \sum_{k=1}^{N} \delta_N \left(F_{M(k)}^{(V_N)}, S_{TH}\right); \quad \delta_N \left(F_{M(k)}^{(V_N)}, S_{TH}\right) = \begin{cases} 0, & F_{M(k)}^{(V_N)} < S_{TH} \\ 1, & F_{M(k)}^{(V_N)} \geq S_{TH} \end{cases} \qquad \textbf{Eq. 7-53}$$

F. Maximum Magnitude Value (F_{Mp}):

Maximum Magnitude Value (F_{Mp} represents absolute maximum value of F_M (i.e., F_{Mp} is the highest peak). This feature relies on the assumption that vehicles with larger structure induce higher disturbance to the earth's magnetic field, hence, produce a higher magnitude peak.

G. Number of Peaks and Valleys:

The number of peaks (local maxima) and valleys (local minima) of a signal can be found by calculating derivatives. However, this method is computationally inefficient. Another method implemented in this study to find extrema points is comparing each point with its neighboring points, given the magnitude vector of a vehicle magnetic signature $S_{V_N}^{(F_M)}$ and including *k* sample point. $S_{V_N}^{(F_M)}[k]$ is a peak if its neighboring points within a moving window *w* are smaller than its value. $S_{V_N}^{(F_M)}[k]$ is a valley if its neighboring points are larger than its value (See Eq. 7-54). A valley is defined as a point with lowest value between *w* points. A peak point always comes between two valleys, and vice versa.

$$S_{V_N}^{(F_M)}[k] = \begin{cases} peak, & S_{V_N}^{(F_M)}[k-w] < S_{V_N}^{(F_M)}[k] > S_{V_N}^{(F_M)}[k+w] \\ valley, & S_{V_N}^{(F_M)}[k-w] > S_{V_N}^{(F_M)}[k] < S_{V_N}^{(F_M)}[k+w] \end{cases} \qquad \textbf{Eq. 7-54}$$

H. Change Ratio in Signal Energy Polarity

The discrete-time RMS energy value calculated using Eq. 7-46 represents overall disturbance on each axle caused by an overpassing vehicle. As stated earlier, when a vehicle approaches the sensor, it pulls the localized flux lines away from the sensor; when it drives away, it pushes it back toward the sensor. This movement changes in signal polarity on each axle. The change ratio in signal energy can be calculated using Eq. 7-55, where $E_{B^Y}^{(P)}$ and $E_{B^Y}^{(N)}$ are the RMS value of positive and negative energy, respectively.

$$Er_{B^\gamma} = \frac{E_{B^\gamma}^{(P)}}{E_{B^\gamma}^{(N)}} \triangleq \frac{\bar{v}}{f_s} \times \frac{\sqrt{\frac{1}{n}\sum_{B^\gamma(k)\geq 0} B^\gamma(k)^2}}{\sqrt{\frac{1}{n}\sum_{B^\gamma(k)<0} B^\gamma(k)^2}};\ \gamma \in \mathbb{R}^3 \qquad \textbf{Eq. 7-55}$$

I. Hill Patterns

Hill pattern is found from the time derivative of VMS, as shown in Eq. 7-57, where δ_{Th+} and δ_{Th-} are the positive and negative thresholds, respectively, and δ_{Th+}=- δ_{Th-}. Hill pattern is sensitive to noise (i.e., fluctuations in VMS). Hence, an MAF should be applied first.

$$\delta(n) = x(nT_s) - \frac{s([n-1]T_s)}{T_s}; n \in \mathbb{Z}$$

$$\overline{\delta(n)} = \begin{cases} +1 & \delta(n) \geq \delta_{Th_+} \\ -1 & \delta(n) < \delta_{Th_-} \\ 0 & otherwise \end{cases} \qquad \textbf{Eq. 7-56}$$

7.8.2.5 *Dimensionality Reduction and Features Selection*

Although an endless number of features can be extracted from vehicle magnetic signatures, using more features might not necessarily result in improving classification accuracy. In fact, additional features might result in poor classification performance, as features from different vehicle classes might overlap. Hence, features with significant variations when compared to others should be selected for best classification accuracy.

Principal Components Analysis (PCA) was used for reducing the dimensionality of 60 extracted features vector and selecting distinctive features that can be efficiently used to distinguish various vehicle classes. PCA is a statistical technique for dimensionality reduction of multivariate data [135] and is defined as the orthogonal projection of the data onto a low dimensional subspace by maximizing variance of projected data. This reduction or transformation will significantly speed up the unsupervised ML algorithm.

Consider a dataset $\{x^{(i)}, x^{(2)}, \dots, x^{(m)}\}$ of *m* with different x features of a vehicle magnetic signature, such as length, mean, STD, variance, and others. Let $x^{(i)} \in \mathbb{R}^n$ for each$i$: $(n \ll m)$. Assume attributes $x_1^{(i)}$and $x_2^{(i)}$are measures of occupancy time vehicle *I*, such that the both attributes are strongly correlated (See Figure 7-70).

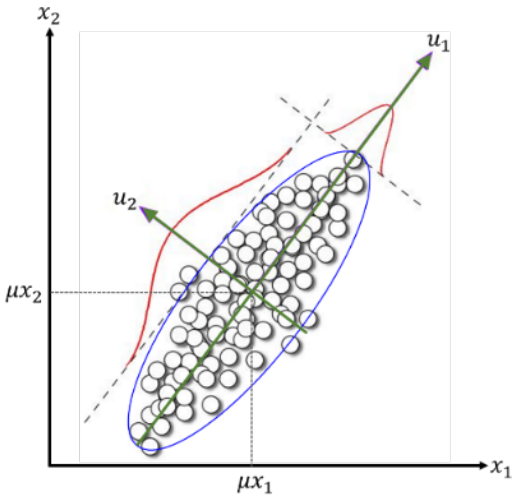

Figure 7-70 Eigenvectors of a hypothetical 2D dataset

Preprocessing is required prior to running PCA to normalize dataset mean and variance. First, if data is not normally distributed with a zero mean, mean must be transferred such that $\mu = 0$ by calculating μ using Eq. 7-57, and each $x^{(i)}$ should be replaced with $x^{(i)} - \mu$. Second, if attributes are not on the same scale, unit variance must rescale each coordinate by calculating σ_j using Eq. 7-58 and substituting each $x_j^{(i)}$ with $x_j^{(i)}/\sigma_j$, where *j* is the feature point of vehicle *i*.

$$\mu = \frac{1}{m}\sum_{i=1}^{m} x^{(i)} \qquad \textbf{Eq. 7-57}$$

$$\sigma_j^2 = \frac{1}{m}\sum_{i}\left(x_j^{(i)}\right)^2 \qquad \textbf{Eq. 7-58}$$

Once dataset is normalized, data must be approximated by finding a subspace direction *u* to project data onto, such that variance of projected data is maximized and data points are far from zero. To formulate this, suppose that *u* is a given unit vector and $x^{(i)}$ is a point in a dataset (i.e., extracted features vector from the i^{th} vehicle signature), then ${x^{(i)}}^T u$ would be the projection of $x^{(i)}$ onto *u*. Hence, u must be chosen as principal eigenvector of the covariance matrixΣ, maximizing projections variance, as shown in Eq. 7-59. Covariance matrix Σ is given in Eq. 7-60. Eigenvectors of Σ can be found by solving Eq. 7-61, where u_i is a column vector and λ_i is the eigenvalue associated with the eigenvector u_i.

$$\frac{1}{m}\sum_{i=1}^{m}\left(x^{(i)^T}u\right)^2 = \frac{1}{m}\sum_{i=1}^{m} x^{(i)}.x^{(i)^T}.u.u^T = \left(\frac{1}{m}\sum_{i=1}^{m} x^{(i)}x^{(i)^T}\right)u.u^T \qquad \textbf{Eq. 7-59}$$

$$\Sigma = \frac{1}{m}\sum_{i=1}^{m} x^{(i)}x^{(i)^T} \qquad \textbf{Eq. 7-60}$$

$$\Sigma u_i = \lambda_i u_i \qquad \textbf{Eq. 7-61}$$

For a *k*-dimensional subspace ($i.e., x^{(i)}$ consists of k features), $\{u_1, \dots, u_k\}$ must be chosen as the top significant *k* eigenvectors (i.e., features) of Σ (calculated in Eq. 7-61) for retaining 99% of the signal's variance using Eq. 7-64. Eq. 7-62 shows a representation for *k* eigenvectors, where u_1 is the principal eigenvector that has the largest eigenvalue λ_1, and so on for $u_k \rightarrow \lambda_k$

$$U = \begin{bmatrix} \vdots & \vdots & \cdots & \vdots \\ u_1 & u_2 & \cdots & u_k \\ \vdots & \vdots & \cdots & \vdots \end{bmatrix} \qquad \textbf{Eq. 7-62}$$

The number of components to the set of eigenvectors *U*—forming a new orthogonal basis of the features set—can now be used to find a new representation of $x^{(i)}$, as in Eq. 7-63, where new vector $\tilde{x}^{(i)} \in \mathbb{R}^k$ provides a lower representation of $x^{(i)} \in \mathbb{R}^n$, such that $k \ll n$.

Of 60 components, PCA algorithm retained only 16 components, which explains 95% variance.

$$\tilde{x}^{(i)} = U^T x^{(i)} = \begin{bmatrix} u_1^T x^{(i)} \\ u_2^T x^{(i)} \\ \vdots \\ u_k^T x^{(i)} \end{bmatrix} \in \mathbb{R}^k \qquad \textbf{Eq. 7-63}$$

$$\frac{\sum_{j=1}^{k}\lambda_j}{\sum_{j=1}^{n}\lambda_j} \geq 0.95 \qquad \textbf{Eq. 7-64}$$

7.8.2.6 Machine Learning Classification Method

Selected features set was divided into two subsets, namely training and testing. The first was used for training the intelligent classifier and the other for testing its accuracy.

The classification algorithm learns to classify vehicles into predefined classes by statistically modeling the relationship between a vehicle's class and the probabilistic distributions of the feature set (i.e., predictors). These models are inferred from a labeled data set called *Training Dataset*. This set consists of features $x^{(i)}$ and corresponding vehicle class $y^{(i)}$ vectors, which is labeled and validated by either video cameras or any accurate vehicle classification method. In this study, RUSBoost classification technique [121] was used to overcome data imbalance and build the system's classification model.

7.8.2.7 *Validation Method*

Validation accuracy score estimates a model's performance on new data when compared to the training data. The classification algorithm used a one-vs.-all approach, meaning that *m-class* models are fitted to the training data—one model for each class. When fitting the model for the *mth* class, training dataset labels are changed. Thus, the model is fitted to simultaneously distinguish between two classes at once. During validation with the test dataset, *m*-individual scores are estimated—one for each model. Subsequently, the highest scoring class is chosen as the predicted class.

Predictive accuracy of fitted models was examined using *k*-fold cross-validation. This validation method builds *k*-different test sets from the same training set, and then trains all models on the remaining training dataset. Finally, the best average working hypothesis is chosen.

Let's assume *m*-models of hypotheses class $\mathcal{M} = \{M^{(i)}\}_{i=1}^{m}$ will be used to classify a dataset $\mathcal{D} = \{X^{(i)}, Y^{(i)}\}_{i=1}^{n}$. *k*-fold cross-validation randomly divides $\mathcal{D}$ into *l/k* subset of *k* examples $S = \{S^{(j)}\}_{j=1}^{l/k}$. By training each $M^{(i)}$ on $\mathcal{D} - S^{(j)}$ training subset, a hypothesis h_{ij} can be obtained, and the empirical error $\varepsilon_{S_j}^{(h_{ij})}$ of h_{ij} using $S^{(j)}$ can be calculated using Eq. 7-65. Overall empirical error $\varepsilon_D^{(M_i)}$ of each $M^{(i)}$ on $\mathcal{D}$ is the average h_{ij} on $S^{(j)}$, where $j = \{1, \dots, l/k\}$, as shown in Eq. 7-66. Once $\varepsilon_D^{(M_i)}$ is calculated for all models, the superior $M^{(i)}$ is the one with minimal $\varepsilon_D^{(M_i)}$.

$$\varepsilon_{S_j}^{(h_{ij})} = \sum_{(x,y)\in S^{(j)}} 1\{h_{ij}(x) \neq y\} \qquad \textbf{Eq. 7-65}$$

$$\varepsilon_D^{(M_i)} = \frac{k}{l}\sum_{j=1}^{l/k} \varepsilon_{S_j}^{(h_{ij})} \qquad \textbf{Eq. 7-66}$$

7.8.2.8 Classification Results

Vehicles were classified into six groups, as illustrated in Table 7-31, based on their structural similarity. Figure 7-69 shows the confusion matrix for the built system's classification model. RUSBoost resulted in an 81% overall classification rate. 30% of group 2 vehicles (i.e., Class 2 and Class 3) were mis-classified as group 4 (i.e., Class 5) and group 5 (i.e., Class 6 and Class 7). 23% of group 4 vehicles (i.e., Class 5) were mis-classified as group 2 and 5. Such a high mis-classification rate in group 2 and group 4 is attributed to enormous variations in both groups' vehicle structures. A general flow diagram of the developed intelligent vehicle classification model is illustrated in Figure 7-72.

Table 7-31 VMS-based Classification Groups

Group	Corresponding FHWA Class
G1	F1
G2	F2—F3
G3	F4
G4	F5
G5	F6—F7
G6	F8—F13

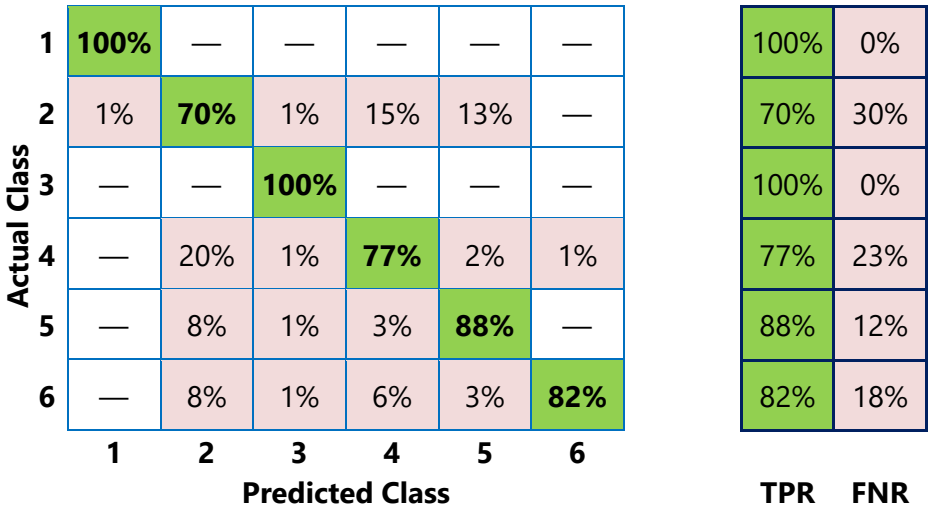

Figure 7-71 Decision Matrix using RUSBoost Classification Model

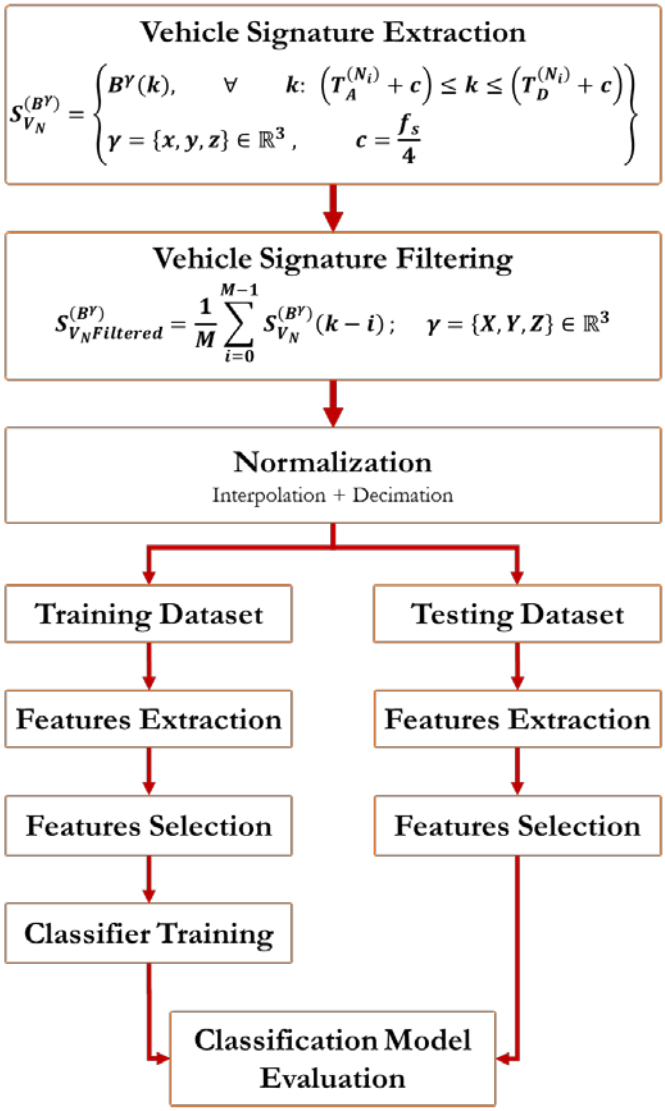

Figure 7-72 Intelligent vehicle classification model development process

7.9 Axle detection using magnetometers

Investigation of magnetic signatures revealed that sharp and short peaks occur when vehicle wheels step over or pass very close to the sensor. This is possibly due to the fact that when wheels step over the sensors, the part of the axle which holds them becomes within a close proximity to the sensor. These parts are usually made of highly magnetic carbon steel and cause strong field disturbance. Figure 7-73 shows the magnetic signature of a two-axle vehicle that stepped over the magnetometer. The red curve shows the position of axles as detected by an accelerometer. Magnetometers ability to detect axles will be evaluated by comparing them to accelerometers placed in the same position. Accelerometers has been proven to detect axles accurately in [50].

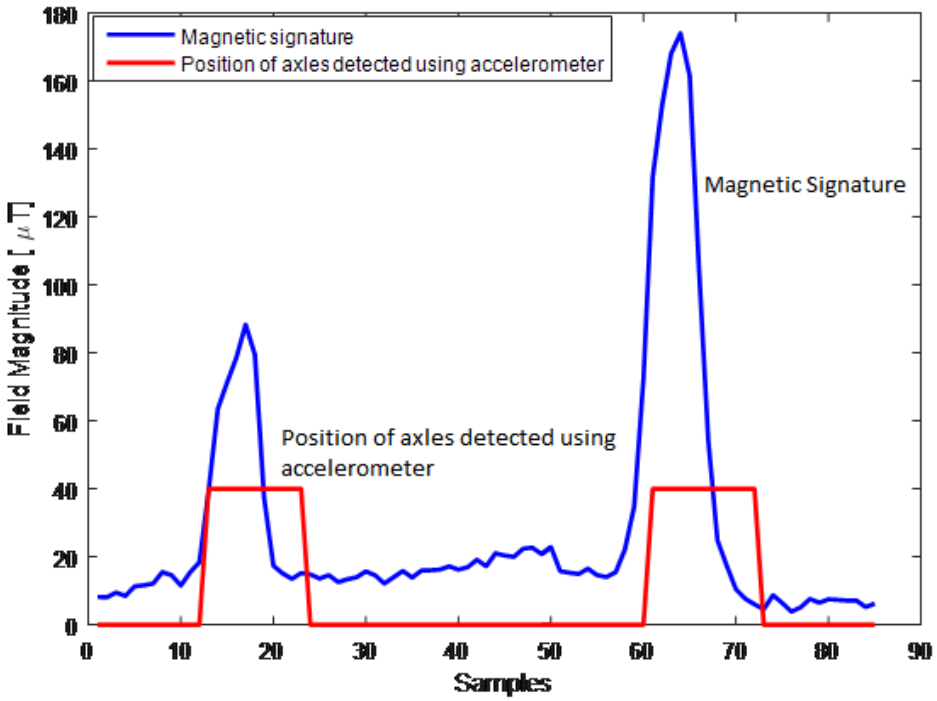

Figure 7-73 Magnetic signature of a two-axle vehicle crossing over the sensor.

Exploiting this phenomenon to detect and count axles improves classification accuracy and allows measuring several vehicle dynamics (e.g. axle spacing) given that vehicle speed is known.

The test depicted in Figure 5-7 was conducted to evaluate axle detection using magnetometers. Sensors SA, SM, and SN were spread over the left half of the lane so that left side wheels would pass very close to at least one of the sensors. SN and SM were also provided with accelerometers to measure wheel vibrations. Axles detected by accelerometer were used as ground-truth to evaluate the magnetometer's ability to detect axles.

The following signature attributes are used to develop the magnetometer-based axle detection algorithm:

1. The amplitude of signal's first derivative is at its highest when wheels are close to the sensor because the wheel's disturbance lasts for a very short interval and causes sudden changes in flux magnitude. Figure 7-74 illustrates the changes in flux first derivative when axles are detected.

2. Signature magnitude is considerably higher when axles are present within the detection zone.

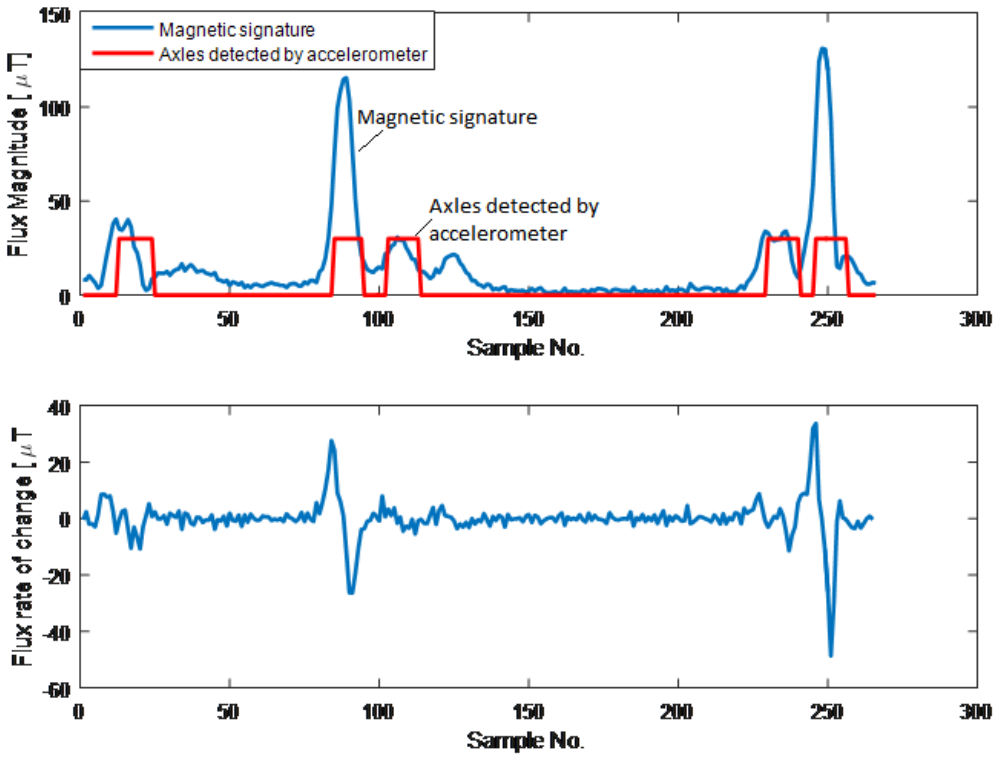

Figure 7-74 Magnetic signature and its first derivative.

Figure 7-75 shows the distribution of signature magnitude recorded by sensor SN. The distribution was assumed resulting from a weighted sum of two Gaussians according to the following Gaussian Mixture Model (GMM) [136].

GMM parameters can be estimated using the Expectation Maximization (EM) method [137]. Figure 7-76 illustrates the result of applying EM to 300 signatures recorded by SN. The first Gaussian has a mean around $14[\mu T]$ and was considered the underlying random process that generates signature samples in vehicle's body (i.e. non-axle samples). The second Gaussian has a mean of $70[\mu T]$ and is considered the random process generating axle samples. Based on the resulting model, a threshold of $35[\mu T]$ was chosen to discriminate between axle and non-axle samples.

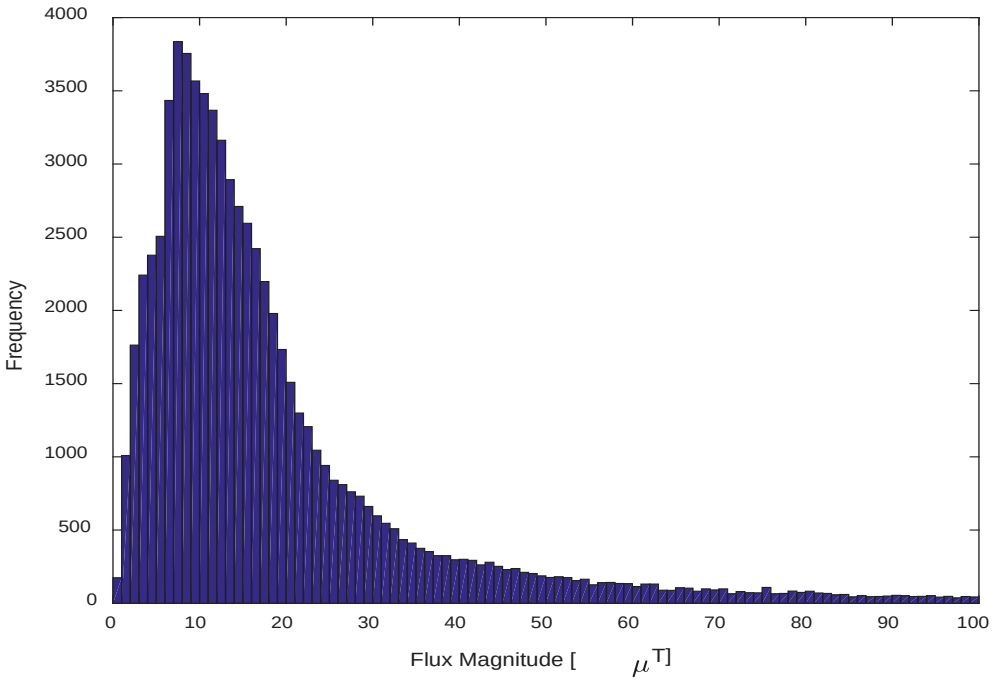

Figure 7-75 Distribution of flux magnitude

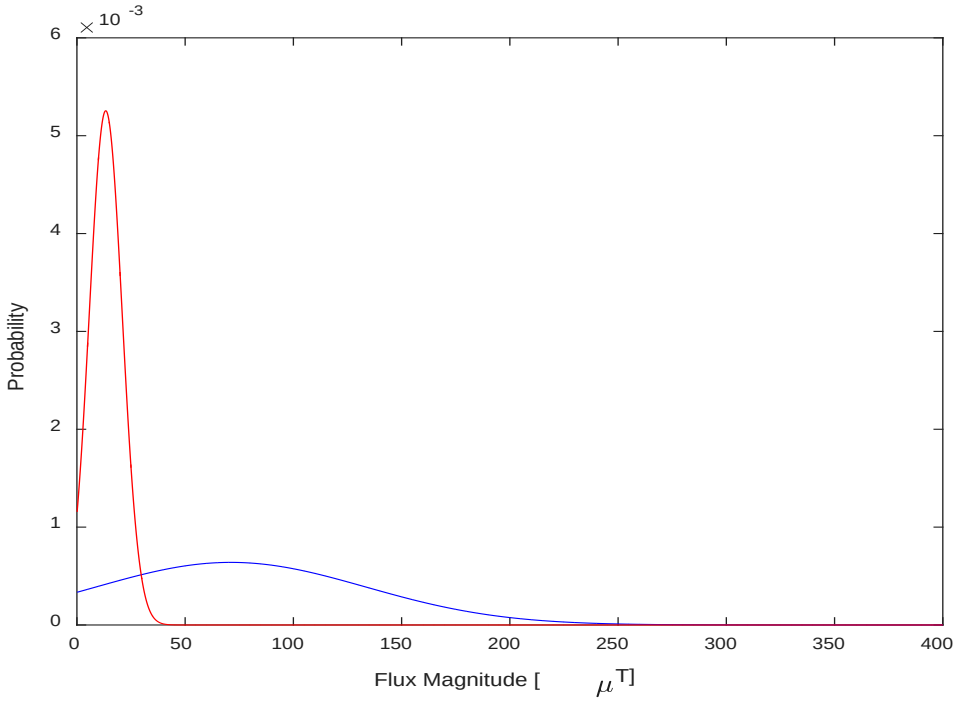

Figure 7-76 EM result when applied to signature magnitude.

GMM and EM were also applied to the absolute value of signature's first derivative. The result was two Gaussian processes, as shown in Figure 7-77. Based on the resulting

model a threshold of 50 $[\mu T]$ was added to the preceding testing criteria to increase the certainty of sample classification.

A signature sample would be classified as axle sample if:

$$(F_M(k) > 35\ [\mu T])\ \&\ \left(\left|F'_{M(k)}\right| > 50\ [\mu T]\right) \qquad \textbf{Eq. 7-67}$$

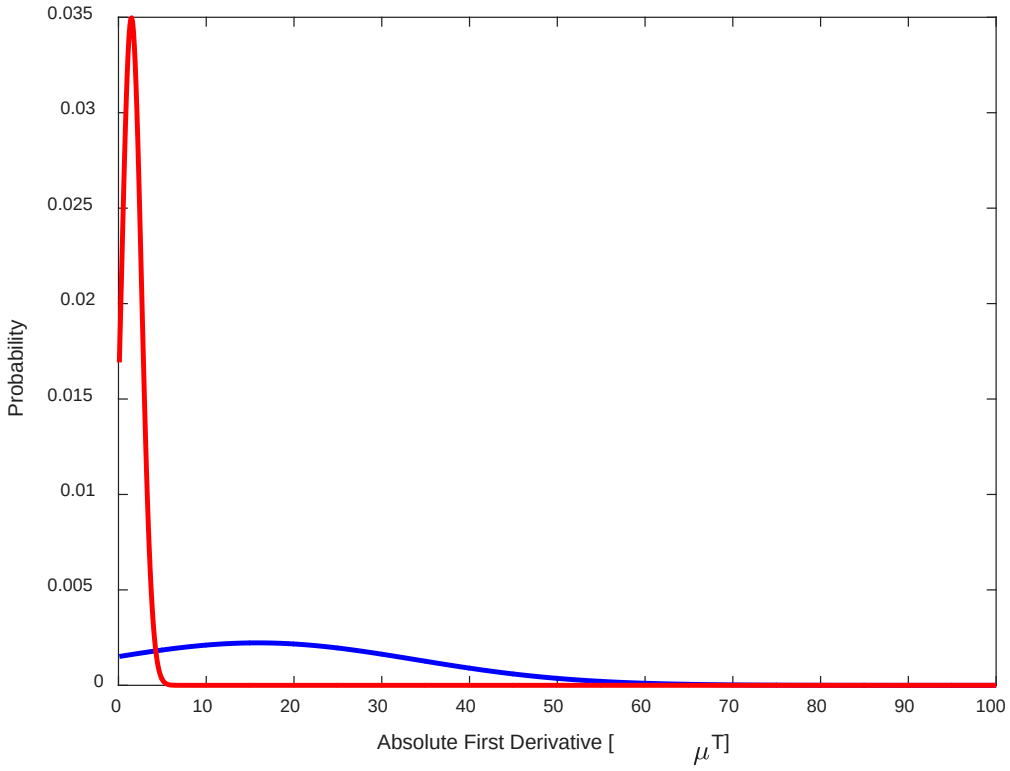

Figure 7-77 EM result when applied to absolute first derivative.

Samples were classified using this method into axle or non-axle samples. Figure 7-78 shows sample classification result in a 5-axle vehicle, and compares it with accelerometer-based axle detection. Sample classification method was applied to 122 vehicle signatures where axle samples were validated using axle positions provided by the accelerometer. The accelerometer detected 221 axles while sample classification detected 220 axles. 24 of the detected axles were false detections. Hence, the total number of correctly detected axles is 196 which translates to 88.6% axle detection accuracy.

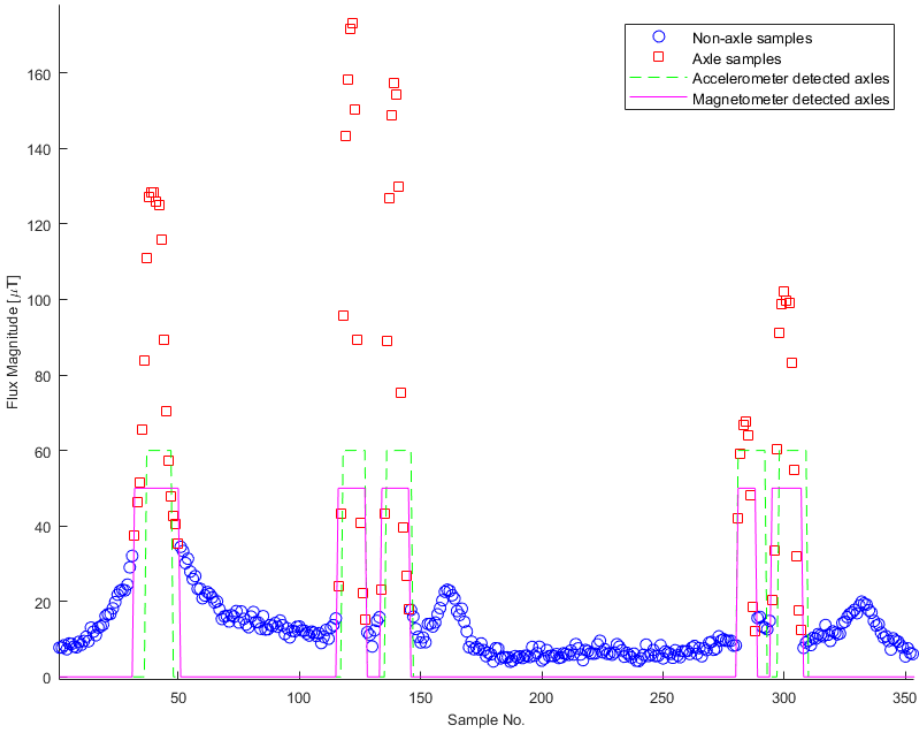

Figure 7-78 The result of axle detection in a 5-axle vehicle.

This result can be enhanced using more sensors to guarantee that wheels would step on at least one sensor. The axle detection system can be used alongside signature based classification to increase classification accuracy. Data fusion algorithms (e.g. Kalman Filter) would benefit from information provided by both systems to increase decision certainty. The downside of this method is that it needs many sensors deployed over the lane which increases cost, power consumption, and the amount of data transmitted to the access point.

7.10 Energy Budget Analysis

As stated earlier, *i*VCCS is a battery-powered, wireless sensor node that uses a 3.7V/2000mAh Lithium Polymer (Li-Po) battery. All *i*VCCS on-board components were carefully selected to achieve minimal power consumption.

A preliminary power consumption analysis in various operation modes showed that maximum current rates in power down, idle, and active modes are 156μA, 50nA, and 65mA, respectively. Considering 3.7V/2000mAh Li-Po Battery, battery life can be roughly estimated in each mode using Eq. 7-68, where μ is external factor allowances

that can affect battery life, and T is the duty-cycle. Given that μ = 0.75 and T=1, estimated battery life in power down mode is limitless. However, the battery can operate *i*VCCS 578 days in idle mode and can survive 40 hours in full active mode. In full active mode, all *i*VCCS components are operating, including GPS, RF engine, and data logging unit. Power consumption for *i*VCCS components and WSM sensors is shown in Table 7-32.

$$BL_{hour} = \frac{1}{T}\left(\frac{Capacity_{mAh}}{Current_{mA}} \times \mu\right) \qquad \textbf{Eq. 7-68}$$

Table 7-32 Power consumption for *i*VCCS components

Component	Idle	Full Active
Atmel XMega A4 Microcontroller	1μA	500μA ~ 8mA
microSD Card	150uA	20mA
Voltage Regulator	500nA	8μA
Li-Po Battery Fuel Gauging	1μA	50μA
MAG Sensor	2μA	40 ~ 575μA[1]
ACCEL Sensor	2μA	40 ~ 575μA[2]
RF Module	0.37μA	20 / 22mA[3]
GPS Module	1μA	20 / 29mA[4]
Passive components	50μA	50μA
Total Current	**160μA**	**60mA ~ 80mA**

The most power consuming components on *i*VCCS is the wireless transceiver engine (e.g., active current is 22mA). Power consumption is reduced given a transition from one state to another (e.g., power-down → Idle → Active), which is driven by

[1] Consumption is related to sensor's sampling rate
[2] Consumption is related to sensor's sampling rate
[3] Consumption depends on the operation, read/write
[4] Consumption depends on the operation, tracking/accusation

interrupt events; a transition from *Power Down* to *Active* mode is triggered by vehicle's arrival event where the MCU samples the magnetic field every T_S (i.e., T_S = 1.563Hz to 800Hz). A cyclic transition between *Active* ⇔ *Idle* modes occurs every T_S until a transition from *Active* → *Power Down* mode is triggered by a vehicle departure event.

Table 7-33 Power consumption for WSN components

Sensor	Power-off	Idle	Active
Digital Lightning Sensor	0	1μA	60μA
Microphone Preamplifier	0	24μA	24μA
Digital Relative Humidity sensor	0	0.1μA	480μA
Digital Pressure/Altitude sensor	0	2μA	8.5μA
Digital Temperature Sensor	0	1μA	10μA
Digital Ambient Light Sensor	0	0.65μA	1μA
MEMS Silicon Microphone	0	50μA	50μA
Voltage Regulator	500nA	500nA	8μA
Analog Impedance grid sensor	0	25μA	25μA
Analog NTC Thermistor	0	25μA	25μA
	500nA	**129μA**	**692μA**

Table 7-34 Power consumption in various operation modes using Li-Po batteries

Li-Po Battery	*i*VCCS Battery-Life (Days)			WSM Battery-Life (Days)		
	Shut-down	Idle	Active	Shut-down	Idle	Active
	500nA	156μA	60~80mA	500nA	129μA	692μA
1000mAh	83333	252	0.69	83333	323	60.21
1500mAh	125000	378	1.04	125000	484	90.32
2000mAh	166666	505	1.39	166666	646	120.42
2500mAh	208333	631	2.08	208333	807	150.53
3000mAh	250000	7578	2.08	250000	969	180.64
4000mAh	333333	1010	2.78	333333	1292	240.85

7.10.1 Power Consumption Implications of Detection Algorithm

MAG (e.g., FXOS8700CQ) has an active mode operation current range between 20—600μA, which is directly related to the sensor's ODR. MCU, on the other hand, has a

slightly higher power consumption. *i*VCCS basically samples the MAG, loges and analyzes acquired data, and then sends timestamps to *i*AP whenever a detection occurs. In reality, average duty-cycle of a detection system could range between 1—8%, meaning the system is idle more than 92% of the time. Hence, power consumption can be significantly reduced by configuring the system to automatically transition to a higher sampling rate when needed (i.e., a detection event triggered). *i*VCCS spends the majority of time in *idle* mode (i.e., no detection event) wherein a very low sampling rate can be used. This method, however, is at the expense of losing samples of vehicle signatures.

Chapter 8: CONCLUSION

8.1 Research Outcomes

With the approaching era of IoT (Internet of Things) and smart cities, market demand will likely drive innovation toward more autonomous wireless sensors. Combining advancements in state-of-the-art ultra-low-power embedded systems, smart physical sensors, WSN, and EH will enable fully autonomous IoT devices that remain operational—ideally without battery replacement—for decades. This technological breakthrough is the key enabler for smart cities, smart homes, and smart energy, among many other perspective innovations.

Real-time traffic monitoring systems play a major role in the transition toward smart cities and more efficient ITS. Autonomous traffic sensing is at the heart of smart cities infrastructure, wherein smart wireless sensors are used to measure traffic flow, predict congestion, and adaptively control traffic routes. Such information enables a more efficient use of resources and infrastructure.

This report introduces the design, development, and implementation of a novel, fully-autonomous, intelligent wireless sensor for various traffic surveillance applications. The sensor integrates state-of-the-art, embedded components, featuring ultralow power, high-performance 32-bit embedded microcontroller, energy-efficient wireless transceiver, smart embedded sensors (i.e., 3D MAG and ACCEL), highly-accurate low-power embedded Global Positioning System (GPS) receiver, dual data storage units, power management unit, battery fuel gauge, and atmospheric sensors. All components are managed by distinctive algorithms designed for implementation in various traffic monitoring applications.

The developed sensor is portable, inexpensive (i.e., $30 per node), easy-to-install into highway surfaces, roadways, or even roadsides without intrusive roadwork, and can accurately detect, count, estimate speed and length, classify, and re-identify vehicles in real-time. The sensor can be used for short-term deployment (e.g., work zone safety, temporary roadway design studies, traffic management in atypical situations such as evacuations) and long-term deployment (e.g., traffic management, turn movement, collision avoidance).

A reliable and distinctive computationally efficient algorithm for real-time traffic monitoring was developed, integrated, and validated. Optimization programming tasks were applied to improve detection algorithm performance at higher sampling rates and compensate for drift in the geomagnetic reference field. An algorithm for adaptive compensation of RTC Frequency Drift resulting from variations in temperature was implemented. Each sensor node relies on an onboard GPS module and RTC unit to maintain an independent local clock that is globally synchronized to the GPS pulse-per-second (PPS) signal. Wireless connectivity is not necessary for accurate *i*VCCS node functioning. Time stamping, timekeeping, and failure recovery functions are enabled by the MCU's internal RTC unit, which is calibrated and aligned using the PPS signal. A time synchronization algorithm based on GPS-PPS signal was developed and evaluated. Results indicated 2~4μSec consistent T-Sync accuracy among the internal RTC of several nodes.

Several field studies and evaluation tests were conducted during this research, many of which were conducted in parking lots at the *University of Oklahoma-Tulsa campus*. Eight additional field tests were conducted on *highways* and *urban roads* in the state of Oklahoma under various traffic conditions. System performance evaluation was conducted using real-time data, offline data, video images, and reports from the highly accurate *Roadrunner Kit 3*.

Repeatability of VMS and consistency of MAG sensor output were investigated. The objective was to find degree of similarity of several magnetic signatures produced by multiple MAG sensors for the same vehicle under like testing conditions. Cross-correlation was used to measure the similarity of two VMS as a function of a time lag applied to one or the other. A correlation coefficients matrix of VMS magnitudes obtained from four sensor nodes was constructed. CDF for all pairwise combinations revealed that most correlation coefficients range between 0.9 and 1, indicating high similarity between sensor outputs across multiple nodes. Furthermore, the p-value matrix returned insignificant p-values (i.e., 2e-138), which reject the null hypothesis and identify significant correlations. Hence, each vehicle has a unique magnetic signature that can be used for vehicle re-identification applications.

Three detection errors were observed during this study: 1) *Mis-detection error*, in which two successive vehicles at close proximity are grouped as one; 2) *Double-detection error*, in which a long vehicle with insignificant ferrous composition in center is detected as two vehicles; and 3) *False-detection error* caused by an interference caused by large

trucks traveling in adjacent lanes. Both mis-detection and double-detection errors were reduced by using statistical analysis to find an optimal *holdover debounce timer* (H_{DT}). False-detection error analysis showed insignificant interference effect on the *z-axis*. This observation was used to reduce false detection by comparing the mean of vertical components to a threshold found statistically.

Vehicle detection and counting accuracy was evaluated using MAPE. Validation studies showed MAPE between 0.4% and 0.7% for detection of all vehicle classes at various traffic conditions and speeds in both roadside and roadway setups.

Speed estimation was evaluated using MAPE and RMSE, indicating 97.4782% speed estimation accuracy with 2.9867mph MAPE and 2.5218% RMSE.

Two methods for vehicle classification using MAG are proposed, namely length-based (LBVC) and magnetic signature-based vehicle classification (SBVC).

Several LBVC schemes were developed, implemented, and evaluated via machine learning algorithms and probabilistic modeling of VML. A case study of Oklahoma classification stations using wireless MAG sensors was performed. This study serves as the first LBVC scheme for the state of Oklahoma; the intended purpose is supplementing or replacing axle-based data collection methods. The developed LBVC models are computationally efficient and can provide real-time data. The methodology and work process proved to be adaptable, thus, can be of a great benefit for other states and territories interested in developing LBVC schemes. This work can be extended for gathering LBVC data using non-intrusive technologies, such as vision systems and microwave radars. An LBVC evaluation study resulted in 97.6951% classification rate when vehicles are binned into four groups based on their magnetic length.

SBVC was implemented to classify vehicles into six groups. A total of 60 features were extracted from VMS dataset. Principal Components Analysis (PCA) was applied to reduce the dimensionality of the extracted features vector to 16 features and to select distinctive features that can be efficiently used to distinguish various vehicle classes. RUSBoost classification techniques were used to overcome data imbalance and to build the system's classification model. Predictive accuracy of the fitted models was examined using *k*-fold cross-validation. The classification model resulted in 81% overall classification rate.

System functionality testing revealed consistent behavior and accurate performance that can be exploited for more advanced applications. System cost was estimated at less than $1000 for eight sensor nodes and an access point, meaning that the system could be promoted as a replacement for expensive and invasive traditional traffic surveillance systems that depend on piezoelectric sensors, magnetic loops, and pneumatic tubes. The research work introduced in this report has been published in [72]–[74], [138]–[140].

8.2 Future Work Plan

Currently, vehicle classification based on VMS collected using MAG is not feasible for more than six classes. The reasoning behind this conclusion centers on the fact that each vehicle has a unique composition of furious materials causing a unique VMS. Characteristics of VMS for vehicles of the same class are quite different. During this research, several methods where exhausted, including neural networks and deep learning. It is nearly impossible to cluster vehicles based on their classes by only analyzing VMS. Hence, two approaches are proposed for more accurate vehicle classification. The first proposed taking advantage of the highly sensitive, low noise 3D accelerometer sensor in *i*VCSS$_{G2}$ design and investigating sophisticated signal processing and data analysis methods for fusing accelerometer and MAG data toward achieving axle-based classification. In a late stage of this research work, measuring road surface vertical acceleration using accelerometer for data collected from a sensor node placed adjacent to the road demonstrated a clear indication of vehicle axle positions. Exploiting this phenomenon to detect and count axles improves classification accuracy and allows the measurement of several vehicle dynamics (e.g., axle spacing), given that vehicle speed is known. The second approach proposed taking advantage of VMS uniqueness for implementing a classification model based on encoding an enormous number of labeled VMS and storing them into a database. Euclidian distance measure can be used to compare a real-time VMS with database and identify a class of vehicles. Additionally, two areas of interest relative to this research are presented. These, include enabling a scalable implementation of the system's wireless sensors network through self-configuration and optimizing sensor node power consumption while maximizing network lifetime by analyzing power consumption characteristics of a sensor node, and then incorporating energy-awareness algorithm to maintain high performance and fidelity operation.

REFERENCES

[1] "FHWA Forecasts of Vehicle Miles Traveled (VMT): May 2014," *Office of Highway Policy Information*, 2014. [Online]. Available: http://www.fhwa.dot.gov/policyinformation/tables/vmt/vmt_forecast_sum.cfm. [Accessed: 17-Apr-2015].

[2] "WHO | Global status report on road safety 2015."

[3] "National Highway Traffic Safety Administration (NHTSA), 2013 Traffic Safety Facts FARS/GES Annual Report." [Online]. Available: http://www-nrd.nhtsa.dot.gov/Pubs/812139.pdf. [Accessed: 14-Feb-2016].

[4] National Highway Traffic Safety Adminstriation, "The Economic and Societal Impact Of Motor Vehicle Crashes, 2010," Washington, DC, 2014.

[5] "2015 Urban Mobility Scorecard and Appendices — Urban Mobility Information." [Online]. Available: http://mobility.tamu.edu/ums/report/. [Accessed: 14-Feb-2016].

[6] C. C. D. US EPA, "Carbon Dioxide Emissions." [Online]. Available: http://www.epa.gov/climatechange/ghgemissions/gases/co2.html. [Accessed: 16-Apr-2015].

[7] "Truck Safety – Advocates for Highway and Auto Safety." [Online]. Available: http://saferoads.org/issues/truck-safety/. [Accessed: 10-Jan-2016].

[8] L. E. Y. Mimbela and L. a Klein, "A Summary of Vehicle Detection and Surveillance Technologies used in Intelligent Transportation Systems."

[9] G. Orosz, R. E. Wilson, and G. Stépán, "Traffic jams: dynamics and control.," *Philos. Trans. A. Math. Phys. Eng. Sci.*, vol. 368, no. 1928, pp. 4455–79, Oct. 2010.

[10] S. (Shawn) Jang, B. Bai, G.-S. Hong, and J. T. O'Leary, "Understanding travel expenditure patterns: a study of Japanese pleasure travelers to the United States by income level," *Tour. Manag.*, vol. 25, no. 3, pp. 331–341, Jun. 2004.

[11] "Industrial electronics Internet of Things opportunity | VentureOutsource.com." [Online]. Available: https://www.ventureoutsource.com/contract-manufacturing/industrial-electronics-internet-of-things-opportunity/.

[12] S. Cheung, "Traffic Surveillance by Wireless Sensor Networks : Final Report," 2007.

[13] F. H. Administration, "Traffic Monitoring Guide," 2013.

[14] I. Khan, F. Belqasmi, R. Glitho, N. Crespi, M. Morrow, and P. Polakos, "Wireless Sensor Network Virtualization: A Survey," *IEEE Commun. Surv. Tutorials*, pp. 1–1, 2015.

[15] F. Losilla, A.-J. Garcia-Sanchez, F. Garcia-Sanchez, J. Garcia-Haro, and Z. J. Haas, "A Comprehensive approach to WSN-based ITS applications: a survey.," *Sensors (Basel).*, vol. 11, no. 11, pp. 10220–65, Jan. 2011.

[16] D. Tacconi, D. Miorandi, I. Carreras, F. Chiti, and R. Fantacci, "Using wireless sensor networks to support intelligent transportation systems," *Ad Hoc Networks*, vol. 8, no. 5, pp. 462–473, Jul. 2010.

[17] A. Haoui, R. Kavaler, and P. Varaiya, "Wireless magnetic sensors for traffic surveillance," *Transp. Res. Part C Emerg. Technol.*, vol. 16, no. 3, pp. 294–306, Jun. 2008.

[18] N. G. D. Center, "NGDC Geomagnetic Calculators."

[19] N. Administrator, "2012: Magnetic Pole Reversal Happens All The (Geologic) Time," Apr. 2015.

[20] S. M. and A. T. Chulliat, A., S. Macmillan, P. Alken, C. Beggan, M. Nair, B. Hamilton, A. Woods, V. Ridley, "The US/UK World Magnetic Model for 2015-2020: Technical Report, National Geophysical Data Center, NOAA.," 2015. [Online]. Available: https://www.ngdc.noaa.gov/geomag/WMM/DoDWMM.shtml. [Accessed: 17-Dec-2015].

[21] N. Wahlstrom and F. Gustafsson, "Magnetometer Modeling and Validation for Tracking Metallic Targets," *IEEE Trans. Signal Process.*, vol. 62, no. 3, pp. 545–556, Feb. 2014.

[22] J. Jackson, *Classical electrodynamics*. New York: Wiley, 1999.

[23] Q. Liu, A. P. Roberts, J. C. Larrasoaña, S. K. Banerjee, Y. Guyodo, L. Tauxe, and F. Oldfield, "Environmental magnetism: Principles and applications," *Rev. Geophys.*, vol. 50, no. 4, p. RG4002, Nov. 2012.

[24] M. T. Report, "Evaluating Detection and Estimation Capabilities of Magnetometer-Based Vehicle Sensors," 2012.

[25] N. Wahlstrom and F. Gustafsson, "Magnetometer Modeling and Validation for Tracking Metallic Targets," *IEEE Trans. Signal Process.*, vol. 62, no. 3, pp. 545–556, Feb. 2014.

[26] S. Rajab, "ACCURATE VEHICLE CLASSIFICATION INCLUDING MOTORCYCLES USING PIEZOELECTRIC SENSORS," University of Oklahoma, 2012.

[27] S. V. Marshall, "Vehicle detection using a magnetic field sensor," *IEEE Trans. Veh. Technol.*, vol. 27, no. 2, pp. 65–68, 1978.

[28] N. Wahlstrom, R. Hostettler, F. Gustafsson, W. Birk, N. Wahlström, S. Member, R. Hostettler, F. Gustafsson, W. Birk, N. Wahlstrom, R. Hostettler, F. Gustafsson, and W. Birk, "Classification of driving direction in traffic surveillance using magnetometers," *IEEE Trans. Intell. Transp. Syst.*, vol. 15, no. 4, pp. 1405–1418, 2014.

[29] K. Liu, H. Xiong, and H. He, "New method for detecting traffic information based on anisotropic magnetoresistive technology," in *Proc. SPIE 8783, Fifth International Conference on Machine Vision (ICMV 2012): Computer Vision, Image Analysis and Processing*, 2013, p. 87830S.

[30] L. Yalong, L. Bin, and W. Zhiqiang, "A novel method of automatic vehicle detection based on active magnetic theory," in *2010 International Conference on Information, Networking and Automation (ICINA)*, 2010, vol. 2, pp. V2-382-V2-385.

[31] J. L. J. Lan and Y. S. Y. Shi, "Vehicle detection and recognition based on a MEMS magnetic sensor," *2009 4th IEEE Int. Conf. Nano/Micro Eng. Mol. Syst.*, pp. 404–408, 2009.

[32] A. Kaadan and H. H. Refai, "iICAS: Intelligent intersection collision avoidance system," in *2012 15th International IEEE Conference on Intelligent Transportation Systems*, 2012, pp. 1184–1190.

[33] A. Daubaras and M. Zilys, "Vehicle Detection based on Magneto-Resistive Magnetic Field Sensor," *Electron. Electr. Eng.*, vol. 118, no. 2, pp. 27–32, Feb. 2012.

[34] Z. Zhang, X. Li, H. Yuan, and F. Yu, "A Street Parking System Using Wireless Sensor Networks," vol. 2013, no. c, 2013.

[35] H. Zhu and F. Yu, "A Vehicle Parking Detection Method Based on Correlation of Magnetic Signals," vol. 2015, 2015.

[36] D. Liu, X. Xu, C. Fei, W. Zhu, X. Liu, G. Yu, and G. Fang, "Direction identification of a moving ferromagnetic object by magnetic anomaly," *Sensors Actuators A Phys.*, vol. 229, pp. 147–153, 2015.

[37] R. D. Komguem, R. Stanica, M. Tchuente, F. Valois, R. Domga Komguem, R. Stanica, M. Tchuente, and F. Valois, "WARIM: Wireless Sensor Networks Architecture for a Reliable Intersection Monitoring," in *17th International IEEE Conference on Intelligent Transportation Systems (ITSC)*, 2014, pp. 1226–1231.

[38] S. Taghvaeeyan and R. Rajamani, "Portable roadside sensors for vehicle counting, classification, and speed measurement," *IEEE Trans. Intell. Transp. Syst.*, vol. 15, no. 1, pp. 73–83, 2014.

[39] B. Koszteczky and G. Simon, "Magnetic-based vehicle detection with sensor networks," in *2013 IEEE International Instrumentation and Measurement Technology Conference (I2MTC)*, 2013, pp. 265–270.

[40] W. Zhang, G. Tan, and N. Ding, "Vehicle Speed Estimation Based on Sensor Networks and Signal Correlation Measurement," pp. 1–12, 2014.

[41] D.-H. Kim, K.-H. Choi, K.-J. Li, and Y.-S. Lee, "Performance of vehicle speed estimation using wireless sensor networks: a region-based approach," *J. Supercomput.*, vol. 71, no. 6, pp. 2101–2120, 2015.

[42] D. Obertov, V. Bardov, and B. Andrievsky, "Vehicle speed estimation using roadside sensors," in *2014 6th International Congress on Ultra Modern Telecommunications and Control Systems and Workshops (ICUMT)*, 2014, pp. 111–117.

[43] D. Nan, T. Guozhen, M. Honglian, L. Mingwen, and S. Yao, "Low-power Vehicle Speed Estimation Algorithm based on WSN," in *2008 11th International IEEE Conference on Intelligent Transportation Systems*, 2008, pp. 1015–1020.

[44] L. Zhang, R. Wang, and L. Cui, "Real-time traffic monitoring with magnetic sensor networks," *J. Inf. Sci. Eng.*, vol. 27, no. 4, pp. 1473–1486, 2011.

[45] X. DENG, Z. HU, P. ZHANG, and J. GUO, "Vehicle Class Composition Identification Based Mean Speed Estimation Algorithm Using Single Magnetic Sensor," *J. Transp. Syst. Eng. Inf. Technol.*, vol. 10, no. 5, pp. 35–39, Oct. 2010.

[46] H. Li, H. Dong, L. Jia, D. Xu, and Y. Qin, "Some practical vehicle speed estimation methods by a single traffic magnetic sensor," in *2011 14th International IEEE Conference on Intelligent Transportation Systems (ITSC)*, 2011, pp. 1566–1573.

[47] J. Lan, Y. Xiang, L. Wang, and Y. Shi, "Vehicle detection and classification by measuring and processing magnetic signal," *Measurement*, vol. 44, no. 1, pp. 174–180, Jan. 2011.

[48] B. Yang and Y. Lei, "Vehicle Detection and Classification for Low-Speed Congested Traffic With Anisotropic Magnetoresistive Sensor," *IEEE Sens. J.*, vol. 15, no. 2, 2015.

[49] D. Kleyko, R. Hostettler, W. Birk, and E. Osipov, "Comparison of Machine Learning Techniques for Vehicle Classification Using Road Side Sensors," *2015 IEEE 18th Int. Conf. Intell. Transp. Syst.*, pp. 572–577, 2015.

[50] W. Ma, D. Xing, A. McKee, R. Bajwa, C. Flores, S. Member, B. Fuller, P. Varaiya, S. Member, B. Fuller, P. Varaiya, C. Author, D. Xing, A. McKee, R. Bajwa, C. Flores, and B. Fuller, "A wireless accelerometer-based automatic vehicle classification prototype system," *IEEE Trans. Intell. Transp. Syst.*, vol. 15, no. 1, pp. 1–8, 2014.

[51] Y. He, Y. Du, L. Sun, and Y. Wang, "Improved waveform-feature-based vehicle classification using a single-point magnetic sensor," *J. Adv. Transp.*, vol. 49, no. 5, pp. 663–682, Aug. 2015.

[52] W. Zhang, G. Z. Tan, H. M. Shi, and M. W. Lin, "A distributed threshold algorithm for vehicle classification based on binary proximity sensors and intelligent neuron classifier," *J. Inf. Sci. Eng.*, vol. 26, no. 3, pp. 769–783, 2010.

[53] E.-H. N. E.-H. Ng, S.-L. T. S.-L. Tan, and J. G. Guzman, "Road traffic monitoring using a wireless vehicle sensor network," *2008 Int. Symp. Intell. Signal Process. Commun. Syst.*, 2009.

[54] B. Coifman and S. Kim, "Speed estimation and length based vehicle classification from freeway single-loop detectors," *Transp. Res. Part C Emerg. Technol.*, vol. 17, no. 4, pp. 349–364, Aug. 2009.

[55] C. H. Wu, J. M. Ho, and D. T. Lee, "Travel-time prediction with support vector regression," *IEEE Trans. Intell. Transp. Syst.*, vol. 5, no. 4, pp. 276–281, 2004.

[56] X. Sun and R. Horowitz, "Set of New Traffic-Responsive Ramp-Metering Algorithms and Microscopic Simulation Results," *Transp. Res. Rec. J. Transp. Res. Board*, vol. 1959, pp. 9–18, Jan. 2006.

[57] C. B. Winkler, "Work Zone Safety ITS Smart Barrel for an Adaptive Queue-Warning System," no. February, 2005.

[58] C. Monsere, C. Nolan, R. Bertini, E. Anderson, and T. El-Seoud, "Measuring the Impacts of Speed Reduction Technologies: Evaluation of Dynamic Advanced Curve Warning System," *Transp. Res. Rec.*, vol. 1918, no. 1, pp. 98–107, 2005.

[59] A. J. Kean, R. a Harley, and G. R. Kendall, "Effects of Vehicle Speed and Engine Load on Motor Vehicle Emissions," *Environ. Sci. Technol.*, vol. 37, no. 17, pp. 3739–3746, 2003.

[60] D. Kleyko, R. Hostettler, W. Birk, and E. Osipov, "Comparison of Machine Learning Techniques for Vehicle Classification Using Road Side Sensors," *2015 IEEE 18th Int. Conf. Intell. Transp. Syst.*, pp. 572–577, 2015.

[61] H. Zhu and F. Yu, "A Cross-Correlation Technique for Vehicle Detections in Wireless Magnetic Sensor Network," vol. 16, no. 11, pp. 4484–4494, 2016.

[62] "Sensor | Sensys Networks." [Online]. Available: http://www.sensysnetworks.com/products/sensor/. [Accessed: 20-Apr-2015].

[63] "Vehicle Detector WD-300 | Sensebit." [Online]. Available: http://www.sensebit.se/products/traffic-measurement/vehicle-detector-wd-300/. [Accessed: 20-Apr-2015].

[64] "M100 Wireless Vehicle Detection System." [Online]. Available: http://www.clearviewtraffic.com/golden-river/products-golden-river/art/44/m100-wireless-vehicle-detection-system.htm. [Accessed: 20-Apr-2015].

[65] H. Refai, N. Bitar, J. Schettler, and O. Al Kalaa, "The Study of Vehicle Classification Equipment with Solutions to Improve Accuracy in Oklahoma."

[66] "Aligning Oversize/Overweight Fees with Agency Costs: Critical Issues." [Online]. Available: http://www.trb.org/Main/Blurbs/169473.aspx. [Accessed: 28-Jan-2016].

[67] "Loop- and Length-Based Vehicle Classi cation , Federal Highway Administration – Pooled Fund Program," vol. 5, no. November, 2012.

[68] "Loop and Length Based Classification Pooled Fund." [Online]. Available: http://www.pooledfund.org/details/study/416. [Accessed: 03-Sep-2015].

[69] H. Wei, Q. Ai, D. Eustace, and B. Coifman, "Length-based Vehicle Classification Models using Dual-loop Data against Stop-and-Go Traffic Flow," in *Transportation Research Board 90th Annual Meeting*, 2011.

[70] B. Coifman, "Vehicle Classification from Single Loop Detectors," Mar. 2007.

[71] T. Mauga, "Development of Florida Length Based Vehicle Classification Scheme Using Support

Vector Machines," Florida State University, 2016.

[72] W. Balid, H. Tafish, and H. H. Refai, "Development of Portable Wireless Sensor Network System For Real-time Traffic Surveillance," in *18th IEEE International Conference on Intelligent Transportation Systems, IEEE - ITSC 2015, September 15-18, 2015*, 2015.

[73] W. Balid, H. Tafish, and H. H. Refai, "Versatile Real-Time Traffic Monitoring System Using Wireless Smart Sensors Networks," in *IEEE Wireless Communications and Networking Conference (WCNC), Track 4 - Services, Applications, and Business,*.

[74] W. Balid, H. Tafish, and H. H. Refai, "Intelligent Vehicle Counting and Classification Sensor for Real-Time Traffic Surveillance," *IEEE Trans. Intell. Transp. Syst.*, no. Under Review, 2016.

[75] D. L. Mills, "Computer Network Time Synchronization: The Network Time Protocol on Earth and in Space, Second Edition," Nov. 2010.

[76] J. Elson, L. Girod, and D. Estrin, "Fine-grained network time synchronization using reference broadcasts," *ACM SIGOPS Oper. Syst. Rev.*, vol. 36, no. SI, p. 147, Dec. 2002.

[77] S. Ganeriwal, R. Kumar, and M. B. Srivastava, "Timing-sync protocol for sensor networks," in *Proceedings of the first international conference on Embedded networked sensor systems - SenSys '03*, 2003, p. 138.

[78] K. Shahzad, A. Ali, and N. D. Gohar, "ETSP: An Energy-Efficient Time Synchronization Protocol for Wireless Sensor Networks," in *22nd International Conference on Advanced Information Networking and Applications - Workshops (aina workshops 2008)*, 2008, pp. 971–976.

[79] H. Xiao, C. Lu, and H. Ogai, "A Multi-hop Low Cost Time Synchronization Algorithm for Wireless Sensor Network in Bridge Health Diagnosis System," in *2012 IEEE International Conference on Embedded and Real-Time Computing Systems and Applications*, 2012, pp. 392–395.

[80] M Maróti, B Kusy, G Simon, Á Lédeczi, "The flooding time synchronization protocol," in *Proceedings of the 2nd international conference on Embedded networked sensor systems - SenSys '04*, 2004, p. 39.

[81] P. Sommer and R. Wattenhofer, "Gradient clock synchronization in wireless sensor networks," pp. 37–48.

[82] J. van Greunen and J. Rabaey, "Lightweight time synchronization for sensor networks," in *Proceedings of the 2nd ACM international conference on Wireless sensor networks and applications - WSNA '03*, 2003, p. 11.

[83] S. Youn, "A Comparison of Clock Synchronization in Wireless Sensor Networks," *Int. J. Distrib. Sens. Networks*, vol. 2013, p. 10, 2013.

[84] I. F. Akyildiz, W. Su, Y. Sankarasubramaniam, and E. Cayirci, "Wireless sensor networks: a survey," *Comput. Networks*, vol. 38, no. 4, pp. 393–422, Mar. 2002.

[85] R. Kim, T. Nagayama, H. Jo, and J. Spencer, "Preliminary study of low-cost GPS receivers for time synchronization of wireless sensors," *Proc. SPIE Sensors Smart Struct. Technol. Civ. Mech. Aerosp. Syst.*, vol. 8345, no. 1, p. 83451A--83451A--9, 2012.

[86] Z. Li, T. Braun, and D. C. Dimitrova, "Methodology for GPS Synchronization Evaluation with High Accuracy," in *2015 IEEE 81st Vehicular Technology Conference (VTC Spring)*, 2015, pp. 1–6.

[87] E. Sazonov, V. Krishnamurthy, and R. Schilling, "Wireless Intelligent Sensor and Actuator Network - A Scalable Platform for Time-synchronous Applications of Structural Health Monitoring," *Struct. Heal. Monit.*, vol. 9, no. 5, pp. 465–476, Apr. 2010.

[88] D. R. Fuhrmann, J. Stomberg, S. Nooshabadi, D. McIntire, and W. Merill, "Node Synchronization in a Wireless Sensor Network Using Unreliable GPS Signals," in *2014 IEEE Military Communications Conference*, 2014, pp. 630–636.

[89] J. Bae and B. Moon, "Time Synchronization in Wireless Sensor Networks," in *Smart Wireless Sensor Networks*, H. D. Chinh and Y. K. Tan, Eds. InTech, 2010, pp. 253–280.

[90] "ATMEL XMEGA MCU - ATxmega128A4U." [Online]. Available: http://www.atmel.com/devices/atxmega128a4u.aspx. [Accessed: 21-Apr-2015].

[91] "Freescale Digital Sensor - FXOS8700CQ." [Online]. Available: http://www.freescale.com/webapp/sps/site/prod_summary.jsp?code=FXOS8700CQ. [Accessed: 21-Apr-2015].

[92] "MEMS-Based Sensor Technology | Freescale." [Online]. Available: http://www.freescale.com/webapp/sps/site/overview.jsp?code=SNSMEMSOVERVIEW. [Accessed: 22-Apr-2015].

[93] "Synapse SM200P81 RF Engine." [Online]. Available: https://www.synapse-wireless.com/documents/products/Synapse-SM200P81-Engine-Product-Brief.pdf. [Accessed: 22-Apr-2015].

[94] "Synapse's SNAP Network Operating System," *David Ewing*. [Online]. Available: http://synapse-wireless.com/documents/white_paper/Synapse-SNAP-OS-White-Paper.pdf. [Accessed: 22-Apr-2015].

[95] "Maxim Integrated - DS3231M Real-Time Clock." [Online]. Available: http://www.maximintegrated.com/en/products/digital/real-time-clocks/DS3231M.html. [Accessed: 22-Apr-2015].

[96] "GlobalTop Technology Inc. - Titan 2 (GMS-G6)." [Online]. Available: http://www.gtop-tech.com/en/product/Titan-2-GMS-G6/GPS_Modules_Gms-g6.html. [Accessed: 22-Apr-2015].

[97] "Maxim Integrated - MAX17043 Compact, Low-Cost 1S/2S Fuel Gauges with Low-Battery Alert." [Online]. Available: http://www.maximintegrated.com/en/products/power/battery-management/MAX17043.html. [Accessed: 22-Apr-2015].

[98] "Semitec's NT-4 Glass NTC Thermistors." [Online]. Available: http://www.atcsemitec.co.uk/nt-glass-thermistors.html.

[99] "TMJ S1gma™ Series – AVX." [Online]. Available: http://www.avx.com/products/tantalum/automotive/tmj-s1gma-series/.

[100] "Industrial External GPRS Wireless Data Transmission Unit." [Online]. Available: http://www.zlg.com/wireless/wireless/product/id/16.html.

[101] M. Ramezani, J. Haddad, and N. Geroliminis, "Dynamics of heterogeneity in urban networks: aggregated traffic modeling and hierarchical control," *Transp. Res. Part B Methodol.*, vol. 74, pp. 1–19, Apr. 2015.

[102] "Econolite :: Wireless In-Ground." [Online]. Available: http://www.econolite.com/index.php/products/detection/wireless/. [Accessed: 20-Dec-2015].

[103] B. Coifman and S. Kim, "Speed estimation and length based vehicle classification from freeway single-loop detectors," *Transp. Res. Part C Emerg. Technol.*, vol. 17, no. 4, pp. 349–364, Aug. 2009.

[104] "SiT1552 Ultra-Small, Precision 32 kHz TCXO." [Online]. Available:

https://www.sitime.com/products/32-khz-temperature-compensated-oscillators-tcxo/sit1552.

[105] "Road Runner 3 Counter and Classifier Kit | Diamond Traffic." [Online]. Available: http://diamondtraffic.com/product/RoadRunner3Kit. [Accessed: 05-Sep-2015].

[106] S. Coleri, S. Y. Cheung, and P. Varaiya, "Sensor Networks for Monitoring Traffic," *Electr. Eng.*, 2004.

[107] R. Hostettler and W. Birk, "Analysis of the Adaptive Threshold Vehicle Detection Algorithm Applied to Traffic Vibrations →2, no. 2011, pp. 2150

[108] H. Lee and B. Coifman, "Identifying and Correcting Pulse-Breakup Errors from Freeway Loop Detectors," *Transp. Res. Rec. J. Transp. Res. Board*, vol. 2256, pp. 68–78, 2011.

[109] L. Chen and A. D. May, "Traffic Detector Errors and Diagnostics," *Transp. Res. BOARD*, no. 1132, pp. 82–93, 1987.

[110] B. Coifman, "Using Dual Loop Speed Traps To Identify Detector Errors," *Transp. Res. Rec.*, vol. 1683, no. 1, pp. 47–58, 1999.

[111] B. Coifman and H. Lee, "A Single Loop Detector Diagnostic: Mode On-Time Test," *Appl. Adv. Technol. Transp. Proc. Ninth Int. Conf. ASCE*, pp. 623–628, 2006.

[112] P. Cheevarunothai, Y. Wang, and N. Nihan, "Using Dual-Loop Event Data to Enhance Truck Data Accuracy," *Transp. Res. Rec.*, vol. 1993, no. 1, pp. 131–137, 2007.

[113] L. N. Jacobson, N. L. Nihan, and J. D. Bender, "DETECTING ERRONEOUS LOOP DETECTOR DATA IN A FREEWAY TRAFFIC MANAGEMENT SYSTEM," *Transp. Res. Rec.*, no. 1287, pp. 151–166, 1990.

[114] D. Cleghorn, F. L. Hall, and D. Garbuio, "IMPROVED DATA SCREENING TECHNIQUES FOR FREEWAY TRAFFIC MANAGEMENT SYSTEMS," *Transp. Res. Rec.*, no. 1320, pp. 17–23, 1991.

[115] R. Turochy and B. Smith, "New Procedure for Detector Data Screening in Traffic Management Systems," *Transp. Res. Board*, no. 1727, pp. 127–131, 2000.

[116] C. Chen, "Detecting Errors And Imputing Missing Data For Single Loop Surveillance Systems," *Transp. Res. Board*, vol. 1855, no. January, pp. 160–167, 2003.

[117] D. Hinkley, "On the ratio of two correlated normal random variables," *Biometrika*, vol. 56, no. 3, pp. 635–639, 1969.

[118] M. Isaksson, "Vehicle Detection using Anisotropic Magnetoresistors," CHALMERS UNIVERSITY OF TECHNOLOGY, Goteborg, Sweden, 2008.

[119] F. Palhinha, D. Carona, A. Serrador, and T. Canas, "Wireless Magnetic Based Sensor System for Vehicles Classification," *Procedia Technol.*, vol. 17, pp. 632–639, 2014.

[120] C. M. Bishop, "Pattern Recognition and Machine Learning (Information Science and Statistics)," Aug. 2006.

[121] C. Seiffert, T. M. Khoshgoftaar, J. Van Hulse, and A. Napolitano, "RUSBoost: A Hybrid Approach to Alleviating Class Imbalance," *IEEE Trans. Syst. Man, Cybern. - Part A Syst. Humans*, vol. 40, no. 1, pp. 185–197, Jan. 2010.

[122] S. Kaewkamnerd, J. Chinrungrueng, R. Pongthornseri, and S. Dumnin, "Vehicle classification based on magnetic sensor signal," *2010 IEEE Int. Conf. Inf. Autom.*, pp. 935–939, 2010.

[123] R. Wang, L. Zhang, K. Xiao, R. Sun, and L. Cui, "EasiSee: Real-Time Vehicle Classification and Counting via Low-Cost Collaborative Sensing," *IEEE Trans. Intell. Transp. Syst.*, vol. 15, no. 1, pp. 414–424, 2014.

[124] H. X. Liu and J. Sun, "Length-based vehicle classification using event-based loop detector data," *Transp. Res. Part C Emerg. Technol.*, vol. 38, pp. 156–166, Jan. 2014.

[125] L. Wu and B. Coifman, "Improved vehicle classification from dual-loop detectors in congested traffic," *Transp. Res. Part C Emerg. Technol.*, vol. 46, pp. 222–234, Sep. 2014.

[126] S.-T. (Cindy) Jeng and S. G. Ritchie, "Real-Time Vehicle Classification Using Inductive Loop Signature Data," *Transp. Res. Rec. J. Transp. Res. Board*, vol. 2086, no. 1, pp. 8–22, 2009.

[127] S. Cheung, S. Coleri, B. Dundar, S. Ganesh, C.-W. Tan, and P. Varaiya, "Traffic Measurement and Vehicle Classification with Single Magnetic Sensor," *Transportation Research Record*, vol. 1917, no. 1. pp. 173–181, 2005.

[128] H. Liu, S.-T. (Cindy) Jeng, A. Tok, and S. G. Ritchie, "Commercial Vehicle Classification Using Vehicle Signature Data," in *the 88th Annual meeting of the Transportation Research Board*, 2009.

[129] R. Bajwa, R. Rajagopal, P. Varaiya, R. Kavaler, and N. Street, "In-Pavement Wireless Sensor Network for Vehicle Classification Categories and Subject Descriptors," pp. 85–96, 2011.

[130] Y. He, Y. Du, and L. Sun, "Vehicle Classification Method Based on Single-Point Magnetic Sensor," *Procedia - Soc. Behav. Sci.*, vol. 43, pp. 618–627, Jan. 2012.

[131] N. V. Chawla, K. W. Bowyer, L. O. Hall, and W. P. Kegelmeyer, "SMOTE: synthetic minority over-sampling technique," *J. Artif. Intell. Res.*, vol. 16, no. 1, pp. 321–357, 2002.

[132] G. E. A. P. A. Batista, R. C. Prati, and M. C. Monard, "A study of the behavior of several methods for balancing machine learning training data," *ACM SIGKDD Explor. Newsl.*, vol. 6, no. 1, p. 20, Jun. 2004.

[133] S. Jessberger, "Axle and Length Classification," *Federal Highway Administration 2011 Highway Information Seminar*, 2011. [Online]. Available: https://www.fhwa.dot.gov/policyinformation/presentations/his_axlelength2011.cfm. [Accessed: 03-Jan-2016].

[134] A. D. Polyanin and A. V. Manzhirov, *Handbook of Mathematics for Engineers and Scientists*, vol. 27. CRC Press, 2006.

[135] J. Shlens, "A Tutorial on Principal Component Analysis," Apr. 2014.

[136] D. a Reynolds, "Gaussian Mixture Models," *Encycl. Biometric Recognit.*, vol. 31, no. 2, pp. 1047–64, 2008.

[137] A. K. Singh, "The EM Algorithm and Related Statistical Models," *Technometrics*, vol. 48, pp. 148–148, 2006.

[138] W. Balid, "Fully-Autonomous Self-Powered Intelligent Wireless Sensor for Real-Time Traffic Surveillance in Smart Cities," University of Oklahoma, 2016.

[139] W. Balid, H. Tafish, and H. H. Refai, "Versatile Real-Time Traffic Monitoring System Using Wireless Smart Sensors Networks," in *IEEE Wireless Communications and Networking Conference (WCNC), Track 4 - Services, Applications, and Business,*.

[140] H. Tafish, W. Balid, and H. H. Refai, "Cost effective Vehicle Classification using a single wireless magnetometer," in *2016 International Wireless Communications and Mobile Computing Conference (IWCMC)*, 2016, pp. 194–199.

APPENDIX A: IVCCS$_{G1}$ SCHEMATIC, LAYOUT, BOM

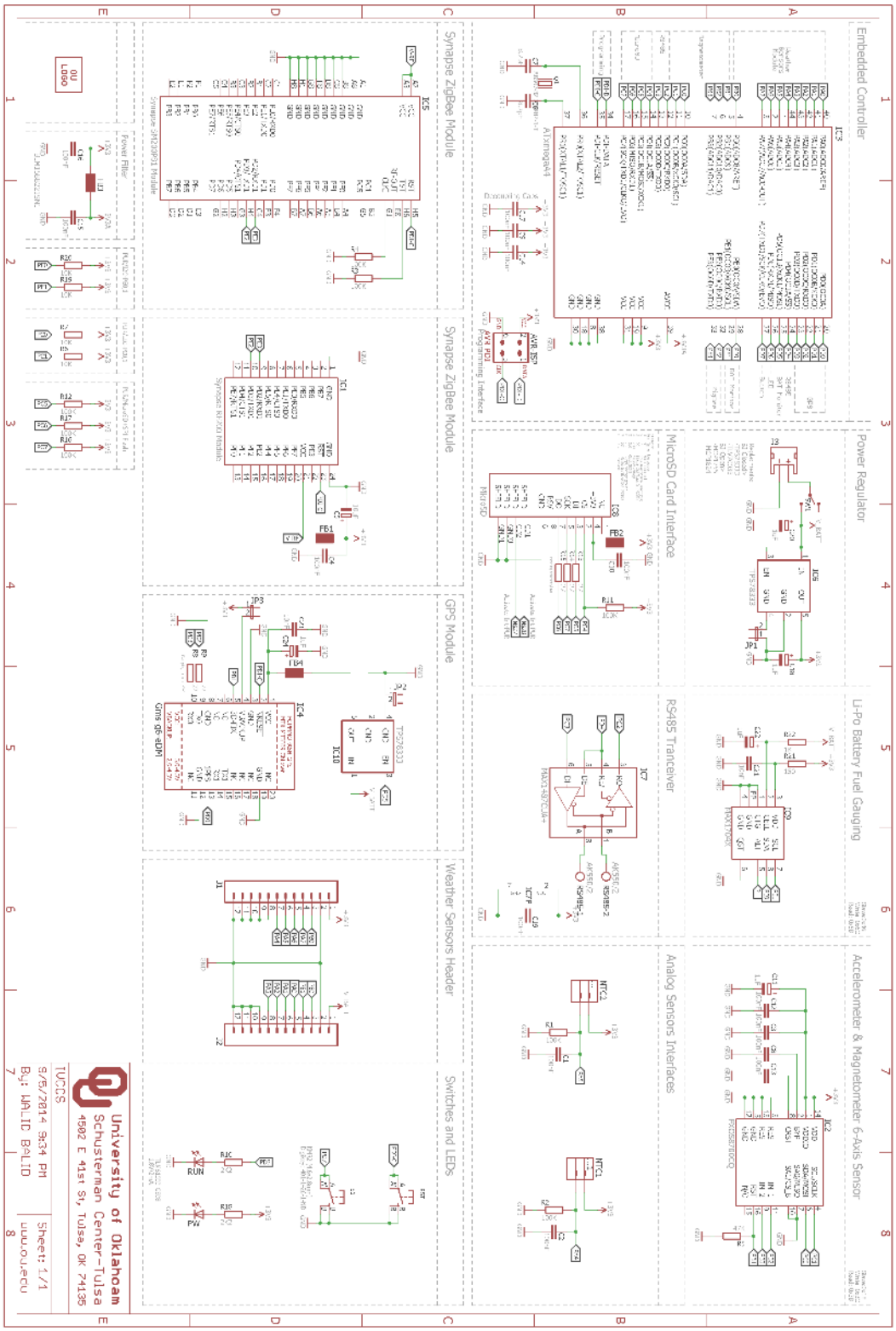

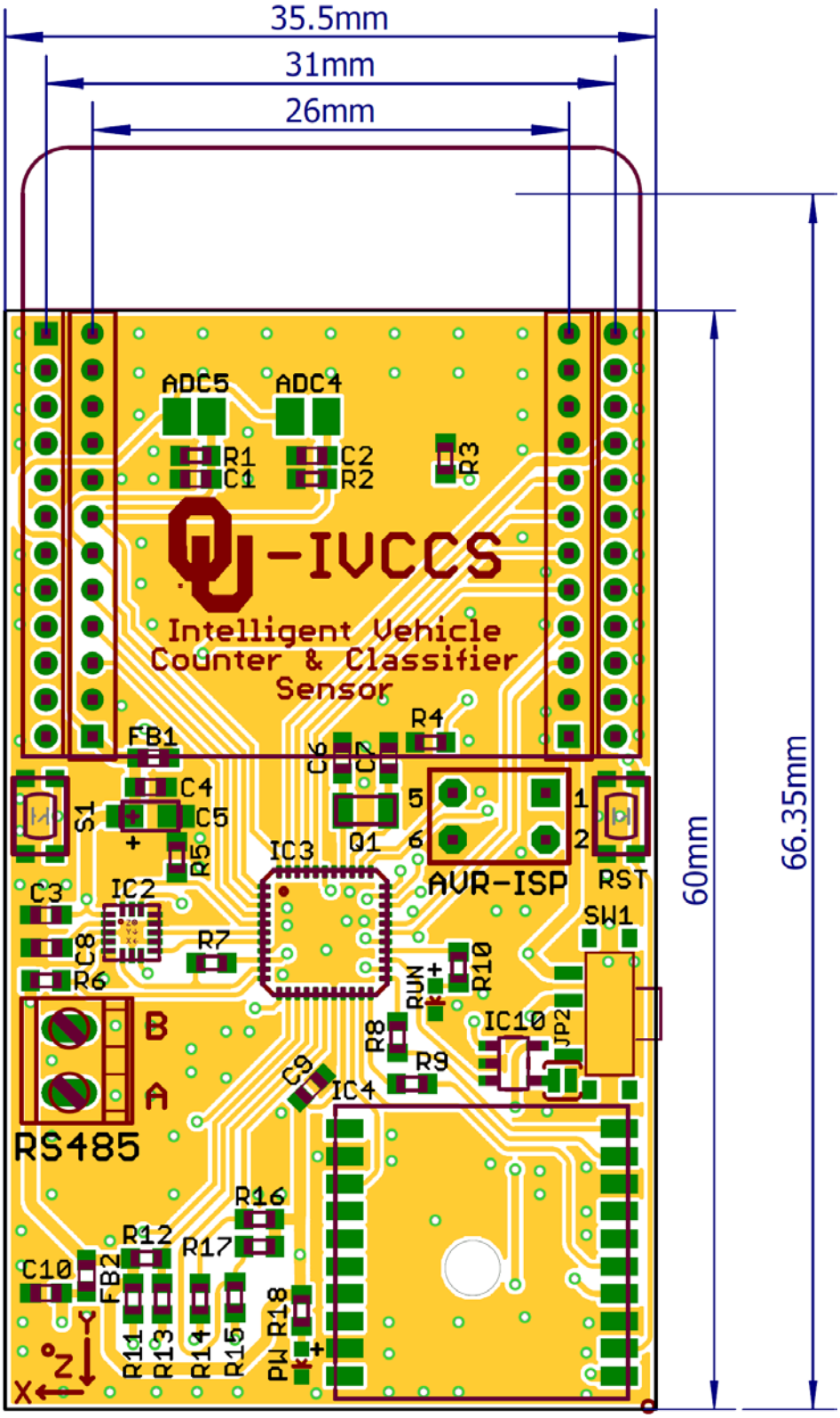
35.5mm
31mm
26mm
60mm
66.35mm
ADC5
ADC4
R1
C1
C2
R2
R3
R4
FB1
C4
C5
C6
C7
S1
Q1
IC3
IC2
C3
C8
R6
R5
R7
AVR-ISP
RST
SW1
JP2
IC10
R10
RUN
R8
R9
C9
IC4
B
A
RS485
R16
R12
R17
C10
FB2
R11
R13
R14
R15
PW
R18
Y
Z
X
Intelligent Vehicle
Counter & Classifier
Sensor

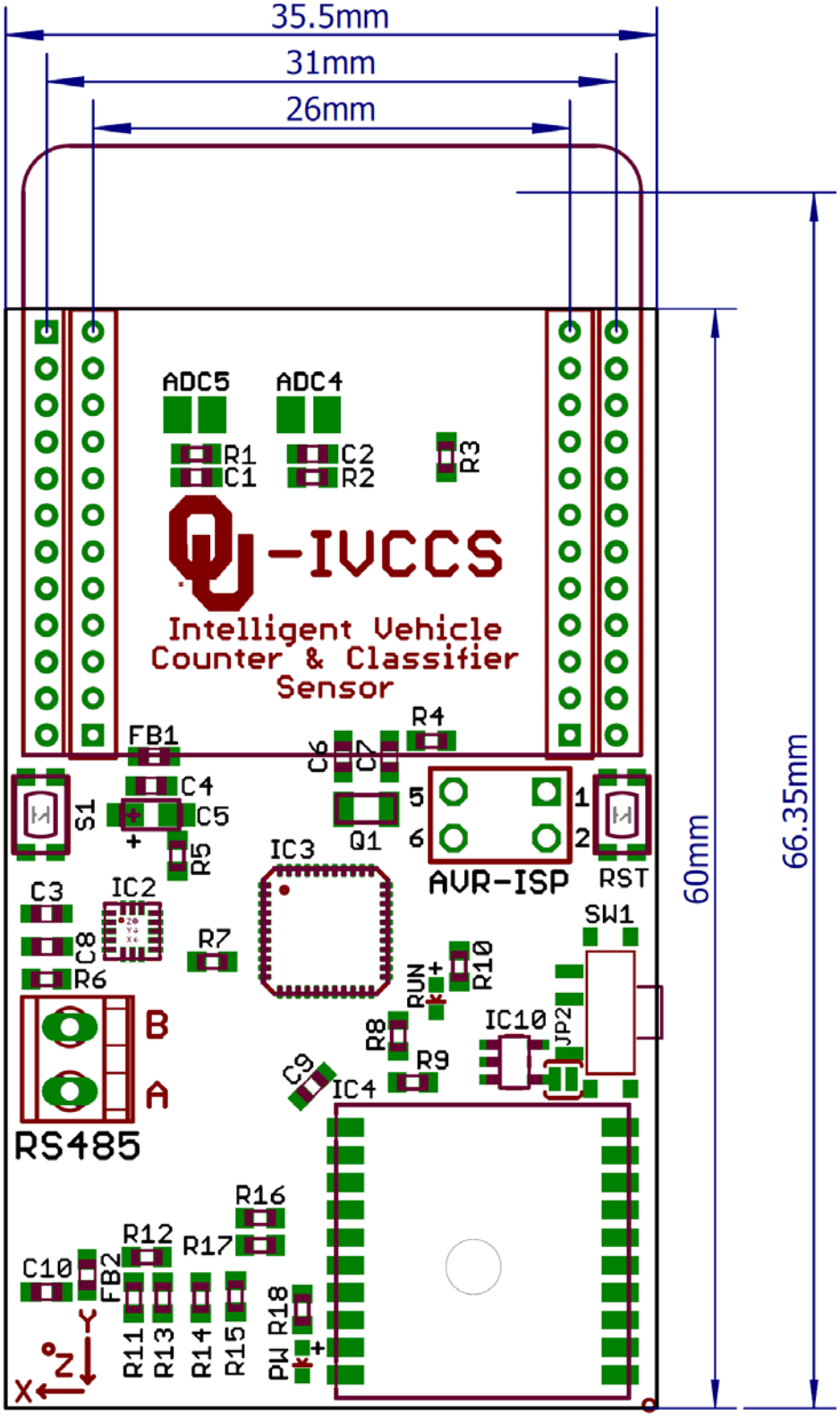
35.5mm
31mm
26mm
66.35mm
60mm
ADC5
ADC4
R1
C1
C2
R2
R3
-IVCCS
Intelligent Vehicle
Counter & Classifier
Sensor
FB1
R4
C6
C7
C4
C5
S1
Q1
5
6
1
2
AVR-ISP
RST
R5
IC3
C3
IC2
C8
R6
R7
SW1
RUN
R10
IC10
JP2
R8
R9
C9
IC4
B
A
RS485
R16
R12
R17
C10
FB2
R11
R13
R14
R15
PW
R18
Y
Z
X

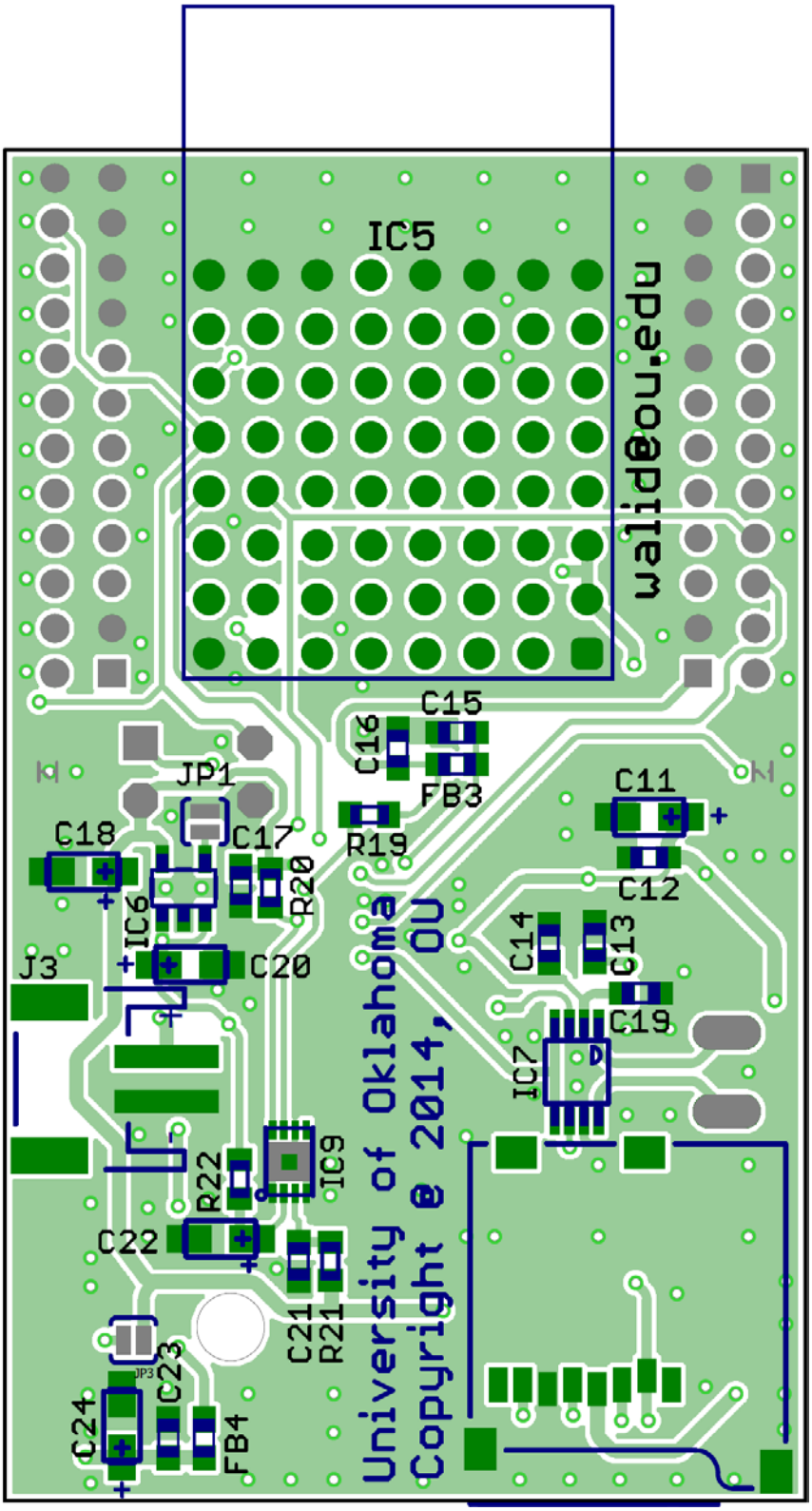
IC5
walid@ou.edu
C15
C16
FB3
JP1
C18
C17
R19
C11
R20
C12
IC6
C14
C13
J3
C20
C19
IC7
IC9
R22
C22
C21
R21
C23
JP3
C24
FB4
University of Oklahoma OU
Copyright @ 2014,

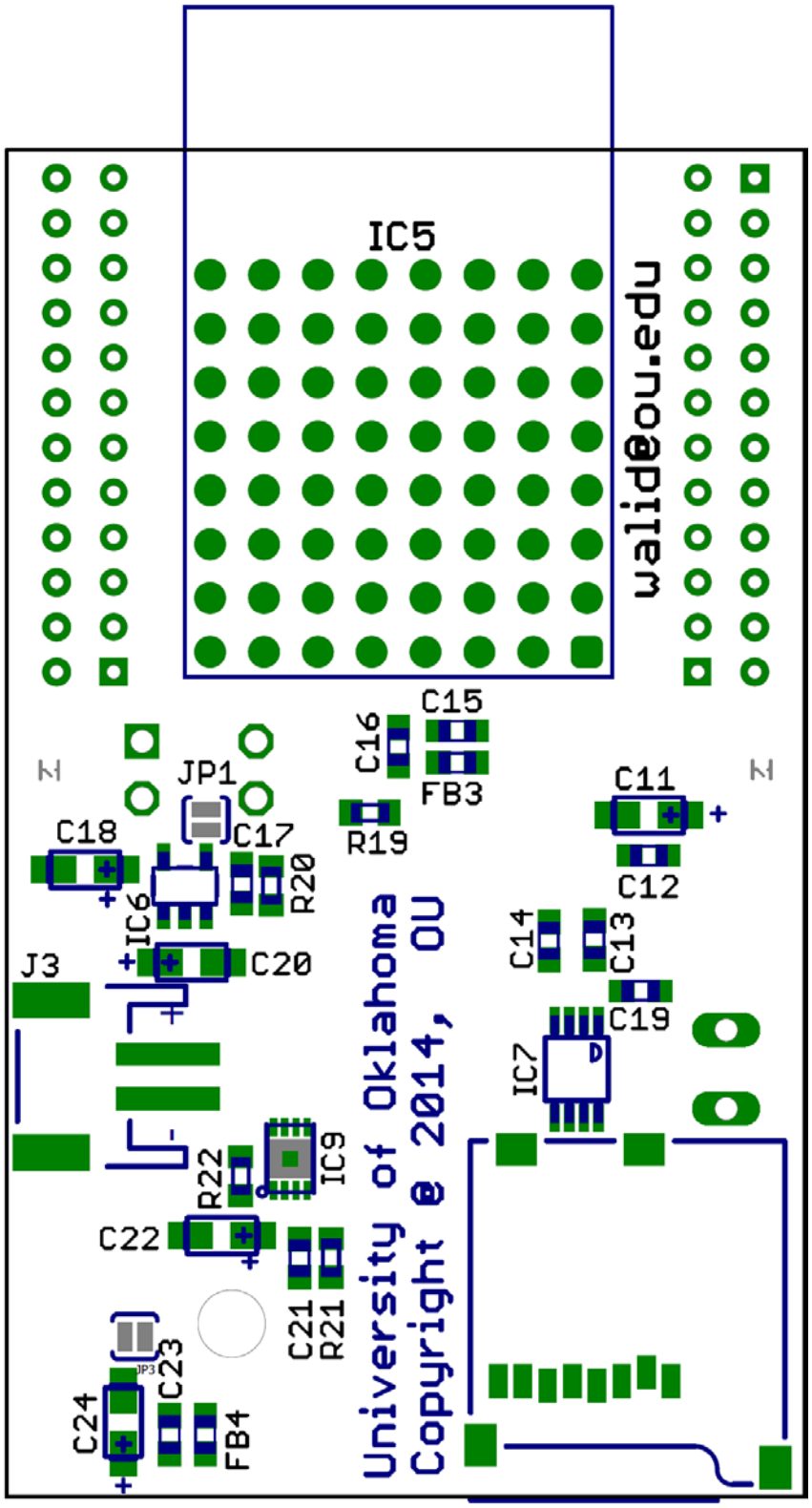
IC5
walid@ou.edu
C15
C16
FB3
R19
JP1
C18
C17
R20
IC6
C20
J3
C11
C12
C14
C13
C19
IC7
R22
IC9
C22
C21
R21
C23
C24
FB4
University of Oklahoma
Copyright @ 2014, OU

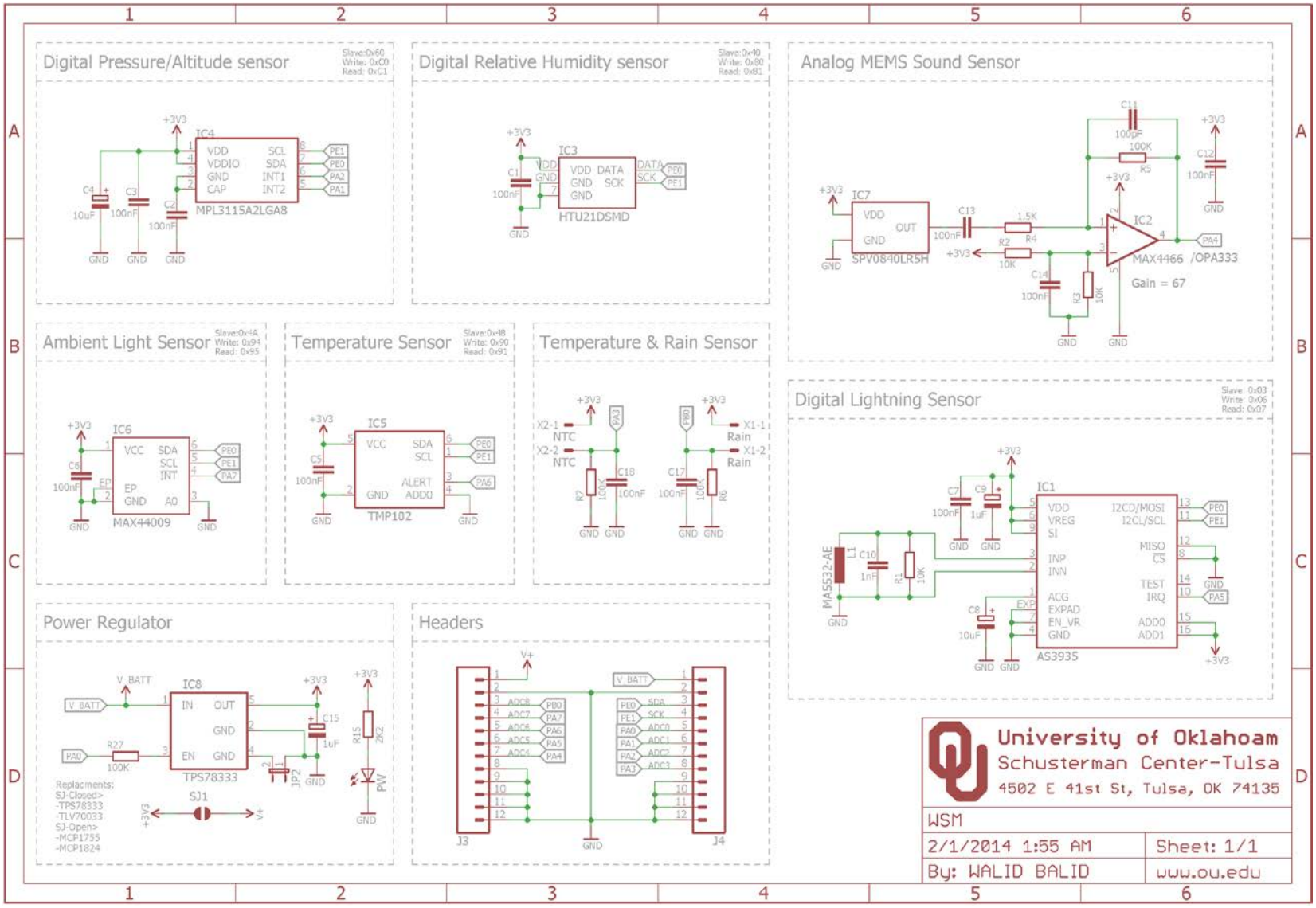
Digital Pressure/Altitude sensor
Slave:0x60
Write: 0xC0
Read: 0xC1
IC4
MPL3115A2LGA8
Digital Relative Humidity sensor
Slave:0x40
Write: 0x80
Read: 0x81
IC3
HTU21DSMD
Analog MEMS Sound Sensor
IC7
SPV0840LR5H
IC2
MAX4466 /OPA333
Gain = 67
Ambient Light Sensor
Slave:0x4A
Write: 0x94
Read: 0x95
IC6
MAX44009
Temperature Sensor
Slave:0x48
Write: 0x90
Read: 0x91
IC5
TMP102
Temperature & Rain Sensor
NTC
Rain
Digital Lightning Sensor
Slave: 0x03
Write: 0x06
Read: 0x07
IC1
AS3935
Power Regulator
IC8
TPS78333
Replacments:
SJ-Closed>
-TPS78333
-TLV70033
SJ-Open>
-MCP1755
-MCP1824
Headers
J3
J4
University of Oklahoam
Schusterman Center-Tulsa
4502 E 41st St, Tulsa, OK 74135
WSM
2/1/2014 1:55 AM
Sheet: 1/1
By: WALID BALID
www.ou.edu

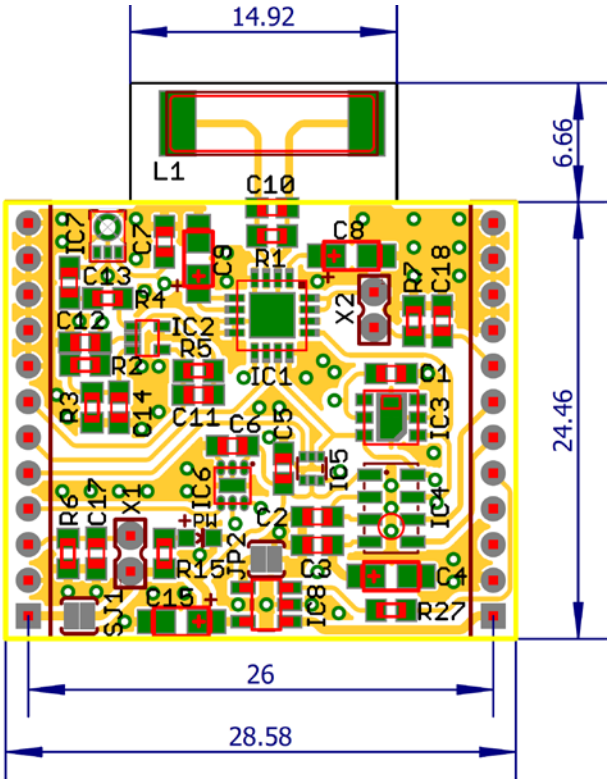
14.92
6.66
L1
C10
24.46
26
28.58

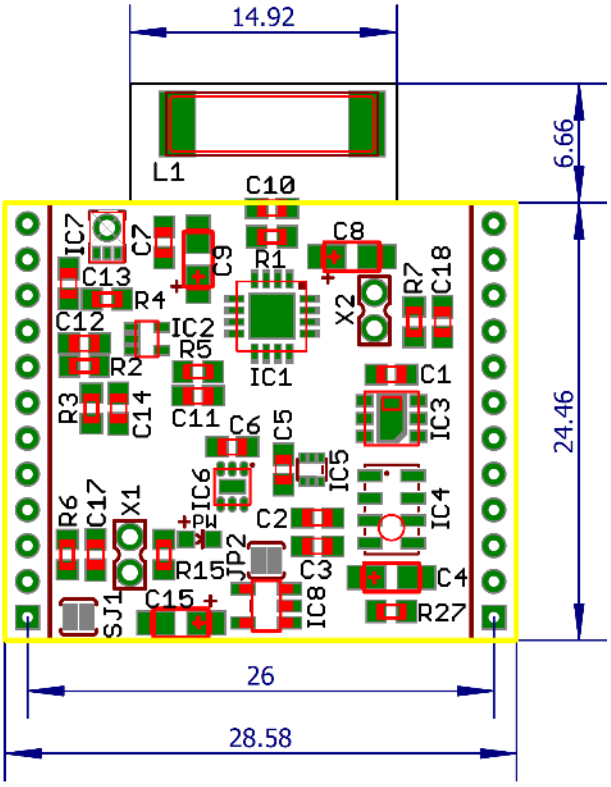
14.92
6.66
L1
C10
24.46
26
28.58

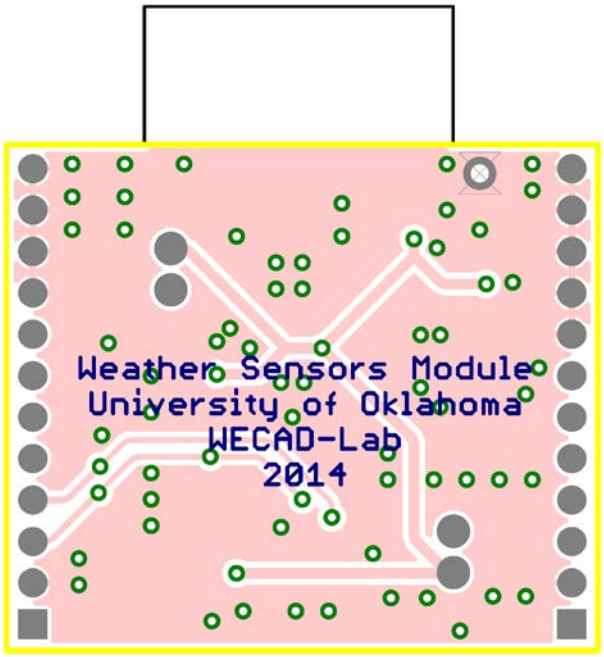
Weather Sensors Module
University of Oklahoma
WECAD-Lab
2014

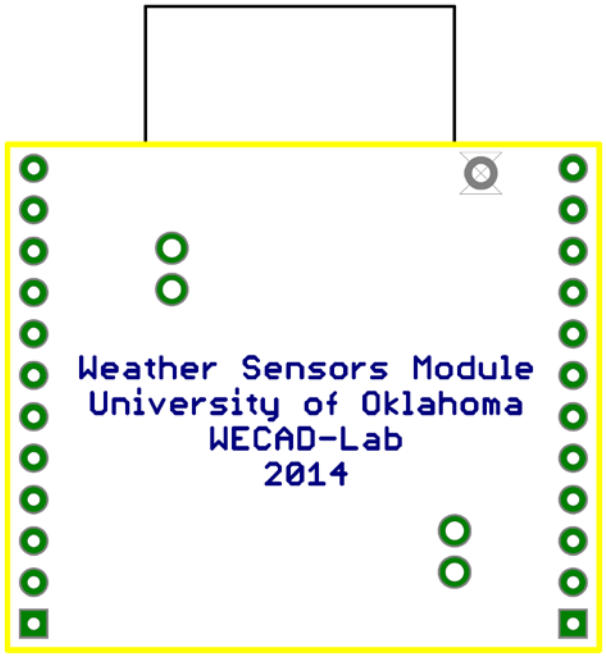
Weather Sensors Module
University of Oklahoma
WECAD-Lab
2014

*i*VCCS$_{G1}$ BOM								
Qty	**Value**	**Device**	**Package**	**Identifier**	**Description**	**Supplier**	**Price**	**Part number**
1	NA	AVR-PDIVERT	AVR-ISP-6	J1	CONN HEADER .100" DUAL STR 6POS	digikey	$0.20	S2011EC-40-ND
4	NA	FB	603	FB1, FB2, FB3, FB4	Chip Ferrite Bead	digikey	$0.10	490-5985-1-ND
1	NA	GPS_FGPMMOPA6H	FGPMMOPA6H	IC8	GPS Module - MTK MT3	G.Top	$15.00	From OK Repr.
1	NA	JST_2MM_MALE	JST-2-SMD	J2	Mates to single-cell	digikey	$0.56	455-1749-1-ND
2	NA	LED0603	LED-0603	LED1, PW	LEDs	digikey	$0.17	475-2506-1-ND
2	100K OHM 1% @ 25C	NTC Thermistors	*	NTC1, NTC2	THERMO STRNG 100K OHM 1% NTC	digikey	$0.90	490-5631-ND
2	NA	M12-2MM	1X12-2MM	J3, J4	CONN 2MM VERT SGL ROW 12POS	digikey	$1.00	S5751-12-ND
1	NA	RF200P81	RF200P81	IC7	RF Engine® Model SM2	digikey	$0.00	51765
1	NA	SM200P81	SM200P81	IC9	RF Engine® Model SM2	robot	$15.00	746-1031-1-ND
1	NA	SWITCH_SPDT	KPS-1290	SW1	Side-actuated SPDT s	digikey	$0.82	401-2016-1-ND
3	NA	SW_TACT_SMT4.6X2.8	BTN_KMR2_4.6X2.8	RST, S3, S4	SMT Tact Switches	digikey	$0.58	401-1426-1-ND
12	100K	R-EU 100K	R0603	R3, R6, R7, R8, R10, R11, R16, R21, R22, R25, R26, R27	RESISTOR	digikey	$0.10	311-100KHRCT-ND
14	100nF	C-EUC603 100nF	C0603	C1, C6, C7, C8, C9, C10, C11, C13, C14, C15, C16, C22, C23, C24	CAPACITOR	digikey	$0.50	399-1096-1-ND
4	10K	R-EU 10K	R0603	R1, R2, R12, R13	RESISTOR	digikey	$0.10	311-10.0KHRCT-ND
2	10nF	C-EUC603 10nF	C0603	C5, C21	CAPACITOR	digikey	$0.10	399-7841-1-ND
1	10uF	CPOL-USCT3216T 10uF	CT3216	C19	POLARIZED CAPACITOR	mouser	$0.10	74-TL3A106K016C1700
1	150	R-EU 150R	R0603	R5	RESISTOR	digikey	$0.10	311-150HRCT-ND
1	1K	R-EU 1K	R0603	R4	RESISTOR	digikey	$0.10	311-1.00KHRCT-ND
5	1uF	CPOL-USCT3216T 1uF	CT3216	C2, C3, C4, C12, C20	POLARIZED CAPACITOR	mouser	$0.10	74-TL3A105K035C6000
5	27	R-EU 27R	R0603	R9, R19, R20, R23, R24	RESISTOR	digikey	$0.10	311-27.0HRCT-ND
2	2K2	R-EU 2K2	R0603	R15, R17	RESISTOR	digikey	$0.10	311-2.20KHRCT-ND
1	47K	R-EU 47K	R0603	R14	RESISTOR	digikey	$0.10	311-47.0KHRCT-ND
2	8.2pF	C-EUC603 8.2pF	C0603	C17, C18	CAPACITOR	digikey	$0.10	399-9130-1-ND
1	ABS07-32.768KHZ-1-T	Q_FC135	FC135	Q1	CRYSTAL 32.768KHZ 12.5PF SMD	digikey	$1.28	535-9808-1-ND
1	ATxmegaA4	ATXMEGA64A4U-MH	QFN44	IC1	Atmel XMega A4 serie	digikey	$3.00	ATXMEGA128A4U-MHRCT-ND
1	FXOS8700CQ	FXOS8700CQ	QFN-16_0.5MM	IC6	FXOS8700CQ 6-Axis Se	digikey	$1.80	FXOS8700CQR1CT-ND
1	MAX1704X	MAX17043	TDFN-8	IC4	MAX17043/MAX17044: B	digikey	$1.20	MAX17043G+T-ND
1	MicroSD	USD-SOCKETNEW	MICRO-SD-SOCKET-PP	IC2	microSD Socket	digikey	$1.84	101-00581-59-1-ND
1	TPS78333	TPS783XXSOT23-5	SOT23-5	IC3	Voltage Regulator	digikey	$0.92	296-27178-1-ND
1	W25Q256FV	W25QXXXSO8-208	SO08-208	IC5	SpiFlashR Memories w	digikey	$2.76	W25Q128FVSIG-ND
1	BAT	BAT	NA	BAT	3.7V/2000mA Li-Po Battery	China	$5.00	NA
1	NA	Shell	NA	NA	Enclosure	China	$2.00	NA
1	FR4	PCB Fabrication	NA	NA	Printed Circuit Board	China	$0.25	NA
1	Lead-Free	PCB Assembly	NA	NA	Assembly	China	$1.50	NA
						TOTAL	$57.48	

Weather Sensing Module BOM

Qty	Value	Device	Package	Identifier	Description	Supplier	Price	Part number
1	NA	LED0603	LED-0603	PW	LEDs	digikey	$0.17	475-2506-1-ND
2	NA	M12-2MM	1X12-2MM	J3, J4	Male Header 2mm	digikey	$0.77	3M9330-ND
1	1.5K	R-EU	R0603	R4	RESISTOR, European s	digikey	$0.01	311-1.50KHRCT-ND
4	100K	R-EU	R0603	R5, R6, R7, R27	RESISTOR, European s	digikey	$0.04	311-100KHRCT-ND
11	100nF	C-EUC603	C0603	C1, C2, C3, C5, C6, C7, C12, C13, C14, C17, C18	CAPACITOR, European	digikey	$0.50	399-1096-1-ND
1	100pF	C-EUC603	C0603	C11	CAPACITOR, European	digikey	$0.10	399-8926-1-ND
3	10K	R-EU	R0603	R1, R2, R3	RESISTOR, European s	digikey	$0.10	311-10.0KHRCT-ND
2	10uF	CPOL-EUCT3216	CT3216	C4, C8	POLARIZED CAPACITOR,	mouser	$0.10	74-TL3A106K016C1700
1	1nF	C-EUC603	C0603	C10	CAPACITOR, European	digikey	$0.10	399-7835-1-ND
2	1uF	CPOL-EUCT3216	CT3216	C9, C15	POLARIZED CAPACITOR,	mouser	$0.10	74-TL3A105K035C6000
1	2K2	R-EU	R0603	R15	RESISTOR, European s	digikey	$0.10	311-2.20KHRCT-ND
1	AS3935	AS3935	16LDMLPQ	IC1	IC SENSOR LIGHTNING	digikey	$8.12	AS3935-BQFTCT-ND
1	HTU21D	HPP828E031	HTU21D	IC3	Digital Relative Hum	digikey	$8.31	223-1144-1-ND
1	MA5532-AE	MA5532-AE	COILCRAFT	L1	MA5532-AE; RFID Tran	coilcraft	$1.50	MA5532-AEB
1	MAX44009	MAX44009	6-UTDFN	IC6	Ambient Light Sensor	digikey	$3.57	MAX44009EDT+TCT-ND
1	MAX4466	MAX4466SC70	SC70	IC2	Single gate rail-to-	mouser	$0.69	700-MAX4466EXKT
1	MPL3115A2LGA8	MPL3115A2LGA8	LGA8	IC4	Altimeter/Pressure S	digikey	$2.88	MPL3115A2-ND
1	100K OHM 1% @ 25C	NTC Thermistors	*	NTC	NTC Thermistors	digikey	$0.90	490-5631-ND
1	SPV0840LR5H	SPV0840LR5H	SPV0840LR5H	IC7	Omnidirection bottom	mouser	$1.82	721-SPV0840LR5H-B
1	TMP102	TMP102	SOT563	IC5	I2C degC temp sensor	digikey	$1.72	296-26834-1-ND
1	TPS78333	TPS783XXSOT23-5	SOT23-5	IC8	Voltage Regulator	digikey	$0.92	296-27178-1-ND
1	FR4	PCB Fabrication	NA	NA	Printed Circuit Board	China	$0.25	NA
1	Lead-Free	PCB Assembly	NA	NA	Assembly	China	$1.00	NA
						TOTAL	**33.77**	